2023

# Understanding the Role of Flower Code in Tumorigenesis

Dénise dos Reis da Rosa de Azevedo Camacho

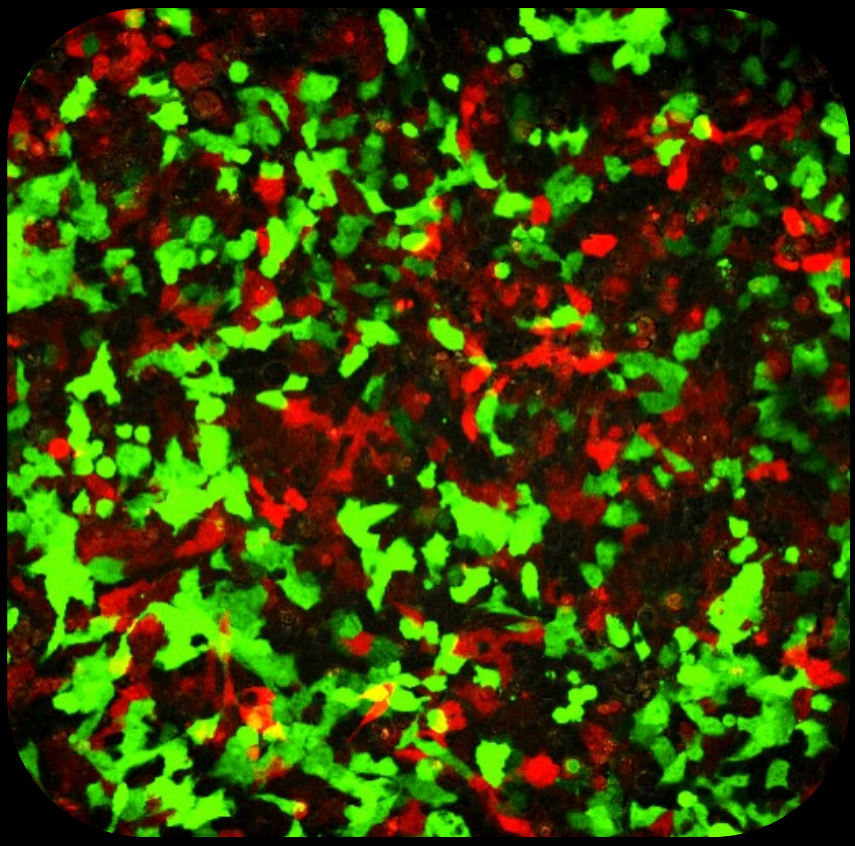

Dissertation presented to obtain the **Ph.D degree in Molecular Biosciences,** speciality in **Biochemistry**

Oeiras, May, 2023

**INSTITUTO DE TECNOLOGIA QUÍMICA E BIOLÓGICA ANTÓNIO XAVIER** | UNIVERSIDADE NOVA DE LISBOA

# Understanding the Role of Flower Code in Tumorigenesis

Dénise dos Reis da Rosa de Azevedo Camacho

Dissertation presented to obtain the Ph.D degree in Molecular Biosciences

Speciality: Biochemistry

Instituto de Tecnologia Química e Biológica António Xavier| Universidade Nova de Lisboa

Research work coordinated by: Champalimaud Foundation

Oeiras, May, 2023

UNIVERSIDADE NOVA DE LISBOA

# Understanding the Role of Flower Code in Tumorigenesis

Dénise dos Reis da Rosa de Azevedo Camacho

Dissertation presented to obtain the Ph.D degree in Molecular Biosciences

Speciality: Biochemistry

Instituto de Tecnologia Química e Biológica António Xavier| Universidade Nova de Lisboa

Supervisor: Doctor Eduardo Moreno

Research work coordinated by: Champalimaud Foundation

Oeiras, May, 2023

*Síma ta Kaí Ta Labanta!!*

**ACKNOWLEDGMENTS**

During my Ph.D., I was lucky to have amazing people who supported and guided me unconditionally. I will not be able to describe in words how important you were in my life during these past years. But let's try ;)

I want to thank my supervisor Eduardo Moreno for accepting me in his lab and for all our scientific discussions during these years. I want to thank Rajan Gogna for all the guidance and discussions and for helping design the project. Also, the opportunity to be part of different projects allows me to enrich my knowledge and competitiveness. A special thanks to Esha Madan for her friendship and for teaching me everything at the beginning of my Ph.D., for her patience and kindness during this process.

I want to thank my thesis committee: Vera Martins and Rita Fior, for all the support and discussion during this journey. You were the fundamental pieces!!!

I want to thank my Ph.D. program PGCD, for the fellowship and a special thanks to Patricia Beldade, Joana Sá, Carla, and Leonor. I am grateful to my colleagues from the 4th edition, especially to Fred (Pulmão), “as viadas” Benilde, Eunice e Deisy, and Ednilson. And to all the students from all editions of the PGCD!!!

I would also like to thank Fundação para a Ciência e Tecnologia (FCT) for the Ph.D. fellowship and the ITQB Academics for all the support in the paperwork. Also, thanks to Teresa Dias from the Champalimaud Graduate Studies.

I big thank all the past and present members of the Moreno Lab Gang. Specially to the “coleguitas” Ana Queirós, Mário Aguilar and Miguel Pinto. For literally everything! The friendship, scientific discussion, and the fights during lunchtime when we disagree on specific subjects. I would also like to thank another important lab member, Catarina Sénior, for always being there to support, help and guide. Thank you for all the great advice and friendship!! For Maria Bettencourt (my partner in the crime), Carolina Rodrigues, Catarina Júnior, Andrea el doctor, Dina, Irene, Inês,

Catarina Normal, Mariana, Andrés, Isaac, Pedro and all the remaining past members of the big Cell Fitness Lab.

Big thanks to Lizyane, Zeta, Abdul, Abdul (from IGC), Jovin, and all the Lemon House people for your friendship and the good conversations to alleviate the stress. You are fantastic!

Thank you to the friends I made at Champalimaud Foundation and the good moments during the happy hours, retreats, and scientific seminars.

For all the Champalimaud platforms: Advanced BioImaging and BioOptics Experimental Platform, especially to Anna and David for helping me set-up and analyze experiments. Flow Cytometry platform for sorting the cells and machine settings. Especially to Ana Vieira, Renato Colaço and André Mozes. To Raquel Tomás and Ana Filipa from the Molecular Platform for the clones and lentiviral production, and to Maria Vito from the Glass Wash Platform for preparing the solutions. I also would like to thank Tânia from the Histopathology Platform for analyzing all the IHC slides and for the discussions.

A big thank you to my family! Without you, nothing of this would have been possible. Thanks to all my sisters and brothers who supported me in this process. It was not easy to be far from home, but I felt you were always here with me. An immeasurable thank you to my parents: unfortunately, my father is not here to witness this, although he was already called me “doutorinha” since I started my Ph.D. And finally, to my beautiful mom, who always believed in me even when I doubted myself. Thank you for supporting me in everything and anything, Mamusca!!

**SUMÁRIO**

As células do nosso corpo estão constantemente interagindo e trocando informações. Um subconjunto dessas interações permite a deteção e eliminação de células estranhas, danificadas ou perigosas. A manutenção da homeostase do tecido saudável envolve fatores intrínsecos e extrínsecos da célula que regulam a seleção celular, o destino e a morte. Em certas situações, as células podem comparar sua aptidão celular relativa e ativar mecanismos que asseguram a eliminação de células não saudáveis. Este processo endógeno é denominado competição celular.

A comparação de aptidão celular é usada em *Drosophila* para a deteção e eliminação de células viáveis, mas danificadas, para retardar o envelhecimento e prevenir malformações do desenvolvimento. As células de *Drosophila* usam um mecanismo único de seleção celular baseado em "impressões digitais de aptidão". A deteção e eliminação de células menos aptas permite que as moscas retardem o envelhecimento, eliminem estruturas defeituosas durante o desenvolvimento e substituam tecidos velhos durante a regeneração. As "impressões físicas" usadas pelas células de *Drosophila* são baseadas em uma proteína de membrana que pertence à família Flower. As proteínas Flower que indicam aptidão reduzida foram chamadas de isoformas Flower Lose, porque são expressas em células marcadas para serem eliminadas, chamadas de "células perdedoras". No entanto, e notavelmente, a presença de isoformas de Flower perdedoras na membrana celular de uma determinada célula não implica que a célula será removida. Se as células vizinhas tiverem níveis semelhantes de proteínas perdedoras, a célula não será eliminada. A eliminação dos perdedores através do mecanismo de impressão digital de aptidão, ocorre quando em contato direto célula-célula com células que expressam a isoforma vencedora da Fwe. Claramente, em *Drosophila*, as proteínas Flower atuam como determinantes moleculares diretos da aptidão celular que são usadas para detetar e eliminar muitos tipos de células viáveis, mas relativamente menos saudáveis.

Em humanos, a seleção celular foi descrita durante o desenvolvimento e o cancro, mas normalmente depende da competição indireta por fatores de sobrevivência ou nutrientes. Um sistema para comparação de aptidão celular ativo em humanos até então era desconhecido. Estudamos as isoformas de Flower humanas e descobrimos que duas das proteínas Flower humanas (1 e 3) se comportam como isoformas perdedoras, enquanto as restantes (2 e 4) se comportam como isoformas vencedoras. As isoformas "vencedoras" dão às células uma vantagem competitiva sobre aquelas que expressam isoformas "perdedoras". As células que expressam a perdedora, não são eliminadas se as células vizinhas tiverem níveis semelhantes de "perdedoras", agindo, portanto, como impressões digitais de aptidão. Além disso, os tumores humanos se beneficiam dessa seleção baseada em aptidão. O tecido cancerígeno mostra um aumento da expressão de "vencedoras" e prolifera na presença de células do estroma que expressam a isoforma "perdedora". Isso permite que o cancro ganhe vantagem competitiva para crescer e ocupar espaço. A inibição da FWE reduz o crescimento do tumor, a metástase e quimio-sensibilização. Nossos resultados ilustram como mecanismos antigos de reconhecimento e seleção celular são conservados e ativos em humanos, impactando o crescimento do tumor.

Portanto, descobrir novos interatores de FWE é crucial para entender o mecanismo de seleção celular e bloquear a progressão do cancro. Para identificar os interatores de FWE, sob expressamos na linha celular do cólon HCT116 as isoformas "vencedoras" e "perdedoras" de FWE e realizamos imunoprecipitação seguida de espectroscopia de massa. O candidato mais promissor foi o biomarcador de cancro PTMA, que descobrimos ser altamente expresso em células "vencedoras" e pouco expresso em células $FWE^{KO}$. Além disso, descobrimos que a regulação negativa do PTMA nas células "vencedoras" bloqueava a competição celular, impedindo a eliminação das células "perdedoras". Também observamos que a localização celular de PTMA muda do núcleo em células $FWE^{KO}$ para o citoplasma nas células "vencedoras". O padrão de expressão citoplasmática e nuclear de PTMA foi também observado em amostras de pacientes. Curiosamente, a expressão de

PTMA foi maior na frente invasiva do tumor em contato com o estroma, onde ocorre a competição celular. Sabendo que FWE e PTMA estão mais expressos no cancro, juntos, esses resultados sugerem uma interação entre eles para promover o crescimento e a progressão do cancro. Nossas descobertas podem abrir caminho para o desenvolvimento de novas estratégias de medicamentos para tratar o cancro, visando essa interação.

**Palavras-chave:** Competição celular, PTMA, Flower, Interação proteína-proteína, Cancro colorretal.

## ABSTRACT

Cells in our body are constantly interacting and exchanging information. A subset of such interactions allows the detection and elimination of foreign, damaged or dangerous cells. Maintenance of healthy tissue homeostasis involves cell-intrinsic and extrinsic factors that regulate cell selection, fate and death. In certain situations, cells may compare their relative cell fitness and activate mechanisms that secure the elimination of unhealthy cells. This endogenous process is termed cell competition.

Cell-fitness comparison is used in *Drosophila* for detection and elimination of viable but impaired cells, to delay aging and prevent developmental malformations. *Drosophila* cells use a unique mechanism of cell selection based on “fitness fingerprints”. Detection and elimination of less fit cells allow flies to delay aging, eliminate defective structures during development and replace old tissues during regeneration. The “fitness fingerprints” used by *Drosophila* cells is based on a membrane protein that belong to the Flower family. The Flower proteins that indicate reduced fitness have been called Flower Lose isoforms, because they are expressed in cells marked to be eliminated, called “Loser cells”. However, and remarkably, the presence of Flower Lose isoforms at the cell membrane of a particular cell does not imply that the cell will be removed. If neighboring cells have similar levels of Lose proteins, the cell will not be eliminated. The elimination of the losers through the fitness fingerprint mechanism occurs when in direct cell-cell contact with FWE win expressing cells. Clearly, in Drosophila, Flower proteins act as direct molecular determinants of cell fitness which are used to detect and eliminate many types of viable but relatively less healthy cells.

In humans, cell selection has been described during development and cancer, but normally relies on indirect competition for survival factors or nutrients. Whether a system for cell-fitness comparison is active in humans was unknown. Here we study human Flower isoforms and found that two of the human Flower proteins (1 and 3)

behave as Lose isoforms, whereas the remaining (2 and 4) behave as Win isoforms. “Win” isoforms give cells a competitive advantage over those expressing “Lose” isoforms. Lose-expressing cells are not culled if neighboring cells have similar levels of Lose, therefore acting as fitness fingerprints. Moreover, human tumors benefit from this fitness-based selection. Cancer tissue shows increased Win expression and proliferate in presence of Lose-expressing stroma cells. This allows cancer to gain competitive advantage to growth and to occupy space. Flower inhibition reduces tumor growth, metastasis and provides chemo-sensitization. Our results illustrate how ancient mechanisms of cell recognition and selection are conserved and active in humans impacting tumor growth.

Therefore, uncovering novel flower interactors is crucial to understand the mechanism of cell selection and block to impair cancer progression. To identify FWE interactors, we overexpressed in the colon cell line HCT116 the win and lose isoforms of FWE and performed Immunoprecipitation followed by Mass Spec. The most promising candidate was the cancer biomarker PTMA, which we found to be highly expressed in winner cells and poorly expressed in $FWE^{KO}$ cells. Furthermore, we discovered that PTMA downregulation in the winners blocked cell competition, preventing loser cell elimination. We also observed that PTMA subcellular localization shifts from the nucleus in $FWE^{KO}$ to the cytoplasm in the winner cells. The cytoplasmic and nuclear expression pattern of PTMA was also observed in patient samples. Interestingly, PTMA expression was higher in the invasive front of the tumor in contact with the stroma, where cell competition occurs. Knowing that FWE and PTMA are more expressed in cancer, together these results suggest an interaction between them to promote cancer growth and progression. Our findings might open the way to the development of new drug strategies to treat cancer by targeting this interaction.

**Keywords:** Cell Competition, PTMA, Flower, Protein-protein interaction, Colorectal cancer.

## ABBREVIATIONS

| | |
|---|---|
| % | Percentage |
| BRAF | B-Raf Proto-Oncogene, Serine/Threonine Kinase |
| BSA | Bovine serum albumin |
| Ca2+ | calcium |
| CACFD1 | Calcium channel flower homolog |
| Cas9 | CRISPR associated protein 9 |
| CC | Cell Competition |
| cDNA | complementary Deoxyribonucleic Acid |
| CO2 | Carbon dioxide |
| CRC | Colorectal cancer |
| CRISPR | Clustered Regularly Interspaced Short Palindromic Repeats |
| CT | Cycle Threshold |
| DAPI | 4',6-diamidino-2-phenylindole |
| dFwe | Drosophila Flower |
| DMEM | Dulbecco's Modified Eagle Medium |
| DMSO | Dimethyl Sulfoxide |
| dMyc | Drosophila Myc |
| DNA | Deoxyribonucleic acid |
| DPP | Decapentaplegic |
| E-cad | Epithelial cadherin/E-cadherin |
| ECM | Extracellular matrix |
| EDAC | Epithelial defense against cancer |
| EGF | Epidermal growth factor |
| EMT | Epithelial Mesenchymal Transition |
| ESMO | European Society for Medical Oncology |
| F-actin | Filamentous actin |
| FACS | Fluorescence-Activated Cell Sorting |
| FBS | Fetal bovine serum |

| | |
|---|---|
| FC | Fold change |
| FCS-A | Forward Scatter - area |
| Fcyto | Flow cytometry |
| FDA | Food and Drug Administration |
| FDR | False Discovery Rate |
| FO | FOLFOX |
| Fwe | Flower |
| GAPDH | Glyceraldehyde-3-phosphate dehydrogenase |
| GFP | Green Fluorescence Protein |
| GO | Gene Ontology |
| GSEA | Gene set enrichment analysis |
| h | Hours |
| H3 | Histone 3 |
| HER2 | Human epidermal growth factor receptor 2 |
| hFWE | Human Flower |
| ICB | Immune checkpoint blocker |
| IHC | Immunohistochemistry |
| IP | Immunoprecipitation |
| IRES | Internal Ribosome Entry Site |
| ITH | Intratumor heterogeneity |
| JNK | Jun N-terminal Kinase |
| KEGG | Kyoto Encyclopedia of Genes and Genome |
| KO | Knockout |
| Mass Spec | Mass spectrometry |
| mFwe | Mouse Flower |
| ml | milliliters |
| mM | millimolar |
| MMR | Mismatch Repair Genes |
| MRI | Magnetic resonance imaging |

| | |
|---|---|
| mRNA | messenger Ribonucleic acid |
| MYC | Myc proto-oncogene protein |
| N | Numbers |
| NCCN | National Comprehensive Cancer Network |
| NGS | Next Generation Sequencing |
| NHEJ | Non-homologous End Joining |
| NS | Non significant |
| PBS | Phosphate-buffered saline |
| PD-1 | Programmed death 1 |
| PD-L1 | Programmed death-ligand 1 |
| PDX | patient derived xenografts |
| PFA | Paraformaldehyde |
| PTEN | Phosphatase And Tensin Homolog |
| Pval | P value |
| RAD | Radiotherapy |
| RFP | Red Fluorescence Protein |
| RNA | Ribonucleic acid |
| RNA-seq | RNA-sequencing |
| RT | Room temperature |
| RT-qPCR | Real Time quantitative Polymerase Chain Reaction |
| SD | Standard deviation |
| shRNA | Short hairpin RNA |
| SPARC | Secreted Protein Acidic and Rich in Cysteine |
| TP53 | Tumor Protein P53 |
| UTR | Untranslated Region |
| WHO | World Health Organization |
| WT | wildtype |
| µg | micrograms |
| µL | microliters |

| | |
|---|---|
| μm | micrometers |
| μM | micromolar |

## TABLE OF CONTENTS

## INDEX OF FIGURES

**Chapter 1**



**Chapter 2**



**Chapter 3**

## INDEX OF TABLES

### Chapter 1



### Chapter 3

# CHAPTER 1

# GENERAL INTRODUCTION

## 1.1 CANCER

Cancer ranks as a primary cause of mortality and a significant barrier to raising life expectancy[1]. In 112 of 183 nations, cancer is the first or second major cause of death before the age of 70, and it ranks third or fourth in another 23 countries, according to estimates from the World Health Organization (WHO) in 2019[1].

Cancer occurs when cells in an organism begin to grow uncontrollably due to mutations in their DNA, resulting in tumors or other abnormal growths. While there are many different types of cancer, they all share certain characteristics such as uncontrolled cell growth and invasion into healthy tissue surrounding them (Figure 1).

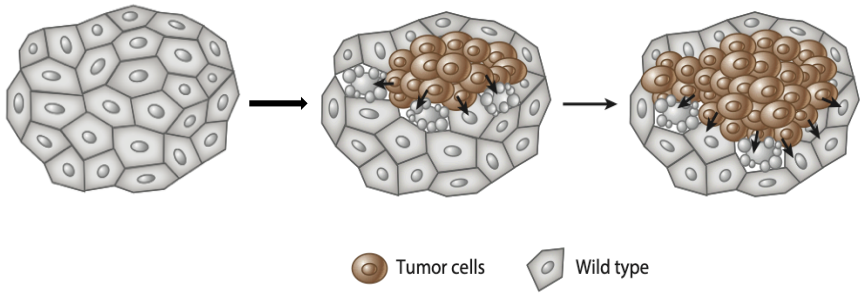


**Figure 1 - Tumor development and invasiveness behavior.** Adapted from[2].

There have been numerous advances made toward understanding how cancer works as well as developing treatments over the past few decades. However, much work still needs to be done before we can fully understand this complex disease. Research into potential cancer treatments has focused on traditional methods such as chemotherapy and radiation therapy alongside newer techniques like immunotherapy which, uses antibodies designed specifically for targeting tumor cells without affecting normal ones nearby or throughout the body. Additionally, research has also explored ways to identify individuals at risk so preventive measures may be taken earlier rather than later if necessary. This includes identifying biomarkers associated with certain cancers through blood tests or imaging scans like

Magnetic Resonance Imaging (MRI) which allow doctors more insight into what is happening inside a patient body before any symptoms arise from these abnormalities.

Cancer is caused by both internal factors (such as inherited mutations, hormones, and immune conditions) and environmental/acquired factors (such as tobacco, diet, radiation, and infectious organisms). Exploring how genetics, diet, lifestyle choices, environmental exposures (such as air pollution), hormones and other factors might contribute to an individual's risk for developing certain types of cancers is extremely urgent. Additionally, determine how these same factors affect tumor growth rates or response to treatment options like chemotherapy or radiation therapy. All while considering potential side effects associated with therapies used in treating patients afflicted with various forms of cancerous tumors/disease states.

## 1.2 THE HALLMARKS OF CANCER

The Hallmarks of Cancer is a set of characteristics that have been commonly observed in cancer cells. Each hallmark is essential for tumor formation and progression and together they form the basis for our understanding of how cancer works.

Professors Weinberg and Hanahan postulated in the beginning of 2000 that cells have unique capacities as they move closer to a neoplastic state[3]. They were referred to as cancer hallmarks and provided a helpful framework for comprehending tumor development. Eight hallmark capabilities and two enabling attributes are currently embodied by the Hallmarks of Cancer. The two preliminary "emerging hallmarks" introduced in 2011[4], "reprogramming cellular metabolism" and "avoiding immune destruction," in addition to the six acquired capabilities proposed in 2000[3], have received enough validation to be included in the core set. In addition to the overarching "genome instability and mutation," which together were fundamentally involved in activating the eight hallmark (functional) capabilities required for tumor

growth and progression, the 2011 follow-up added "tumor-promoting inflammation" as a second enabling characteristic[4].

The hallmarks of cancer graphic have been adapted to incorporate four additional proposed emerging hallmarks and enabling characteristics involving “unlocking phenotypic plasticity,” “nonmutational epigenetic reprogramming,” “polymorphic microbiomes,” and “senescent cells” (Figure 2 - C).

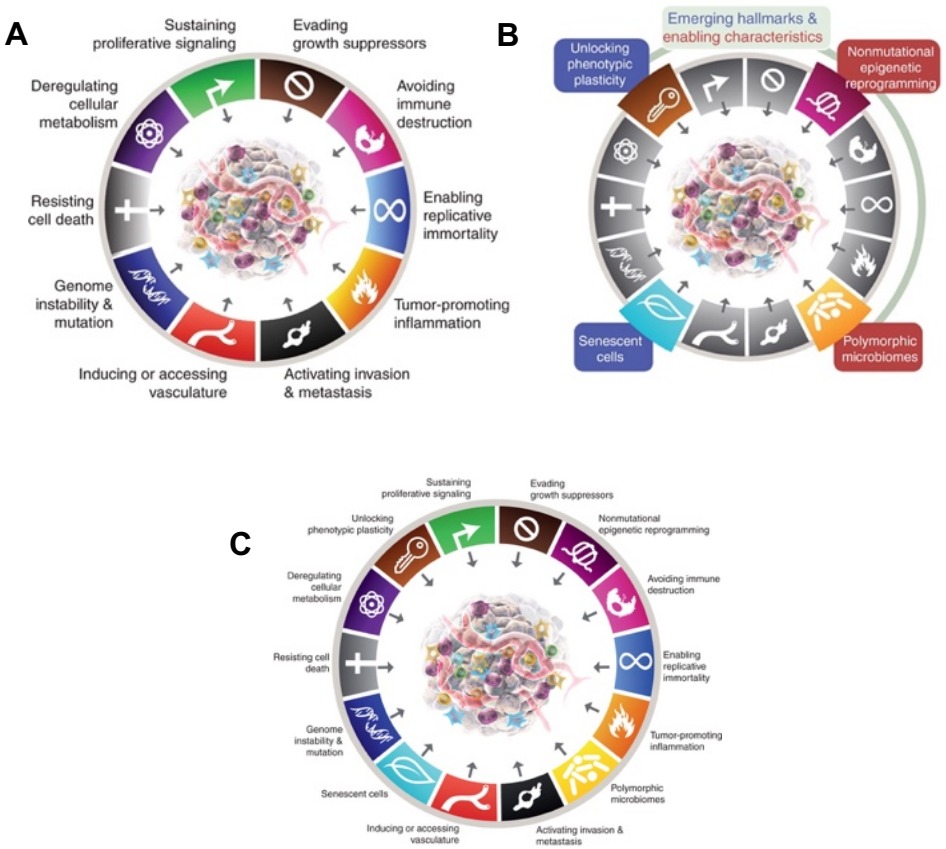


**Figure 2 - The Hallmarks of Cancer. A)** Currently Hallmarks of Cancer; **B)** Incorporation of additional proposed emerging hallmarks and enabling characteristics; **C)** The new core conceptualization of the hallmarks of cancer. Adapted from[4].

In order to encourage discussion, debate, and experimental elaboration, this treatise raises the possibility that some or all of the four new parameters will be recognized as being applicable to various types of human cancer and thus appropriate to be incorporated into the fundamental conceptualization of the hallmarks of cancer.

Understanding hallmarks is critical for the development of effective cancer therapies, as each hallmark represents a potential target for intervention. In the following lines we are going to explore more about some of the hallmarks of cancer.

Sustained proliferative signaling refers to the ability of cancer cells to continuously signal their own proliferation even when normal cellular signals would stop them from doing so. This is done through genetic mutations or epigenetic changes which allow the tumor-promoting genes to be expressed more than they should be normally. Evading growth suppressors refer to how some cancers can bypass pathways that usually keep cell division under control by mutating certain proteins or turning off other proteins involved in suppressing abnormal cell division. This allows uncontrolled reproduction of these mutated cancerous cells[3,4].

Resisting cell death is another hallmark where apoptosis (programmed cellular suicide) does not occur as it would with healthy noncancerous cells due to mutations preventing such an event from happening. This allows mutated cancerous cells to live longer than they otherwise should do if left unchecked by any form of apoptosis mechanism present within healthy noncancerous tissue/cells. Enabling replicative immortality involves telomerase activity which allows for unlimited replication potential without undergoing senescence (aging process). Inducing angiogenesis involves stimulating new blood vessel formation around tumors via secreted cytokines and chemokines. Thus, providing oxygenated nutrients necessary for further tumor progression while also helping spread those same malignant tissues throughout the body via metastasizing effects[3,4].

In conclusion, the Hallmarks of Cancer provide us with an insight into how different types of malignancies arise and progress over time as well as their potential

therapeutic targets needed in order to combat them effectively, therefore, providing us with better hope of achieving successful treatment outcomes.

## 1.3 COLORECTAL CANCER (CRC)

### 1.3.1 EPIDEMIOLOGY

Colorectal cancer (CRC) is the third most common cancer worldwide and the second most common cause of cancer-related death beaten only by lung cancer. Annually, 900 000 deaths are related to CRC[5].

CRC is the second most prevalent cancer among women (9.4%) and third in men (10.6%)[1]. Although, the mortality rate of CRC in women is 9.5% taking third place, after breast (15.5%) and Lung (13.7%) cancer. In men, CRC mortality rate takes also third place in the ranking with 9.3%, after Lung (21.5%) and Liver (10.5%) cancer. Western nations account for the majority of CRC cases, but due to advancements achieved in health systems and the introduction of screening programs, their percentage of CRC-related deaths has been decreasing[5].

The percentage of CRC patients already with metastasis at the time of the diagnosis is around 20% which can compromise the disease response. After receiving surgical treatment, 40% of patients with stage II-III cancer die from recurrence during the following five years[6]. About 90% of patients with stage IV illness had metastasis to the liver, lung, brain, or peritoneum. Liver metastases are frequently only discovered once the illness has progressed, and even when resection is used in conjunction with advanced adjuvant systemic regimens, only 20% of cure is observed, with 70% facing recurrence[7,8].

### 1.3.2 RISK FACTORS

Personal characteristics or behaviors are considered risk factors since they enhance the probability of developing colorectal cancer. Age is the primary risk factor

for colorectal cancer. CRC is uncommon (apart from inherited cancers) before the age of fifty, but it is considerably more common among individuals over fifty years old[9,10].

Additionally, heavy alcohol consumption, cigarette smoking, and ingesting of red or processed meat also play an important role. However, it appears that taking calcium supplements and consuming whole grains, fiber, and dairy products reduces the risk. Another significant risk factor for CRC is obesity, which is associated with a sedentary lifestyle[5,10].

The existence of a positive family history of CRC, particularly in relatives who were younger than fifty at the time of diagnosis, is another risk factor that should be taken into consideration. An increased risk due to familial history can be derived from inherited mutations or the environment[11].

Risk factors which are related to lifestyle can be reduced by implementing modest lifestyle changes in terms of dietary and physical activity habits. Moderate physical exercise has been shown to boost metabolic rates and gastrointestinal motility as well as, over time, to increase metabolic efficiency and lower blood pressure[10,12].

### 1.3.3 SIGNALING PATHWAY

Colorectal cancer (CRC) is a complex disease that can be caused by various genetic and environmental factors. One of the majors signaling pathways involved in CRC development is the Wnt signaling pathway, which plays a critical role in regulating cell proliferation, differentiation, and survival[13,14].

The Wnt signaling pathway is activated when Wnt ligands bind to frizzled (Fz) receptors and low-density lipoprotein receptor-related protein (LRP) co-receptors on the cell surface. This leads to the stabilization and nuclear translocation of beta-

catenin, a transcription factor that regulates the expression of downstream target genes[14].

In normal cells, the Wnt signaling pathway is tightly regulated by a complex network of proteins that control the stability of beta-catenin. One of these proteins is adenomatous polyposis coli (APC), which promotes the degradation of beta-catenin by recruiting it to a complex containing the E3 ubiquitin ligase, beta-transducing repeat-containing protein (beta-TrCP). In CRC, mutations in the APC gene or other genes in the Wnt signaling pathway can lead to the accumulation of beta-catenin and the constitutive activation of downstream target genes, such as cyclin D1 and c-myc, that promote cell proliferation and inhibit apoptosis[13,14].

Another important signaling pathway involved in CRC is the MAPK/ERK pathway, which is activated by growth factors and cytokines and regulates cell growth and differentiation. In CRC, mutations in the KRAS or BRAF genes can lead to the constitutive activation of the MAPK/ERK pathway and contribute to the development of tumor cells[15,16].

Other pathways that may be involved in CRC include the PI3K/Akt/mTOR pathway, which regulates cell survival and metabolism, and the TGF-beta pathway, which can act as a tumor suppressor or promoter depending on the stage of CRC development[15,16].

Overall, the development and progression of CRC involve complex interactions between multiple signaling pathways, and understanding these pathways is essential for developing new therapies and improving patient outcomes.

### 1.3.4 TREATMENT

Colorectal cancer (CRC) treatment depends on the stage of the disease, the location and size of the tumor, the patient age and overall health, and other individual factors. The main treatment options for CRC include surgery, chemotherapy, radiation therapy, and targeted therapy[17,18].

In addition to these standard treatments, there are also emerging treatments such as immunotherapy and gene therapy that are being studied for their potential in treating CRC. It is important to note that a multidisciplinary team of healthcare professionals, including medical oncologists, surgeons, radiation oncologists, and other specialists, work together to develop a treatment plan that is tailored to the individual patient needs.

Surgery is usually the first line of defense against colorectal cancer when it has been detected early enough to be removed surgically without causing any further damage to surrounding organs or tissues in the body. Radiation Therapy uses high-energy X-rays directed towards affected area in order to destroy remaining malignant cells after surgical resection while minimizing the risk of damaging healthy tissue nearby thus helping reduce the recurrence rate by eliminating residual disease left behind postoperatively. Chemotherapy uses drugs to destroy rapidly dividing cells such as tumor cells in order to reduce their growth and spread throughout the body. Targeted therapy uses drugs that target specific molecules or proteins in cancer cells, such as EGFR or VEGF, to block their growth and spread. Examples of targeted therapy drugs for CRC include cetuximab, panitumumab, etc. This type of treatment can be especially helpful when other treatments are not effective against advanced stages of colorectal cancers with certain genetic mutations present within them[18].

Tyrosine kinase inhibitors (TKIs) are a group of pharmacologic agents that interfere with the activity of specific enzymes known as tyrosine kinases by several modes of inhibition[19]. These enzymes play a crucial role in various cellular processes, including cell growth, division, and angiogenesis (the formation of new blood vessels). TKI can be generally categorized into small molecules and macromolecules

(e.g., monoclonal antibodies, polypeptides, antibody–drug conjugates, and nucleic acids)[20,21]. Ninety tyrosine kinases have been found in the human genome, including thirty-two cellular tyrosine kinases and fifty-six receptor tyrosine kinases[19].

In the context of cancer, abnormal activation of tyrosine kinases is often associated with uncontrolled cell growth and the development of tumors. TKIs are designed to target and inhibit these kinases, thereby disrupting the signaling pathways that contribute to cancer progression. These pathways may involve intracellular kinases or the receptor tyrosine kinase[21–23]. The potency, mechanism of action, selectivity, and safety profile of different TKIs are influenced by how selectively they bind to their targets[24].

TKIs work by blocking the activity of tyrosine kinases, which are often associated with cell surface receptors. Many TKIs are designed to target specific receptor tyrosine kinases (RTKs) involved in cancer growth. Different TKIs may have varying specificities, targeting different tyrosine kinases. Common targets include vascular endothelial growth factor receptors (VEGFR), epidermal growth factor receptors (EGFR), platelet-derived growth factor receptors (PDGFR), and others[25].

Targeted therapies such as tyrosine kinase inhibitors (TKIs) aim to interfere with the biological processes that control the proliferation of malignant cells. It has been approved for the treatment of various cancers, including colorectal cancer. They are often used in advanced or metastatic stages of the disease, and some TKIs are indicated when standard treatments have not been effective. Regorafenib is an example of a TKI used in colorectal cancer treatment. It is an oral multi-kinase inhibitor that targets various protein kinases involved in tumor angiogenesis and oncogenesis (the process of tumor formation). It had been approved for the treatment of metastatic colorectal cancer in patients who had previously received standard therapies without success. It is often used as a last-line treatment option. Regorafenib inhibits specific receptors, including vascular endothelial growth factor receptors (VEGFR), platelet-derived growth factor receptors (PDGFR), and fibroblast growth

factor receptors (FGFR). By blocking these receptors, regorafenib interferes with angiogenesis and tumor cell proliferation. Axitinib, lenvatinib, and sorafenib are other TKIs that have been investigated for their potential in colorectal cancer therapy[19,20,23,25–27]. It is essential to note that the use of TKIs and other cancer treatments is highly individualized. The choice of therapy depends on factors such as the specific characteristics of the tumor, the patient's overall health, and the presence of any genetic mutations.

The type of treatment to be chose also depends on the patient MSI status, as either “MSI-high (MSI-H)” or “MSS (non-MSI).” More than 80% of the colorectal cancer patients are classified as MSS (Microsatellite Stable) or non-MSI**.** Generally, they are one of the most highly mutated tumors and also do not respond to immunotherapies. Biomarkers such as the *RAS family,* BRAF or HER2, can help to identify the best treatment option. For instance, the presence of *KRAS* mutation can predict resistance to anti-EGFR therapy. MSI-high or MSI-H (Microsatellite Instable) results from the dysregulation in the Mismatch Repair Genes (MMR), leading to genetic errors in the DNA during cell division. Patients who test MSI positive are considered to have an MSI-High tumor. These MSI-H tumors respond positively to immunotherapy treatment such us anti-PD1 checkpoint blockers pembrolizumab or nivolumab[28].

According to the tumor stage, the ESMO guidelines suggest different treatment strategies for colorectal cancer as you can see in the table below (Table 1). In a metastatic disease condition (stage IV), many systemic therapeutic options are available (Table 1) based on the molecular tumor characterization, the treatment outcome (curative or palliative) and the toxicity of the drugs. According to the ESMO guidelines, here, patients can be classified into clinically defined groups in order to have a more specialized or recommended treatment. The guideline also presents a first, second, third and a fourth line treatment option in case of side effects and/or relapse (Table 1)[18].

**Table 1 -** Treatment strategy recommended for colorectal cancer patient. Adapted from [18,28] ESMO Guidelines 2014.

| | | | |
|---|---|---|---|
| **Stage I** | Surgical removal of the tumor and lymph nodes is usually the only treatment needed. | | |
| **Stage II** | Surgery is mostly the first treatment. In some cases, adjuvant chemotherapy and radiation therapy in combination with chemotherapy (before or after surgery) may be recommended. | | |
| **Stage III** | Treatment usually involves surgical removal of the tumor followed by adjuvant chemotherapy. Radiation therapy may be used with chemotherapy before or after surgery, along with adjuvant chemotherapy. | | |
| **Stage IV** | Metastatic Colorectal Cancer (mCRC) Treatment Strategy | | |
| | **Scenario I** | **Scenario II** | **Scenario III** |
| **1st line** | Cytotoxic doublet[1] + bevacizumab | Cytotoxic doublet[1] + bevacizumab | Cytotoxic doublet[1] + anti-EGFR antibody[2] |
| **2nd line** | Cytotoxic doublet[1] + bevacizumab or aflibercept[3] | Cytotoxic doublet[1] + anti-EGFR antibody[2] | Cytotoxic doublet[1] + bevacizumab or aflibercept[3] |
| **3rd line** | Irinotecan or FOLFIRI + anti-EGFR antibody[2] | Regorafenib | Regorafenib |
| **4th line** | Regorafenib | | |

[1]cytotoxic doublets: fluoropyrimidine + oxaliplatin or irinotecan; [2]Ras wild type; [3]aflibercept only in combination with FOLFIRI

**Scenario I:** Metastatic disease that may be removed with a curative goal. After chemotherapy has reduced the size of the tumor, the aim is to be disease-free, which enables secondary surgery and may increase the chance of long-term survival or a cure.

**Scenario II:** Disseminated disease, technically 'never'/unlikely resectable intermediate intensive treatment. The goal of the treatment is primarily palliative. The best approach seems to be the first-line treatment with a high possibility of causing metastases regression in patients with more aggressive or widespread illnesses.

**Scenario III:** Non-intensive/sequential treatment for a metastatic illness that is never resectable. The maximum metastasis regression is not the main goal of treatment for these individuals. The goal is to prevent tumor progression and extend life with the least amount of treatment burden possible in the absence of current or imminent symptoms and with a low risk of rapid deterioration.

Overall, there have been advances made towards treating different forms and stages of colorectal cancers. More research still needs to be done to have a better understanding of how to treat this illness both medically and psychologically.

## 1.4 Cell Competition

Natural selection, sometimes known as the survival of the fittest, is a Charles Darwin theory to explain how species evolve. Due to genetic variations that give some organisms a functional advantage over others in the same environment, better-adapted species have the capacity to outcompete other members. According to Wilhelm Roux, this idea may be extended to tissues and cells, which fight with one another for resources and available space. As a result, only the fittest cells are allowed to survive in the tissue, while the less fit cells are eliminated[29].

Maintenance of healthy tissue homeostasis involves cell-intrinsic and extrinsic factors that regulate cell selection, fate and death. In certain situations, cells may

compare their relative cell fitness and activate mechanisms that secure the elimination of unhealthy cells. This endogenous process is termed cell competition[30].

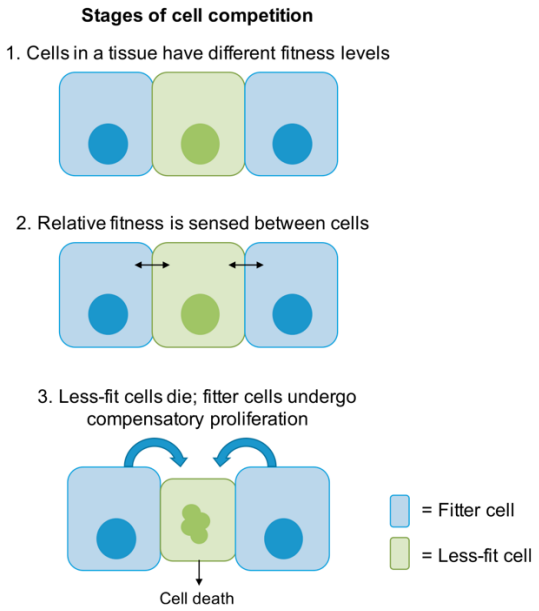


**Figure 3 - Schematic representation of the Key Stages of the Cell Competition.** First, cell fitness differences in will trigger cell competition. Next, these fitness level differences in will be sensed by the prospective winner and loser cells, and translated into a compensatory proliferation or apoptotic response. Adapted from[31].

This process was first reported in the *Drosophila melanogaster* wing imaginal disc by Ginés Morata through a series of landmark experiments aimed to study the phenotype of the *Minute* dominant mutation which encodes a ribosomal protein. The homozygous *Minute* mutation revealed itself to be lethal, since cells become unable to produce proteins and ultimately die, due to a cell autonomous effect and not related to a competitive interactions[32]. In heterogeneity (M+/M-), the *Minute* mutants presented with a deficient ribosomal protein, led to reduced growth and proliferation rates[33–35], but clones were viable (individuals reached adulthood). However, when these cells were surrounded by wild-type (WT) cells (M+/M+), they were eliminated[33],

which sparked the belief that these heterozygous cells underwent apoptosis when in contact with WT cells. Further investigation confirmed that Minute +/- clones elimination by wildtype clones was indeed apoptosis dependent[32,36].

Since then, numerous other genes and mutations have been linked to this mechanism, emphasizing the significance of an active cell selection in an organism[31]. Certain cells may suffer mutations during their formation or develop them over time, or they may be subjected to insults that impair their capacity to manufacture proteins, proliferate and not be exposed to survival factors - leading to their fitness decrease. This imbalance causes a heterogeneous population of cells in a tissue, which ultimately affects the health of the organism's organs.

In order to detect and eliminate a wide variety of those viable but suboptimal cells, it has been shown that *Drosophila* cells can directly exchange cell fitness information[29,37–40]. Direct comparison of cell fitness is therefore used in *Drosophila* to detect and eliminate many types of viable but impaired cells in order to delay ageing[38], eliminate defective structures during development[29,38–42] or replace old tissues during regeneration[31,43].

The “fitness fingerprints”[29,37–39] that reveal optimal or suboptimal cell fitness to neighboring cells are encoded by different isoforms of the transmembrane protein Flower[29,37–40]. The isoforms that indicate reduced fitness are called Lose isoforms[37,38], because they are expressed in viable cells marked to be eliminated, provided that fitter cells expressing Win isoforms are available[37]. Importantly, the proliferation of winner cells occurs at the expense of losers, so total cell numbers do not change, maintaining the correct pattern of the organ while maximizing its fitness[44].

Cell competition takes place in this so-called heterotypic environment to eliminate of unfit cells. However, cell competition is not triggered when losers are in contact with loser cells. This can cause the accumulation of the unfit populations[37]. Therefore, competition is activated in a heterogenous scenario and not in a homogenous scenario.

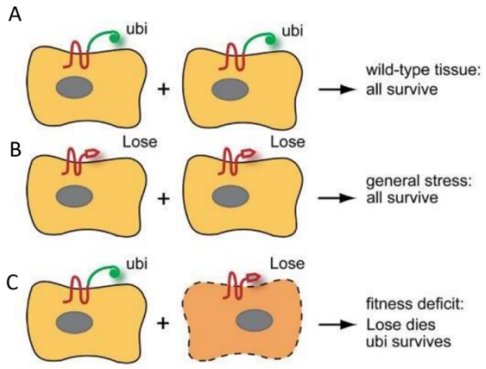


**Figure 4 - Model representing Fwe-dependent cell-cell communication decisions. A)** Winner cells interact with winners, all cells survive and competition does not occur. **B)** Loser cells interacting with losers, all survive. Cell competition is not triggered. **C)** Unfit cells will express a $fwe^{lose}$ isoform into the extracellular matrix, which is detected by the nearby winner cell expressing $fwe^{ubi}$. When a winner cell identifies a loser cell it triggers the elimination of the unfit loser cell from the tissue. Adapted from[37].

This cell selection mechanism has an important role in maintaining tissue homeostasis. For instance, in the early in life, the selection of healthy and viable cells enables the proper growth of the organism by removing unhealthy or malformed cells[42]. The maintenance of the healthiest stem cells is crucial since they give rise to all of the organism's cells and, once they reach adulthood, specialize into younger, healthier cells that can replace older, damaged cells in tissues[29,45].

Cell competition has also been implicated in Alzheimer's Disease to select fit neurons, contrarily to the initial thought that all neuronal death in this context was prejudicial. However, a lack of cell selection may cause developmental problems, accelerated aging, and cancer formation.

The same mechanism gives premalignant cells a competitive advantage to grow at the expense of neighboring cells[39]. In humans, opportunities for fitness-based cell selection have also been described during development and cancer, but they

normally rely on the indirect competition for survival factors or nutrients[46–48], and if a system dedicated to direct fitness comparison is active in humans was unknown.

### 1.4.1 SUPERCOMPETITION

Supercompetition is a mechanism of cell competition associated with cancer development, based that mutations acquired by some cells improve their fitness and proliferation, turning them into a supercompetitors cells. These supercompetitors are capable of eliminating WT neighboring cells[49,50]. Many genes linking to the supercompetiton process have been described. The proto-oncogene Drosophila Myc (dMyc), which codes for a transcription factor that controls cell proliferation and ribosome biogenesis, has been the subject of the most research in Drosophila[30]. Supercompetitive cells expressing higher levels of dMyc, outcompete neighboring WT cells which express normal levels of dMyc[37,51]. Therefore, cell competition may cause cancer by considering cancerous cells to be fitter than normal cells[50,52].

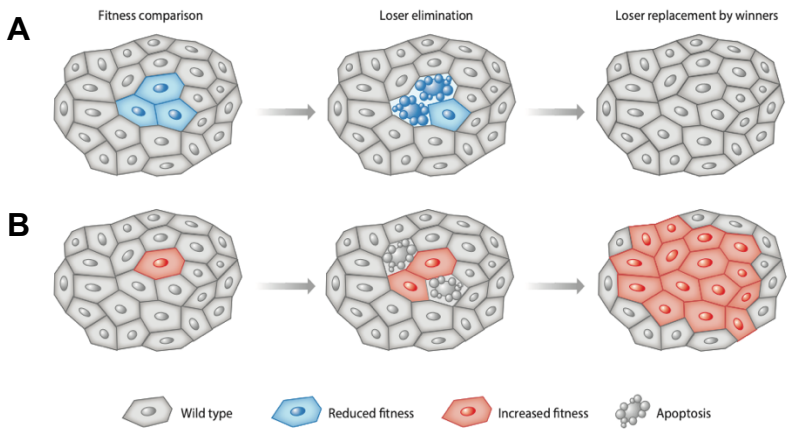


**Figure 5 - The mechanism of cell competition. A)** Cells locally exchange fitness-related information during competition (comparison phase, left). Lower-fitness cells (losers) are eliminated when fitness differences are identified, most frequently via apoptosis (elimination phase, middle) and the process is complete when winner cells

replace the eliminated cells (replacement phase, right). **B)** Cell competition may also lead to the expansion of high-fitness cells, also known as supercompetition, by expressing high levels of the fitness marker and therefore leading to the death of the surrounding well type cells. Adapted from[2].

### 1.4.2 MECHANISMS OF CELL COMPETITION

#### 1.4.2.1 COMPETITION FOR SURVIVAL FACTORS

Competition for trophic factors is the one that most mimic the ecological phenomenon since it takes place when less fit cells have more difficulty collecting nutrients or other molecules necessary for their survival than healthier cells, which causes their starvation and eventually dead. Identical to what is depicted in Darwinian competition in ecology, the trophic theory for competition described cells competing for limiting amounts of survival factors.

According to, in Minute-mediated cell competition, the extracellular growth factor Dpp levels were decreased in the loser mutants. A decrease in Dpp signaling was sufficient to cause elimination[32].

In contrast to other competition models, no direct contact between cells is necessary. Depending on the rate of ligand capture and the distance to the extracellular growth factors, the elimination of cells may take place at a distance[50].

#### 1.4.2.2 MECHANICAL CELL COMPETITION

Cell populations with different growth rates and movement, leads to the accumulation of mechanical stress in the tissue. It was initially hypothesized, using mathematical modeling, that in the presence of space constraints, rapidly proliferating cells would apply compression stress on the population of slowly expanding cells. Given that the compression forces tend to be locally concentrated and that both populations are equally healthy and resistant to mechanically induced

cell death, the rapidly proliferating population will be forced to undergo apoptosis, which will cause it to die.

However, if the slow-growing population has reduced fitness and is more sensitive to mechanically induced cell death, these cells will die, alleviating the overall effect on the tissue[53]. Later, it was demonstrated that the mechanical stress caused by crowded conditions, in fact, triggers cell death and extrusion[31]. Both in vitro and in vivo studies using the Drosophila and zebrafish have shown the importance of mechanical forces in cell competition[49,53–55].

Mechanical cell competition can act as a tumor expansion or tumor suppression mechanism. If tumors acquire increased resistance to compression, they can promote wild-type cell elimination and expand even more, but if tumor cells are more sensitive to compression, adjacent wild-type cells can trigger their elimination and prevent cancer development[56]. Equally, to trophic competition, mechanically induced death does not require direct winner-loser cell contact.

#### 1.4.2.3 COMPETITION THROUGH COMPARISON OF FITNESS FINGERPRINTS

In contrast to the initial two conditions of elimination, in this scenario cells requires cell-cell contact between the loser and winner cells to trigger the elimination of the unfit loser cells. Cells display on the surface their fitness status level to the neighboring cells. Relative comparison will be used to eliminate the unfit cells when differences in fitness level are detected[57,58].

This form of cell competition can be seen as a series of events that start with the detection of relative fitness between cells, which can then trigger a pro-apoptotic signal in less fit cells, leading to their exclusion from the tissue. The first evidence for this concept came from the discovery of the flower gene (fwe), which codes for a several isoforms known as "Fitness Fingerprints"[57,58].

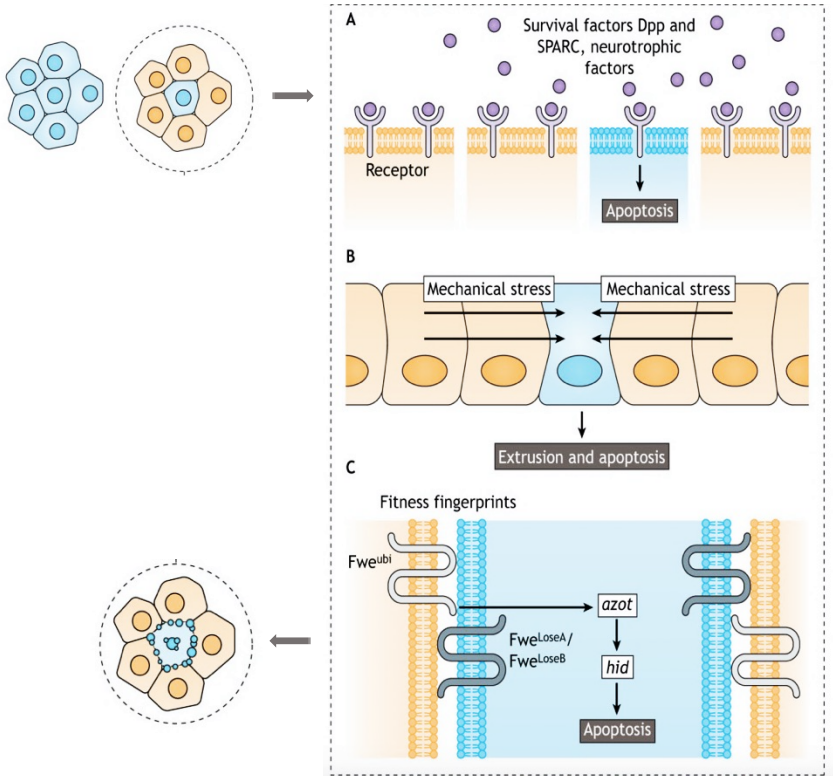


**Figure 6 - Different types of cell competition. A)** Competition for limiting survival factors. Winner cells (orange) have a higher capacity to bind pro-survival factors, reducing the abundance of available survival factors for loser cells (blue) leading to their elimination. **B)** Mechanical cell competition. Differential growth and/or tissue movement leads to the compression (arrows) of the loser cells, triggering their elimination. **C)** Competition through comparison of fitness fingerprints. Loser cells express on their surface an unfit marker (FweLose), and winner cells express a fit marker (FweWin). Interaction between FweLose and FweWin expressing cells leads to the transcription of azot, which triggers the expression of hid (a pro-apoptotic gene) and ultimately leads to loser cell elimination from the tissue. Importantly, this is the only type of CC that requires direct contact between Loser and Winner cells to trigger the elimination of the losers. Adapted from[58].

### 1.4.3 THE FLOWER CODE

During development and ageing, damaged but viable cells accumulate within tissues. The process of cell competition eliminates suboptimal cells from tissues to mitigate organ dysfunction and disease[30,32,33,42,43,46–48,59]. Loser cells are directed by receptor signaling, mechanical forces, or fitness fingerprint markers to undergo caspase-dependent apoptosis. Fitness fingerprints reveal optimal or suboptimal cell fitness to neighboring cells by expressing membrane proteins, such as Flower proteins[32,34–36]. Loser cell fitness signals, including Azot and Flower Lose isoforms, were identified by their upregulation in a Drosophila screen of *dMyc*-overexpressing cells competing with wild-type cells. Winner cells expressing Flower-Win isoforms outcompete and eliminate Loser cells bearing Flower-Lose isoforms in a mixed population[34,35,50,53]. In this sense, Flower isoforms form a "code" of markers for comparison of relative cellular fitness.

Furthermore, the Fitness Fingerprints were reported to be tissue specific. While Fwe loseA or Fwe loseB expression is necessary to trigger loser cell elimination in the epithelia of the Drosophila wing disc, in neuronal cells Fwe loseA isoform does not correspond a loser marker[37,38,42,43].

**Table 2 -** The fitness marker Flower is conserved from flies to mammals. Overview of Fwe isoform's role in *Drosophila* (dFwe) and mouse (mFwe). Adapted from[58].

| Fitness markers | | |
|---|---|---|
| | Loser isoforms | Winner isoforms |
|  | $Fwe^{LoseA}$<br>$Fwe^{LoseB}$ | $Fwe^{ubi}$ |
|  | mFwe1<br>mFwe3 | mFwe2<br>mFwe4 |

It has been shown that Fwe is conserved in mammals, despite the fact that Fwe was initially found in Drosophila, which has since been the most often utilized model to explore its functions[60]. One mouse-specific putative homologue of the Drosophila FWE (dFwe) in mice encodes four distinct isoforms known as mFwe1, mFwe2, mFwe3, and mFwe4, all believed to be transmembrane proteins.

Therefore, it is important to study, whether a human homologous of Flower plays a role in cell competition and consequently if the Flower code is also conserved in human.

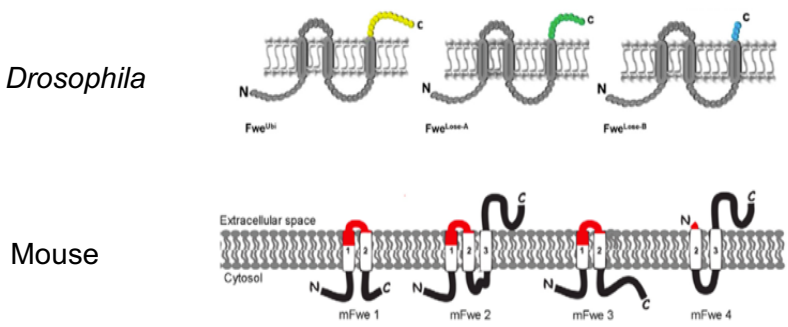


**Figure 7 - Structure of Fwe isoforms in *Drosophila* and mice.** Adapted from[37,60].

#### 1.4.3.1 AZOT

In Drosophila, Azot ("cell fitness checkpoint") is expressed in the loser cells marked to be eliminated during cell competition. Loss of Azot in these cells leads to their survival and growth, suggesting that Azot plays a role in promoting cell death.

The Azot transcription factor integrates the relative differences in flowerLoseB expression between the cell and its neighbors, as well as the endogenous SPARC expression itself[38]. In less fit cells, azot transcription occurs upstream of the activation

of pro-apoptotic genes *Hid*, leading to cell death, although SPARC can block this process by inhibiting Azot functions[38,62]. Both the mechanisms that Azot incorporates this knowledge and those that cause the upregulation of flowerLoseB are still unknown.

Overall, the role of Azot in cell competition appears to be to promote the elimination of weaker or damaged cells through the activation of cell death pathways[38].

#### 1.4.3.2 SPARC

Secreted protein acidic and rich in cysteine (SPARC), also called Osteonectin or BM-40, is involved in cell–cell interactions, extracellular matrix (ECM) remodeling and bone mineralization[63–66]

SPARC physiological functions include the maintenance of a wide range of cells and tissues, including bone, pancreatic tissue, nerve tissue and contractible cells like cardiomyocytes and vascular smooth cells[63,67–72]. Due to its wide range of functions, SPARC also plays a key role in tumor growth, invasion and metastasis by remodeling the extracellular matrix (ECM) and promoting epithelial-mesenchymal transition (EMT)[68,69,71–73]. However, SPARC expression depends on cancer type and its stages, providing different outcomes[74,75] since it may act as a tumor-suppressor[66] or a tumor-promoter[76].

SPARC is a critical survival factor because it can protect cells from being eliminated during active competition. Interestingly, upregulation of SPARC on prospective loser cells initiates a compensatory mechanism to inhibit caspase activation and transiently protect the cells from elimination[50,59,77]. Induction of Fwe-Lose isoforms marks loser cells for death, but SPARC overexpression can rescue the loser cell fate.

In a cancer context, stroma cells can upregulate SPARC as a defence mechanism to stave off elimination, preventing cancer initiation and growth[38]. It is

also likely that SPARC acts in an autocrine manner and activates a signaling pathway that prevents apoptosis[77].

Epigenetic silencing of SPARC is also frequent in CRC and it correlates with cancer progression and resistance to chemotherapy[78,79]. Yet, treating CRC cells overexpressing SPARC can rescue its expression and enhance sensitivity to therapy[79,80] corroborating its tumor-suppressing role.

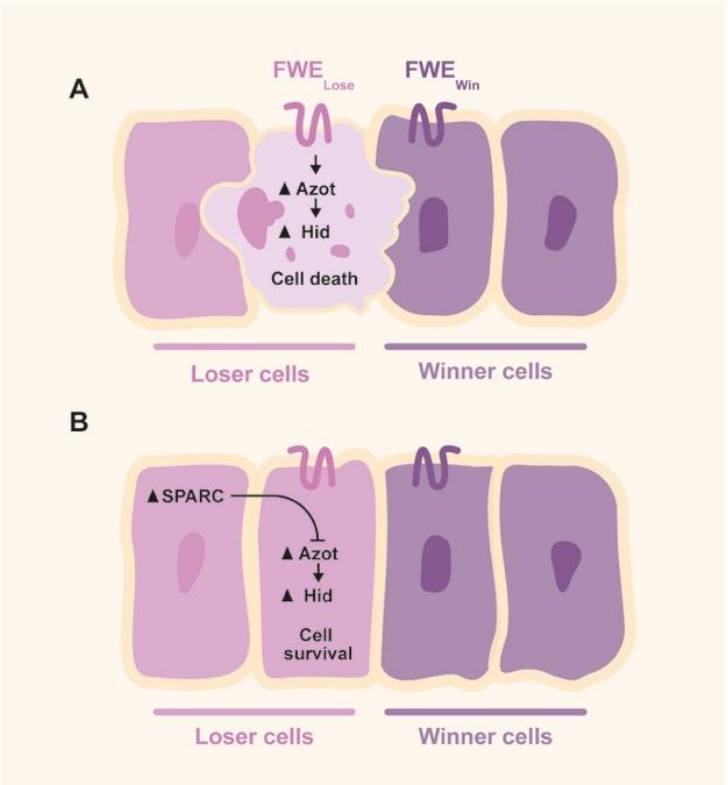


**Figure 8 - SPARC in cell competition. A)** Normal scenario of competition by fitness fingerprints. Cells compare their relative fitness status by expressing a fit or unfit marker, flower win or flower lose respectively, on their surface. This fitness comparison leads to azot transcription, consequently, activation of hid expression (a proapoptotic gene) and loser cells die. **B)** Overexpression of SPARC in loser cells

downregulates Azot activity, protecting these cells from elimination. Thus, Loser cells in the tumor microenvironment upregulate SPARC as a defence mechanism, which functions as a natural strategy to prevent cancer growth. Adapted from[57].

### 1.4.4 Cell Competition in Cancer

It has been described that through a process of cell competition, cancer cells expand and overtake a microenvironment by targeting stromal cells for elimination.

In normal CC scenario, the relative comparison of cell fitness levels can activate mechanisms that eliminates unhealthy cells from a tissue. However, in a super competition scenario, tumour cells can acquire mutations that make them "fitter" than their neighbors, triggering their elimination. This fitness comparison mechanism gives premalignant cells a competitive advantage to grow and gain space at the cost of neighboring cells[39]. In humans, cell selection based on fitness status, has also been described during development and in oncogenesis[30].

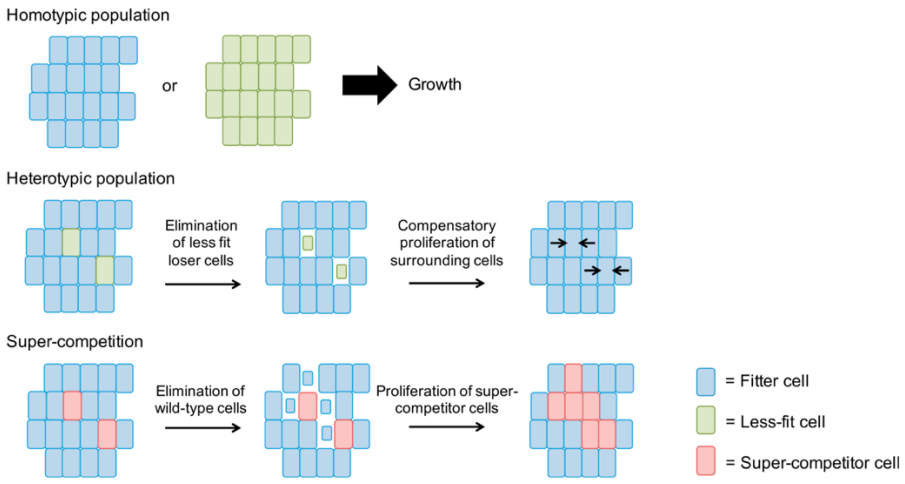


**Figure 9 - Modes of Cell Competition.** Suboptimal cells are eliminated when surrounded by their fitter counterparts during cell competition. In a supercompetition

scenario, Myc-overexpressing cells eliminate their wild-type neighbors promoting cancer growth. Fitter and Less-fit cells remain viable in a homotypic environment. Adapted from[31].

In this sense, CC in a cancer context can act as a tumor promoter, helping the malignant cell to grow and inducing the death of the neighboring stroma cells, or as a tumor suppressor by eliminating this malignant cell, maintaining tissue homeostasis.

### 1.4.5 Cell Competition in Tumor Growth

Cell competition occurs when highly fit cells overtake a population by killing off viable loser cells. However, limited attention has been given to the ability of cancer cells to eliminate healthy cells. Pro-oncogenic cells can exploit competition pathways to promote caspase activation and elimination of neighboring healthy stromal cells. A simple perception is that tumor formation is driven by the uncontrolled division of highly proliferative cancer cells. However, most carcinomas initially spread through affected organs without disrupting tissue architecture. The fitness of the microenvironment can determine if cancer expansion occurs or not[81].

Tumor growth can also be enhanced from the invasion caused by cell mixing, which exacerbates interactions between winners and losers, as well as by the elimination of healthy tissue derived by increasing mechanical tension as the tumor grows – showing how cancer cells can manipulate cell competition mechanisms for their benefit[39].

Tumor cell subpopulations compete versus heterotypic host stromal tissue cells (fibroblasts, immune cells, endothelial cells, epithelial cells). In effect, boosting the fitness of host tissues (i.e. via caspase inhibition) can block the spread of cancerous cells[40,41].

### 1.4.6 Cell Competition as Tumor Suppressor

Cell competition can act as a tumor suppressor when healthy epithelial cells recognize and remove tumor cells from the tissue, halting the development of cancer[51,61].

Cells with the RAS-V12 mutation, one of the most common mutations in cancers, are extruded from the WT epithelium by CC, inhibiting their proliferation both in vitro and in vivo studies[82–84]. Similar evidence is shown in cells that have been activated by Src, ERBB2-overexpressing cells, YAP component-activated cells, and cells activated by CDC4277[85–87], all of which have been thoroughly documented as oncoproteins or connected to cancer. Moreover, TP53-mutant cells on a WT epithelium underwent necroptosis by cell competition[88,89].

In the mammalian thymus, young T cells outcompete their old progenitors, preventing the development of acute lymphoblastic leukaemia due to cumulative genetic insults[47].

The process of removing cells from the epithelium that carry potentially cancer-causing mutations is known as an epithelial defence against cancer (EDAC)[36]. Early in the process of carcinogenesis, EDAC functions as a protective mechanism against cancer[90].

### 1.4.7 Competition between Tumor and Stroma

Organs and tissues in our bodies are made of specialized cells. A balance between cell growth, division, and death is necessary for tissue health. Cancer cells can engage in competition with neighboring cells, including epithelial cells and fibroblasts[30,91,92]. The phenomenon of cell competition has several functions in the development of cancer. Tumor clones and the surrounding stroma may have active or inactive competition signaling pathways. Active competition can produce stimulatory, inhibitory, or neutral effects on tumor cell proliferation. The stromal tissue microenvironment is a crucial defence mechanism in resistance to oncogenesis[93].

Oncogenesis entails intricate cell-cell interactions between the host tissue and the tumor[94]. Myc and YAP (Hippo pathway) protein level heterogeneity is seen

in the tumor-stroma microenvironment of human cancer tissues such as breast, colon, and lung, and correlates with functional alterations[91]. Higher c-Myc and YAP levels in tumor cells linked with caspase-3 positive apoptotic stromal cells in the neighboring compartment were observed in studies of the tumor-stroma interface[91]. This demonstrates that super competitor tumor cells appear to further invade a tissue compartment by causing the surrounding, viable stromal cells to undergo programmed cell death[91]. In fact, Myc amplification is associated with worse prognosis in breast cancer patients and higher intratumor heterogeneity[95].

## 1.5 AIMS

Direct comparison of cell fitness is therefore used in *Drosophila* to detect and eliminate many types of viable but impaired cells in order to delay ageing[38], eliminate defective structures during development[29,38–42] or replace old tissues during regeneration . Based in previous studies that demonstrate that *Drosophila* cells can directly exchange cell fitness information , it was therefore unknown whether a similar mechanism of cell-fitness comparison is present in human cells.

In **Chapter 2**, we studied the functional role of the four human Flower isoforms. We characterize which one works as a Win and Lose isoform in human cells by establishing an *in-vitro* competition assay. We also proved that FWE role is conserved in humans. We propose that in the early stages of cancer, cells express high levels of FWE Win and are able to outcompete normal cells, and thereby monopolize tissue space. Based on these achievements, in **Chapter 3**, we focused in understanding the mechanisms of cell competition by identifying hFWE binding partners and study their role in CC and cancer progression. We are faced with difficult challenges to develop effective therapies against cancer. Therefore, this study is important for helping add a puzzle in the development of new drugs that could suppress tumor cell proliferation and block cancer progression.

## 1.6 REFERENCES


1. Bray, F., Laversanne, M., Weiderpass, E. & Soerjomataram, I. The ever-increasing importance of cancer as a leading cause of premature death worldwide. *Cancer* **127**, 3029–3030 (2021).

2. Clavería, C. & Torres, M. Cell Competition: Mechanisms and Physiological Roles. *Annu. Rev. Cell Dev. Biol.* **32**, 411–439 (2016).

3. Hanahan, D. & Weinberg, R. A. The Hallmarks of Cancer. *Cell* **100**, 57–70 (2000).

4. Hanahan, D. & Weinberg, R. A. Hallmarks of Cancer: The Next Generation. *Cell* **144**, 646–674 (2011).

5. Sung, H. *et al.* Global Cancer Statistics 2020: GLOBOCAN Estimates of Incidence and Mortality Worldwide for 36 Cancers in 185 Countries. *CA. Cancer J. Clin.* **71**, 209–249 (2021).

6. Qiu, M., Hu, J., Yang, D., Cosgrove, D. P. & Xu, R. Pattern of distant metastases in colorectal cancer: a SEER based study. *Oncotarget* **6**, 38658–38666 (2015).

7. Zarour, L. R. *et al.* Colorectal Cancer Liver Metastasis: Evolving Paradigms and Future Directions. *Cell. Mol. Gastroenterol. Hepatol.* **3**, 163–173 (2017).

8. Poturnajova, M. *et al.* Molecular features and gene expression signature of metastatic colorectal cancer (Review). *Oncol. Rep.* **45**, 10 (2021).

9. Levin, B. *et al.* Screening and surveillance for the early detection of colorectal cancer and adenomatous polyps, 2008: a joint guideline from the American Cancer Society, the US Multi-Society Task Force on Colorectal Cancer, and the American College of Radiology. *CA. Cancer J. Clin.* **58**, 130–160 (2008).

10. Mármol, I., Sánchez-de-Diego, C., Pradilla Dieste, A., Cerrada, E. & Rodriguez Yoldi, M. Colorectal Carcinoma: A General Overview and Future Perspectives in Colorectal Cancer. *Int. J. Mol. Sci.* **18**, 197 (2017).

11. Johns, L. E. & Houlston, R. S. A systematic review and meta-analysis of familial colorectal cancer risk. *Am. J. Gastroenterol.* **96**, 2992–3003 (2001).

12. Robertson, D. J. ABC of Colorectal Cancer. *Gastroenterology* **143**, 868–869

(2012).

13. Fearon, E. R. & Vogelstein, B. A genetic model for colorectal tumorigenesis. *Cell* **61**, 759–767 (1990).

14. Clevers, H. & Nusse, R. Wnt/β-Catenin Signaling and Disease. *Cell* **149**, 1192–1205 (2012).

15. Bardelli, A. & Siena, S. Molecular Mechanisms of Resistance to Cetuximab and Panitumumab in Colorectal Cancer. *J. Clin. Oncol.* **28**, 1254–1261 (2010).

16. Stefani, C. *et al.* Growth Factors, PI3K/AKT/mTOR and MAPK Signaling Pathways in Colorectal Cancer Pathogenesis: Where Are We Now? *Int. J. Mol. Sci.* **22**, 10260 (2021).

17. Argilés, G. *et al.* Localised colon cancer: ESMO Clinical Practice Guidelines for diagnosis, treatment and follow-up. *Ann. Oncol.* **31**, 1291–1305 (2020).

18. Van Cutsem, E., Cervantes, A., Nordlinger, B. & Arnold, D. Metastatic colorectal cancer: ESMO Clinical Practice Guidelines for diagnosis, treatment and follow-up. *Ann. Oncol.* **25**, iii1–iii9 (2014).

19. Broekman, F. Tyrosine kinase inhibitors: Multi-targeted or single-targeted? *World J. Clin. Oncol.* **2**, 80 (2011).

20. Wilkes, G. M. Targeted Therapy: Attacking Cancer with Molecular and Immunological Targeted Agents. *Asia-Pac. J. Oncol. Nurs.* **5**, 137–155 (2018).

21. Wu, F. *et al.* Signaling pathways in cancer-associated fibroblasts and targeted therapy for cancer. *Signal Transduct. Target. Ther.* **6**, 218 (2021).

22. Nair, P., Prado, M., Perea-Gil, I. & Karakikes, I. Concise Review: Precision Matchmaking: Induced Pluripotent Stem Cells Meet Cardio-Oncology. *Stem Cells Transl. Med.* **8**, 758–767 (2019).

23. Zhong, L. *et al.* Small molecules in targeted cancer therapy: advances, challenges, and future perspectives. *Signal Transduct. Target. Ther.* **6**, 201 (2021).

24. Grossman, M. & Adler, E. Protein Kinase Inhibitors - Selectivity or Toxicity? in *Biochemistry* (ed. Kumar Singh, R.) vol. 24 (IntechOpen, 2021).

25. Shyam Sunder, S., Sharma, U. C. & Pokharel, S. Adverse effects of tyrosine kinase inhibitors in cancer therapy: pathophysiology, mechanisms and clinical

management. *Signal Transduct. Target. Ther.* **8**, 262 (2023).

26. Ettrich, T. J. & Seufferlein, T. Regorafenib. in *Small Molecules in Oncology* (ed. Martens, U. M.) vol. 211 45–56 (Springer International Publishing, 2018).

27. Hurwitz, H. *et al.* Bevacizumab plus Irinotecan, Fluorouracil, and Leucovorin for Metastatic Colorectal Cancer. *N. Engl. J. Med.* **350**, 2335–2342 (2004).

28. Benson, A. B. *et al.* Colon Cancer, Version 2.2021, NCCN Clinical Practice Guidelines in Oncology. *J. Natl. Compr. Canc. Netw.* **19**, 329–359 (2021).

29. Moreno, E. & Rhiner, C. Darwin's multicellularity: from neurotrophic theories and cell competition to fitness fingerprints. *Curr. Opin. Cell Biol.* **31**, 16–22 (2014).

30. Gogna, R., Shee, K. & Moreno, E. Cell Competition During Growth and Regeneration. *Annu. Rev. Genet.* **49**, 697–718 (2015).

31. Di Gregorio, A., Bowling, S. & Rodriguez, T. A. Cell Competition and Its Role in the Regulation of Cell Fitness from Development to Cancer. *Dev. Cell* **38**, 621–634 (2016).

32. Moreno, E., Basler, K. & Morata, G. Cells compete for decapentaplegic survival factor to prevent apoptosis in Drosophila wing development. *Nature* **416**, 755–759 (2002).

33. Morata, G. & Ripoll, P. Minutes: mutants of drosophila autonomously affecting cell division rate. *Dev. Biol.* **42**, 211–221 (1975).

34. Kongsuwan, K. *et al.* A Drosophila Minute gene encodes a ribosomal protein. *Nature* **317**, 555–558 (1985).

35. Lambertsson, A. The minute genes in Drosophila and their molecular functions. *Adv. Genet.* **38**, 69–134 (1998).

36. Kajita, M. & Fujita, Y. EDAC: Epithelial defence against cancer-cell competition between normal and transformed epithelial cells in mammals. *J. Biochem. (Tokyo)* **158**, 15–23 (2015).

37. Rhiner, C. *et al.* Flower Forms an Extracellular Code that Reveals the Fitness of a Cell to its Neighbors in Drosophila. *Dev. Cell* **18**, 985–998 (2010).

38. Merino, M. M. *et al.* Elimination of Unfit Cells Maintains Tissue Health and Prolongs Lifespan. *Cell* **160**, 461–476 (2015).

39. Levayer, R., Hauert, B. & Moreno, E. Cell mixing induced by myc is required for competitive tissue invasion and destruction. *Nature* **524**, 476–480 (2015).

40. Vincent, J.-P., Fletcher, A. G. & Baena-Lopez, L. Al. Mechanisms and mechanics of cell competition in epithelia. *Nat. Rev. Mol. Cell Biol.* **14**, 581–591 (2013).

41. Yao, C.-K. *et al.* A Synaptic Vesicle-Associated Ca2+ Channel Promotes Endocytosis and Couples Exocytosis to Endocytosis. *Cell* **138**, 947–960 (2009).

42. Merino, M. M., Rhiner, C., Portela, M. & Moreno, E. 'Fitness fingerprints' mediate physiological culling of unwanted neurons in Drosophila. *Curr. Biol. CB* **23**, 1300–1309 (2013).

43. Moreno, E., Fernandez-Marrero, Y., Meyer, P. & Rhiner, C. Brain Regeneration in Drosophila Involves Comparison of Neuronal Fitness. *Curr. Biol.* **25**, 955–963 (2015).

44. Levayer, R. & Moreno, E. Mechanisms of cell competition: themes and variations. *J. Cell Biol.* **200**, 689–698 (2013).

45. Rhiner, C. & Moreno, E. Super competition as a possible mechanism to pioneer precancerous fields. *Carcinogenesis* **30**, 723–728 (2009).

46. Raff, M. C. Social controls on cell survival and cell death. *Nature* **356**, 397–400 (1992).

47. Martins, V. C. *et al.* Cell competition is a tumour suppressor mechanism in the thymus. *Nature* **509**, 465–470 (2014).

48. Chang, C.-H. *et al.* Metabolic Competition in the Tumor Microenvironment Is a Driver of Cancer Progression. *Cell* **162**, 1229–1241 (2015).

49. Levayer, R., Dupont, C. & Moreno, E. Tissue Crowding Induces Caspase-Dependent Competition for Space. *Curr. Biol. CB* **26**, 670–677 (2016).

50. Merino, M. M., Levayer, R. & Moreno, E. Survival of the Fittest: Essential Roles of Cell Competition in Development, Aging, and Cancer. *Trends Cell Biol.* **26**, 776–788 (2016).

51. Moreno, E. Is cell competition relevant to cancer? *Nat. Rev. Cancer* **8**, 141–147 (2008).

52. Madan, E., Gogna, R. & Moreno, E. Cell competition in development: information from flies and vertebrates. *Curr. Opin. Cell Biol.* **55**, 150–157 (2018).

53. Shraiman, B. I. Mechanical feedback as a possible regulator of tissue growth. *Proc. Natl. Acad. Sci. U. S. A.* **102**, 3318–3323 (2005).

54. Wagstaff, L. *et al.* Mechanical cell competition kills cells via induction of lethal p53 levels. *Nat. Commun.* **7**, 11373 (2016).

55. Eisenhoffer, G. T. *et al.* Crowding induces live cell extrusion to maintain homeostatic cell numbers in epithelia. *Nature* **484**, 546–549 (2012).

56. Brás-Pereira, C. & Moreno, E. Mechanical cell competition. *Curr. Opin. Cell Biol.* **51**, 15–21 (2018).

57. Camacho, D. *et al.* SPARC-p53: The double agents of cancer. *Adv. Cancer Res.* **148**, 171–199 (2020).

58. Costa-Rodrigues, C., Couceiro, J. & Moreno, E. Cell competition from development to neurodegeneration. *Dis. Model. Mech.* **14**, dmm048926 (2021).

59. Vanneste, E. *et al.* Chromosome instability is common in human cleavage-stage embryos. *Nat. Med.* **15**, 577–583 (2009).

60. Petrova, E., López-Gay, J. M., Rhiner, C. & Moreno, E. Flower-deficient mice have reduced susceptibility to skin papilloma formation. *Dis. Model. Mech.* **5**, 553–561 (2012).

61. Madan, E. *et al.* Flower isoforms promote competitive growth in cancer. *Nature* **572**, 260–264 (2019).

62. de Beco, S., Ziosi, M. & Johnston, L. A. New frontiers in cell competition†. *Dev. Dyn.* **241**, 831–841 (2012).

63. Melouane, A., Yoshioka, M., Kanzaki, M. & St-Amand, J. Sparc, an EPS-induced gene, modulates the extracellular matrix and mitochondrial function via ILK/AMPK pathways in C2C12 cells. *Life Sci.* **229**, 277–287 (2019).

64. Omi, S., Yamanouchi, K., Nakamura, K., Matsuwaki, T. & Nishihara, M. Reduced fibrillar collagen accumulation in skeletal muscle of secreted protein acidic and rich in cysteine (SPARC)-null mice. *J. Vet. Med. Sci.* **81**, 1649–1654 (2019).

65. Ramu, I. *et al.* SPARC dependent collagen deposition and gemcitabine

delivery in a genetically engineered mouse model of pancreas cancer. *EBioMedicine* **48**, 161–168 (2019).

66. Sailaja, G. S. *et al.* The secreted protein acidic and rich in cysteine (SPARC) induces endoplasmic reticulum stress leading to autophagy-mediated apoptosis in neuroblastoma. *Int. J. Oncol.* **42**, 188–196 (2013).

67. Atorrasagasti, C. *et al.* SPARC is required for the maintenance of glucose homeostasis and insulin secretion in mice. *Clin. Sci. Lond. Engl. 1979* **133**, 351–365 (2019).

68. Bradshaw, A. D. & Sage, E. H. SPARC, a matricellular protein that functions in cellular differentiation and tissue response to injury. *J. Clin. Invest.* **107**, 1049–1054 (2001).

69. Deckx, S. *et al.* Extracellular SPARC increases cardiomyocyte contraction during health and disease. *PloS One* **14**, e0209534 (2019).

70. Li, T. *et al.* SPARC induces phenotypic modulation of human brain vascular smooth muscle cells via AMPK/mTOR-mediated autophagy. *Neurosci. Lett.* **712**, 134485 (2019).

71. Okura, Y. *et al.* Interaction of Nerve Growth Factor β with Adiponectin and SPARC Oppositely Modulates its Biological Activity. *Int. J. Mol. Sci.* **20**, 1541 (2019).

72. Wang, Q. *et al.* Silencing of SPARC represses heterotopic ossification via inhibition of the MAPK signaling pathway. *Biosci. Rep.* **39**, BSR20191805 (2019).

73. Podhajcer, O. L. *et al.* The role of the matricellular protein SPARC in the dynamic interaction between the tumor and the host. *Cancer Metastasis Rev.* **27**, 523–537 (2008).

74. Nagai, M. A. *et al.* Prognostic value of NDRG1 and SPARC protein expression in breast cancer patients. *Breast Cancer Res. Treat.* **126**, 1–14 (2011).

75. Zhu, A. *et al.* SPARC overexpression in primary tumors correlates with disease recurrence and overall survival in patients with triple negative breast cancer. *Oncotarget* **7**, 76628–76634 (2016).

76. Ledda, M. F. *et al.* Suppression of SPARC expression by antisense RNA abrogates the tumorigenicity of human melanoma cells. *Nat. Med.* **3**, 171–176

(1997).

77. Portela, M. *et al.* Drosophila SPARC Is a Self-Protective Signal Expressed by Loser Cells during Cell Competition. *Dev. Cell* **19**, 562–573 (2010).

78. Tai, I. T., Dai, M., Owen, D. A. & Chen, L. B. Genome-wide expression analysis of therapy-resistant tumors reveals SPARC as a novel target for cancer therapy. *J. Clin. Invest.* **115**, 1492–1502 (2005).

79. Yang, E. *et al.* Frequent inactivation of SPARC by promoter hypermethylation in colon cancers. *Int. J. Cancer* **121**, 567–575 (2007).

80. Tang, M. J. & Tai, I. T. A novel interaction between procaspase 8 and SPARC enhances apoptosis and potentiates chemotherapy sensitivity in colorectal cancers. *J. Biol. Chem.* **282**, 34457–34467 (2007).

81. Pelham, C. J., Nagane, M. & Madan, E. Cell competition in tumor evolution and heterogeneity: Merging past and present. *Semin. Cancer Biol.* **63**, 11–18 (2020).

82. Kon, S. *et al.* Cell competition with normal epithelial cells promotes apical extrusion of transformed cells through metabolic changes. *Nat. Cell Biol.* **19**, 530–541 (2017).

83. Bos, J. L. ras oncogenes in human cancer: a review. *Cancer Res.* **49**, 4682–4689 (1989).

84. Hogan, C. *et al.* Characterization of the interface between normal and transformed epithelial cells. *Nat. Cell Biol.* **11**, 460–467 (2009).

85. Chiba, T. *et al.* MDCK cells expressing constitutively active Yes-associated protein (YAP) undergo apical extrusion depending on neighboring cell status. *Sci. Rep.* **6**, 28383 (2016).

86. Leung, C. T. & Brugge, J. S. Outgrowth of single oncogene-expressing cells from suppressive epithelial environments. *Nature* **482**, 410–413 (2012).

87. Kajita, M. *et al.* Interaction with surrounding normal epithelial cells influences signalling pathways and behaviour of Src-transformed cells. *J. Cell Sci.* **123**, 171–180 (2010).

88. Watanabe, H. *et al.* Mutant p53-Expressing Cells Undergo Necroptosis via Cell Competition with the Neighboring Normal Epithelial Cells. *Cell Rep.* **23**, 3721–

3729 (2018).

89. Muller, P. A. J. & Vousden, K. H. p53 mutations in cancer. *Nat. Cell Biol.* **15**, 2–8 (2013).

90. Hill, W. & Hogan, C. Normal epithelial cells trigger EphA2-dependent RasV12 cell repulsion at the single cell level. *Small GTPases* **10**, 305–310 (2019).

91. Di Giacomo, S. *et al.* Human Cancer Cells Signal Their Competitive Fitness Through MYC Activity. *Sci. Rep.* **7**, 12568 (2017).

92. Petrova, E., Soldini, D. & Moreno, E. The expression of SPARC in human tumors is consistent with its role during cell competition. *Commun. Integr. Biol.* **4**, 171–174 (2011).

93. Enomoto, M., Vaughen, J. & Igaki, T. Non-autonomous overgrowth by oncogenic niche cells: Cellular cooperation and competition in tumorigenesis. *Cancer Sci.* **106**, 1651–1658 (2015).

94. Tape, C. J. *et al.* Oncogenic KRAS Regulates Tumor Cell Signaling via Stromal Reciprocation. *Cell* **165**, 1818 (2016).

95. Oltmann, J. *et al.* Aneuploidy, TP53 mutation, and amplification of MYC correlate with increased intratumor heterogeneity and poor prognosis of breast cancer patients. *Genes. Chromosomes Cancer* **57**, 165–175 (2018).

# CHAPTER 2

# Flower isoforms promote competitive growth in cancer

**This Chapter is already published:** Madan, E., Pelham, C.J., Nagane, M., Parker, T.M., Canas-Marques, R., Fazio, K., Shaik, K., Yuan, Y., Henriques, V., Galzerano, A., Yamashita, T., Pinto, M.A.F., Palma, A.M., **Camacho, D.,** Vieira, A., Soldini, D., Nakshatri, H., Post, S.R., Rhiner, C., Yamashita, H., Accardi, D., Hansen, L.A., Carvalho, C., Beltran, A.L., Kuppusamy, P., Gogna, R., Moreno, E. Flower isoforms promote competitive growth in cancer. **Nature**, Volume 572, Issue 7768, 8 August 2019 https://doi.org/10.1038/s41586-019-1429-3

**Author contributions:** Camacho, D. assisted with experiments and analysis (Bapta-AM; Immunohistoquemestry; Immunocytochemistry).

## 2.1 ABSTRACT

In humans, the adaptive immune system uses the exchange of information between cells to detect and eliminate foreign or damaged cells; however, the removal of unwanted cells does not always require an adaptive immune system[1,2]. For example, cell selection in *Drosophila,* uses a cell selection mechanism based on 'fitness fingerprints', which allow it to delay ageing[3], prevent developmental malformations[3,4] and replace old tissues during regeneration[5]. At the molecular level, these fitness fingerprints consist of combinations of Flower membrane proteins[3,4,6]. Proteins that indicate reduced fitness are called Flower-Lose, because they are expressed in cells marked to be eliminated[6]. However, the presence of Flower-Lose isoforms at a cell's membrane does not always lead to elimination, because if neighbouring cells have similar levels of Lose proteins, the cell will not be killed[4,6,7]. Humans could benefit from the capability to recognize unfit cells, because the accumulation of damaged but viable cells during development and ageing causes organ dysfunction and disease[8–17.] However, in *Drosophila* this mechanism is hijacked by premalignant cells to gain a competitive growth advantage[18]. This would be undesirable for humans because it might make tumours more aggressive[19–21]. It is unknown whether a similar mechanism of cell-fitness comparison is present in humans. Here we show that two human Flower isoforms (hFWE1 and hFWE3) behave as Flower-Lose proteins, whereas the other two isoforms (hFWE2 and hFWE4) behave as Flower-Win proteins. The latter give cells a competitive advantage over cells expressing Lose isoforms, but Lose-expressing cells are not eliminated if their neighbours express similar levels of Lose isoforms; these proteins therefore act as fitness fingerprints. Moreover, human cancer cells show increased Win isoform expression and proliferate in the presence of Lose-expressing stroma, which confers a competitive growth advantage on the cancer cells. Inhibition of the expression of Flower proteins reduces tumour growth and metastasis, and induces sensitivity to chemotherapy. Our results show that ancient mechanisms of cell recognition and selection are active in humans and affect oncogenic growth.

## 2.2 MAIN

*C9ORF7* (also known as *CACFD1*; referred to here as *hFWE*) encodes human Flower (hFWE) and generates four protein-coding splice variants (*hFWE1*–*hFWE4*) (Fig. 1a). Mining of the Encode database[22] showed high levels of acetylation at the 27th lysine residue of the histone H3 protein (H3K27Ac) and hypersensitivity to DNAase-I around the +1 open reading frame (ORF) (Extended Data Fig. 1a, b), suggesting that the *hFWE* locus is transcriptionally active[23]. The *hFWE* exons are conserved (Extended Data Fig. 1c), and alternative splicing produces four hFWE isoforms of transmembrane proteins, with membrane-spanning domains as predicted (Fig. 1b). To identify potential $hFWE^{Win}$ or $hFWE^{Lose}$ isoforms (as observed in *Drosophila*[6]), we generated CRISPR-assisted MCF-7 $hFWE^{KO}$ cells that expressed individual hFWE isoforms and used them for a co-culture protocol (Extended Data Fig. 1d). MCF-7 $hFWE^{KO}$ cells lacked expression of *hFWE* mRNA (Extended Data Fig. 1e), but did not differ from wild- type cells in terms of proliferation (BrdU and MTT assays), cell- cycle, reactive oxygen species (ROS), annexin-V, and clonogenic assays (Extended Data Fig. 1f–k). Lentivirus-assisted overexpression of the four hFWE isoforms had no effect on cell proliferation, cell death, cell volume, cellular sphericity, or annexin-V staining when compared to MCF-7 $hFWE^{KO}$ cells (Extended Data Figs. 1l, m, 2a–f, Supplementary Video 1). From these data, we conclude that, as in *Drosophila*[3,6,18,24], human cells homogenously expressing single hFWE isoforms do not undergo apoptosis.

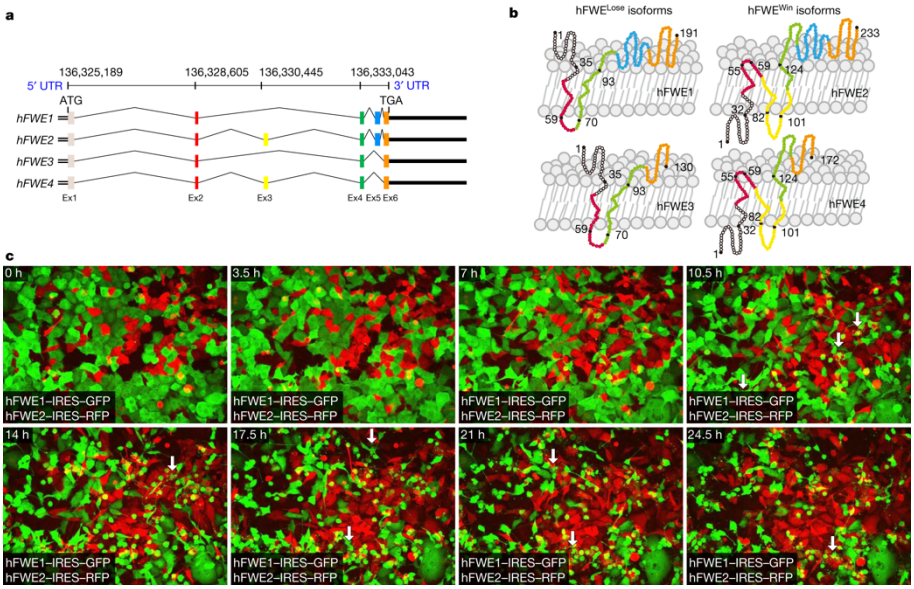


**Figure 1 - Characterization of human flower isoforms and competition between winner and loser cells. a**, A schematic representing the *hFWE* gene locus and its six exons, which alternatively splice to generate four hFWE isoforms (hFWE1–hFWE4). **b**, Model depicting the transmembrane structures of the four hFWE proteins. The colour coding of amino acid chains is complementary to the colour coding of *hFWE* exons and shows the contributions and locations of the amino acid sequences coded by each exon. **c**, Live-cell imaging shows competition between *hFWE*$^{KO}$ MCF-7 cells expressing hFWE1–IRES–GFP (green) and hFWE2–IRES–RFP (red) isoforms; cells carrying the hFWE1 isoform are eliminated. $n$ = 3 biologically independent experiments with similar results.

To identify potential hFWE$^{Win}$ and hFWE$^{Lose}$ isoforms, we performed live-cell imaging (Extended Data Fig. 1d), which showed that cells expressing hFWE1 or hFWE3 undergo cell death only when co-cultured with cells expressing either hFWE2 or hFWE4; cell death was accompanied by increased proliferation of cells expressing hFWE2 or hFWE4 (Fig. 1c, Extended Data Figs. 3a, b, 4a, Supplementary Videos 2–

5). These findings suggest that hFWE2 and hFWE4 function as hFWE$^{Win}$ isoforms whereas hFWE1 and hFWE3 function as hFWE$^{Lose}$ isoforms. Furthermore, elimination of hFWE$^{Lose}$-expressing cells occurred through caspase-dependent apoptosis, because the addition of the caspase inhibitor Z-VAD-FMK inhibited this process and annexin-V staining (Extended Data Figs. 4b, 5a, b, 6a, Supplementary Videos 6, 7). Cells expressing individual isoforms (hFWE1–hFWE4) did not induce loss of co-cultured *hFWE$^{KO}$* cells, indicating that hFWE-mediated cell elimination requires cells that express both hFWE$^{Win}$ and hFWE$^{Lose}$ (Extended Data Fig. 6b, Supplementary Video 8). Elimination of hFWE$^{Lose}$ cells was dependent on contact with hFWE$^{Win}$ cells, because no apoptosis was observed during imaging of low-density-plated hFWE1–GFP$^{+}$ and hFWE2–RFP$^{+}$ cells (Extended Data Fig. 6c, Supplementary Video 9). We tested whether factors secreted by hFWE$^{Win}$-expressing cells were involved in cell elimination by transferring conditioned medium from hFWE2-expressing cells onto hFWE1-expressing cells and found that it had no significant effect on cell death (Extended Data Fig. 6d). Live-cell calcium imaging using Fluo-4AM dye showed that expression of individual hFWE isoforms in MCF-7 *hFWE$^{KO}$* cells had no effect on cellular calcium levels (Extended Data Fig. 7a, b), and the calcium chelator BAPTA-AM did not interfere with the elimination of hFWE$^{Lose}$- expressing cells (Extended Data Fig. 7c), suggesting that hFWE isoforms do not function as calcium transporters[25–27] and their function is calcium-independent. We conclude that human Flower proteins work as canonical fitness fingerprints.

To study the role of Flower proteins in human cancer, we used quantitative PCR (qPCR) to measure the expression of hFWE isoforms in laser-captured formalin-fixed paraffin-embedded (FFPE) samples of cancerous and adjacent stromal tissue from individuals with malignant tumours (25 breast, 21 colon), benign tumours (10 breast, 10 colon), and normal tissue (10 breast, 10 colon, from matched

patients; Fig. 2a). All hFWE isoforms showed poor expression in normal tissue. The tumour tissue showed increased expression of hFWE$^{Win}$ isoforms, and stromal tissue showed significant upregulation of hFWE$^{lose}$ isoforms (more in malignant tumours than in benign tumours and their stroma; Fig. 2a). Sequential laser capture of breast and colon stromal tissue showed a significant increase in expression of hFWE$^{Lose}$ isoforms in the first 400 μm from the edge of the tumour tissue (Extended Data Fig. 7d), where genes involved in the regulation of apoptosis were concurrently upregulated (Extended Data Fig. 7e). Fluorescence in situ hybridization (FISH) showed increased expression of hFWE$^{Win}$ isoforms exclusively in breast cancer cells (Extended Data Fig. 7f); further qPCR showed that, unlike tumour epithelial cells, normal epithelial cells do not exhibit high hFWE$^{Win}$ expression (Extended Data Fig. 7g). MCF-7 *hFWE$^{KO}$* cells expressing hFWE2 induced apoptosis of co-cultured primary epithelial cells or fibroblasts (isolated from normal breast tissue; Extended Data Fig. 8a).

We generated two anti-hFWE antibodies (one against the N terminus that is common to all four isoforms, and the other specific to the hFWE$^{Win}$ isoforms (encoded by exon 3)). We used immunohistochemistry to validate the antibody specificity in sections of *hFWE$^{KO}$* cells overexpressing hFWE1, hFWE2, hFWE3 or hFWE4 (Extended Data Figs. 8b, 9a). Immunostaining with anti-hFWE$^{Win}$ and anti-hFWE-N-term antibodies produced positive membrane staining in breast cancer cells (Extended Data Fig. 9b). Immunohistochemistry with the anti-hFWE$^{Win}$ antibody showed that hFWE$^{Win}$ was expressed exclusively in breast, colon, and squamous cell carcinoma (SCC) cancers (Fig. 2b, Extended Data Figs. 7h, 9c). Immunohistochemistry of the same breast, colon, and SCC cancers with anti-hFWE-N-term anti-bodies —which recognize both hFWE$^{Win}$ and hFWE$^{Lose}$ isoforms— showed staining of both cancer and stromal cells (Fig. 2b, Extended Data Figs. 7h, 9c). Both antibodies showed poor staining in normal tissue (Extended Data Fig. 9c).

Our main observations from this analysis were that both types of hFWE isoform tend to be low in healthy tissue, hFWE$^{Win}$ isoforms are upregulated in cancer tissue (more in malignant than in benign cancers), and levels of hFWE$^{Lose}$ isoforms are unusually high in the cancer-adjacent stroma.

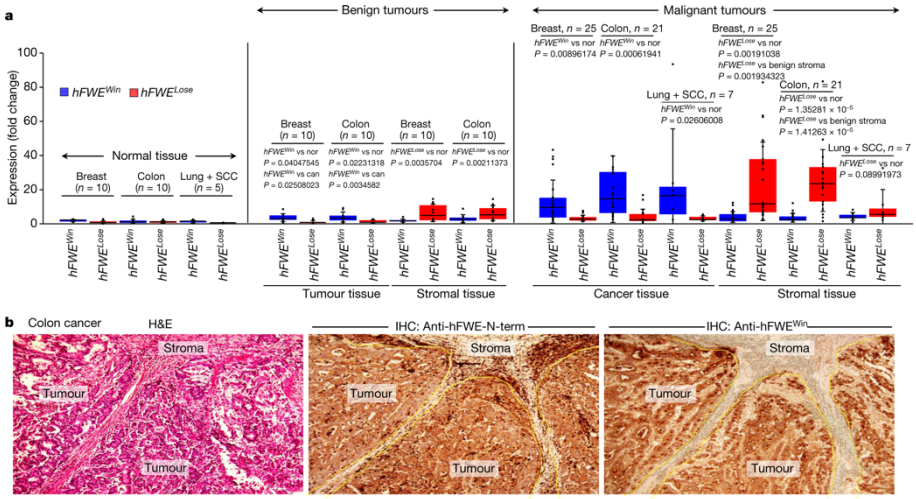


**Figure 2 - Flower isoforms and human cancer. a**, Expression of hFWE$^{Win}$ and hFWE$^{Lose}$ mRNA is observed in benign and malignant tumours, their respective stroma (from same samples) and healthy tissue (laser microdissected, FFPE samples). Poor expression was observed in healthy tissue; hFWE$^{Win}$ isoforms were upregulated in benign tumour tissue; and hFWE$^{Lose}$ isoforms were upregulated in stromal tissue. In malignant tumours, hFWE$^{Win}$ isoforms were significantly upregulated in cancer tissue and hFWE$^{Lose}$ isoforms were significantly upregulated in stromal tissue. hFWE$^{Win}$ expression ratio for normal:benign tumour:malignant tumour, 1:2.328:11.369. hFWE$^{Lose}$ expression ratio for normal:benign stroma:malignant stroma, 1:6.513:24.694. By binary logistic regression analysis, hFWE$^{Win}$ in cancer (with $P = 0.006$) and hFWE$^{Lose}$ in stroma (with $P = 0.015$) together have predictive capacity for malignant tumours of 86.3%. *n* represents the number of biologically independent experiments and fold change is calculated against the expression of hFWE$^{Win}$ isoforms in normal breast tissue. Box plots show median, first

and third quartiles, positive and negative error values (s.d.). All statistically significant *P* values are shown (two-tailed *t*-test). Nor, normal tissue; can, cancer tissue. **b**, Left, haematoxylin and eosin (H&E) stained colon cancer and stromal samples. Right, immunostaining of colon cancer samples shows the abundance of $hFWE^{Win}$ isoforms. Middle, staining with anti-hFWE-N-term antibody shows staining in both tumour and stroma. This experiment was repeated independently three times with similar results.

These results suggested that tumour cells exhibit high $hFWE^{Win}$ expression and tend to grow in areas of stroma with high $hFWE^{Lose}$ expression. To investigate whether overexpression of $hFWE^{Lose}$ in host tissue and $hFWE^{Win}$ in the tumour might result in aggressive tumour growth, we generated $Fwe^{KO}$ mice[26] bearing orthotopic breast tumours derived from MCF-7 cells. Individual hFWE isoforms were overexpressed in the mammary tissue of $Fwe^{KO}$ mice to study the effects of host cells, and $hFWE^{KO}$ MCF-7 cells overexpressing GFP-tagged individual hFWE isoforms were used to generate the tumours (Fig. 3a). When we analysed all possible combinations, we found that MCF-7 $hFWE^{KO}$ cells expressing hFWE2–GFP or hFWE4–GFP generated isoform expression within $Fwe^{KO}$ mouse mammary tissue (28-day study). Reduced tumour growth was observed when mammary tissue expressed $hFWE^{Win}$ isoforms and cancer cells expressed $hFWE^{Lose}$ isoforms. Increased tumour growth was observed when mammary tissue expressed $hFWE^{Lose}$ isoforms and cancer cells expressed $hFWE^{Win}$ isoforms. $n$ = 3, all statistically significant *P* values shown, two-tailed *t*-test, mean ± s.d. aggressive tumours when implanted into mammary tissue expressing hFWE1 or hFWE3 (Fig. 3b, Extended Data Fig. 9d). The results suggest that interactions between expression of $hFWE^{Win}$ isoforms in tumours and $hFWE^{Lose}$ isoforms in the stroma are important for tumour growth.

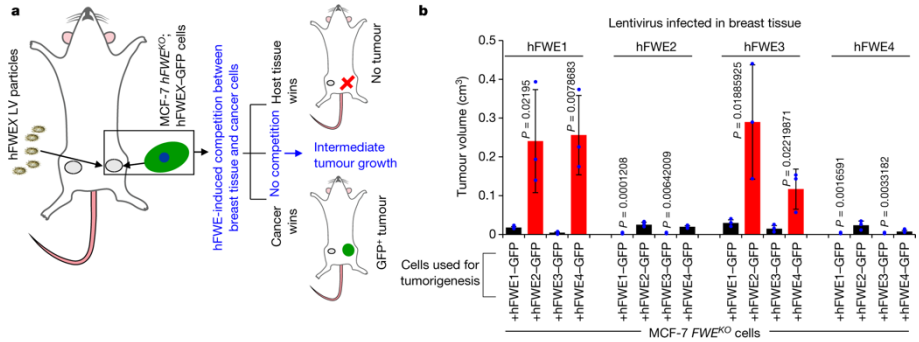


**Figure 3 - Lose isoform in stroma and Win isoform in tumour cooperate to induce aggressive cancer growth. a**, Schematic of mouse model used to study competition between injected hFWE$^{Win}$- or hFWE$^{Lose}$-expressing cancer cells and hFWE$^{Win}$- or hFWE$^{Lose}$-expressing host tissue. hFWE*X* represents any one of hFWE1–hFWE4. LV, lentivirus. **b**, Tumour volumes were measured and analyzed for each of the 16 combinations of hFWE*X*–IRES–GFP expression in MCF-7 *hFWE*$^{KO}$ xenografted cells and hFWE isoform expression within *Fwe*$^{KO}$ mouse mammary tissue (28-day study). Reduced tumour growth was observed when mammary tissue expressed hFWE$^{Win}$ isoforms and cancer cells expressed hFWE$^{Lose}$ isoforms. Increased tumour growth was observed when mammary tissue expressed hFWE$^{Lose}$ isoforms and cancer cells expressed hFWE$^{Win}$ isoforms. $n$ = 3, all statistically significant $P$ values shown, two-tailed $t$-test, mean ± s.d.

We investigated the role of host tissue hFWE isoforms by using hFWE2-overexpressing *hFWE*$^{KO}$ HCT-116 and MCF-7 cells to generate tumours in *Fwe*$^{WT}$ and *Fwe*$^{KO}$ mice. Both HCT-116 hFWE2$^{+}$ and MCF-7 hFWE2$^{+}$ tumours were larger with higher incidences of metastasis in *Fwe*$^{WT}$ mice than in *Fwe*$^{KO}$ mice (Extended Data Fig. 9e–g). The expression of hFWE$^{Lose}$ isoforms was upregulated in wild-type MCF-7 cells when they were co-cultured with hFWE2-expressing *hFWE*$^{KO}$ MCF-7 cells (Extended Data Fig. 10a, b). Similarly, expression of hFWE$^{Lose}$ isoforms was increased in tumour-adjacent tissue from *Fwe*$^{WT}$ mice after implantation of hFWE2-

expressing MCF-7 tumours when compared with before (Extended Data Fig. 10c). From these experiments, we conclude that the expression of Win isoforms in the tumour is sufficient to induce increased expression of Lose isoforms non-autonomously in the surrounding cells. These data show that stromal Lose and tumoral Win isoforms cooperate to promote aggressive cancer growth.

Next, we tested whether inhibition of Flower could provide anti- cancer benefits. Amongst ectopic tumours derived from *hFWE*$^{WT}$ and *hFWE*$^{KO}$ HCT-116 cells, those derived from *hFWE*$^{WT}$ cells were larger (Extended Data Fig. 10d, e). Knockdown of *hFWE* expression by short hairpin RNA (shRNA) in *hFWE*$^{WT}$ HCT-116 cells before xenografting (Extended Data Fig. 10g, h) reduced both tumour volume and probability of metastasis (Extended Data Fig. 10d–f). The growth (Extended Data Fig. 10d, e) and metastatic potential (Extended Data Fig. 10f) of HCT-116 tumours treated with shRNA targeting *hFWE* was rescued by ectopic expression of codon-optimized *hFWE2* cDNA (which is unaffected by anti-*hFWE* shRNA) (Extended Data Fig. 10h). In a gain-of-function experiment, we overexpressed hFWE2 in CCL-218 (colon cancer) cells, which express low levels of hFWE$^{Win}$ isoforms; this resulted in a nearly threefold increase in their tumour growth potential (Extended Data Fig. 10i, j).

We screened a panel of 18 metastatic cell lines of multiple origins (breast, colon, prostate, pancreatic, and ovarian) for hFWE$^{Win}$ expression (Extended Data Fig. 10j). Cells with higher (HCT-116 colon and DU-145 prostate) or lower (CCL-218 colon and OVCAR-8 ovarian) expression of hFWE$^{Win}$ were selected, and their tumorigenic potential was observed. We tested the therapeutic potential of *hFWE* gene knock- down (Extended Data Fig. 10g) in combination with standard-of-care chemotherapy against the tumorigenic potential of these cancer cell lines. DU-145 and HCT-116 cells had significantly higher tumorigenic potential and generated larger tumours than CCL-218 and OVCAR-8 cells (Fig. 4a, b). *hFWE* knockdown

significantly reduced tumour volumes (Fig. 4a, b). Control xenografts and those treated with scrambled shRNA generated much larger tumours than xenografts treated with anti-*hFWE* shRNA or chemotherapy (fluorouracil (5-FU) for colon cancer[28], or cisplatin and docetaxel for prostate[29] and ovarian[30] cancer). Treatment with a combination of anti-*hFWE* shRNA and chemotherapy further reduced, and in some cases completely eliminated, tumorigenesis (Fig. 4a, b). Control experiments demonstrated the efficiency of *hFWE* shRNA in all tumours (Extended Data Fig. 10k). Metastatic probability was reduced markedly upon *hFWE* knockdown and even further by combined treatment with chemotherapy (Fig. 4c). Thus, we conclude that human hFWE proteins can have a powerful effect on tumorigenicity and propose that therapies targeting these proteins have the potential to impair cancer growth and metastasis.

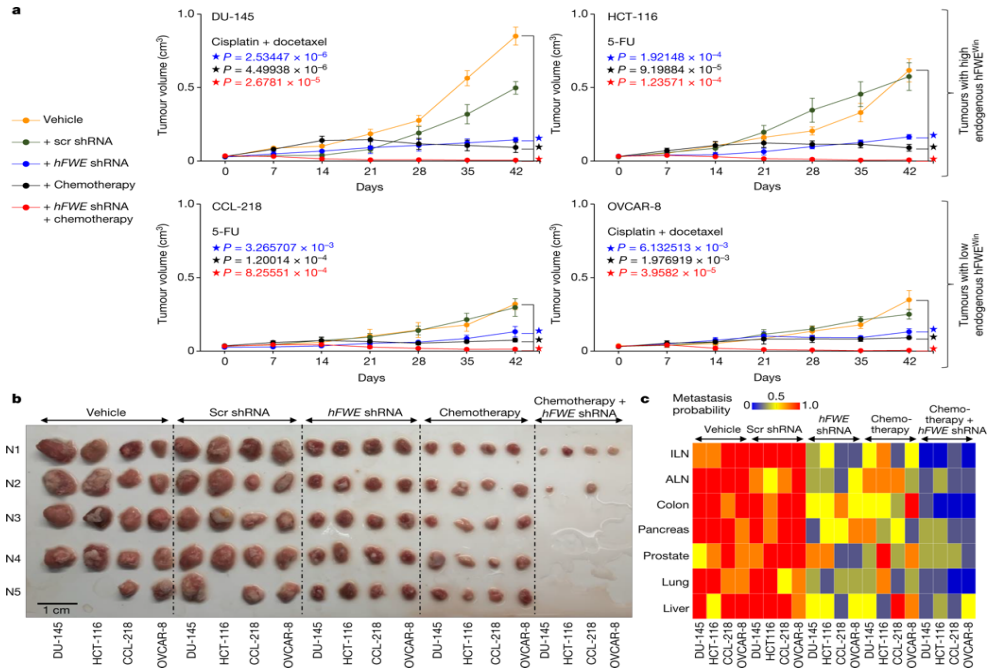


**Figure 4 - hFWE knockdown inhibits tumorigenicity and improves chemotherapy efficiency. a**, **b**, The effect of shRNA-mediated *hFWE* knockdown on the tumour growth potential of DU-145 (prostate), HCT-116 (colon), CCL-218

(colon) and OVCAR-8 (ovarian) cell lines was tested. Orange, control vehicle-treated tumours; green, negative control non-specific scrambled (Scr) shRNA-treated tumours; blue, tumours treated with a cocktail of anti-*hFWE* shRNA, resulting in a significant reduction in tumour volume; black, cisplatin + docetaxel for prostate (DU-145) and ovarian (OVCAR-8) lines and 5-FU for colon cancer lines (HCT-116 and CCL-218); red, a combination of *hFWE* knockdown with chemotherapy abolishes tumour burden in several cases and overall significantly reduces tumour growth. $n = 5$ biologically independent experiments, $P$ values shown, mean ± s.d., one-tailed $t$-test. **c**, The effect of treatment with vehicle, scrambled shRNA, *hFWE* shRNA, chemotherapy, and a combination of *hFWE* shRNA and chemotherapy on metastasis. Heat map scale indicates the probability of metastasis, which is significantly reduced by treatment with *hFWE* shRNA or a combination of *hFWE* shRNA and chemotherapy (compare groups 1 and 2 with groups 3, 4 and 5; $n = 5$ each group).

We have shown that the human Flower protein code mediates competitive interactions that depend on cell contact and caspase-dependent apoptosis but not on calcium transport. Homogeneous expression of any of the four Flower proteins does not trigger cell elimination or affect cell fitness in terms of proliferation, survival, or clonogenicity. Cell elimination requires different levels of Win and Lose isoforms in neighbouring cells, demonstrating that relative levels of these proteins are more important than absolute levels for cell selection. In addition, we find that human tumours use cell fitness markers to gain a competitive advantage over neighbouring cells. This work represents a conceptual advance in understanding the role of cell fitness comparisons in the progression of human cancer. It describes a concrete molecular mechanism that regulates oncogenic growth and metastasis via the Flower fitness comparison system. This appears to be a striking general feature of solid tumours and an unrecognized prerequisite for tumour growth. Notably, we also show that inhibition of cell competition can be combined with standard-of-care

chemotherapy to further prevent tumour growth and metastasis of colon, ovarian and prostate cancers.

## 2.3 METHODS

### 2.3.1 BIO-INFORMATICS ANALYSIS.

Encode data for the *CACFD1* (*hFWE*) gene were collected systematically from the UCSC Genome Browser. The trans-membrane structures for human hFWE isoforms were predicted using Predictprotein 2013 software from the Technical University of Munich.

### 2.3.2 ESTABLISHED CELL LINES AND CULTURE CONDITIONS.

A2780-CR, A2780-CS, CCL-218, DU-145, HCC-1954, HCT-116, MCF-7, MCF 10A, MD-4, MD-7, MDA-MB-231, MDA-MB-468, PC-3, SK-BR-3, TR-127, TR-182 and ZR-75 cells were procured with certificates of authentication from the American Type Culture Collection (ATCC). HEK293 cells were procured from Cell Biolabs. OVCAR-4 and OVCAR-8 cells were kindly provided by S. Karuppaiyah (Ohio State University). In brief, all cell lines were cultured as suggested by the ATCC in Dulbecco's modified Eagle's medium (DMEM) or RPMI 1640 (Corning) supplemented with 10% (v/v) heat-in- activated fetal bovine serum (FBS) (Gibco) and 1% (v/v) penicillin/streptomycin (Thermo Fisher Scientific) and incubated at 37 °C in a humidified atmosphere of 95% air and 5% $CO_2$. Cell lines were tested for mycoplasma contamination.

### 2.3.3 TRANSFECTIONS AND PREPARATION OF LENTIVIRAL PARTICLES.

All transfections were per- formed using Lipofectamine 3000 (Thermo Fisher Scientific). Lentiviral particles encoding Cas9 + *hFWE* single guide RNA (sgRNA), *hFWE* shRNA, and cDNA for hFWE1–hFWE4 were generated using HEK293T cells and their respective packaging. The viral particles were concentrated by centrifuging the supernatant at 22,000 r.p.m. for 2 h at 20 °C. The pellet was re-suspended in 200 µl 1× HBSS, purified by layering the 200 µl of viral preparation on 1.5 ml of 20% sucrose (in HBSS) and centrifugation at 22,000 r.p.m. for 2 h at 20 °C, and then the pellet was re-suspended in 100 µl 1× HBSS. The titre of lentiviral particles was determined using a p24 ELISA kit (Cell Biolabs); $10^9$ TU $ml^{-1}$ was used for cell culture experiments, and $10^{11}$ TU $ml^{-1}$ was used for in vivo infections. For infection of target cells, lentiviral particles were diluted in culture medium containing 5 µg $ml^{-1}$ polybrene (Thermo Fisher Scientific).

### 2.3.4 Generation of MCF-7 and HCT-116 hFWEKO cells.

Stable knockout of *hFWE* was performed using lentiCRISPR V2 vector (Addgene) expressing both Cas9 and sgRNA targeting the *hFWE* gene loci. Cloning of sgRNA targeting *hFWE* gene loci was performed as described previously[31,32]. Lentiviral particles were generated by transfection of HEK293T cells with lentiCRISPRs, psPAX2, and pMD2.G plasmids (Addgene) and the virus was collected 48 h later[31,32]. MCF-7 and HCT-116 cells were infected with lentiviral particles, and 48 h later the medium was replaced with culture medium containing 2 µg $ml^{-1}$ puromycin (Thermo Fisher Scientific). After 2 weeks of puromycin selection, single-cell colonies were isolated via ring cloning. DNA from each colony was extracted using QuickExtract (Epicentre). To confirm that an indel was present at both alleles, the region, including the target site, was amplified using PCR. The PCR products were ligated into pBlueScript (Addgene) for cloning and sequencing. Oligos for creating CRISPRs: CACFD1-csp1a: CACCGCATGACGTGGTGGTACCGC, CACFD1-csp1b: AAACGCGGTACCACCACGTCATGC, CACFD1-csp2a: caccT-TTCAAGCTTGCGCGATCTC, CACFD1-csp2b: aaacGAG ATC GCG CAA GCT TGA

AA, CACFD1-csp3a: CACCGGGCTGTGAGCTGCGCCTGA, CACFD1- csp3b: AAACTCAGGCGCAGCTCACAGCCC. Primers used for PCR to check deletion: CACFD1-PCR-csp1F: aagcttTAT GCT CCC TCT CCC ACA AGG C, CACFD1-PCR-csp1R: ctcgagGAC TGG ATA CTC ACA GAC TGC CC, CACFD1- PCR-csp2F: aagcttCTT CTG GGT GCT GTG AGA ACT GTG, CACFD1-csp2R: ctcgagGGA CGG CCA TGC ATT ACT CAC.

### 2.3.5 shRNAs.

Stable knockdown of *hFWE* was performed using lentiviral constructs (Genscript) containing shRNA targeting *hFWE*. The shRNA sequences were: 5′-TCTGGCCTCTTCAACTGCATCACCATCCA-3′; 5′-TGAATGCC TTCATCTTGTTGCTGTGTGAG-3′; 5′-CGCTCCTGGCAGAAGGCT GTCTTCTACTG-3′; and 5′-GGCAGCAGGCGGATGAGGAGAAGCTCGCG-3′. The lentiviral packaging was performed in 293FT cells using ViraSafe Lentivirus Packaging System (Pantropic Cell Biolabs), as per the manufacturer's instructions and previously stated. Forty-eight hours after transduction, cells were selected with 2 μg $ml^{-1}$ puromycin in growth medium for 10 days and single colonies were selected and propagated. Gene knockdown efficiency was assessed by qPCR.

### 2.3.6 hFWE cDNA overexpression.

The pCDH-CMV-MCS-EF1α-copGFP and pCDH- CMV-MCS-EF1α-RFP vectors expressing individual hFWE isoforms 1–4 were obtained from System BioSciences. GFP-IRES-Isoform-1-4_OptHs vectors were obtained from ATUM. The lentiviral packaging was performed in 293FT cells using ViraSafe Lentivirus Packaging System (Pantropic Cell Biolabs) per the manufacturer's instructions.

### 2.3.7 MTT assay.

We seeded 1 × $10^4$ MCF-7 wild-type of *hFWE*$^{KO}$ cells into 96-well plates overnight. Next, the culture medium was removed and cells were washed with PBS, and then incubated with 0.5 mg/ml 4,5-dimethylthiazol-2-yl-2,5-diphe- nyltetrazolium bromide (MTT; Sigma-Aldrich) in fresh culture medium for 3 h at 37 °C. The culture medium was carefully aspirated, and the formazan product was dissolved in 180 µl DMSO. Cell viability was measured as the difference between the absorptions at wavelengths of 570 and 650 nm. All experiments were performed in triplicate and repeated three times.

### 2.3.8 COLONY FORMATION ASSAY.

MCF-7 wild-type and MCF-7 *hFWE*$^{KO}$ cells were seeded into 6-well culture plates (1 × $10^3$ cells per well) and then cultured under standard conditions over 21 days. The medium was replaced every third day. Finally, the cells were fixed with methanol and then stained with crystal violet (Sigma Aldrich). All experiments were performed in triplicate and replicated three times.

### 2.3.9 BRDU ASSAY.

Cellular proliferation was measured using the Cell Proliferation ELISA BrdU Colorimetric Assay Kit (Roche Applied Science). We plated 1 × $10^3$ MCF-7 wild-type or *hFWE*$^{KO}$ cells per well in 96-well plates. Twenty-four hours after plating, cells were labelled with BrdU in fresh culture medium overnight at 37 °C. Cells were then fixed and denatured for 30 min, followed by incubation with peroxidase substrate solution at 25 °C and the reaction was stopped using 1 M $H_2SO_4$. An absorbance wavelength of 450 nm and reference wavelength of 690 nm were used. All experiments were performed in triplicate and replicated three times.

### 2.3.10 ROS MEASUREMENT.

ROS levels were determined by incubating MCF-7 wild-type and *hFWE*$^{KO}$ cells in serum-free DMEM containing 10 μM 2′,7′-dichlorodihydro- fluorescein diacetate (H-DCFDA; Thermo Fisher Scientific) for 30 min at 37 °C. Cells were trypsinized and were washed twice in PBS, and the final cell pellet was re-suspended in PBS. DCF intensity was measured by flow cytometry using the BD-LSRII H274 per manufacturer's instructions. All experiments were performed in triplicate and replicated three times.

### 2.3.11 Apoptosis and cell cycle analysis.

At the endpoint of monoculture or co-culture experiments, cells were stained with annexin-V (Thermo Fisher Scientific) per the manufacturer's instructions. Flow cytometry was performed to detect apoptotic cells by observing FITC-conjugated and pacific blue-conjugated annexin-V staining. For cell cycle analysis, MCF-7 wild-type and MCF-7 *hFWE*$^{KO}$ cells were fixed in 70% ethanol. Fixed cells were washed with cold PBS and stained with 50 μg ml$^{-1}$ propidium iodide (Thermo Fisher Scientific). Flow cytometry for apoptosis detection and cell cycle distribution profiles was performed using MACSQuant Analyzer (Miltenyi Biotec) and analysed using FlowJo software (Treestar).

### 2.3.12 Live-cell imaging of cell competition assay.

MCF-7 *hFWE*$^{KO}$ cells were infected with lentiviral particles expressing GFP- or RFP-tagged hFWE1–hFWE4 isoforms and cultured for 24 h. RFP$^{+}$ and GFP$^{+}$ cells were sorted by flow cytometry using the BD FACS ARIA III (BD Biosciences). Overexpression of *hFWE* in sorted cell populations was measured by qPCR and only sorted batches with high expression of hFWE1–hFWE4 (characterized by *hFWE* Ct value of ~14, with *GAPDH* Ct value of ~21) were used. Equal numbers of MCF-7 cells expressing GFP- or RFP-tagged hFWE1–hFWE4 were co-plated in a glass-bottom dish (Matek) in the specified combinations and co-cultured under normal

conditions for 24 h. Cells were then subjected to live-cell imaging for the indicated times and processed for apoptosis detection by annexin-V staining. To study caspase-dependency for cell death, MCF-7 *hFWE*$^{KO}$ cells expressing hFWE$^{Win}$ were co-cultured with MCF-7 *hFWE*$^{KO}$ cells expressing hFWE$^{Lose}$ in the presence of the caspase inhibitor Z-VAD-FMK (20 μM, Sigma-Aldrich) for 24 h. We next performed live-cell imaging at the indicated times, and, at the study endpoint, cells were processed for apoptosis detection by annexin-V staining when indicated. To observe the contact-dependency of cell competition, an equal number of MCF-7 *hFWE*$^{KO}$ cells expressing hFWE1–GFP and MCF-7 *hFWE*$^{KO}$ cells expressing hFWE2–RFP were co-plated at low density, followed by live-cell imaging. For conditioned medium experiments, medium was collected from MCF-7 *hFWE*$^{KO}$ cells expressing hFWE2 cDNA, centrifuged at 1,000 r.p.m. for 5 min, and then added to target MCF-7 *hFWE*$^{KO}$ cells expressing hFWE1–GFP. Cells were subsequently cultured for 24 h, then we performed live- cell imaging at the indicated times. Live-cell imaging was performed using Leica TCS SP8 confocal laser microscopy (Leica Microsystems), a Nikon A1 HD25 confo- cal microscope (Nikon), and a Zeiss LSM-800 with Airy Scan Confocal Microscope (Zeiss). Analysis of cell motility, cell count and cell death was performed manually using Fiji software (http://fiji.sc/) and the analysis of average cell volume and aver- age cell sphericity were performed using Imaris7.6.5 software (Bitplane).

### 2.3.13 Cell competition assay with normal breast cells.

MCF-7 *hFWE*$^{KO}$ cells were infected with lentiviral particles expressing hFWE2–GFP and cultured for 24 h. MCF-7 *hFWE*$^{KO}$ cells expressing hFWE2–GFP were subsequently cultured on their own or co-cultured with an equal number of normal breast primary epithelial cells or fibroblasts. Cells from each combination were collected at the indicated times for annexin-V staining and the percent of apoptotic cells was measured in the GFP-positive and GFP-negative populations using flow

cytometry. Human epithelial cells and fibroblasts were isolated from normal breast tissue from fresh or cryopreserved, de-identified tissues; samples were obtained from the Komen Tissue Bank (KTB) at IU School of Medicine, Indianapolis, after informed consent from the donors. All experiments were carried out in accordance with the approved guidelines of the Indiana University Institutional Review Board, which determined the study to be non-human subjects research. International Ethical Guidelines for Biomedical Research Involving Human Subjects were followed. Proceedures for isolation of primary cells from biopsies and propagation have been described[33].

### 2.3.14 Determination of cellular calcium levels.

MCF-7 *hFWE*$^{KO}$ cells and MCF-7 *hFWE*$^{KO}$ cells infected with lentiviral particles expressing hFWE1–4 isoforms individually were plated in glass-bottom dishes (Matek). After 24 h, cells were incubated with the fluorescent dye Fluo-4AM (Thermo Fisher Scientific) as per the manufacturer's protocol for 40 min, washed with PBS, and then incubated for an additional 15 min to complete the de-esterification of the dye. Live-cell imaging was immediately performed at the indicated times to determine cellular $Ca^{2+}$ levels using TCS SP8 (Leica) confocal imaging. An excitation wavelength of 494 nm and an emission wavelength of 506 nm were used. Results were quantified by measuring the $Ca^{2+}$ indicator mean fluorescence intensity (MFI) in all cell combinations using Fiji. All experiments were performed in triplicate and repeated three times.

### 2.3.15 BAPTA-AM.

MCF-7 *hFWE*$^{KO}$ cells were infected with lentiviral particles express- ing hFWE1–RFP or hFWE2–GFP and cultured for 24 h. Then, MCF-7 *hFWE*$^{KO}$ cells expressing hFWE1–RFP and MCF-7 *hFWE*$^{KO}$ cells expressing hFWE2–GFP were co-plated in equal numbers and co-cultured for 24 h in the presence or absence of BAPTA-AM

(10 μM, Thermo Fisher Scientific). Cells were collected for annexin-V staining and flow cytometry analysis.

### 2.3.16 Laser-capture microdissection.

FFPE tissue sections (5-μm thick) were subjected to laser capture microdissection using the Leica Microsystems at UNMC; Zeiss Palm MicroBeam IV Laser Capture Microdissection system at Thornwood facility and Michigan University. Matched H&E-stained sections were used to demarcate cancer versus stroma. Adjacent normal tissues were microdissected in precise increments of 200 μm in distance perpendicular from the boundary of tumour mass. Captured tissue was collected into the adhesive cap (Zeiss).

### 2.3.17 Immunohistochemistry.

Matched normal and tumour patient samples of breast and colon origin were formalin-fixed and paraffin-embedded. FFPE tissues were cut into sections of 5 μm and were stained with H&E or hFWE antibodies. Samples were deparaffinized in xylene and rehydrated in a graded series of ethanol. Antigen retrieval was performed in 10 mM EDTA buffer pH 9 for 20 min at 96–98 °C. Samples were allowed to cool at room temperature for 20 min, and blocked in 1% peroxide solution for 10 min, followed by washing with TBS + 0.5% Triton X-100. Slides were blocked in 3% bovine serum albumin (BSA, Sigma-Aldrich), then incubated with anti-hFWE-N-term (Ab1; 1:500) and anti-hFWE$^{Win}$ (Ab4; 1:500) primary antibodies (Genscript) in blocking solution overnight at 4 °C. The sections were incubated in goat anti-mouse IgG HRP-conjugated secondary anti- body (1:2,000, Thermo Fisher Scientific) for 1 h at 25 °C and then developed with 3,3′-diaminobenzidine (DAB, Vector Labs) for 10 min to visualize the colour of the reaction.

### 2.3.18 Immunofluorescence.

For immunofluorescent and immunocytological staining for hFWE in human tissue and cells, anti-hFWE-N-term (Ab1) and anti- hFWE$^{Win}$ (Ab4) antibodies were used at 1:500 final dilution, and goat anti-mouse IgG AlexaFluor 488 (1:1,000, Thermo Fisher Scientific) was used as the secondary antibody. SCC, colon, and normal skin FFPE samples were cut into 5-µm sections and stained with H&E or hFWE antibodies. Immunofluorescence experiments were performed as described previously[34] and refined for the hFWE antibodies. Serial sections were incubated with anti-hFWE-N-term and anti-hFWE$^{Win}$ anti- bodies overnight at 4 °C. Sections were incubated with secondary antibody for 2 h and nuclei were counterstained with 4′,6-diamidino-2-phenylindole (DAPI, Sigma-Aldrich, 1 µg ml$^{-1}$).

### 2.3.19 IMMUNOCYTOCHEMISTRY.

MCF-7 *hFWE$^{KO}$* cells and MCF-7 *hFWE$^{KO}$* cells express- ing one of hFWE1–hFWE4 were collected by trypsinization and the cell pellet was resuspended in pre-heated 1.5% agarose + 2% sucrose solution, homogenized, and allowed to solidify. The agarose block was placed in 30% sucrose overnight. Eight-micrometre-thick sections were prepared using a Cryostat 3050S (Leica) and slides were stained using the Bond Polymer Refine Detection Kit (Leica) per the manufacturer's instructions. Slides were then incubated with anti-hFWE-N-term and anti-hFWE$^{Win}$ antibodies for 15 min and subsequently processed using Leica Detection Polymer and developed with DAB according to the kit instructions.

To analyse the membrane topology of hFWE isoforms, MCF-7 *hFWE$^{KO}$* cells were plated in Nunc LabTek-II 4-chambered coverglass (Thermo Fisher Scientific) overnight and then transfected with cDNA for hFWE1–hFWE4 using Lipofectamine 3000. After 24 h, the cells were fixed with 3.7% paraformaldehyde in PBS for 15 min, and then permeabilized with 0.1% Triton X-100 in TBS for 7 min or non-permeabilized. Subsequently, the cells were blocked with 3% BSA and incubated

with anti-hFWE-N-term or anti-hFWE$^{Win}$ primary antibody in 3% BSA for 4 h, washed three times with 1× PBS and stained with secondary antibody for 2 h. Nuclei were counterstained with Hoechst 33258 (Thermo Fisher Scientific). Images were acquired with a Zeiss LSM880 inverted by using a Plan- ApoChromat 20×/0.8 dry lens. An argon laser with 25 mW of head power and a 405 Diode laser with 30 mW head power were used to excite AlexaFluor488 and Hoechst, respectively. The signal detected was limited to the portions of the visible spectrum between 495 and 545nm and 420 and 480nm by using BP filters in front of a ZEISS Airy Scan detector. The images were acquired in super-resolution mode with an XY sampling factor (pixel size) of 55 nm. A volume of approximately 12 µm was acquired around the central plane of each cell with a *z*-step of 342 nm. After the acquisition, the images were processed in order to reassign the information collected by the 32 Airy detectors to their source point and obtain a theoretical resolution of 233 nm for the A488 channel and 204 nm for the Hoechst channel.

### 2.3.20 Fluorescent in situ hybridization.

FFPE breast cancer sections (5-µm thick) were stained with H&E to verify that the slides included both cancer and normal tissue. Next, 5-µm-thick serial sections were prepared for processing with the in situ + ISH Tissue Assay kit (Affymetrix) according to the manufacturer's instructions. Probe sets were designed by Affymetrix to detect exon 3 and exon 4 of *CACFD1* mRNA. After deparaffinization, slides were subjected to heat pretreatment (90 °C, 30 min) and protease digestion, (40 °C, 20 min). Then sections were hybridized with probe following the signal-amplification step. Sections were developed using kit-supplied Fast Red substrate and counterstained with DAPI. All sections were mounted with DAKO UltraMount Permanent Mounting Medium (Agilent). Fluorescent images were acquired using a BZ-X700 microscope (Keyence).

### 2.3.21 RNA isolation and quantitative RT–PCR analysis.

Total RNA was isolated from cancer cell lines, patient tumour samples, and mouse tumour xenografts using the PureLink RNA Mini kit (Qiagen). Total RNA was isolated from laser-captured FFPE tissue samples using the RNeasy FFPE kit (Qiagen). Ten nanograms of total RNA was reverse-transcribed to complementary DNA using Superscript Vilo cDNA synthesis kit (Thermo Fisher) per the manufacturer's instructions. Quantitative PCR (qPCR) was performed with PowerUp SYBR Green master mix (Thermo Fisher) using the Rotor Gene Q (Qiagen), BioRad CFX96, QuantStudio 6 (ABI) or Light cycler 96 instrument (Roche). The reaction conditions included an initial denaturation step at 95 °C for 2 min, followed by 40 cycles of 95 °C for 15 s and 60 °C for 60 s. Data were analysed using the comparative *C*t method[35]. The *C*t values of samples and controls were normalized to the expression level of the *GAPDH* housekeeping gene. All qPCR reactions were set up in triplicate and the experiments were performed with at least three different samples. The following primers were used (F: forward; R: reverse): *GAPDH*: 5′-GGATGCAGGGAT GATGTTC-3′ (F) and 5′-TGCACCACCAACTGCTTAG-3′ (R); *hFWE1*: Ex2–4 5′-GCGTGTGGATGATGATGG′ (F) and Ex5 5′-CCTGTCTTGTCCCCTC TGA-3′ (R); *hFWE2*: Ex3 5′-CTGCCAGTTCATCGAGTTTG-3′ (F) and Ex5 5′-CCTGTCTTGTCCCCTCT GA-3′ (R); *hFWE3*: Ex2–4 5′-GCGTGTGG ATGATGATGG-3′ (F) and Ex4–6 5′-AGATCGCATCGCCCTTT-3′ (R); *hFWE4*: Ex3 5′-CTGCCAGTTCATCGAGTTTG-3′ (F) and Ex4–6 5′-GATCGCATCGCCCTTTT-3′ (R); *hFWE*$^{Win}$: 5′-GCCTTCATCTTGT TGCTGTG-3′ (F) and 5′-CATCCCGCAGTAGAAGACAG-3′ (R); *hFWE*$^{Lose}$: 5′-GCGTGTGGATGATGATGG-3′ (F) and 5′-AGCAGAGAGTCCGTACA GCA- 3′ (R); mouse *Fwe1* 5′-TCCACACTTCTCTGGTTCTG-3′ (F) and 5′-GTGAGTA CTGC TGTC TAGCC-3′ (R); mouse *Fwe2* 5′-CGATGCCATTTCTTATGCTC-3′ (F) and 5′-TGACACTCAGTCTTCTCCAG-3′ (R); mouse *Fwe3* 5′-CAAA CACAGTAGCTGAGAAGG-3′ (F) and 5′- TAGAGGGAAATGGTGTTT CT G-3′ (R); mouse *Fwe4* 5′- GTTTGCTAAATCCTGGGTGTC-3′ (F) and 5′-GCGTTCAT

GATCATCCACAC-3′ (R); mouse *Gapdh* 5′-GTATGT CGTGGAGTCTACTG-3′ (F) and 5′-TCATCATACTTGGCAGGTTT-3′ (R) as described previously[26].

### 2.3.22 THE HUMAN APOPTOSIS PCR ARRAY.

The Human Apoptosis RT2 Profiler PCR array kit (PAHS-3012; SA-Bio Sciences) was used to profile the expression of 354 genes involved in apoptosis and qPCR was performed per the manufacturer's instructions.

### 2.3.23 EPITHELIAL CELL ISOLATION.

hFWE$^{Win}$ expression was observed in the total normal tissue and the epithelial fraction isolated from breast, colon, and lung tissue samples. All samples were purchased from Tissue For Research, UK (https://biobankonline. com/) and all tissue samples were procured with donor consent. For extraction of the epithelial cells, approximately 120–150 g of the normal tissue samples were used as starting material for tissue digestion. Samples were handled in sterile conditions. Fatty tissue was manually separated, using sterile scalpels and forceps. Subsequently, the epithelial-enriched tissue was manually minced into small pieces. The tissue was sequentially digested using a slow digestion process (overnight at low enzymatic concentration) followed by sequential filtering to support the growth of the epithelial cell fractions as described previously[36].

### 2.3.24 PATIENT SAMPLES.

For FISH, breast tumour specimens were provided by the Department of Breast Surgery, Hokkaido University Hospital. For qPCR experiments, samples of benign (10 breast and 10 colon) and malignant tumour (25 breast and 21 colon) were provided by the Department of Pathology, UAMS, USA; samples of malignant lung (4) and normal tissue (2 lung and 1 skin) were procured from the Department of Pathology, Locarno Hospital, Switzerland; and samples of SCC (3) and normal skin

(2) were obtained from the Department of Pathology, Creighton University School of Medicine, USA. The same set of nor- mal and malignant SCC samples were also used for immunofluorescent staining. FFPE breast and colon cancer samples used for immunohistochemistry (IHC) and fresh normal breast samples were provided by the Pathology Department, Champalimaud Foundation.

All samples used in the study were de-identified, FFPE archived samples with no attached patient information, and were collected with informed consent from donors. All samples were reviewed by the IRB boards at UAMS, Hokkaido University Hospital, Locarno Hospital, Creighton University School of Medicine, Champalimaud Foundation and determined to qualify as non-human subjects research.

### 2.3.25 CANCER XENOGRAFTS.

C57BL/6 mice were obtained from the Geisel School of Medicine, Dartmouth College. Male and female Swiss nude mice were purchased from Charles River. All animal protocols were approved by the Institutional Animal Care and Use Committee of Dartmouth, and the Institutional Animal Ethics Committee at Champalimaud Foundation. All mice were housed in laminar flow cabinets under specific pathogen-free conditions. Food and water were available ad libitum for the duration of the studies. *Fwe*$^{KO}$ mice were generated using female C57BL/6 mice as described earlier[1]. For the generation of tumours in C57BL/6 mice, cyclosporin A (30 mg kg$^{-1}$; Sigma-Aldrich) was injected intraperitoneally as described[37]. Cell line xenografts were established as described previously[38,39,40]. In brief, MCF-7, HCT-116, DU-145, CCL-218, and OVCAR-8 cells at 70–90% confluency were trypsinized and cell viability, required to be at least >95%, was determined by Trypan blue exclusion assay. Cells were re-suspended in 80 µl serum-free medium with 1:1 Matrigel at a final concentration of 1 × 10^6 cells ml$^{-1}$ and stored on ice. For all tumour cell injections, animals were first anaesthetized with 1.5 - 3% isoflurane with 30% oxygen.

For overexpression of individual hFWE isoforms in mouse mammary tissue, 50 µl lentiviral particles ($10^{11}$ TU $ml^{-1}$) expressing individual GFP-tagged hFWE1–hFWE4 isoforms were injected into the mammary tissue of immunosuppressed C57BL/6 *Fwe*$^{KO}$ mice as described[41]. For injection of MCF-7 *hFWE*$^{KO}$ cells expressing GFP-tagged hFWE1–hFWE4, a pellet of 17-β-oestradiol (0.18 mg per pellet, 60-day release; Innovative Research of America) was subcutaneously implanted into *Fwe*$^{KO}$ mice 3 days before cell injection. One week after lentiviral treatment, MCF-7 *hFWE*$^{KO}$ cells expressing GFP-tagged hFWE1–hFWE4 were injected into the mammary tissue. After 4 weeks, mice were monitored for bioluminescent signal using an IVIS 200 system (Xenogen).

For cell line xenograft tumour studies established in male and female Swiss athymic nude mice (age 4–6 weeks), an 80-µl cell suspension containing $1 \times 10^6$ cells was subcutaneously injected into the hind legs of athymic mice. The vehicle control used for these studies was DMSO. To rescue hFWE2 expression in HCT-116 *hFWE*$^{WT}$ tumours, 14 days after cell line injection, tumour-bearing mice were randomly selected and lentiviral particles expressing hFWE2 were injected directly into the established tumour as described previously[42,43]. Chemotherapy treatments were initiated when tumours reached an approximate size of 0.03 $cm^3$; tumour-bearing mice were randomized to receive 30 mg $kg^{-1}$ 5-FU as described[28] or 4 mg $kg^{-1}$ cisplatin + docetaxel as described[30]. Tumour volumes were carefully monitored after treatment using Vernier caliper measurements of length, width, and height, and volumes were calculated using the formula for a semi-ellipsoid ($4/3\pi r^3/2$), as described previously[38,44]. Tumour size did not exceed the maximum size of 1.28 $cm^3$ as specified by institutional policies. The investigators were blinded during experiments or outcome assessment. No statistical methods were used to predetermine sample size.

### 2.3.26 STATISTICAL ANALYSIS.

All values are expressed as means ± s.d. of independent experiments. Differences between groups were evaluated by Student's *t*-test (two-sided) or Tukey–Kramer test, and considered to be significant at $P < 0.05$.

### 2.4 Reporting summary.

Further information on research design is available in the Nature Research Reporting Summary linked to this paper.

### 2.5 Data availability.

All data generated or analyzed during this study are included in the paper, its Extended Data and its Supplementary Information. The source data for Figs. 2–4 and Extended Data Figs. 1–10 are available online. (https://doi.org/10.1038/s41586-019-1429-3)

### 2.6 Acknowledgements

This study was supported by ERC, SNSF, Josef Steiner Cancer Research Foundation, Swiss Cancer League and Champalimaud Foundation to E.M.; and Swiss Cancer League, LB692, LB506, Seeds of Science, Winthrop P Rockefeller Cancer Institute and Creighton University startup funds to R.G. We thank K. Polyak for experimental suggestions; J. Billheimer and A. Dhiman for help with analysis; A. Gogna for support; and the MTT platform (R. Tomás), the Histopathology Platform (I. Terras Marques, M. I. Romano, S. Casimiro and S. Dias) and the Rodent platform at the Champalimaud Centre for the Unknown.

### 2.7 Author contributions

R.G. and E. Moreno conceptualized the idea, initiated the project, provided research support, designed, analysed, and interpreted the experiments and wrote the manuscript. E. Madan analysed the experiments, wrote the manuscript, and

performed imaging, qPCR, flow-cytometry and mouse studies. R.G. designed and analysed the experiments, wrote the manuscript, created molecular biology design, and performed imaging analysis, clonogenicity assay, FISH-molecular design, IHC, mouse studies, and chemotherapy designs. C.J.P. analysed the experiments, helped in the preparation of figures, formatted and wrote the manuscript and performed statistical analysis, cell culture experiments, calcium imaging, low-density plating and conditioned medium experiments, and knockout and wild-type cell interactions. M.N. analysed the experiments, helped in the preparation of figures, and performed statistical analysis, flow-cytometry experiments and analysis, and FISH. T.M.P. analysed the experiments, helped in preparation of figures, formatted and wrote the manuscript, performed statistical analysis and cell culture experiments, extracted and cultured normal and epithelial cells from breast tissue, and performed laser-capture microdissection, qPCR, flow-cytometry and virus production. R.C.-M., A.G., V.H., Y.Y., T.Y., D.S., S.R.P. and H.Y. assisted in procuring tissue samples and IHC. K.F. performed IHC. K.S., A.M.P. and D.C. assisted with experiments and analysis. C.R. assisted with manuscript writing. M.A.F.P. and A.V. assisted with flow-cytometry experiments. D.A. assisted with confocal microscopy. H.N. provided normal breast cells. L.A.H. provided SCC samples, supervised K.F. for IHC in SCC and edited the manuscript. P.K. provided research support, and helped with data analysis, organization, and editing of the manuscript. C.C. and A.L.B. provided a clinical perspective, and helped with the procurement of tissue samples, design of IHC experiments, and design of clinical experiments such as the inclusion of chemotherapy.

## 2.8 REFERENCES


1. Medzhitov, R. & Janeway, C. A. Decoding the patterns of self and nonself by the innate immune system. *Science* **296**, 298–300 (2002).
2. Vivier, E. *et al.* Innate or adaptive immunity? The example of natural killer cells. *Science* **331**, 44–49 (2011).
3. Merino, M. M. *et al.* Elimination of unfit cells maintains tissue health and prolongs lifespan. *Cell* **160**, 461–476 (2015).
4. Merino, M. M., Rhiner, C., Portela, M. & Moreno, E. 'Fitness fingerprints' mediate physiological culling of unwanted neurons in Drosophila. *Curr. Biol. CB* **23**, 1300–1309 (2013).
5. Moreno, E., Fernandez-Marrero, Y., Meyer, P. & Rhiner, C. Brain regeneration in Drosophila involves comparison of neuronal fitness. *Curr. Biol. CB* **25**, 955–963 (2015).
6. Rhiner, C. *et al.* Flower forms an extracellular code that reveals the fitness of a cell to its neighbors in Drosophila. *Dev. Cell* **18**, 985–998 (2010).
7. Merino, M. M., Levayer, R. & Moreno, E. Survival of the Fittest: Essential Roles of Cell Competition in Development, Aging, and Cancer. *Trends Cell Biol.* **26**, 776–788 (2016).
8. Gogna, R., Shee, K. & Moreno, E. Cell Competition During Growth and Regeneration. *Annu. Rev. Genet.* **49**, 697–718 (2015).
9. Di Gregorio, A., Bowling, S. & Rodriguez, T. A. Cell Competition and Its Role in the Regulation of Cell Fitness from Development to Cancer. *Dev. Cell* **38**, 621–634 (2016).
10. Greaves, M. & Maley, C. C. Clonal evolution in cancer. *Nature* **481**, 306–313 (2012).
11. Jacobs, K. B. *et al.* Detectable clonal mosaicism and its relationship to aging and cancer. *Nat. Genet.* **44**, 651–658 (2012).
12. Kennedy, S. R., Loeb, L. A. & Herr, A. J. Somatic mutations in aging, cancer and neurodegeneration. *Mech. Ageing Dev.* **133**, 118–126 (2012).

13. Laurie, C. C. *et al.* Detectable clonal mosaicism from birth to old age and its relationship to cancer. *Nat. Genet.* **44**, 642–650 (2012).

14. López-Otín, C., Blasco, M. A., Partridge, L., Serrano, M. & Kroemer, G. The hallmarks of aging. *Cell* **153**, 1194–1217 (2013).

15. Vanneste, E. *et al.* Chromosome instability is common in human cleavage-stage embryos. *Nat. Med.* **15**, 577–583 (2009).

16. Vijg, J. Somatic mutations, genome mosaicism, cancer and aging. *Curr. Opin. Genet. Dev.* **26**, 141–149 (2014).

17. Neves, J., Demaria, M., Campisi, J. & Jasper, H. Of flies, mice, and men: evolutionarily conserved tissue damage responses and aging. *Dev. Cell* **32**, 9–18 (2015).

18. Levayer, R., Hauert, B. & Moreno, E. Cell mixing induced by myc is required for competitive tissue invasion and destruction. *Nature* **524**, 476–480 (2015).

19. Klein, C. A. Selection and adaptation during metastatic cancer progression. *Nature* **501**, 365–372 (2013).

20. Maruyama, T. & Fujita, Y. Cell competition in mammals - novel homeostatic machinery for embryonic development and cancer prevention. *Curr. Opin. Cell Biol.* **48**, 106–112 (2017).

21. Moreno, E. Is cell competition relevant to cancer? *Nat. Rev. Cancer* **8**, 141–147 (2008).

22. ENCODE Project Consortium. An integrated encyclopedia of DNA elements in the human genome. *Nature* **489**, 57–74 (2012).

23. Ji, X. *et al.* Chromatin proteomic profiling reveals novel proteins associated with histone-marked genomic regions. *Proc. Natl. Acad. Sci. U. S. A.* **112**, 3841–3846 (2015).

24. Moreno, E. & Rhiner, C. Darwin's multicellularity: from neurotrophic theories and cell competition to fitness fingerprints. *Curr. Opin. Cell Biol.* **31**, 16–22 (2014).

25. Chang, H.-F. *et al.* Cytotoxic granule endocytosis depends on the Flower protein. *J. Cell Biol.* **217**, 667–683 (2018).

26. Petrova, E., López-Gay, J. M., Rhiner, C. & Moreno, E. Flower-deficient mice have reduced susceptibility to skin papilloma formation. *Dis. Model. Mech.* **5**, 553–561 (2012).

27. Xue, L. *et al.* Voltage-dependent calcium channels at the plasma membrane, but not vesicular channels, couple exocytosis to endocytosis. *Cell Rep.* **1**, 632–638 (2012).

28. Zhang, P. *et al.* Retraction Note: Curcumin synergizes with 5-fluorouracil by impairing AMPK/ULK1-dependent autophagy, AKT activity and enhancing apoptosis in colon cancer cells with tumor growth inhibition in xenograft mice. *J. Exp. Clin. Cancer Res. CR* **41**, 197 (2022).

29. Davies, A. H., Wang, Y. & Zoubeidi, A. Patient-derived xenografts: A platform for accelerating translational research in prostate cancer. *Mol. Cell. Endocrinol.* **462**, 17–24 (2018).

30. Chang, C.-E. *et al.* Novel application of pluronic lecithin organogels (PLOs) for local delivery of synergistic combination of docetaxel and cisplatin to improve therapeutic efficacy against ovarian cancer. *Drug Deliv.* **25**, 632–643 (2018).

31. Sanjana, N. E., Shalem, O. & Zhang, F. Improved vectors and genome-wide libraries for CRISPR screening. *Nat. Methods* **11**, 783–784 (2014).

32. Shalem, O. *et al.* Genome-scale CRISPR-Cas9 knockout screening in human cells. *Science* **343**, 84–87 (2014).

33. Prasad, M. *et al.* Dual TGFβ/BMP Pathway Inhibition Enables Expansion and Characterization of Multiple Epithelial Cell Types of the Normal and Cancerous Breast. *Mol. Cancer Res. MCR* **17**, 1556–1570 (2019).

34. Yanagida, J. *et al.* Accelerated elimination of ultraviolet-induced DNA damage through apoptosis in CDC25A-deficient skin. *Carcinogenesis* **33**, 1754–1761 (2012).

35. Schmittgen, T. D. & Livak, K. J. Analyzing real-time PCR data by the comparative C(T) method. *Nat. Protoc.* **3**, 1101–1108 (2008).

36. Zubeldia-Plazaola, A. *et al.* Comparison of methods for the isolation of human breast epithelial and myoepithelial cells. *Front. Cell Dev. Biol.* **3**, 32 (2015).

37. Jivrajani, M., Shaikh, M. V., Shrivastava, N. & Nivsarkar, M. An improved and versatile immunosuppression protocol for the development of tumor xenograft in mice. *Anticancer Res.* **34**, 7177–7183 (2014).

38. Gogna, R., Madan, E., Kuppusamy, P. & Pati, U. Chaperoning of mutant p53 protein by wild-type p53 protein causes hypoxic tumor regression. *J. Biol. Chem.* **287**, 2907–2914 (2012).

39. Hadjal, Y., Hadadeh, O., Yazidi, C. E. I., Barruet, E. & Binétruy, B. A p38MAPK-p53 cascade regulates mesodermal differentiation and neurogenesis of embryonic stem cells. *Cell Death Dis.* **4**, e737 (2013).

40. Madan, E. *et al.* SCO2 induces p53-mediated apoptosis by Thr845 phosphorylation of ASK-1 and dissociation of the ASK-1-Trx complex. *Mol. Cell. Biol.* **33**, 1285–1302 (2013).

41. Annunziato, S. *et al.* Modeling invasive lobular breast carcinoma by CRISPR/Cas9-mediated somatic genome editing of the mammary gland. *Genes Dev.* **30**, 1470–1480 (2016).

42. Akhtar, J., Wang, Z., Yu, C. & Zhang, Z. P. Effectiveness of local injection of lentivirus-delivered stathmin1 and stathmin1 shRNA in human gastric cancer xenograft mouse. *J. Gastroenterol. Hepatol.* **29**, 1685–1691 (2014).

43. Zheng, J. *et al.* Regression of prostate cancer xenografts by a lentiviral vector specifically expressing diphtheria toxin A. *Cancer Gene Ther.* **10**, 764–770 (2003).

44. Madan, E. *et al.* TIGAR induces p53-mediated cell-cycle arrest by regulation of RB-E2F1 complex. *Br. J. Cancer* **107**, 516–526 (2012).

## 2.9 SUPPLEMENTARY INFORMATION

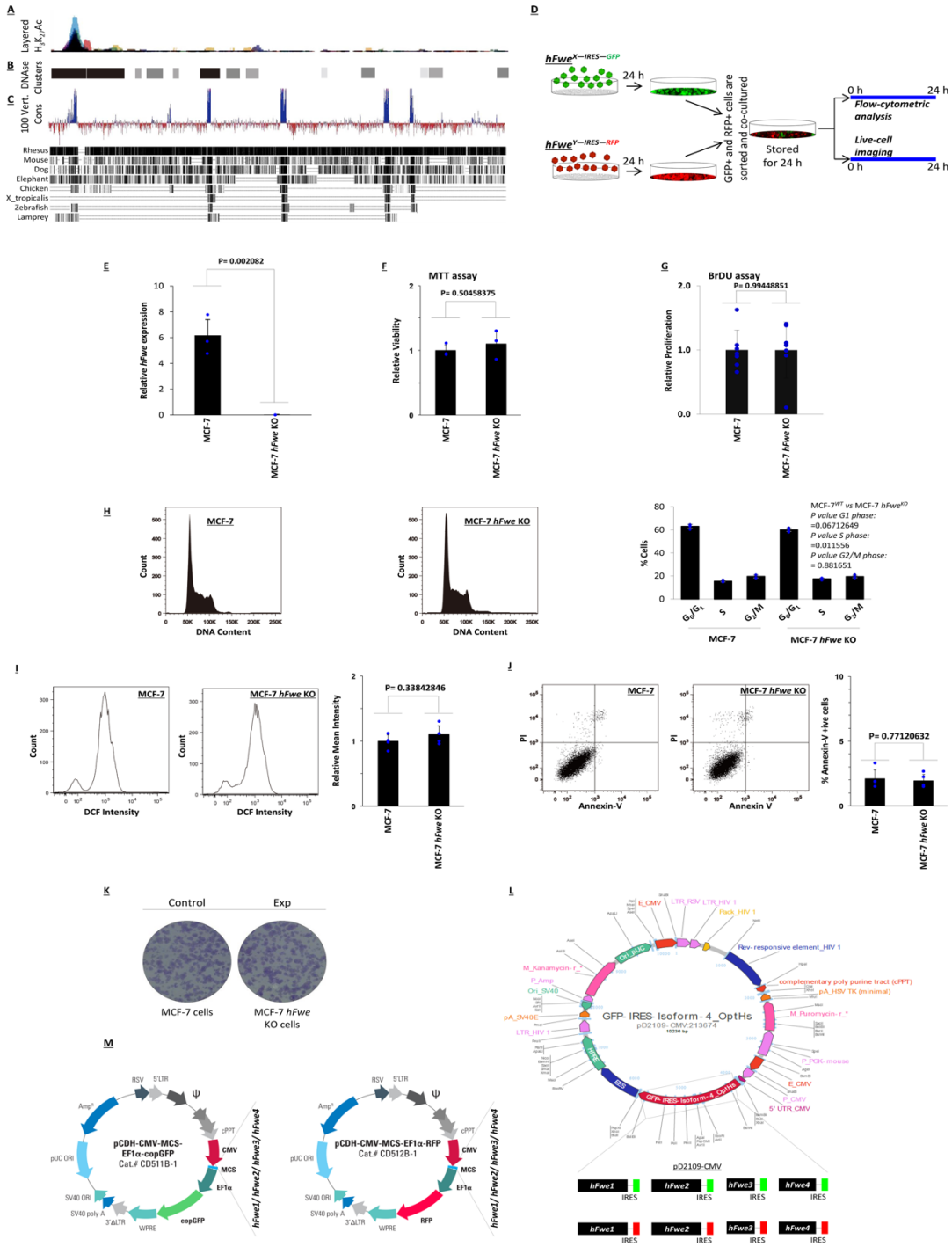


**Extended Data Fig. 1** | See next page for caption.

**Extended Data Fig. 1 | Knockout of the *hFWE* gene in MCF-7 cells does not affect their cellular functions. a**, ENCODE data mining for chromatin immunoprecipitation (ChIP) with $H_3K_2Ac$ antibody shows active euchromatin status of the *hFWE* promoter. **b**, ENCODE data mining for DNAase-I hypersensitivity analysis shows footprints of DNA unwinding at the locations of *hFWE* exons. **c**, Phylogenetic analysis. Exon sequences are highly conserved amongst vertebrates except exon 5, which is more specific to mammals. **d**, Pictorial representation of the protocol for the functional analysis of hFWE isoforms in cell culture. MCF-7 $hFWE^{KO}$ cells were infected with lentiviruses encoding each hFWE isoform alongside an independent GFP or RFP tag. Transduced cells were sorted for $RFP^+$ and $GFP^+$ populations, plated together and co-cultured for 24 h. Co-cultured cells were then studied for a further 24 h using live-cell imaging and flow cytometry. **e**, To obtain human cells expressing single hFWE isoforms, MCF-7 cells (breast cancer origin) were selected and MCF-7 $hFWE^{KO}$ cells were generated. qPCR analysis of relative transcript synthesis of *hFWE* exon 1 from MCF-7 $hFWE^{WT}$ and MCF-7 $hFWE^{KO}$ cells shows lack of gene product in the knockout cells ($n$ = 3 biologically independent experiments). **f**, MTT assay shows that knockout of the *hFWE* gene does not affect cell viability and mitochondrial activity in MCF-7 cells ($n$ = 3 biologically independent experiments). **g**, BrdU assay shows that knockout of the *hFWE* gene does not affect cellular proliferation rates of MCF-7 cells ($n$ = 7 biologically independent experiments). **h**, Cell-cycle distribution was examined by analysing DNA content. Propidium iodide staining and subsequent flow cytometric analysis show that knockout of the *hFWE* gene does not affect the cell- cycle progression of the MCF-7 cells ($n$ = 3 biologically independent experiments). **i**, Flow cytometric analysis of ROS via measurement of DCF fluorescence shows that knockout of the *hFWE* gene does not alter cellular ROS in MCF-7 cells ($n$ = 4 biologically independent experiments). **j**, Annexin-V staining shows that knockout of the *hFWE* gene does not affect cellular apoptosis in MCF-7 cells ($n$ = 4 biologically independent experiments). **k**, The clonogenic assay shows that knockout of the *hFWE* gene does not affect the ability of MCF-7 cells to form colonies ($n$ = 3). **l**,

Diagrammatic representation of the hFWE*X*–IRES–GFP/RFP lentiviral constructs. Eight lentiviral constructs were prepared by cloning *hFWE1/2/3/4–IRES–GFP/RFP* into pD2109-CMV lentiviral vectors. **m**, Eight additional constructs were prepared by cloning *hFWE1/2/3/4* into dual promoter pCDH-CMV-MCS-EF1α-copGFP and pCDH-CMV-MCS-EF1α-copRFP (System Biosciences), respectively. **e**–**j**, *P* values shown, two-tailed *t*-test, mean ± s.d.

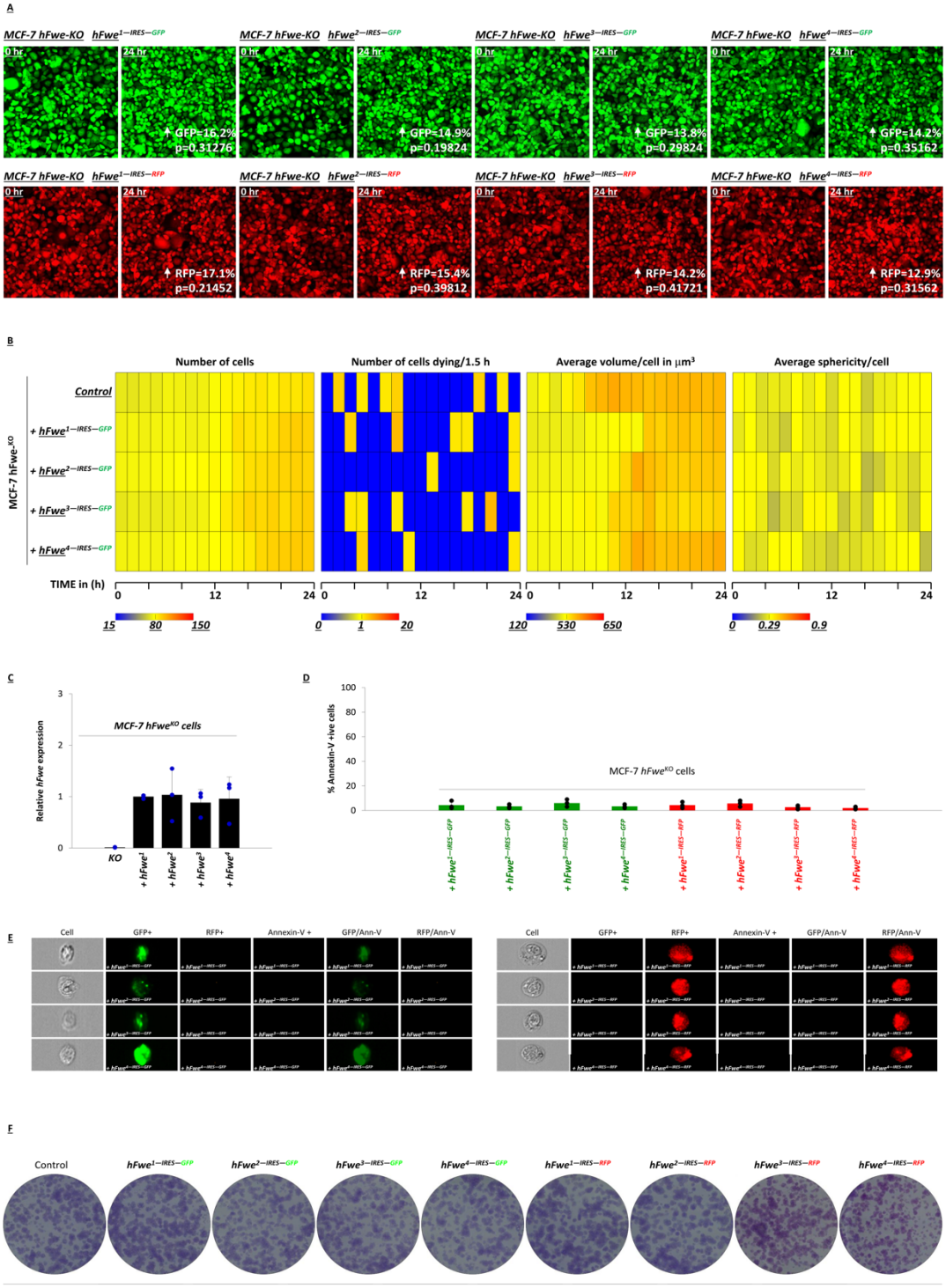


**Extended Data Fig. 2** | See next page for caption.

**Extended Data Fig. 2 | Overexpression of single hFWE isoforms in MCF-7 *hFWE*$^{KO}$ cells does not alter viability. a**, MCF-7 *hFWE*$^{KO}$ cells were infected with each *hFWE1/2/3/4–GFP/RFP* construct independently and the cells were monitored via live-cell imaging. Images at 24 h show that MCF-7 *hFWE*$^{KO}$ cells homogenously expressing single hFWE isoforms do not undergo cell death ($n$ = 3 biologically independent experiments, $P$ values shown, two-tailed $t$-test). **b**, Analysis of live-cell imaging is shown as heat maps to represent the total number of cells, number of cells dying every 1.5 h, average cellular volume and average cellular sphericity; each block represents a gradient scale of low (blue), medium (yellow) and high (red) number or shape or size of the cells ($n$ = 3, analysis performed using manual tool from Fiji and automated tools from Imaris, Genie tool used for representing data as heat maps). **c**, qPCR analysis of MCF-7 *hFWE*$^{KO}$ cells expressing each of four hFWE isoforms showed comparable lentiviral-mediated expression of hFWE1, hFWE2, hFWE3 or hFWE4 ($n$ = 3 biologically independent experiments, mean ± s.d., ANOVA showed no significant differences). **d**, Flow cytometry-based annexin-V staining shows that overexpression of individual hFWE1/2/3/4–GFP/ RFP isoforms does not induce apoptosis in MCF-7 *hFWE*$^{KO}$ cells ($n$ = 3 biologically independent experiments, mean ± s.d., ANOVA showed no significant differences). **e**, Annexin-V staining and flow cytometry-based cell imaging (image stream) also show that overexpression of individual hFWE isoforms does not induce apoptosis ($n$ = 3). **f**, Long-term effect of overexpression of single hFWE isoforms with GFP or RFP reporters over 21 days using clonogenic assay. The overexpression of hFWE isoforms does not affect the colony formation ability of MCF-7 *hFWE*$^{KO}$ cells ($n$ = 3).

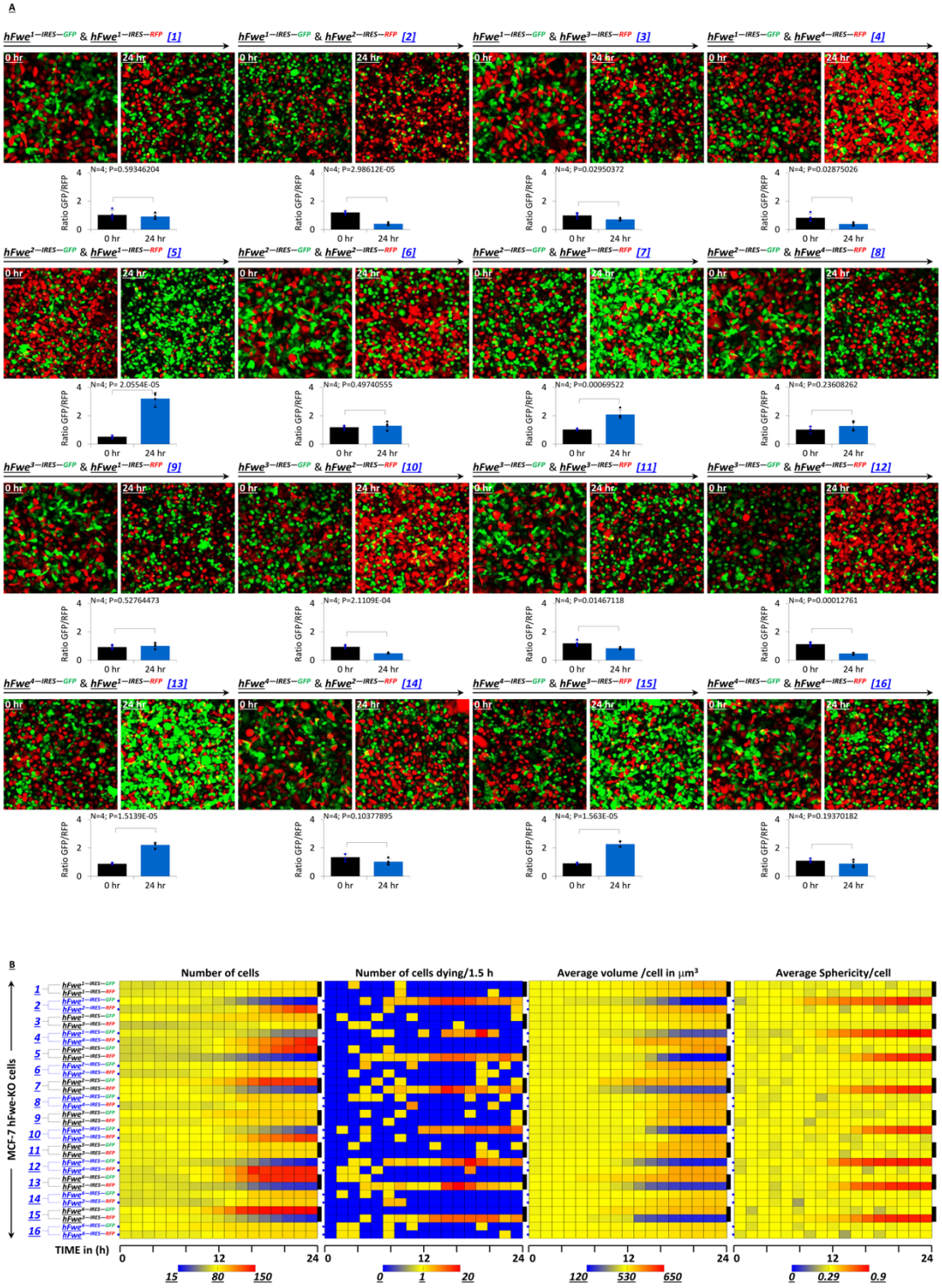


**Extended Data Fig. 3** | See next page for caption.

**Extended Data Fig. 3 | Live-cell imaging of co-culture assay using MCF-7 *hFWE*$^{KO}$ cells transduced with hFWE isoforms. a**, Results from 24-h live-cell imaging experiments of co-cultures of MCF-7 *hFWE*$^{KO}$ cells expressing the four hFWE isoforms. In [1], MCF-7 *hFWE*$^{KO}$ cells expressing hFWE1–IRES–GFP were co-cultured with cells expressing hFWE1–IRES–RFP. GFP$^{+}$ and RFP$^{+}$ cells were monitored at 0 and 24 h to follow the effects of hFWE isoforms on cell proliferation. The ratio of GFP$^{+}$ to RFP$^{+}$ cells did not vary significantly between 0 and 24 h. In co-culture experiments [2], MCF-7 *hFWE*$^{KO}$ cells expressing hFWE1– IRES–GFP were co-cultured with cells expressing hFWE2–IRES–RFP. The population of RFP$^{+}$ cells was significantly higher at 24 h than at 0 h, indicating competition between hFWE1–IRES–GFP and hFWE2–IRES– RFP cells. Each co-culture combination is presented amongst the four hFWE isoforms along with IRES–GFP or IRES–RFP co-expression. Cells expressing hFWE2 or hFWE4 emerged as winners when co-cultured with cells expressing hFWE1 or hFWE3 regardless of GFP or RFP reporter. The ratio of GFP$^{+}$ to RFP$^{+}$ cells at 0 and 24 h for each co-culture experiment is presented quantitatively below. The ratios at 0 and 24 h for each combination were compared statistically using a two-tailed *t*-test assuming unequal variances; $n = 4$ biologically independent experiments, *P* values shown, mean ± s.d. **b**, Analysis of live-cell imaging is shown as heat maps to represent the total number of cells, the number of cells that died every 1.5 h, average cellular volume, and average cellular sphericity. The co- culture combinations are indicated on the left. For example, the co-culture combination of cells expressing hFWE1–IRES–GFP with cells expressing hFWE2–IRES–RFP results in the death of hFWE1–IRES–GFP cells at the expense of an increase in the number of hFWE2–IRES–RFP cells. Analysis of all co-culture combinations is presented. The data support the idea that cells expressing hFWE1 or hFWE3, when co-cultured with cells expressing hFWE2 or hFWE4, undergo cell death accompanied by loss of differentiated cellular architecture, indicated by decreased

cellular volume (blue) and increased cellular sphericity (red). Each block represents a gradient scale of low (blue), medium (yellow) and high (red) for the number, size or shape of the cells (*n* = 4, analysis performed using the manual tool from Fiji and automated tools from Imaris, Genie tool used for representing data as heat maps).

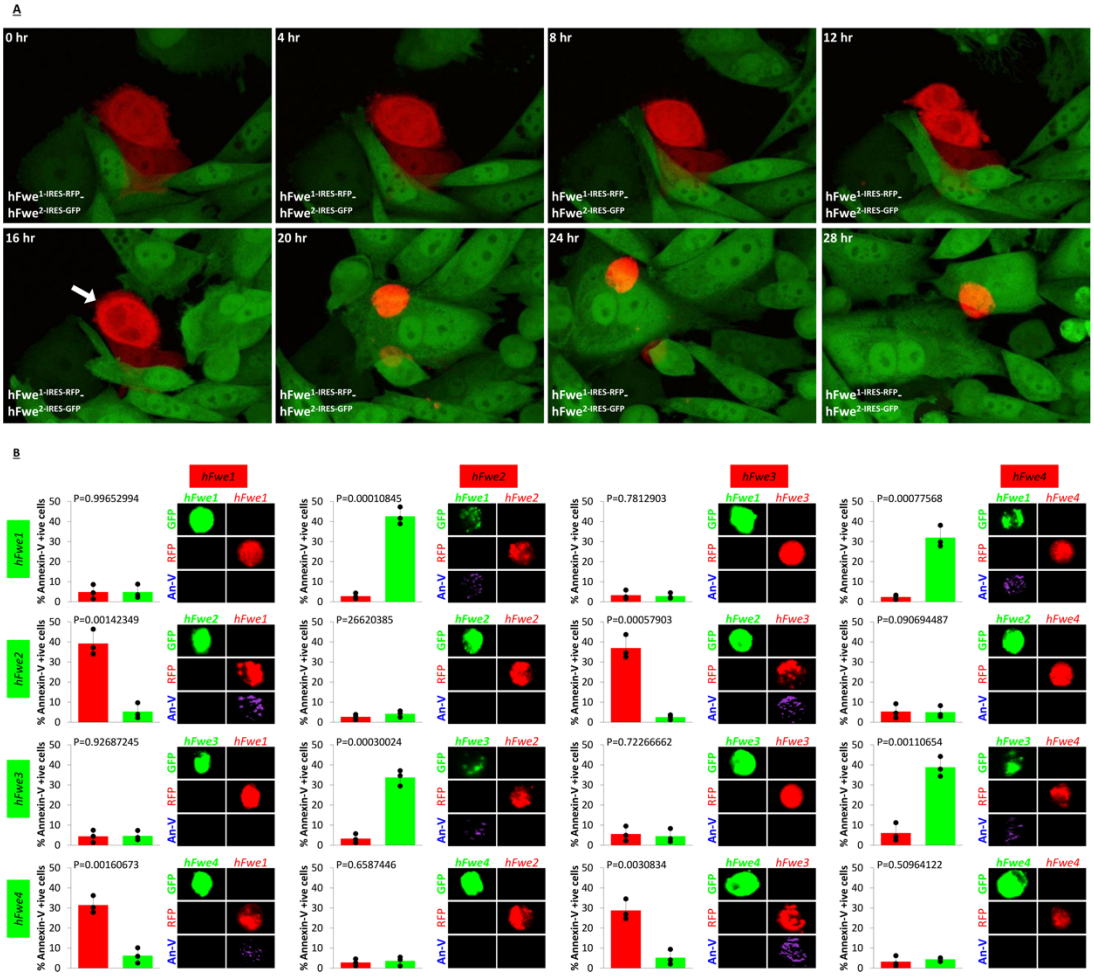


**Extended Data Fig. 4 | High-resolution imaging of competition- induced Loser cell death. a**, High-resolution live-cell imaging experiment (28 h) showing cell competition in MCF-7 *hFWE*$^{KO}$ cells expressing hFWE1–IRES–RFP and hFWE2–IRES–GFP isoforms. The co-culture results show elimination of cells carrying the Lose isoform (hFWE1– IRES–GFP); *n* = 3 biologically independent experiments with similar results. **b**, The results of live-cell imaging were confirmed using annexin-V staining and flow-cytometry-based imaging of GFP$^{+}$ and RFP$^{+}$ cells for each co-culture combination. Cells were sorted following 24 h of co- culture, and the percentage of apoptotic cells is displayed. The flow-based imaging of these cells is

also presented and shows no $GFP^+$ signal in RFP- sorted cells or $RFP^+$ signal in GFP-sorted cells. The annexin-$V^+$ signal is shown in purple. For example, co-culture of cells expressing hFWE1– IRES–GFP with cells expressing hFWE2–IRES–RFP results in apoptosis of hFWE1–IRES–GFP cells, as indicated by the annexin-$V^+$ signal. Together, results from live-cell imaging and flow cytometry demonstrate that cells expressing $hFWE^{Lose}$ isoforms (hFWE1 or hFWE3) undergo apoptosis when in competition with cells expressing $hFWE^{Win}$ isoforms (hFWE2 or hFWE4) ($n$ = 3 biologically independent experiments, $P$ values shown, two-tailed $t$-test, was performed for $P$-value calculations, mean ± s.d.).

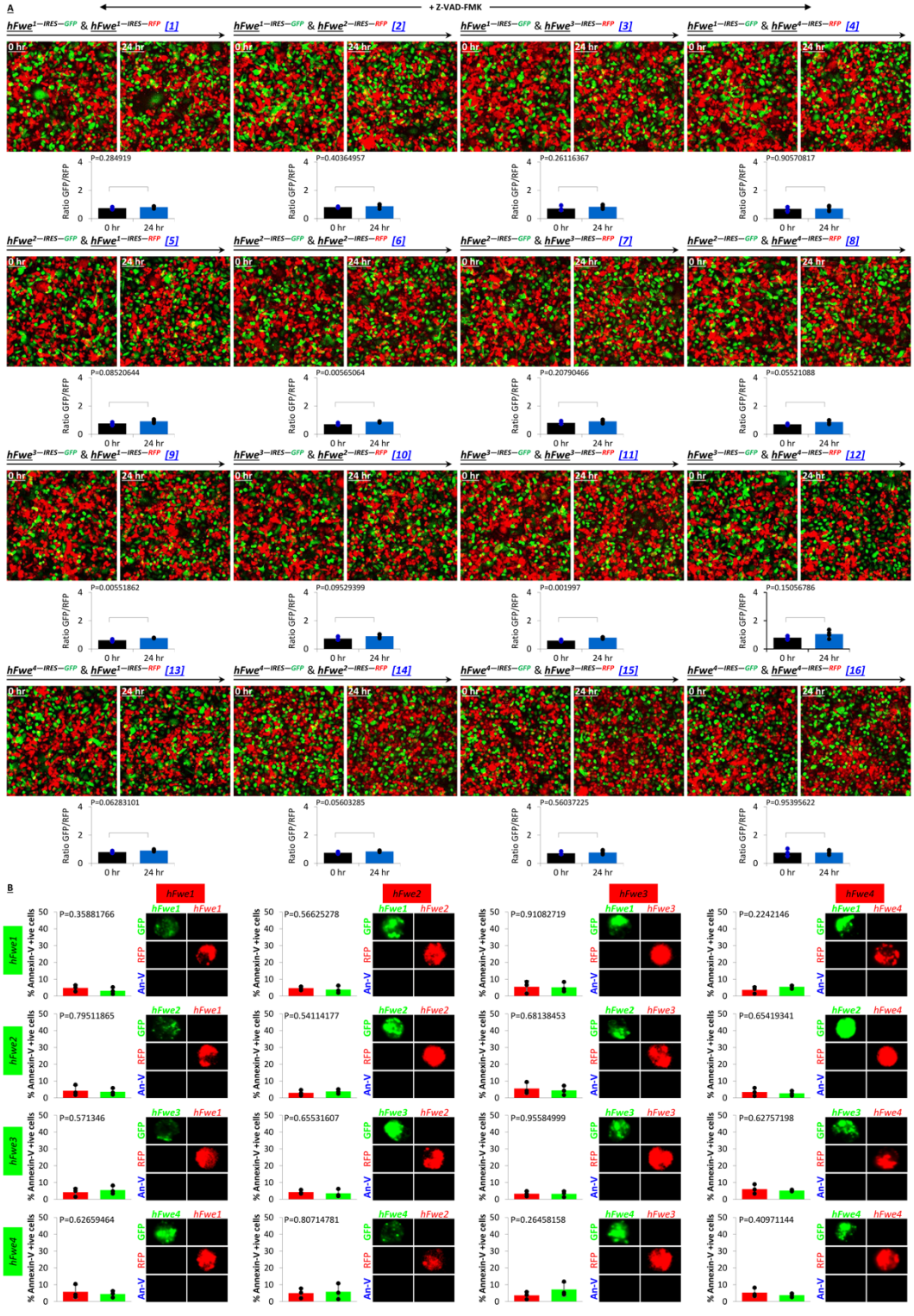
A
+ Z-VAD-FMK
hFwe1—IRES—GFP & hFwe1—IRES—RFP [1]
hFwe1—IRES—GFP & hFwe2—IRES—RFP [2]
hFwe1—IRES—GFP & hFwe3—IRES—RFP [3]
hFwe1—IRES—GFP & hFwe4—IRES—RFP [4]
hFwe2—IRES—GFP & hFwe1—IRES—RFP [5]
hFwe2—IRES—GFP & hFwe2—IRES—RFP [6]
hFwe2—IRES—GFP & hFwe3—IRES—RFP [7]
hFwe2—IRES—GFP & hFwe4—IRES—RFP [8]
hFwe3—IRES—GFP & hFwe1—IRES—RFP [9]
hFwe3—IRES—GFP & hFwe2—IRES—RFP [10]
hFwe3—IRES—GFP & hFwe3—IRES—RFP [11]
hFwe3—IRES—GFP & hFwe4—IRES—RFP [12]
hFwe4—IRES—GFP & hFwe1—IRES—RFP [13]
hFwe4—IRES—GFP & hFwe2—IRES—RFP [14]
hFwe4—IRES—GFP & hFwe3—IRES—RFP [15]
hFwe4—IRES—GFP & hFwe4—IRES—RFP [16]
0 hr
24 hr
Ratio GFP/RFP
P=0.284919
P=0.40364957
P=0.26116367
P=0.90570817
P=0.08520644
P=0.00565064
P=0.20790466
P=0.05521088
P=0.00551862
P=0.09529399
P=0.001997
P=0.15056786
P=0.06283101
P=0.05603285
P=0.56037225
P=0.95395622
B
hFwe1
hFwe2
hFwe3
hFwe4
% Annexin-V +ive cells
GFP
RFP
An-V
P=0.35881766
P=0.56625278
P=0.91082719
P=0.2242146
P=0.79511865
P=0.54114177
P=0.68138453
P=0.65419341
P=0.571346
P=0.65531607
P=0.95584999
P=0.62757198
P=0.62659464
P=0.80714781
P=0.26458158
P=0.40971144

**Extended Data Fig. 5 | Cells expressing hFWE$^{Lose}$ isoforms undergo caspase-dependent apoptosis during co-culture with cells expressing hFWE$^{Win}$ isoforms. a**, The effect of incubation with the pan-caspase inhibitor Z-VAD-FMK (20 μM) on co-culture of cells expressing hFWE$^{Win}$ or hFWE$^{Lose}$ isoforms. Caspase inhibition by Z-VAD-FMK rescued hFWE$^{Lose}$ cells expressing hFWE1 or hFWE3 from undergoing cell death induced by co-culture with hFWE$^{Win}$ cells expressing hFWE2 or hFWE4. The ratio of GFP$^{+}$ to RFP$^{+}$ cells at 0 and 24 h for each co-culture experiment is presented quantitatively below. The ratios at 0 and 24 h for each combination were compared statistically using a two-tailed *t*-test assuming unequal variances ($n = 4$ biologically independent experiments, *P* values shown, mean ± s.d.). **b**, Annexin-V staining and flow cytometry- based imaging of GFP$^{+}$ and RFP$^{+}$ cells for each co-culture combination confirms that incubation with Z-VAD-FMK prevents apoptosis in co-culture of cells expressing hFWE$^{Win}$ or hFWE$^{Lose}$ isoforms ($n = 3$ biologically independent experiments, *P* values shown, two-tailed *t*-test, mean ± s.d.).

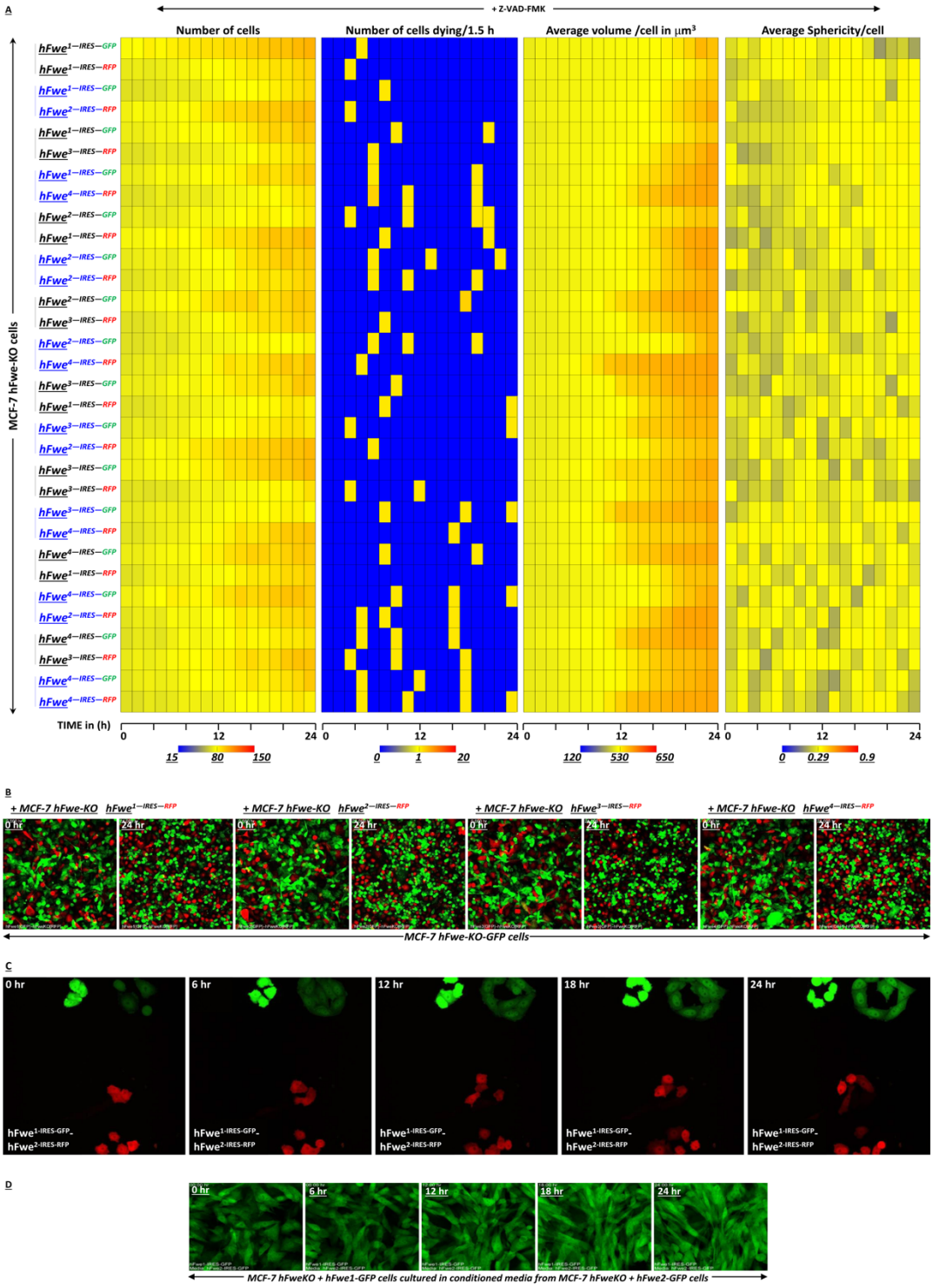


**Extended Data Fig. 6** | See next page for caption.

**Extended Data Fig. 6 | Characterization of competition in co-culture assay of cells expressing hFWE$^{Win}$ or hFWE$^{Lose}$ isoforms. a**, Analysis of live-cell imaging is shown as heat maps to represent the total number of cells, number of cells that died every 1.5 h, average cellular volume, and average cellular sphericity. Each block represents a gradient scale of low (blue), medium (yellow) and high (red) number, shape or size of cells. Treatment with Z-VAD-FMK blocked hFWE$^{Win}$ cell-induced death of co-cultured hFWE$^{Lose}$ cells, resulting in equal ratios of GFP$^{+}$ and RFP$^{+}$ populations ($n$ = 4, analysis performed using the manual tool from Fiji and automated tools from Imaris, Genie tool used for representing data as heat maps). **b**, Imaging results show that MCF-7 *hFWE*$^{KO}$ cells expressing each hFWE isoform independently do not outcompete co- cultured *hFWE*$^{KO}$ cells, consistent with a mechanism of *hFWE*-mediated cell death supported by the presence of both hFWE$^{Win}$ and hFWE$^{Lose}$ isoforms ($n$ = 3). **c**, Culling of cells expressing hFWE$^{Lose}$ isoforms appeared to be contact dependent. Live-cell imaging was performed on low-density-plated MCF-7 *hFWE*$^{KO}$ cells expressing hFWE1–IRES–GFP and hFWE2–IRES–RFP. Results show cell proliferation and absence of cell death in either cell population under conditions of low-density plating ($n$ = 3 biologically independent experiments). **d**, The potential effect of secreted factors from cells expressing hFWE$^{Win}$ isoforms was investigated. Conditioned medium from MCF-7 *hFWE*$^{KO}$ cells expressing hFWE2–IRES–GFP did not affect viability when transferred to a culture of MCF-7 *hFWE*$^{KO}$ cells expressing hFWE1–IRES–GFP and imaged over 24 h ($n$ = 3).

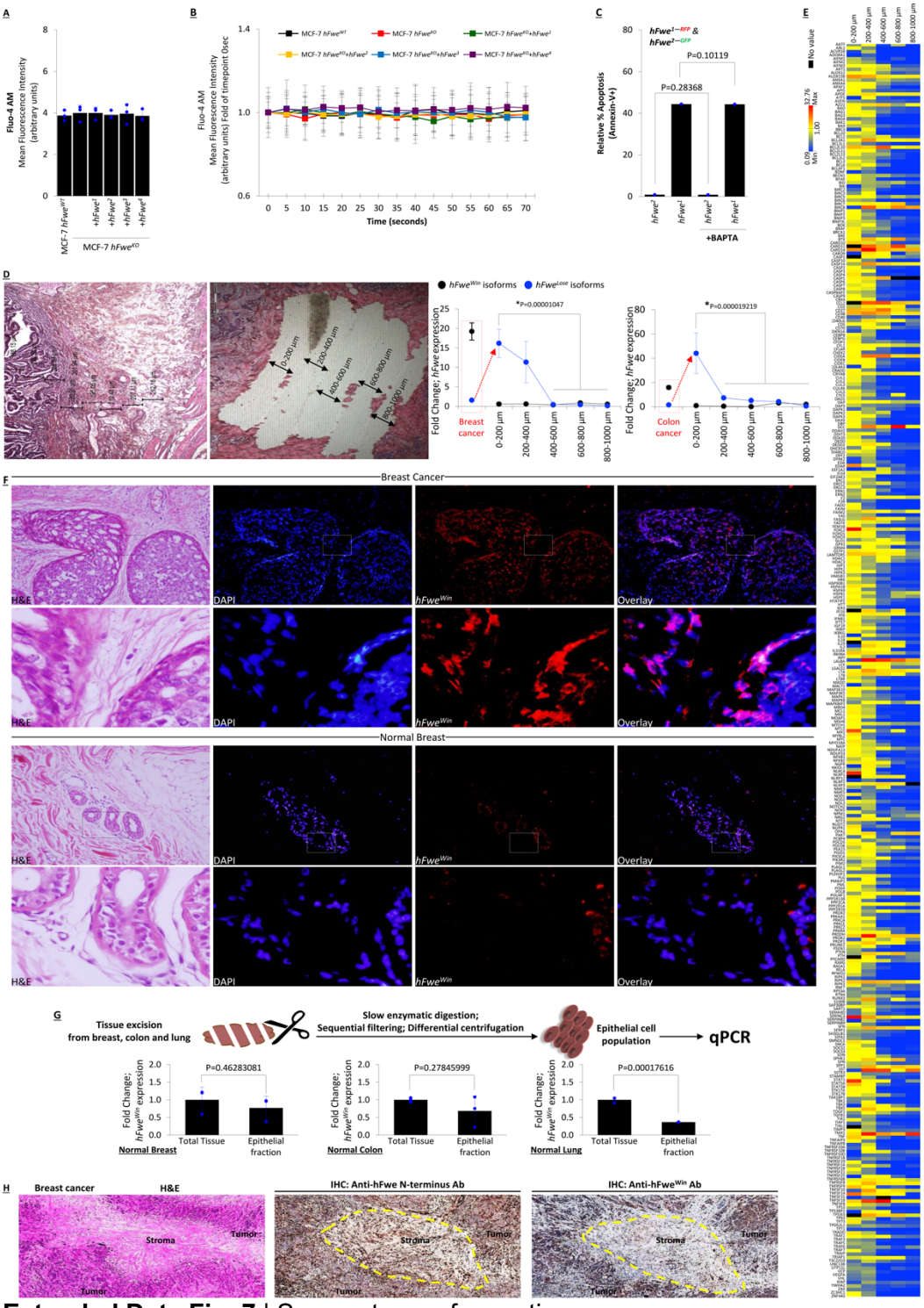


**Extended Data Fig. 7** | See next page for caption.

**Extended Data Fig. 7 | Calcium-independent mechanism of hFWE- mediated cell competition. a**, The potential effect of individual hFWE isoforms on intracellular calcium levels was investigated. Live-cell imaging was performed to detect levels of Fluo-4AM in MCF-7 *hFWE*$^{KO}$ cells and MCF-7 *hFWE*$^{KO}$ cells overexpressing single hFWE isoforms (*n* = 3 biologically independent experiments, ANOVA showed no significant differences, mean ± s.d.). **b**, Live-cell imaging at 5-s intervals over 1 min showed constant levels of Fluo-4AM in MCF-7 *hFWE*$^{KO}$ cells and MCF-7 *hFWE*$^{KO}$ cells overexpressing single hFWE isoforms (*n* = 3 biologically independent experiments, ANOVA showed no significant differences, mean ± s.d.). **c**, hFWE-mediated cell competition assay carried out in the presence or absence of the calcium chelator BAPTA-AM. Treatment with BAPTA-AM did not affect the ability of MCF-7 *hFWE*$^{KO}$ cells expressing hFWE2 to kill co-cultured MCF-7 *hFWE*$^{KO}$ cells expressing hFWE1 (*n* = 3 biologically independent experiments, *P* values shown, two-tailed *t*-test found no significant differences, mean ± s.d.). **d**, Laser- capture microdissection was performed in increments of 200 μm in distance perpendicular to the defined boundary of breast tissue tumour mass. Representative images are shown for breast cancer tissue section before and after laser capture. hFWE$^{Lose}$ isoforms were upregulated in tumour-adjacent host tissue nearest to breast cancer (0–400 μm) or colon cancer (0–200 μm). hFWE$^{Win}$ isoforms were highly enriched within breast or colon tumour tissue but not adjacent tissue (*n* = 3 biologically independent experiments, mean ± s.d., fold change calculated relative to the external reference of the expression of hFWE$^{Win}$ isoforms in normal breast tissue, *P* values shown, two-tailed *t*-test). **e**, qPCR array was used to examine the expression of 354 genes involved in apoptotic pathways in samples of laser-captured tumour-adjacent host tissue. Gene expression heat map shows that host tissue in the immediate vicinity of cancer (0–400 μm) displayed upregulation of genes involved in apoptotic pathways. Host tissue farther away (400–1,000 μm) from the tumour edge displayed basal levels of apoptosis-related genes. The heat map shows apoptotic genes that were induced (red), suppressed (blue) or unchanged (yellow) in expression. Black

represents unsuccessful runs (*n* = 3). **f**, FISH shows the expression of hFWE$^{Win}$ isoforms in FFPE samples of breast cancer tissue (top) and normal breast tissue (bottom). First column, H&E staining; second column, control DAPI staining; third column, expression of hFWE$^{Win}$ isoforms within tumour tissue; fourth column, overlay of DAPI and hFWE$^{Win}$ isoforms. Magnified images below each panel show expression of hFWE$^{Win}$ isoforms specifically in tumour tissue, as these isoforms are poorly expressed in the stromal tissue surrounding the tumour and normal breast tissue (*n* = 3 for all staining). **g**, Schematic depicting the process of epithelial cell isolation from normal breast, colon, and lung tissue. Expression of the four hFWE isoforms was compared in epithelia versus total tissue by qPCR analysis (*n* = 3 biologically independent experiments, all statistically significant *P* values shown, two-tailed *t*-test, mean ± s.d.). **h**, IHC staining of FFPE samples of breast cancer with newly developed antibodies against hFWE. Breast cancer and stromal regions are shown in the H&E images (left). The anti-hFWE$^{Win}$ antibody is specific to Win isoforms hFWE2 and hFWE4 whereas the anti- hFWE-N-term antibody targets the common N terminus and recognizes all four isoforms. Immunohistochemistry staining shows the abundance of hFWE$^{Win}$ isoforms within the breast cancer samples in human tumours. From this, we conclude that hFWE$^{Win}$ proteins are expressed in the tumour but not in the stroma. To demonstrate the expression of Lose isoforms in the stroma, we compared the staining of all hFWE isoforms using our N-terminal-specific antibody with the poor expression of hFWE$^{Win}$ in the stroma. The anti-hFWE-N-term antibody shows strong immunoreactivity and equal distribution of staining in the tumour and stromal tissue. We find no positive signal for hFWE$^{Win}$ isoforms in the stroma, but we find strong expression of total hFWE (hFWE$^{Win}$ and hFWE$^{Lose}$ combined) in the stroma near the tumour. From this, we can conclude that Lose isoforms are expressed in the stroma. This experiment was repeated independently three times with similar results.

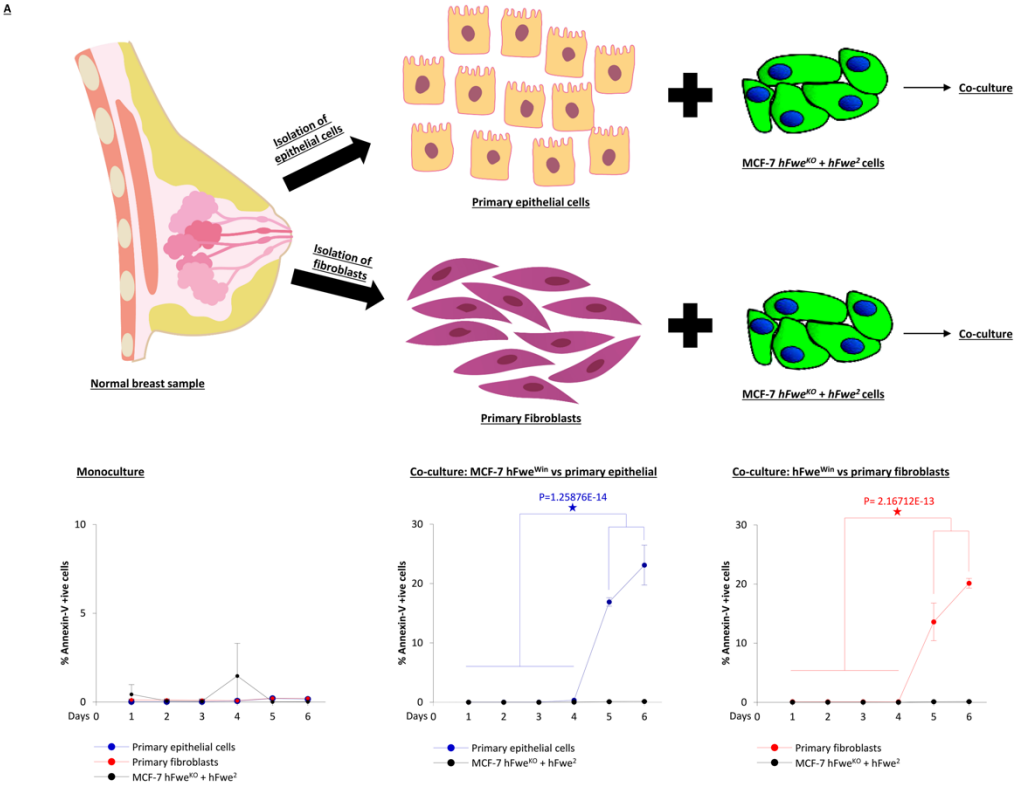
A
Isolation of epithelial cells
Isolation of fibroblasts
Normal breast sample
Primary epithelial cells
Primary Fibroblasts
MCF-7 hFwe^KO + hFwe² cells
Co-culture
Monoculture
Co-culture: MCF-7 hFwe^Win vs primary epithelial
Co-culture: hFwe^Win vs primary fibroblasts
P=1.25876E-14
P= 2.16712E-13
% Annexin-V +ive cells
Days 0
Primary epithelial cells
Primary fibroblasts
MCF-7 hFwe^KO + hFwe²

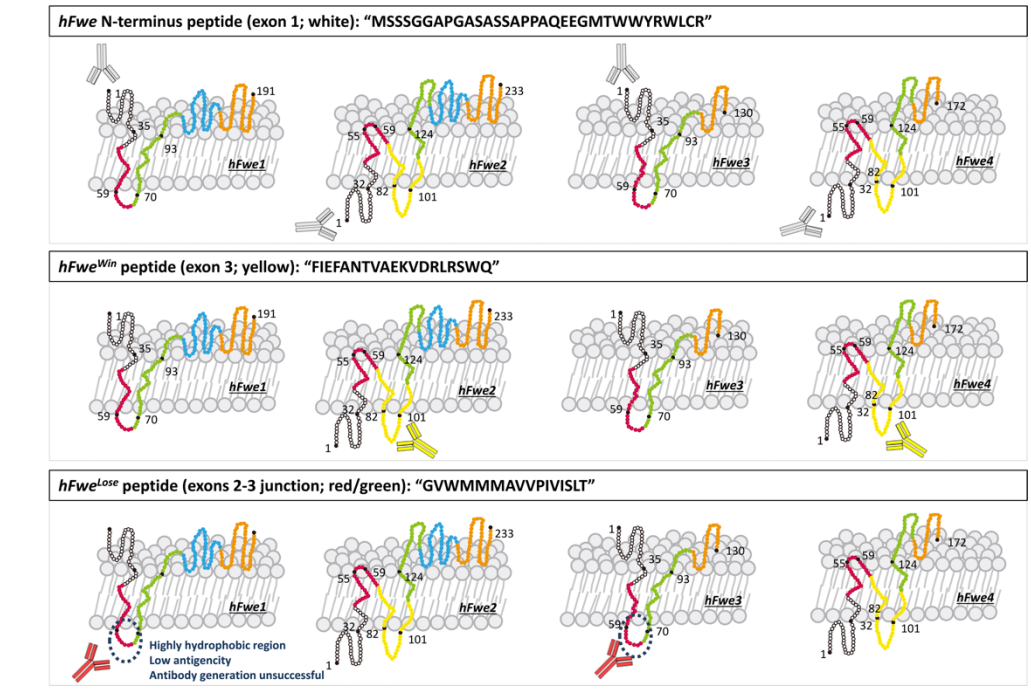
B
hFwe N-terminus peptide (exon 1; white): "MSSSGGAPGASASSAPPAQEEGMTWWYRWLCR"
hFwe^Win peptide (exon 3; yellow): "FIEFANTVAEKVDRLRSWQ"
hFwe^Lose peptide (exons 2-3 junction; red/green): "GVWMMMAVVPIVISLT"
hFwe1
hFwe2
hFwe3
hFwe4
Highly hydrophobic region
Low antigencity
Antibody generation unsuccessful

**Extended Data Fig. 8 | Dynamics of hFWE-mediated cell competition between cancer and normal cells. a**, Protocol for observing hFWE- mediated cell competition between $hFWE^{Win}$-expressing cancer cells and primary cultures of human epithelial cells and fibroblasts. MCF-7 *hFWE*$^{KO}$ cells overexpressing $hFWE^{Win}$ isoforms outcompeted and induced apoptosis of co-cultured primary breast normal epithelial cells or fibroblasts over 6 days ($n$ = 3 biologically independent experiments, all statistically significant $P$ values are shown, ANOVA, mean ± s.d.). **b**, $hFWE^{Win}$ isoforms (hFWE2 and hFWE4) and $hFWE^{Lose}$ isoforms (hFWE1 and hFWE3) are characterized by intra-exonic inclusions. The in silico model shows predicted transmembrane structures of the four hFWE proteins. An antibody was raised against the common N terminus (exon 1), which is included in all four isoforms. Another antibody was raised to specifically recognize the $hFWE^{Win}$ isoforms (which share exon 3). Owing to the similarity in sequences to $hFWE^{Win}$ isoforms and low antigenicity of the peptide sequence at the junction of exons 2 and 4, generation of an antibody specific to $hFWE^{Lose}$ isoforms was not possible.

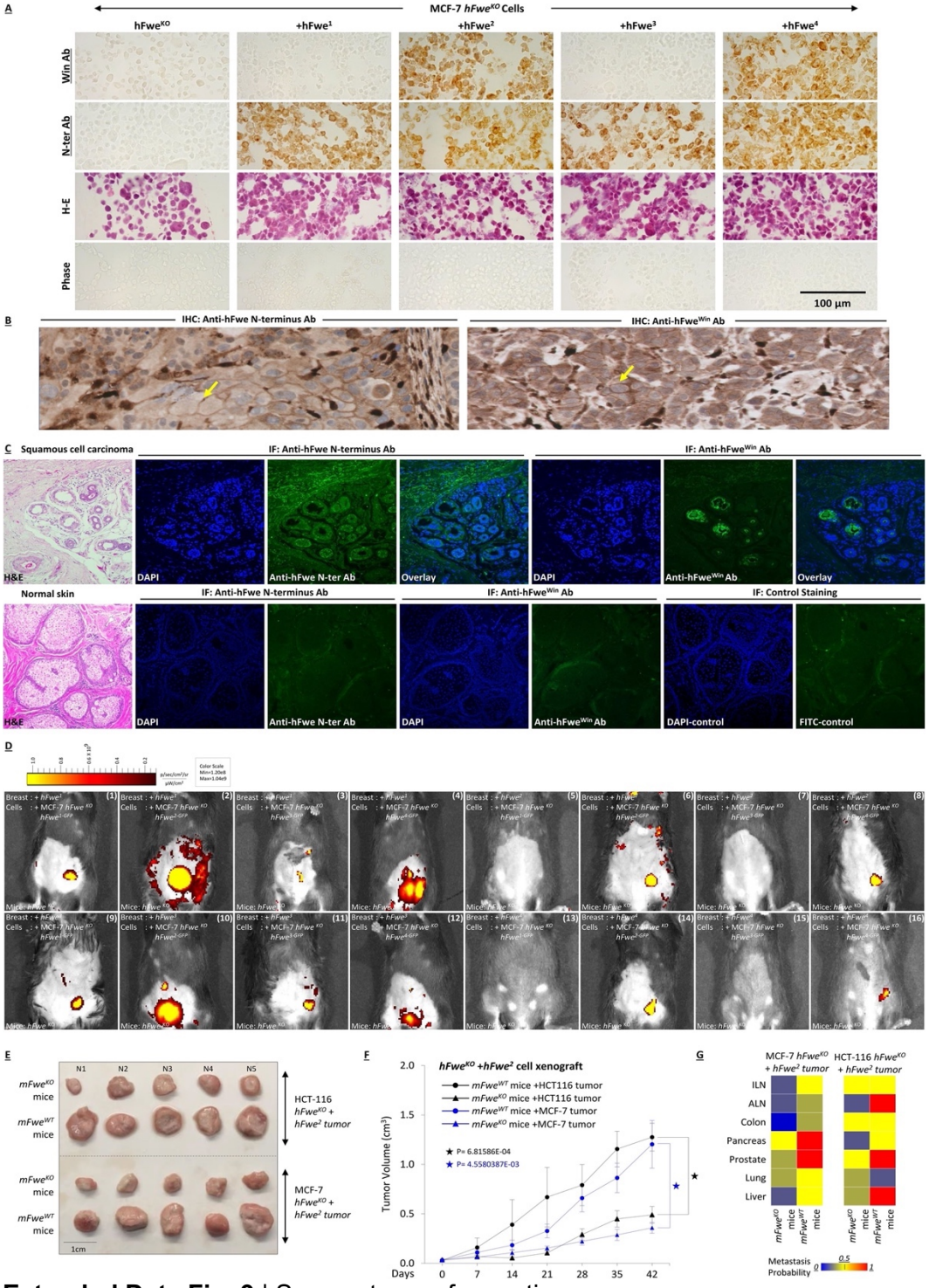


**Extended Data Fig. 9** | See next page for caption.

**Extended Data Fig. 9 | Generation of antibodies against hFWE$^{Win}$ isoforms (hFWE2 and hFWE4) or the common hFWE N terminus and expression in human cancers. a**, Immunocytochemistry of hFWE isoforms in paraffin-embedded and sectioned human MCF-7 cells using novel anti-hFWE antibodies. The specificity was validated by immunocytochemistry of MCF-7 *hFWE$^{KO}$* cells with or without overexpression of individual hFWE isoforms. Cells were stained with anti-hFWE-N-term antibody or anti-hFWE$^{Win}$ antibody. Immunocytochemistry results confirm antibody specificity in paraffin sections with MCF-7 *hFWE$^{KO}$* cells with or without overexpression of individual hFWE isoforms. The anti-hFWE$^{Win}$ antibody does not stain sections with *hFWE$^{KO}$* cells, and recognizes specifically hFWE2 and hFWE4, but not the hFWE$^{Lose}$ isoforms hFWE1 and hFWE3 (row 1). The anti-hFWE-N-term antibody is also negative for staining in control *hFWE$^{KO}$* cells but detected positive membrane staining for each of the four hFWE isoforms (row 2; *n* = 3). **b**, Immunohistochemistry of hFWE proteins in sections from clinical breast cancer samples (*n* = 3). Arrows indicate membrane staining. **c**, Immunofluorescence staining of hFWE proteins in human SCC tissue shows an abundance of hFWE$^{Win}$ isoforms within defined cancer lesions, whereas the anti-hFWE-N- term antibody stained both stroma and cancer tissue (top; *n* = 3) when compared with normal skin (bottom; *n* = 3). **d**, Tumour volumes were measured and analysed for each of the 16 combinations of hFWE*X*– IRES–GFP expression in MCF-7 *hFWE$^{KO}$* xenografted cells and hFWE isoform expression within *Fwe$^{KO}$* mouse mammary tissue (*n* = 3). In vivo bioluminescence imaging (using the IVIS system) was used to detect and measure the fluorescence of GFP$^{+}$ cancer cells in tumours resulting from all genetic combinations at 28 days post-implantation. Substantially reduced tumour growth was observed when mammary tissue expressed hFWE$^{Win}$ isoforms and cancer cells expressed hFWE$^{Lose}$ isoforms. By contrast, tumour growth is strongly promoted when mammary tissue expresses hFWE$^{Lose}$ isoforms and cancer cells express

hFWE$^{Win}$ isoforms ($n$ = 3). **e**, Tumorigenic potential of HCT-116 (colon origin) or MCF-7 (breast origin) *hFWE*$^{KO}$ cells overexpressing hFWE2 in recipient *Fwe*$^{WT}$ and *Fwe*$^{KO}$ mice. Tumour growth of both *Fwe*$^{KO}$ breast and colon cancer cell lines overexpressing the Win isoform hFWE2 was greater in *Fwe*$^{WT}$ mice than in *Fwe*$^{KO}$ mice. Photos of resected tumours are shown. **f**, Tumour volumes were measured every week over 42 days for groups shown in **a**. *hFWE*$^{KO}$ colon- or breast-derived tumours overexpressing hFWE2 showed significantly higher growth in *Fwe*$^{WT}$ mice than in *Fwe*$^{KO}$ mice ($n$ = 5, $P$ values shown, one-tailed $t$-test, mean ± s.d.). **g**, At the conclusion of tumour growth experiments, mice were examined for the presence or absence of metastases in inguinal lymph nodes (ILN), axillary lymph nodes (ALN), colon, pancreas, prostate, lung, and liver. Heat map scale indicates the probability of metastasis. Results show a marked reduction in the metastatic potential of both breast and colon cancer *hFWE*$^{KO}$ cells overexpressing hFWE2 when xenografted into *Fwe*$^{KO}$ mice as compared to *Fwe*$^{WT}$ mice ($n$ = 5 each group).

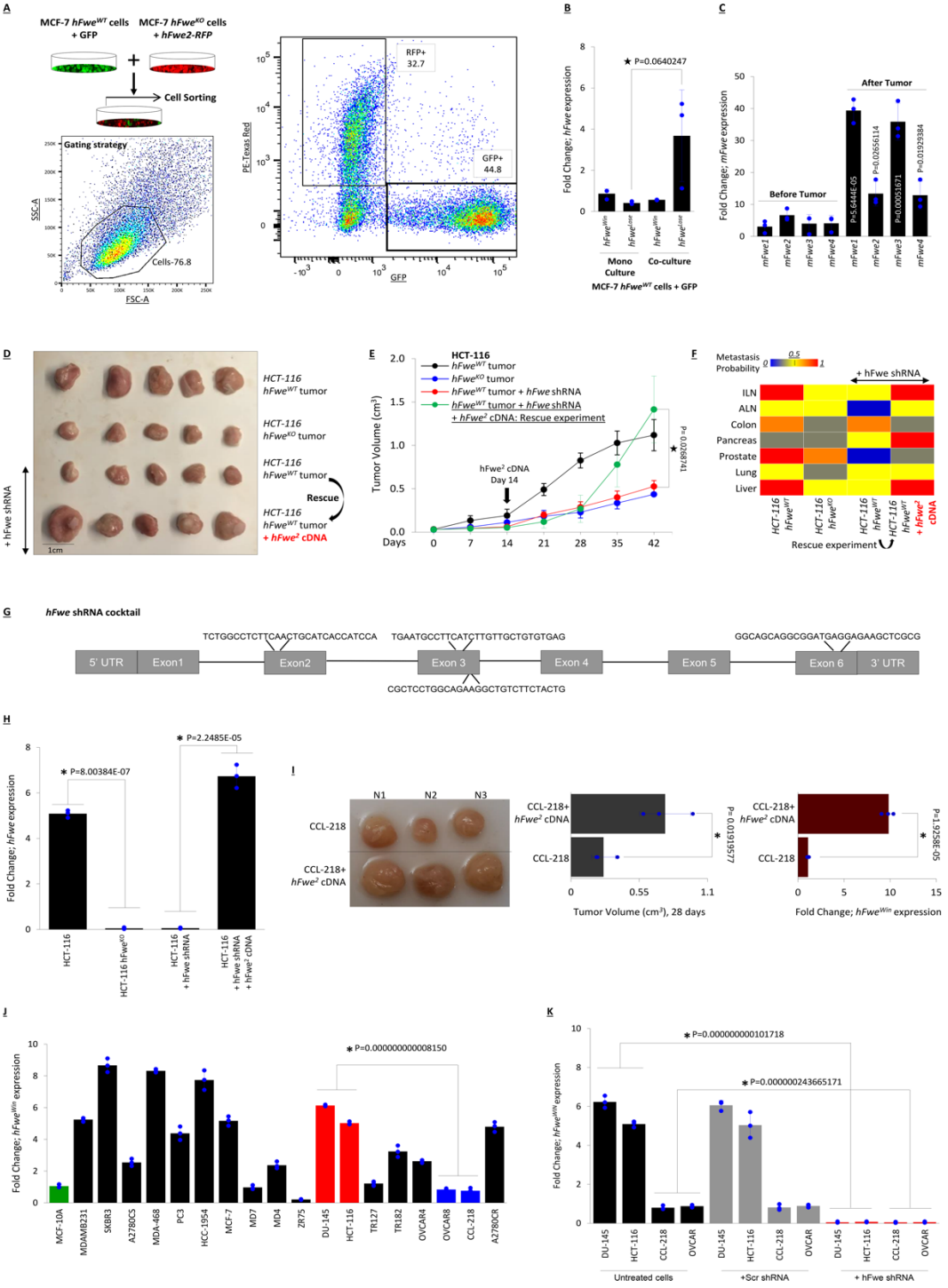


**Extended Data Fig. 10** | See next page for caption.

**Extended Data Fig. 10 | Endogenous hFWE in human cancer cell lines and tumorigenic potential. a**, Culture experiments were conducted to examine the dynamics of $hFWE^{Win}$ and $hFWE^{Lose}$ isoform expression. MCF-7 $hFWE^{KO}$ cells expressing hFWE2–RFP were co-cultured with wild-type MCF-7 cells expressing GFP for 24 h and sorted for analysis of hFWE isoform expression. *n* = 3 biologically independent experiments with similar results. **b**, Co-culture of MCF-7 $hFWE^{KO}$ cells expressing hFWE2–RFP with wild-type MCF-7 cells expressing GFP caused upregulation of $hFWE^{Lose}$ isoforms in wild-type MCF-7 cells. qPCR analysis of the expression of $hFWE^{Win}$ and $hFWE^{Lose}$ isoforms in $GFP^+$ wild-type MCF-7 cells sorted from co-culture shows a significant increase in $hFWE^{Lose}$ isoforms (bar 4) when compared with monocultured wild- type MCF-7 cells (bar 2). *n* = 3 biologically independent experiments with similar results; fold change calculated relative to the expression of $hFWE^{Win}$ isoforms in monocultured $GFP^+$ wild-type MCF-7 cells, all statistically significant *P* values shown, two-tailed *t*-test, mean ± s.d. **c**, MCF-7 cells expressing hFWE2 were xenografted into $Fwe^{WT}$ mice to assess their tumorigenic potential and the host expression of endogenous hFWE isoforms compared to control. The mouse tissue adjacent to the tumour showed a significant increase in expression of $hFWE^{Lose}$ isoforms at 21 days post-xenograft. *n* = 3 biologically independent experiments with similar results; all statistically significant *P* values shown, one-tailed *t*-test, mean ± s.d. **d**, The effect of anti-*hFWE* shRNA cocktail on the tumorigenic potential of HCT-116 cells. Row 1, growth potential of HCT- 116 $hFWE^{WT}$ cells. Row 2, knockout of *hFWE* in these cells significantly reduced tumour growth. Row 3, treatment of HCT-116 $hFWE^{WT}$ cells with anti-*hFWE* shRNA reduced tumour volume. Row 4, Rescue experiment in which similar *hFWE* shRNA-treated tumours to row 3 were infected with lentivirus overexpressing hFWE2 14 days after implantation. These tumours are significantly larger than those in row 3. **e**, Tumour volumes for experiments shown in Fig. 4a were measured weekly, and growth patterns were analysed over 42 days for groups shown in **a**. Growth curves

show the reduced growth of tumours from HCT-116 *hFWE*$^{KO}$ cells (blue) and *hFWE* shRNA-treated HCT-116 *hFWE*$^{WT}$ cells (red). Green line shows rescue experiment and growth pattern changes in *hFWE* shRNA-treated HCT-116 *hFWE*$^{WT}$ tumours expressing with hFWE2 (*n* = 5, *P* values shown, one-tailed *t*-test, mean ± s.d.). **f**, All mice used in the study were examined for the presence or absence of metastases in ILN, ALN, colon, pancreas, prostate, lung and liver. Heat map scale indicates the probability of metastasis. Metastatic potential was reduced by knockout or knockdown of *hFWE* in HCT-116 cells (compare column 1 with columns 2 and 3). The rescue of tumour growth by re-introduction of *hFWE2* cDNA was accompanied by an increase in metastasis of these cells (compare column 3 with column 4; *n* = 5 each group). **g**, A cocktail of shRNAs were designed to knock down all four isoforms of hFWE. All shRNAs were checked for off-target effects. **h**, Gene expression analysis confirmed deletion of total *hFWE* in HCT-116 *hFWE*$^{KO}$ cells. Exogenous expression of *hFWE2* cDNA was detectable as the total *hFWE* expression in wild-type HCT-116 cells co-treated with anti-*hFWE* shRNA (observed in resected tumours). *n* = 3 biologically independent experiments, fold change calculated relative to expression of hFWE$^{Win}$ isoforms in MCF-10A cells, *P* values shown, two- tailed *t*-test, mean ± s.d. **i**, Tumorigenic potential of wild-type CCL-218 cells and CCL-218 cells overexpressing hFWE2. Xenografts overexpressing *hFWE2* cDNA showed increased tumour volume at 28 days. Photos of resected tumours are shown. *n* = 3 biologically independent experiments with similar results, all statistically significant *P* values shown, ANOVA, mean ± s.d. Control qPCR experiment demonstrates the overexpression of *hFWE2* in CCL-218 tumours at day 28. *n* = 3 biologically independent experiments, fold change calculated relative to expression of hFWE$^{Win}$ isoforms in MCF-10A cells, *P* values shown, two-tailed *t*-test, mean ± s.d. **j**, Endogenous expression of the four hFWE isoforms in 19 cancer cell lines of multiple origins (*n* = 3 biologically independent experiments, fold change is calculated relative to expression of hFWE$^{Win}$ isoforms in MCF-10A cells, *P* values shown, ANOVA, mean ± s.d.). **k**, Gene expression analysis shows efficient shRNA-mediated

knockdown of total *hFWE* in HCT-116, DU-145, CCL-218 and OVCAR-8 tumours (observed in resected tumours). $n$ = 3 biologically independent experiments, fold change calculated relative to expression of $hFWE^{Win}$ isoforms in MCF-10A cells, $P$ values shown, ANOVA, mean ± s.d.

# CHAPTER 3

# PTMA interacts with Flower “Win” isoform promoting cancer growth and invasion

**3.1 ABSTRACT:** Through the process of cell competition, human cells compete due to their relative fitness levels by displaying the "Win" and “Lose” isoforms of the human Flower (hFWE) protein. We proposed that in the early stages of cancer, tumoral cells express high levels of $hFWE^{Win}$ and can outcompete normal cells, thereby monopolizing tissue space. Therefore, uncovering novel human Flower interactors is crucial to understand the mechanism of cell competition and blocking it to impair cancer progression. To identify hFWE interactors, we overexpressed in the colon cell line (HCT 116) the Win and Lose isoforms of hFWE and performed Immunoprecipitation (IP) followed by Mass Spec. We found several proteins that interact with both hFWE isoforms. The most promising candidate was the cancer biomarker PTMA, which we found to be highly expressed in winner cells and poorly expressed in $hFWE^{KO}$ cells. Furthermore, we discovered that PTMA downregulation in the Winner cells blocked cell competition, preventing loser cell elimination. We also observed that PTMA subcellular localization shifts from the nucleus in $hFWE^{KO}$ to the cytoplasm in the winner cells. Finally, we analyzed PTMA expression in patient samples. Interestingly we found that PTMA expression was higher in tumor invasive front in contact with the stroma, where cell competition occurs. These results suggest an interaction between Flower and PTMA to promote cancer growth and progression. Our findings might open the way to the development of new drug strategies to treat cancer by targeting this interaction.

**Keywords:** Cell Competition, PTMA, Flower, Protein-protein interaction

## 3.2 INTRODUCTION

Damaged but viable cells can accumulate in tissues during development and aging, possibly leading to organ dysfunction and diseases[1–9]. It was first demonstrated in *Drosophila* that cells could directly exchange cell fitness information, enabling the identification and elimination of a wide range of those viable but suboptimal cells[1–5]. In neighbour cells with a competitive advantage, cell competition (CC), an active cell selection mechanism, promotes eliminating the unfit cells in a tissue[6,7].

“Fitness fingerprints” that reveal optimal (or suboptimal) fitness status to neighboring cells are encoded by different isoforms of the transmembrane protein Flower. The isoforms that indicate reduced fitness are called Lose isoforms because they are expressed in viable cells marked to be eliminated, provided that fitter cells expressing Win isoforms are available[1–8]. Therefore, a direct comparison of cell fitness is used in *Drosophila* to detect and eliminate many viable but impaired cells with important physiological outcomes at the organism level, such as delaying aging, eliminating defective structures during development, or replacing old tissues during regeneration. The exact mechanism in human epithelia gives premalignant cells a competitive advantage to grow at the expense of neighboring cells[1,2,9].

C9ORF7 (CACFD1) encodes four protein-coding splice variants of the human Flower (hFWE) protein: hFWE1, hFWE2, hFWE3, and hFWE4. The isoforms hFWE1 and hFWE3 with extracellular N-terminus function as Lose isoforms. When cells that express Lose isoforms get in contact with cells that express $hFWE^{Win}$ isoforms (hFWE2 and hFWE4, N-terminus internalized), $hFWE^{Lose}$-expressing cells are eliminated. Thus, hFWE gene isoforms form an extracellular code for comparing relative cellular fitness amongst human cells[8].

Cell competition can also play a role in cancer development and progression. In healthy tissue, less fit cells due to harmful mutations or other damage are typically

outcompeted by healthier cells. However, in the context of cancer, cells can outcompete neighboring healthy cells, leading to the development of a tumor.[8] This can occur, for example, when a cell with a mutation in a cancer-promoting gene, such as the proto-oncogene Myc, gains a selective advantage over its neighboring cells, allowing it to divide and proliferate more rapidly[1]. Understanding the mechanisms of cell competition is essential for developing new drugs that could suppress tumor cell proliferation and block cancer progression[10].

Colorectal cancer (CRC) is the third most common cancer worldwide and the second most common cause of cancer-related death, beaten lung cancer. It is the second most prevalent cancer among women (9.4%) and third in men (10.6%)[11]. The percentage of CRC patients already with metastasis at the time of the diagnosis is around 20% which can compromise the disease response[12].

Prothymosin-α (PTMA) is a small and highly acidic protein found in many cell types and locations, but its exact function is not fully understood. Studies suggest it regulates transcription, cell cycle, apoptosis[13], proliferation, cell growth, and carcinogenesis[13,14]. PTMA has been implicated in a range of diseases, including cancer. Plays a critical role in the survival and proliferation of lung cancer[15,16], breast squamous cell carcinoma[17], and colorectal cancer[18–20].

In this study, we aim to identify and elucidate the physiologic role of the hFWE-binding proteins during cell competition. We performed IP followed by Mass Spec to identify hFWE interactors. After analyzing the expression levels of the candidates by qPCR in HCT 116, HCT 116 *hFWE*$^{KO}$, HCT 116 *hFWE*$^{KO + hFWE1\text{-}GFP}$; and HCT 116 *hFWE*$^{KO + hFWE2\text{-}GFP}$, we observed that PTMA was more expressed in FWE$^{Win}$-expressing cells and poorly expressed in *hFWE*$^{KO}$ cells. Suggesting that the upregulation of PTMA in cancer cells seems to be FWE-dependent. We then analyzed the sub-cellular location of PTMA using the Immunofluorescence (IF) technic. We observed a shift from the nucleus to the cytoplasm in HCT 116 *hFWE*$^{KO}$

to HCT 116 *hFWE*$^{KO + hFWE2\text{-}GFP}$ (winner), respectively. Moreover, in human patient samples, PTMA is more expressed in cancer tissue when compared to normal tissue. Previous studies showed that hFWE2 is also overexpressed in cancer tissue compared to normal stroma tissue[10].

We propose that hFWE$^{Win}$, a transmembrane protein expressed in cancer cells, sequesters PTMA and keeps it in the cytoplasm promoting cancer growth and progression. Our findings might open a new drug strategy to treat cancer targeting PTMA and hFWE$^{Win}$ interaction.

## 3.3 Materials and Methods

### 3.3.1 Cell Culture condition.

HCT 116, HCT 116 *hFWE KO*, and HEK 293T cell lines were cultured in Dulbecco's Modified Eagle Medium (DMEM, Biowest, L0104-500) supplemented with 10% fetal bovine serum (FBS, Gibco, 10270106) and 1% penicillin-streptomycin (HyClone). Cells were maintained in the incubator at 37°C, 5% CO2, and in a humidified atmosphere of 95%. Subsequent cell lines resulting from the lentiviral transfection of the parental lines were grown under the same conditions. Mycoplasma test was performed frequently to identify eventual contaminations.

### 3.3.2 Cell line transfections and transduction.

Lentiviral particles were generated according to the Lipofectamine 3000 protocol (ViraPower Lentiviral Expression System, Invitrogen). HEK 293T cells were seeded in a 10cm dish in complete DMEM HG without pen-strep. The lentiviral construct hFWE1::GFP; hFWE2::GFP; PTMA shRNA; scramble shRNA (Addgene #1864); hFWE1-RFP; hFWE2-GFP and lentiviral packaging mix (pLP1, pLP2, and pLP/VSVG) were cotransfected into HEK 293T cells using Lipofectamine 3000 reagent. The lentiviral packaging mix concentration used was: 3,34 µg of pLP1; 2,21

µg of pLP2; 3,34 µg VSV-G, and 3 µg of each lentiviral construct. Supernatants containing lentivirus were collected 48h after transfection and centrifuged at 2000 rpm for 10 min to remove cell debris. After the centrifugation, supernatants were filtered using a 45µm pore filter to remove any remaining cellular debris. The virus was then stored at -80◦C aliquoted. The titer of lentiviral particles was determined using One-Wash Lentivirus Titer Kit (Cat: TR30038, Origene). For infection of target cells in a T-25 flask, lentiviral particles and 8 µg/mL of Polybrene Transfection Reagent (TR-1003-G, Sigma) were added in culture medium and after overnight incubation, the medium with the viral particles was removed and replaced by a fresh complete medium. Cells were then maintained in culture for two passages. GFP-positive cells were sorted through fluorescence-activated cell sorting (FACS) to select only the positive cells. For cells transduced with PTMA shRNA and scramble shRNA (Addgene #1864), a selection with neomycin antibiotics was performed for approximately three weeks. Downregulation of the gene was confirmed by qPCR and Western Blot. All the procedures were handled in a BSL2 lab facility.

### 3.3.3 IMMUNOPRECIPITATION - GFP TRAP MA KIT.

HCT116, HCT116 *hFWE*$^{KO}$, HCT116 *hFWE*$^{KO\text{-}GFP}$, HCT116$^{hFWE1::GFP}$, and HCT116$^{hFWE2::GFP}$ cells, were washed three times in ice-cold PBS followed by the addition of RIPA buffer containing protease and phosphatase inhibitors (Cat: A32961, Thermo Scientific). After 10 min incubation on ice, cells were scraped from the t-flask and transferred to a low-binding Eppendorf. Tubes were centrifuged at 14,000 rpm for 20 min at 4°C. Lysate-supernatants were transferred to a pre-cooled low-binding Eppendorf, and the pellet was discarded. GFP Trap MA beads were equilibrated in 500ul of ice-cold dilution buffer and separated magnetically until the supernatant is clear. In total, 40 ug of lysate-supernatant was added to equilibrate GFP Trap MA beads and incubated overnight at 4 °C, with end-over-end rotation. Beads were separated with a DynaMag™- Spin Magnet (Cat: 12320D, Invitrogen) and washed three times with a 500 µL wash buffer. Eighty microliters of 2× SDS sample buffer

was added to the GFP Trap beads and boiled for 5 min at 95 °C to dissociate immunocomplexes from the beads. The beads were separated magnetically and SDS-PAGE was performed with the supernatant in NuPAGE 4-12% Bis-Tris precast polyacrylamide gel - followed by Western Blot.

### 3.3.4 WESTERN BLOT.

Cells lysates were obtained using RIPA lysis buffer, composed of 50 mM Tris-HCl pH 8.0, 150 mM NaCl, 1% Triton X-100, 0.1% SDS, 0.5% Sodium deoxycholate supplemented with protease and phosphatase inhibitor (Thermo Scientific, A32961), after 10 min incubation. The total protein concentration was quantified by Pierce BCA protein assay kit (Thermo Scientific, 23225) and then separated by sodium dodecyl sulfate–polyacrylamide gel electrophoresis - NuPage 4-12% Bis-Tris precast polyacrylamide gel (Invitrogen NPO336BOX). Subsequently, proteins were transferred to a nitrocellulose membrane (iBlot 2 Dry Blotting System; program 1; 7 minutes - Invitrogen) and then blocked with 5% BSA in TBS -T (10 mM Tris, pH 7.4, 150 mM NaCl, 0.1% Tween 20) for 1 hour at room temperature. Next, the membranes were incubated with rabbit anti-PTMA abx128206 (2 µg/ml), rabbit anti-GFP (cat: ab290, Abcam) antibodies in TBS-T 5% BSA at 4°C overnight, respectively. Membranes were washed three times for 10min in TBS-T and incubated with HRP-conjugated secondary antibodies (anti-rabbit HRP, Invitrogen #31460) in TBS-T (dilution 1:10,000) at room temperature, for one hour. After three times washing steps, the membrane was revealed by Enhanced Chemiluminescence detection (Thermo Scientific, 32106) and imaged with Amersham Imager 600 (GE Life Sciences).

### 3.3.5 IMMUNOFLUORESCENCE.

HCT 116$^{WT}$, HCT 116 *hFWE*$^{KO}$, HCT 116 *hFWE*$^{KO}$ $^{+ \text{ hFWE2::GFP}}$ cells were seeded onto glass coverslips at 70% confluence. After 24h, cells were washed with PBS and then fixed in 4% PFA in PBS for 15 min at RT. Coverslips were washed

three times in PBS and were permeabilized in 0.1% (vol/vol) Triton X-100 in PBS for 15 min on ice and blocked in 10% BSA (Sigma-Aldrich) in PBS for one hour at RT. The primary antibodies rabbit anti-PTMA abx128206 (15µg/ml) antibody were diluted in blocking buffer (BB) and incubated overnight at 4°C in the dark. Coverslips were washed three times with TBS and incubated with the following secondary antibodies in a blocking solution for 1h at room temperature: anti-rabbit Alexa 488 (cat. A-21206, Invitrogen), anti-rabbit Alexa 647 (cat. A-31573, Invitrogen). Coverslips were washed three times in TBS, and cells were stained with 2 µg/mL DAPI (Sigma, D9542) for 5 minutes in TBS. After five washes, cells were mounted on Vectashield (H-1000, Vector Laboratories), and fluorescence images were acquired with the Zeiss LSM 880 confocal microscope, with immersion objective 40x. Brightness and contrast adjustments were applied using Image J software (NIH).

### 3.3.6 CELL COMPETITION ASSAY AND LIVE CELL IMAGING.

HCT 116 *hFWE*$^{KO}$ cells were infected with lentiviral particles expressing hFWE1-RFP and hFWE2-GFP isoforms. HCT 116 *hFWE*$^{KO}$ + hFWE1-RFP and HCT 116 *hFWE*$^{KO}$ + hFWE2-GFP cells were transfected with scramble shRNA and PTMA shRNA, respectively. RFP+ and GFP+ positive cells were sorted by flow cytometer using the BD FACS Aria Fusion (BD Biosciences). Cells transfected with scramble shRNA and PTMA shRNA were selected using neomycin antibiotic for approximately three weeks. Equal amounts of HCT 116 *hFWE*$^{KO}$ cells expressing hFWE1 and hFWE2 tagged with RFP and GFP respectively, were co-cultured in a glass-bottom dish. HCT 116 cells expressing hFWE1-RFP + scramble shRNA (Addgene #1864) and hFWE2-GFP + PTMA shRNA were also co-cultured in parallel for 48h. The cells were subsequently processed for apoptosis detection using annexin-V staining and undergoing live-cell imaging for the given periods. Live-cell imaging was performed using Zeiss LSM-880 Confocal Microscope and analyses using Fiji software and Imaris 9.9.1 software.

### 3.3.7 APOPTOSIS ANALYSIS.

Cells were stained with annexin-V (Thermo Fisher Scientific) as per the manufacturer's instructions at the end of monoculture and co-culture assays. Flow cytometry detected apoptotic cells by spotting Annexin-V (Pacific Blue conjugated, Invitrogen and 7AAD Viability Staining Solution, BioLegend) staining using BD LSRFortessa X-20. Apoptosis percentages were achieved using FlowJo software.

### 3.3.8 RNA ISOLATION AND QPCR ANALYSIS.

The RNA was isolated from cell lines using the RNeasy Mini Kit (Cat: 74106, Qiagen) and from FFPE tissue samples using the RNeasy FFPE Kit (Cat: 73504, Qiagen). cDNA QuantiTect Reverse Transcription Kit (Cat: 205313, Qiagen) was used to reverse-transcribe 1ug of the total RNA from cells and FFPE samples, respectively to complementary DNA (cDNA) as per the manufacturer's instructions. Quantitative PCR (qPCR) was performed using PowerUp SYBR Green Master Mix (Cat: 100029284, Applied Biosystems) in QuantStudio 5 Real-time PCR System (Applied Biosystems) at standard reaction conditions. All qPCR reactions were done in triplicate, and the experiments were repeated three times. Data were analyzed using the comparative Ct method and normalized to the expression level of the GAPDH housekeeping gene. The table represents the primers (Fw: forward; Rv: reverse) used in the experiment.

| GENES | PRIMERS | |
|---|---|---|
| NONO | Fw: CCCAACGAAGCCGTCTTTTTG | Rv: GCTAGGGTTCGGGTTTCCAAG |
| PTMA | Fw: TGAGTCAGCTACGGGCAAG | Rv: GCTGTCTAGTCATCCTCGTCG |
| MDK | Fw: CGCGGTCGCCAAAAAGAAAG | Rv: CAGTCGGCTCCAAACTCCT |
| BPTF | Fw: TGTGCAGTTAAACCAGTTGTGA | RV: TTTTACCCATGTCGCTTGCTG |
| TRIM32 | Fw: GGCGGTCAGGAATTTGAC | Rv: CTCTTCCTTTGAAGGGTATTGC |
| SMEK2 | Fw: CAGTGGAAAAACCTAAGCCAGA | Rv: CACCAGGAGATGTCCTTTTGG |
| ATP2B4 | Fw: TTCGCCATAGAGGAGGAGTTG | Rv: CTGTAGAGAGCTGTCCGACTG |
| CALM3 | Fw: AGAGGCGTTCCGTGTCTTTG | Rv: CCCCAGGTTCGTCATTACGTG |

| | | |
|---|---|---|
| EFCAB11 | Fw: GGTACAAGCCCTCCAAGATAGA | Rv: AAGATGTGTCTTACTTCGTTCCG |
| VPS28 | Fw: CAAGCCGGAGCTGTATGAGG | Rv: CCATGTTGTCGTACTTCTCCC |
| SFPQ | Fw: GGTTATGAAGCTAATCCTGGCG | Rv: GCCTTCGTACTCTTCTCTCCC |
| LYPLA1 | Fw: GTGTCACTGCACTCAGTTGCT | Rv: CACCACCGATAGGACCCTG |
| CAST | Fw: TGAAGATGCTAAACTTGCTGCT | Rv: GTCACTCTGCGAGGTATCACG |
| PROSC | Fw: AGTTGGCAGACAAAGTGAACA | Rv: CTTGGCGTTTATGTGCTCCAC |
| ARRDC1 | Fw: GGGTGACCTGCATAGGTTCC | Rv: GATCTTCCCGAAAGGACCCT |
| GAPDH | Fw: TGTTCGTCATGGGTGTGAAC | Rv: ATGGCATGGACTGTGGTCAT |

### 3.3.9 PATIENT STUDY SAMPLES.

FFPE tissue blocks of normal and cancer colon tissue were provided by Dr. António Beltran and Dr. Antonio Galzerano from the Pathology Department of Champalimaud Foundation. Dr. Joaquim Gago also provided clinical data. The samples were used to perform IHC and qPCR.

### 3.3.10 IMMUNOHISTOCHEMISTRY.

Formalin-fixed and paraffin-embedded human colorectal cancer (CRC) samples were selected for PTMA immunohistochemistry (n=40). Samples were sectioned at 4µm, deparaffinized and antigen retrieval was performed (citrate buffer, pH 6, 95 °C, 30 min). After blocking with 3% $H_2O_2$ in MeOH for 30 min, sections were incubated with anti-PTMA antibody (Abbexa, 128206, 1:250) for 1h at room temperature, followed by an HRP conjugated secondary antibody (Dako envision anti-rabbit ready to use) for 30 min at room temperature. Sections were then incubated with 3,3'-diaminobenzidine (DAB, Dako) and counterstained with Harris Haematoxylin. Slides were examined for PTMA expression in an Axioscope 5 microscope (Zeiss) coupled to an Axiocam 208 color camera (Zeiss). Scoring of PTMA expression in each CRC sample was performed for the following parameters: (1) presence/absence; (2) cellular distribution: nuclear, cytoplasmic, both; (3) staining

intensity in hotspots (areas with higher expression) using a 4-tier system (minimal, mild, moderate, marked); and (4) discrepancy in expression levels in tumor core and invasive front (Figure 5). The invasive front was defined as the area corresponding to the tumor border, immediately adjacent to the peri-tumoral stroma, and the tumor core, as the central part of the tumor, most distant from the border. PTMA expression was also examined in tumor-distant normal colorectal mucosa from these CRC patients.

### 3.3.11 MASS SPECTROMETRY TECHNIC AND ANALYSIS.

Proteins were eluted with 100 mM Tris pH 8.5, 1% sodium deoxycholate, 10 mM tris(2-carboxyethyl) phosphine (TCEP), 40 mM chloroacetamide for 10 minutes at 95ºC at 1000 rpm (Thermomixer, Eppendorf). Next, proteins, including the IP beads, were processed for proteomics analysis following the solid-phase-enhanced sample-preparation (SP3) protocol as described in PMID30464214. Enzymatic digestion was performed with Trypsin/LysC (2 micrograms) overnight at 37ºC at 1000 rpm. The resulting peptides were cleaned-up and desalted with C18 micro columns and further quantified. Protein identification was performed by nanoLC-MS/MS at I3S - Proteomics Scientific Platform. This equipment is composed by an Ultimate 3000 liquid chromatography system coupled to a Q-Exactive Hybrid Quadrupole-Orbitrap mass spectrometer (Thermo Scientific, Bremen, Germany). 500 ng of peptides were loaded onto a trapping cartridge (Acclaim PepMap C18 100Å, 5 mm x 300 µm i.d., 160454, Thermo Scientific) in a mobile phase of 2% ACN, 0.1% FA at 10 µL/min. After 3 min loading, the trap column was switched in-line to a 50 cm by 75µm inner diameter EASY-Spray column (ES803, PepMap RSLC, C18, 2 µm, Thermo Scientific, Bremen, Germany) at 300 nL/min. Separation was generated by mixing A: 0.1% FA, and B: 80% ACN, with the following gradient: 5 min (2.5% B to 10% B), 120 min (10% B to 30% B), 20 min (30% B to 50% B), 5 min (50% B to 99% B) and 10 min (hold 99% B). Subsequently, the column was equilibrated with 2.5% B for 17 min. Data acquisition was controlled by Xcalibur 4.0 and Tune 2.9 software (Thermo

Scientific, Bremen, Germany). The mass spectrometer was operated in data-dependent (dd) positive acquisition mode alternating between a full scan (m/z 380-1580) and subsequent HCD MS/MS of the 10 most intense peaks from full scan (normalized collision energy of 27%). ESI spray voltage was 1.9 kV. Global settings: use lock masses best (m/z 445.12003), lock mass injection Full MS, chrom. peak width (FWHM) 15s. Full scan settings: 70k resolution (m/z 200), AGC target 3e6, maximum injection time 120 ms. dd settings: minimum AGC target 8e3, intensity threshold 7.3e4, charge exclusion: unassigned, 1, 8, >8, peptide match preferred, exclude isotopes on, dynamic exclusion 45s. MS2 settings: microscans 1, resolution 35k (m/z 200), AGC target 2e5, maximum injection time 110 ms, isolation window 2.0 m/z, isolation offset 0.0 m/z, spectrum data type profile. The raw data was processed using the Proteome Discoverer software v2.4.0.305 (Thermo Scientific) and searched against the UniProt database for Homo sapiens taxonomic selection. The Sequest HT search engine was used to identify tryptic peptides. The ion mass tolerance was 10 ppm for precursor ions and 0.02 Da for fragment ions. Maximum allowed missing cleavage sites was set to 2. Cysteine carbamidomethylation was defined as constant modification. Methionine oxidation and protein N-terminus acetylation were defined as variable modifications. Peptide confidence was set to high. The processing node Percolator was enabled with the following settings: maximum delta Cn 0.05; decoy database search target FDR 1%, validation based on q-value. Protein label free quantitation was performed with the Minora feature detector node at the processing step. Precursor ions quantification was performing at the processing step with the following parameters: Peptides to use unique plus razor, precursor abundance was based on intensity, normalization mode was based on total peptide amount, pairwise protein ratio calculation, hypothesis test was based on t-test (background based).

### 3.3.12 STATISTICAL ANALYSIS.

All values are expressed as means ± s.d. of independent experiments. Differences between groups were evaluated by Student's t-test (two-sided) and considered to be significant at $P < 0.05$.

## 3.4 RESULTS

### 3.4.1 IMMUNOPRECIPITATION OF THE HFWE ISOFORMS FROM CELL LINES

To discover human FWE protein partners, we performed a proteomic study using immunoprecipitation (IP) of the human FWE isoforms 1 and 2 fused with GFP. Total cell lysates from HCT 116$^{hFWE1::GFP}$ (Lose), HCT 116$^{hFWE2::GFP}$ (Win), HCT116 *hFWE*$^{KO\text{-}GFP}$, and HCT 116 *hFWE*$^{KO}$ were immunoprecipitated following GFP-Trap Magnetic Agarose kit protocol. Western Blot analysis of IP fractions confirmed that both hFWE isoforms were successfully immunoprecipitated from cell extracts. We also performed Immunoprecipitation detected by Flow Cytometry (IP-FCM) to confirm the previous result with a different technique. The results showed GFP positive signal in HCT 116$^{hFWE1::GFP}$ (Lose), HCT 116$^{hFWE2::GFP}$ (Win), and HCT116 *hFWE*$^{KO\text{-}GFP}$. No positive signal was detected for HCT116 *hFWE*$^{KO}$, corroborating what was observed in Western Blot (WB). The eluted fraction from the IP was sent to Mass Spectrometry (MS) for protein identification. IP experiments were performed in triplicate for each sample group, and MS-identified proteins were combined for analysis.

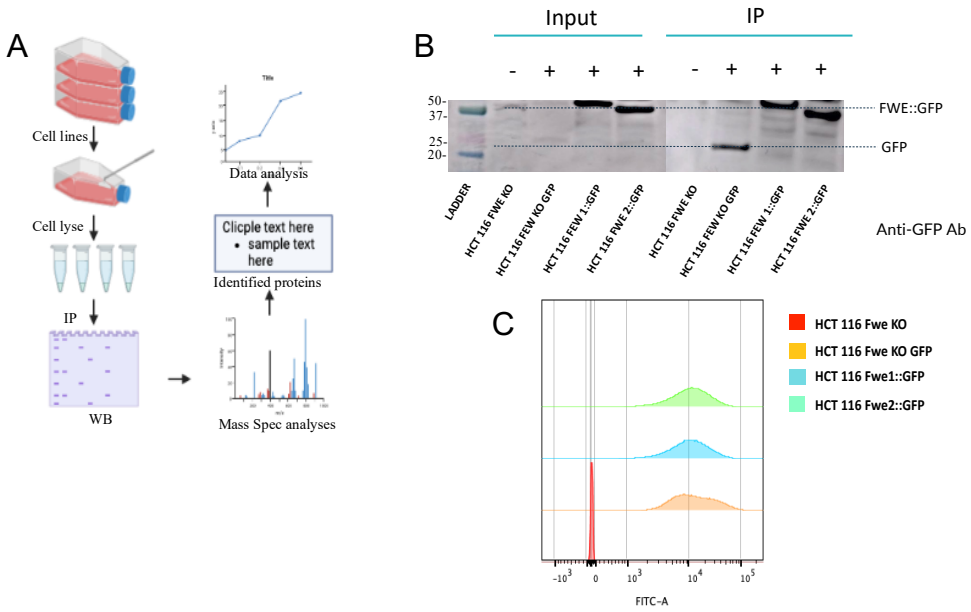


**Figure 1 - Immunoprecipitation of the hFWE isoforms from stable overexpressing cell lines. A)** Workflow scheme from cell culture, complex separation by Immunoprecipitation to Mass Spec procedure, and data analysis. **B-C)** hFWE Win and Lose isoforms were immunoprecipitated from the total cell lyse. **B)** Western blot assay analyses showed a positive band in the Input and IP fractions of HCT 116$^{hFWE1::GFP}$ and HCT 116$^{hFWE2::GFP}$. HCT116 *hFWE*$^{KO}$ cells were used as a negative control, and HCT116 *hFWE*$^{KO\text{-}GFP}$ as a positive control. **C)** Immunoprecipitation followed by Flow Cytometry (IP-FCM) showed GFP positive signal in cells expressing GFP. No signal was detected in HCT 116 *hFWE*$^{KO}$ cells after incubation with anti-GFP ab.

### 3.4.2 IDENTIFICATION OF HFWE INTERACTORS AND GENE EXPRESSION ANALYSIS

In total, 3184 proteins were identified for hFWE$^{Lose}$ and 4212 for hFWE$^{Win}$ (Figure 2 - A) using Proteome Discoverer software v2.4.0.305 (Thermo Scientific).

To find the strongest hFWE ligantes and to discard possible non-FWE protein partners (false positives), we excluded all the proteins that bind to GFP from the list. Then, we applied filters described in the literature such as: a) Found in the Sample Group – has High Confidence; b) Abundance Ratio Adj. P-Value – Is less than or equal to 0.05; c) Abundance Ratios – is greater than or equal to 3.00; and d) Unique Peptides - is greater than or equal to 2, to achieve statistic significant and strongest candidates.

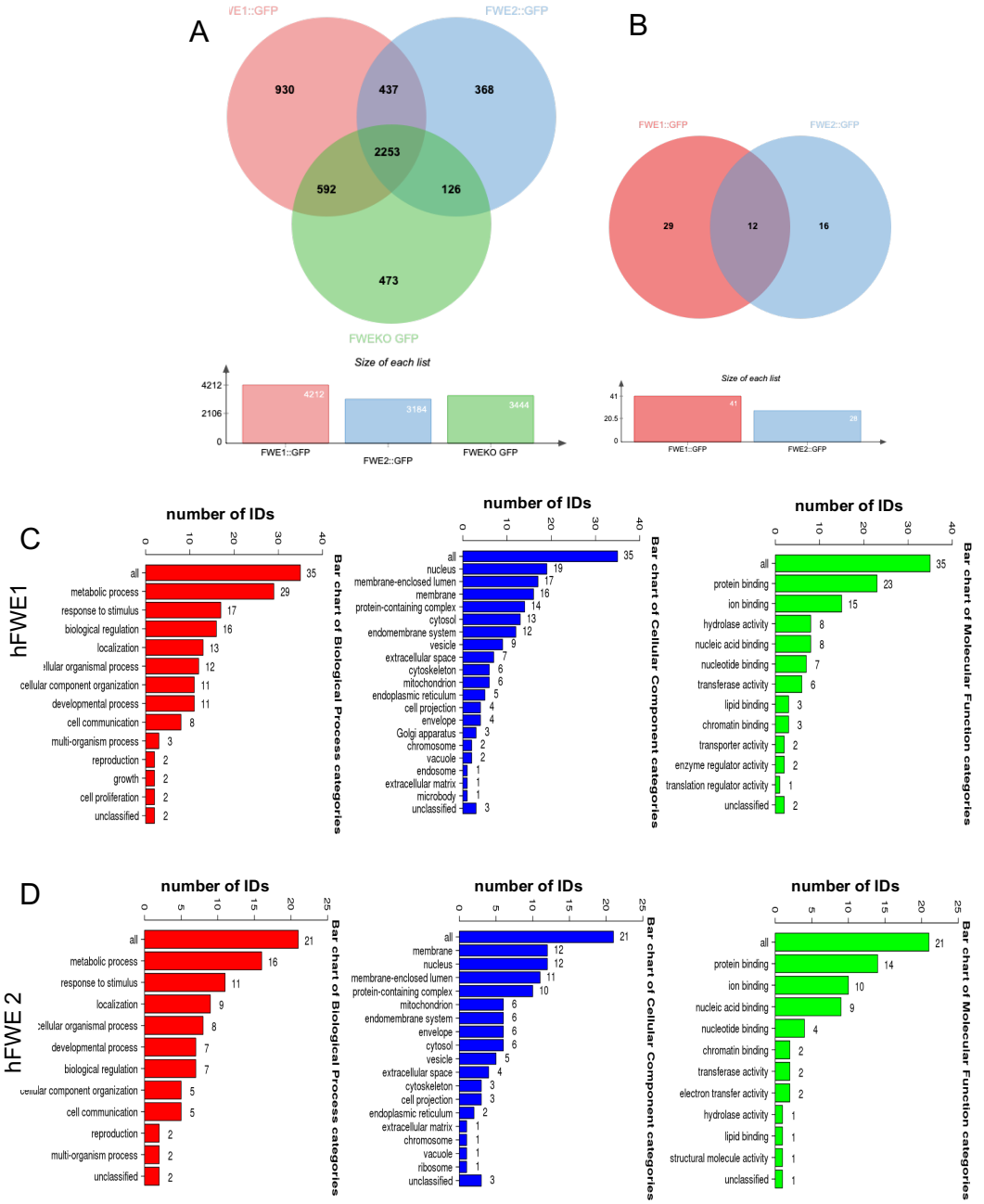


**Figure 2 - Venn diagram and enrichment analysis of identified Mass Spec proteins. A)** Venn diagram represents all the binding proteins from each sample tested and the relation between the groups. To identify proteins immunoprecipitated

with hFWE, IP products were analyzed by Mass Spec. Identification of the binding proteins was performed using Thermo Proteome Discoverer software. **B)** Representation of the number of proteins that specifically binds to $hFWE^{Lose}$ (pink) and $hFWE^{Win}$ (blue) isoforms. The common protein between both was also represented in the Veen diagram. **C) & D)** Classification of identified proteins based on their biological process, cellular component, and molecular function. Analysis performed by WebGestalt software.

The final list of the most promising candidates was the following: for HCT $116^{hFWE1::GFP}$ (Lose) expressing cells, we identified 41 candidates (Figure 2 – B) and 28 candidates for HCT $116^{hFWE2::GFP}$ (Win) cells (Figure 2 – B). We also observed that these two hFWE isoforms shared 12 common proteins (Figure 2 – B; Table 3). There are 23 proteins specifically found in HCT $116^{hFWE1::GFP}$ (Lose) (Table 1) and 16 proteins that specifically bind to HCT $116^{hFWE2::GFP}$ (Win) (Table 2).

The biological significance of these proteins, including the biological process, cellular component, and molecular function, was analyzed using WebGestalt software. Most hFWE1 and hFWE2 binding proteins, in terms of biological process, belong to metabolic process, response to stimulus and localization, biological regulation, and multicellular organismal process. Related to the cellular component, for hFWE1, most are nuclear, membrane-enclosed lumen, and membranal protein. While for hFWE2 is mainly membrane protein, followed by nucleus protein and then membrane-enclosed lumen. The molecular function of both hFWE isoforms, belongs to protein binding and ion binding (Figure 2 – C; D).

**Table 1 -** List of proteins that were uniquely identified in hFWE$^{Lose}$ cells

| Gene Symbol | Description |
|---|---|
| RLTPR; CARMIL2 | Capping protein, Arp2/3 and myosin-I linker protein 2 |
| HINT2 | Histidine triad nucleotide-binding protein 2 |
| ATP2B4 | Plasma membrane calcium-transporting ATPase 4 |
| INTS2 | Integrator complex subunit 2 |
| SMEK2; PPP4R3B | Serine/threonine-protein phosphatase 4 regulatory subunit 3B |
| CHAF1A | Chromatin assembly factor 1 subunit A |
| LYPLA2 | Acyl-protein thioesterase 2 |
| DPP7 | Dipeptidyl peptidase 2 |
| TP53RK | EKC/KEOPS complex subunit TP53RK |
| DYRK1A | Dual-specificity tyrosine-phosphorylation-regulated kinase 1A |
| RNF213 | E3 ubiquitin-protein ligase RNF213 |
| STARD7 | StAR-related lipid transfer protein 7 |
| ARRDC1 | Arrestin domain-containing protein 1 |
| GDF15 | Growth/differentiation factor 15 |
| PKP3 | Plakophilin-3 |
| ADI1 | 1,2-dihydroxy-3-keto-5-methylthiopentene dioxygenase |
| UBE2G1 | Ubiquitin-conjugating enzyme E2 G1 |
| SBF1 | Myotubularin-related protein 5 |
| SCD | Acyl-CoA desaturase |
| SLC4A1AP | Kanadaptin |
| GSE1 | Genetic suppressor element 1 |
| IDI1 | Isopentenyl-diphosphate Delta-isomerase 1 |
| ALG5 | Dolichyl-phosphate beta-glucosyltransferase |
| CYCS | Cytochrome c |
| PDCD6 | HCG1985580, isoform CRA_c |
| CDH3 | Cadherin-3 |
| FIP1L1 | Pre-mRNA 3'-end-processing factor FIP1 |
| ABHD10 | Mycophenolic acid acyl-glucuronide esterase |
| TRIM32 | E3 ubiquitin-protein ligase TRIM32 |

**Table 2 -** List of proteins that were uniquely identified in hFWE$^{Win}$ cells

| Gene Symbol | Description |
|---|---|
| BPTF | Nucleosome-remodeling factor subunit BPTF |
| WDR33 | pre-mRNA 3' end processing protein WDR33 |
| VPS28 | Vacuolar protein sorting-associated protein 28 homolog |
| MDK | Midkine |
| BTAF1 | TATA-binding protein-associated factor 172 |
| CHCHD2P9 | Putative coiled-coil-helix-coiled-coil-helix domain-containing protein |
| LYPLA1 | Acyl-protein thioesterase 1 |
| MAOB | Amine oxidase [flavin-containing] B |
| GTF3C1 | General transcription factor 3C polypeptide 1 |
| UQCRQ | Cytochrome b-c1 complex subunit 8 |
| NUDT1 | 7,8-dihydro-8-oxoguanine triphosphatase |
| B2M | Beta-2-microglobulin |
| CAST | Calpastatin |
| PROSC; PLPBP | Pyridoxal phosphate homeostasis protein |
| RPS10 | 40S ribosomal protein S10 |
| PTMA | Prothymosin alpha |

**Table 3 -** List of common proteins between hFWE$^{Lose}$ and hFWE$^{Win}$ cells

| Gene Symbol | Description |
|---|---|
| ACSL5 | Long-chain-fatty-acid--CoA ligase 5 |
| SREK1IP1 | Protein SREK1IP1 |
| ALDOC | Fructose-bisphosphate aldolase C |
| FABP5 | Fatty acid-binding protein 5 |
| CKMT1B; CKMT1A | Creatine kinase U-type |
| RNMT | mRNA cap guanine-N7 methyltransferase |
| RP9 | Retinitis pigmentosa 9 protein |
| SFPQ | Splicing factor, proline- and glutamine-rich |
| PALLD | Palladin |
| ATAD3B | ATPase family AAA domain-containing protein 3B |
| NONO | Non-POU domain-containing octamer-binding protein |
| CAPG | Macrophage-capping protein |

### 3.4.3 PTMA IS REQUIRED FOR CELL COMPETITION

We decided to focus on the proteins that interact specifically with hFWE$^{Win}$ because it is the isoform overexpressed in cancer tissue. By studying the cancer cell interactors, we intended to understand how cancer cells can use the FWE code to grow and invade new tissue. To select the most promising candidates, we first excluded from the list, all the protein that binds to GFP. Knowing that FWE is a transmembrane protein, we eliminate all the proteins not localized in the cytoplasm or in the cell membrane.

Under curiosity, we analyzed by qPCR the expression levels of these candidates in the HCT 116 cell line and HCT 116 *hFWE$^{KO}$* cells (Figure 3 - A). Two proteins (PTMA and CAST) were less expressed in the absence of hFWE compared with WT cells and one was overexpressed in the winner's cells (PTMA). After reviewing the literature on these two candidates (PTMA and CAST), we selected PTMA since it is known that it is associated with cellular proliferation and carcinogenesis and is involved in the negative regulation of the apoptotic process[18–21]. Furthermore, according with the qPCR analises, the expression levels of PTMA it's regulated by hFWE.

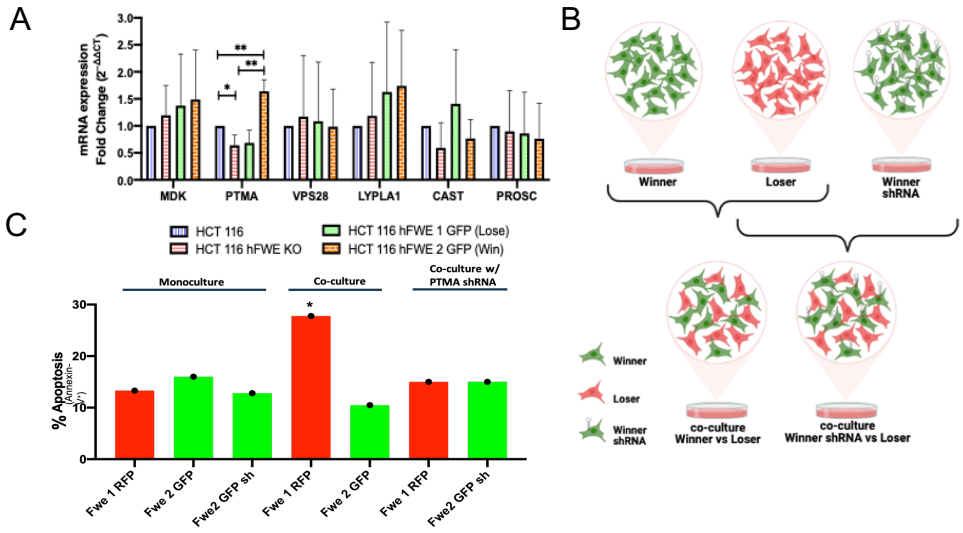

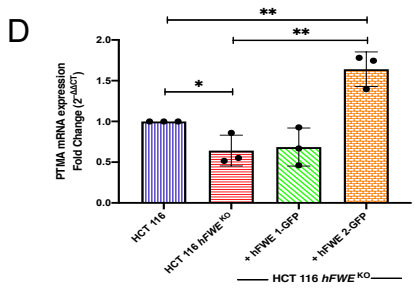


**Figure 3 - Functional Role of PTMA in Cell Competition. A)** Differential expression levels of the most promising candidates in the presence and absence of the hFWE protein (HCT 116 and HCT 116 *hFWE*$^{KO}$ cells, respectively). **B)** Functional analysis scheme protocol: HCT 116 *hFWE*$^{KO + hFWE1\text{-}RFP}$ cells and HCT 116 *hFWE*$^{KO + hFWE2\text{-}GFP}$ cells were co-cultured in equal amounts for 48h. In parallel, HCT 116 *hFWE*$^{KO + hFWE1\text{-}RFP}$ (+ scramble shRNA) and HCT 116 *hFWE*$^{KO + hFWE2\text{-}GFP}$ + PTMA shRNA were also co-cultured in the same condition as well as the respective monocultures. **C)** The downregulation of PTMA expression in the Winner cells blocked cell competition. Winners' cells no longer induced the dead of the Losers cells. **D)** The expression levels analysis of PTMA by qPCR showed that PTMA is overexpressed in Winner cells and less expressed in the absence of hFWE protein (*hFWE KO* cells).

To understand if PTMA plays a role in cell competition based on the FWE code, we performed the competition assay described in Madan *et al* 2019. Co-culture between HCT 116 *hFWE*$^{KO + hFWE1\text{-}RFP}$ (Lose isoform) and HCT 116 *hFWE*$^{KO + hFWE2\text{-}GFP}$ (Win isoform) were performed. In parallel, we co-culture HCT 116 *hFWE*$^{KO + hFWE1\text{-}RFP}$ + scramble shRNA with HCT 116 *hFWE*$^{KO + hFWE2\text{-}GFP}$ + PTMA shRNA, with the respective monoculture for 48h (Figure 3 - B). We analyze the apoptosis level using Annexin V protocol 48h after the co-culture. The downregulation of PTMA in the Winner cells protected the Losers from elimination and blocked cell competition, suggesting that PTMA is necessary for competition (Figure 3 - C). Interestingly, when analyzing the expression levels of PTMA by qPCR, we observed that PTMA is overexpressed in Winner cells compared with *KO* or *WT* cells. Suggesting a correlation between PTMA and hFWE$^{Win}$ expression (Figure 3 - D).

### 3.4.4 PTMA SUB-CELLULAR LOCATION SHIFTS ACCORDING TO HFWE ISOFORMS

It is known that PTMA can localize in the cytoplasm or the nucleus, and this difference in the subcellular location can be related to its role in a particular tissue. We analyzed the subcellular location of PTMA by immunofluorescence in HCT 116 cells, HCT 116 *hFWE*$^{KO}$ cells, and HCT 116 *hFWE*$^{KO + FWE2::GFP}$ cells using an anti-PTMA antibody. We observed that in the HCT 116 cells, PTMA localizes to the cytoplasm and the nucleus (Figure 4 - A). Interestingly, PTMA localization in HCT 116 *hFWE*$^{KO}$ cells shifts to the nucleus from the cytoplasm (Figure 4 - B). When we analyzed the subcellular localization of PTMA in cells overexpressing hFWE$^{Win}$, we observed a strong cytoplasmic localization compared with the *KO* and *WT* cells (Figure 4 - C). These data suggest that PTMA might be kept in the cytoplasm in cancer cells expressing hFWE$^{Win}$ to help them grow and expand.

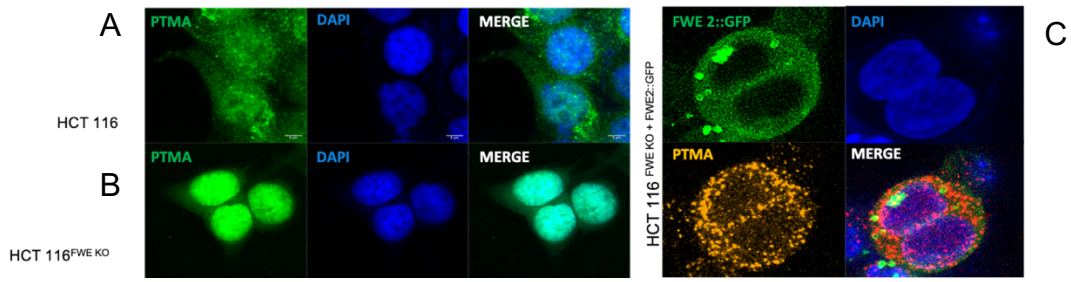


**Figure 4 - Sub-cellular localization of PTMA in colon cell line by Immunofluorescent using an anti-PTMA Ab. A)** PTMA sub-cellular localization in HCT 116 cells is distributed in the nucleus and cytoplasm, but mainly in the nucleus. **B)** In HCT 116 *hFWE*$^{KO}$ cells, PTMA has a strong localization in the nucleus compared with the cytoplasm. **C)** In the HCT 116 *hFWE*$^{KO + hFWE2::GFP}$ the sub-cellular localization is mainly in the cytoplasm and poorly in the nucleus.

### 3.4.5 PTMA EXPRESSION IN HUMAN CRC BIOPSIES

To investigate the expression of PTMA in patient sample, we performed immunohistochemistry in CRC and normal tissue using anti-PTMA Ab (Figure 5). In the normal colon, PTMA was expressed in the nucleus and in the cytoplasm of the epithelial cells, diffusely distributed along the mucosa (Figure 7) in all samples analyzed. Staining intensity was minimal for the cytoplasm and mild in the nucleus. Expression in stromal cells was rare.

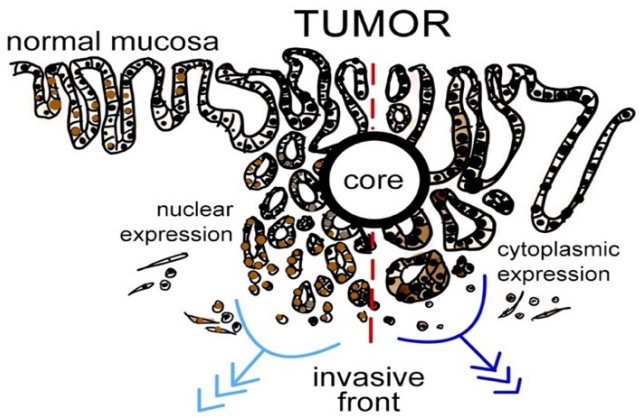


**Figure 5 - Features of PTMA protein expression, analyzed in human CRC biopsies.** Parameters analyzed: presence/absence of PTMA expression in the tumor; distribution in cellular compartments: nuclear, cytoplasmic and both; staining intensity; and distribution within the tumor, i.e., tumor core and/or tumor border (invasive front).

In human CRC, 73% of the tumors in our sample were positive for PTMA, and 67% showed exclusive nuclear PTMA expression (Figure 6). Expression levels were generally higher than in normal mucosa, with staining intensity varying from mild to marked (Figure 6). However, the staining pattern was rarely diffuse and homogeneous throughout the tumor. Instead, the pattern was multifocal or patchy, with positive and negative areas admixed (Figure 7 - F), with tumors where most cells

expressed PTMA (Figure 7 - B; F), and others with low expression levels (Figure 7 - C; G).

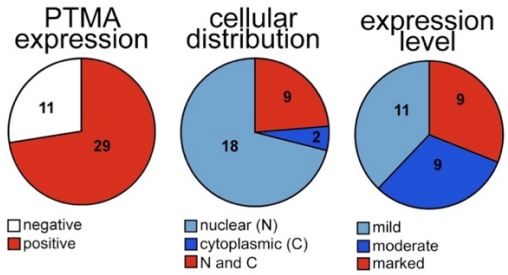


**Figure 6 - PTMA protein expression in human CRC biopsies.** PTMA expression was seen in 29 out of 40 CRC samples analyzed (73%), and staining intensity (expression levels) varied from mild to marked. Distribution was predominantly nuclear, occasionally nuclear and cytoplasmic, and rarely restricted to the cytoplasm.

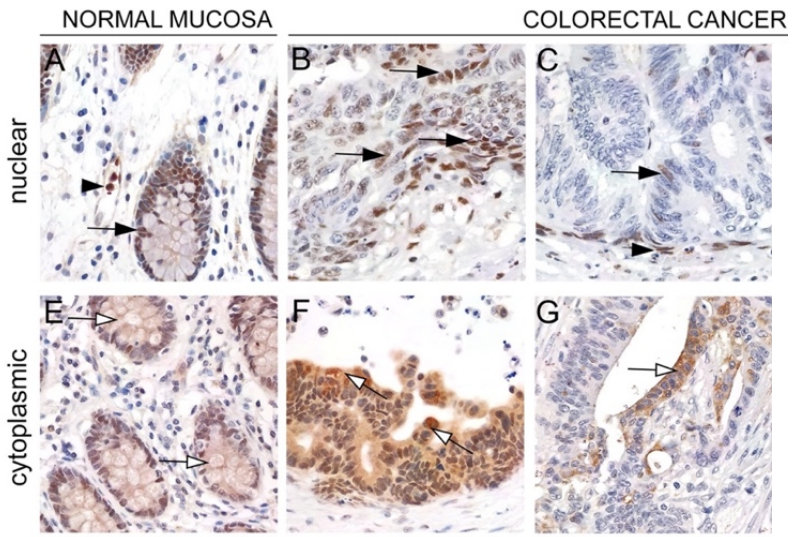


**Figure 7 - Representative microphotographs PTMA immunohistochemistry in human samples of colorectal carcinoma. A)** PTMA expression in the nucleus of

colonocytes, in normal mucosa in the margin of CRC (black arrow). **B)** CRC with PTMA nuclear expression in most tumor cells (black arrow) and with marked staining intensity. **C)** CRC with PTMA nuclear expression in a few tumor cells (black arrow), with moderate staining intensity and with PTMA expression also in the nucleus of tumor-associated fibroblasts (black arrowhead). **E)** PTMA expression in the cytoplasm of colonocytes, in normal mucosa in the margin of CRC (white arrow). **F)** CRC with PTMA marked and diffuse PTMA expression in tumor cells (white arrow). **G)** CRC with patchy PTMA cytoplasmic expression in fewer tumor cells (white arrow), with moderate staining intensity. *DAB counterstained with Harris Hematoxylin; original magnification, 40x.*

Another finding was that in 59% of CRC samples, there was a discrepancy in staining intensity and/or percentage of PTMA-positive cells when comparing the tumor core and tumor border (invasive front). PTMA expression was higher in tumor invasive front (Figure 8), with an expression of higher levels of PTMA, PTMA expression in a higher percentage of cells, or both.

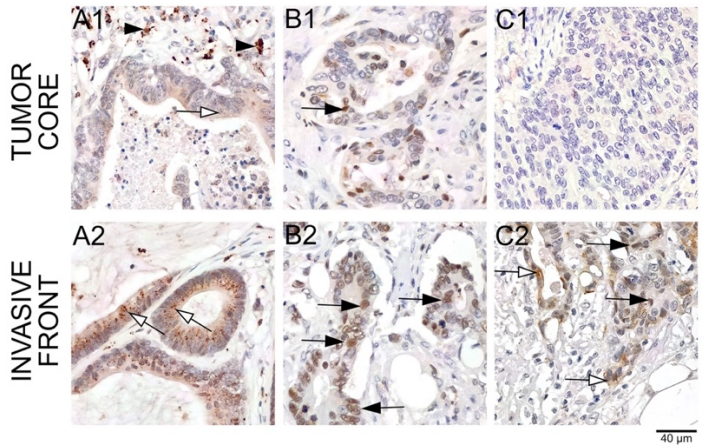


**Figure 8 - Representative microphotographs of PTMA expression in tumor core and invasive front in human colorectal carcinoma**. **A)** CRC with cytoplasmic PTMA expression (white arrow), where tumor cells in the invasive front show

increased PTMA expression levels with higher staining intensity. Stromal cells were also seen to express PTMA (black arrowhead). **B)** CRC with nuclear PTMA expression (black arrow), with a higher number of PTMA-positive cells in the invasive front. **C)** CRC, where PTMA is almost exclusively expressed in the nucleus (black arrow) and cytoplasm (white arrow) of tumor cells in the invasive front. *A, B, and C correspond to three different tumors; 1 and 2 correspond to the tumor core and invasive front, respectively). DAB counterstained with Harris Hematoxylin; original magnification, 40x*

## 3.5 DISCUSSION

The transmembrane protein Flower plays a role in specific biological processes. There are four isoforms of hFlower, which differ in their structure and function. Our group demonstrated that human Flower isoforms 1 and 3 (hFWE1 and hFWE3) function as Flower-Lose proteins, while hFWE2 and hFWE4 act as Flower-Win proteins. Cancer cells express high levels of $hFWE^{Win}$ (hFWE2 and hFWE4), giving them a competitive advantage to grow and kill surrounding stroma cells expressing $hFWE^{Lose}$ isoforms[7,10]. Understanding the mechanisms of cell competition based on FWE code and its role in cancer may provide new insights into the development and progression of tumors.

In this study, we aimed to identify new players in the CC mechanism mediated by the hFWE protein. We performed Immunoprecipitation followed by Mass Spectrometry (Mass Spec) to identify proteins interacting with hFWE since protein-protein interactions (PPIs) can provide insight into specific biological pathways. We identified that Prothymosin α (PTMA) interacts specifically with hFWE2, and its expression seems FWE-dependent. PTMA is more expressed in HCT116 colon cell lines overexpressing hFWE2 - the isoform overexpressed in cancer tissue. On the other hand, its expression is significantly reduced in hFWE1 and $hFWE^{KO}$ cells. Several studies have shown that PTMA is more abundant in cancer compared with normal tissue. Interestingly, it is also involved in a range of biological processes such as cell proliferation as observed in several types of cancer and apoptosis[14,22–25]. Therefore, the correlative expression profile between $hFWE^{Win}$ – expressed in cancer cells and PTMA observed by qPCR agrees with the tissue expression and functional profile database.

Moreover, when using a PTMA shRNA to downregulate its expression in Winner cells co-cultured with Lose-expressing cells, PTMA was necessary for CC to occur, and Winners no longer induced the death of the Loser cells. We also observed that PTMA subcellular localization shifts from the nucleus in $hFWE^{KO}$ to the cytoplasm in the winner cells. Different cell types may influence how PTMA functions, as its

expression and localization may change in response to external stimuli and signal transduction pathways. It is found in the nucleus and the cytoplasm of the cells. In the cytoplasm, PTMA regulates translation, cell division, and negative regulation of proapoptotic pathways by inhibiting apoptosome formation[18,21,26,27].

Interestingly, PTMA has been identified as a novel cancer biomarker (oncogene), as its expression is increased in various cancer types, including colorectal cancer[18,20]. PTMA likely helps to predict CRC prognosis by measuring the expression of both PTMA and mutant TP53[18]. The malignant phenotype of colorectal cancer is linked to the high PTMA expression in the tumor. Loss- and gain-of-function assays showed that circ-0004277 (oncogene in CRC) leads to tumor cell proliferation and inhibition of apoptosis. circ-0004277 promotes colorectal cancer proliferation by sponging miR-512-5p to upregulate the expression of PTMA in the CRC cells[20]. Finally, PTMA has been investigated for its potential therapeutic use in various diseases, such as cancer. Here, we propose that hFWE$^{Win}$ is sequestering PTMA, and keeping it in the cytoplasm, helping cancer grow and invade new tissue. Ongoing studies are exploring a possible correlation between PTMA expression pattern and clinicopathological parameters, such us tumor size, tumor stage, disease progression, recurrence, treatment response, and metastases.

### 3.6 REFERENCES


1. Levayer, R., Hauert, B. & Moreno, E. Cell mixing induced by myc is required for competitive tissue invasion and destruction. *Nature* **524**, 476–480 (2015).
2. Merino, M. M. *et al.* Elimination of Unfit Cells Maintains Tissue Health and Prolongs Lifespan. *Cell* **160**, 461–476 (2015).
3. Moreno, E. & Rhiner, C. Darwin's multicellularity: from neurotrophic theories and cell competition to fitness fingerprints. *Curr. Opin. Cell Biol.* **31**, 16–22 (2014).
4. Rhiner, C. *et al.* Flower Forms an Extracellular Code that Reveals the Fitness of a Cell to its Neighbors in Drosophila. *Dev. Cell* **18**, 985–998 (2010).
5. Vincent, J.-P., Fletcher, A. G. & Baena-Lopez, L. Al. Mechanisms and mechanics of cell competition in epithelia. *Nat. Rev. Mol. Cell Biol.* **14**, 581–591 (2013).
6. Parker, T. M. *et al.* Cell competition in intratumoral and tumor microenvironment interactions. *EMBO J.* **40**, (2021).
7. Camacho, D. *et al.* SPARC-p53: The double agents of cancer. in *Advances in Cancer Research* vol. 148 171–199 (Elsevier, 2020).
8. Madan, E. *et al.* Flower isoforms promote competitive growth in cancer. *Nature* **572**, 260–264 (2019).
9. Merino, M. M., Rhiner, C., Portela, M. & Moreno, E. "Fitness Fingerprints" Mediate Physiological Culling of Unwanted Neurons in Drosophila. *Curr. Biol.* **23**, 1300–1309 (2013).
10. Madan et al. - 2019 - Flower isoforms promote competitive growth in canc.pdf.
11. Vanneste, E. *et al.* Chromosome instability is common in human cleavage-stage embryos. *Nat. Med.* **15**, 577–583 (2009).
12. Kennedy, S. R., Loeb, L. A. & Herr, A. J. Somatic mutations in aging, cancer and neurodegeneration. *Mech. Ageing Dev.* **133**, 118–126 (2012).
13. Karetsou, Z. Prothymosin alpha modulates the interaction of histone H1 with chromatin. *Nucleic Acids Res.* **26**, 3111–3118 (1998).

14. Eschenfeldt, W. H. & Berger, S. L. The human prothymosin alpha gene is polymorphic and induced upon growth stimulation: evidence using a cloned cDNA. *Proc. Natl. Acad. Sci.* **83**, 9403–9407 (1986).

15. Ha, S. Y., Song, D. H., Hwang, S. H., Cho, S. Y. & Park, C.-K. Expression of prothymosin α predicts early recurrence and poor prognosis of hepatocellular carcinoma. *Hepatobiliary Pancreat. Dis. Int.* **14**, 171–177 (2015).

16. Jiang, G., Yu, H., Li, Z. & Zhang, F. lncRNA cytoskeleton regulator reduces non-small cell lung cancer radiosensitivity by downregulating miRNA-206 and activating prothymosin α. *Int. J. Oncol.* **59**, 88 (2021).

17. Magdalena, C., Dominguez, F., Loidi, L. & Puente, J. L. Tumour prothymosin alpha content, a potential prognostic marker for primary breast cancer. *Br. J. Cancer* **82**, 584–590 (2000).

18. Zhang, M. *et al.* Increased expression of prothymosin-α, independently or combined with TP53, correlates with poor prognosis in colorectal cancer. *Int. J. Clin. Exp. Pathol.* **7**, 4867–4876 (2014).

19. Chen, K. *et al.* Prothymosin-α and parathymosin expression predicts poor prognosis in squamous and adenosquamous carcinomas of the gallbladder. *Oncol. Lett.* (2018) doi:10.3892/ol.2018.7824.

20. Yang, L. *et al.* Circular RNA hsa_circ_0004277 contributes to malignant phenotype of colorectal cancer by sponging miR-512-5p to upregulate the expression of PTMA. *J. Cell. Physiol.* jcp.29484 (2020) doi:10.1002/jcp.29484.

21. Jiang, X. *et al.* Distinctive Roles of PHAP Proteins and Prothymosin-α in a Death Regulatory Pathway. *Science* **299**, 223–226 (2003).

22. Malicet, C. *et al.* Regulation of apoptosis by the p8/prothymosin α complex. *Proc. Natl. Acad. Sci.* **103**, 2671–2676 (2006).

23. Enkemann, S. A., Wang, R.-H., Trumbore, M. W. & Berger, S. L. Functional discontinuities in prothymosin ? caused by caspase cleavage in apoptotic cells. *J. Cell. Physiol.* **182**, 256–268 (2000).

24. Ueda, H., Fujita, R., Yoshida, A., Matsunaga, H. & Ueda, M. Identification of prothymosin-α1, the necrosis–apoptosis switch molecule in cortical neuronal cultures. *J. Cell Biol.* **176**, 853–862 (2007).

25. Fujita, R. & Ueda, H. Prothymosin-α1 prevents necrosis and apoptosis following stroke. *Cell Death Differ.* **14**, 1839–1842 (2007).

26. Evstafieva, A. G. *et al.* Apoptosis-related fragmentation, translocation, and properties of human prothymosin alpha. *Exp. Cell Res.* **284**, 209–221 (2003).

27. Lal, A., Kawai, T., Yang, X., Mazan-Mamczarz, K. & Gorospe, M. Antiapoptotic function of RNA-binding protein HuR effected through prothymosin α. *EMBO J.* **24**, 1852–1862 (2005).

# CHAPTER 4

# General Discussion

Cell competition is a process that takes place when cells with different fitness levels compete for survival within a tissue. First described in *Drosophila*, more fit cells typically have a competitive advantage over less fit cells, which leads to their propensity to survive and multiply faster. This process is a way for tissues to maintain health and function. It is a crucial process that promotes tissue health and prevents the spread of harmful mutations[1–6].

According to earlier studies in the *D. melanogaster*, the decision between cell survivor or death during cell competition is due to different expressions of the FWE isoforms on the surface of the cells[6]. The isoforms that codify an unfit marker are called Lose because cells are marketed to be eliminated when in contact with FWE Win-expressing cells. Cell competition in *Drosophila* can have important implications during development, tissue homeostasis, and disease[2,3,6]. Abnormal cell competition can contribute to developing cancer and other diseases - highlighting the importance of understanding the mechanisms underlying this process[3].

The research described in this thesis is based on these previous observations and aims to understand whether a comparable FWE system was conserved in humans. We demonstrate that two human Flower isoforms, hFWE1 and hFWE3, function as Flower-Lose proteins, whereas hFWE2 and hFWE4 act as Flower-Win proteins (Chapter 2). The human Flower protein code mediates competitive interactions dependent on cell contact and caspase-dependent apoptosis but independent of calcium transport. Homogeneous expression levels of any of the four Flower proteins do not trigger cell elimination nor affect cell fitness. hFWE Win provides cells an advantage over cells expressing Lose isoforms[3].

Furthermore, in the presence of stroma cells (that express hFWE Lose), cancer cells express higher levels of Win isoform, giving them a competitive growth advantage. We also saw that when the expression of Flower proteins is inhibited, there is a reduction in tumor growth and metastasis and an increase in chemotherapy

sensitivity. Overall, in Chapter 2, we demonstrated that ancient cell recognition and selection mechanisms are conserved in humans[3].

These finds have an essential impact on the cancer fight since it suggests an FWE code-based mechanism that helps cancer cells to grow and eliminate surrounding tissue. To understand this mechanism that triggers the elimination of neighbors, Loser-cells, we identified proteins interacting with the Winner and Loser isoforms and studied their role during cell competition (Chapter 3). We listed several proteins that bind to both isoforms. We saw that PTMA binds specifically to hFWE Win, and its expression is higher when compared with WT cells and poorly expressed in $hFWE^{KO}$ cells. The downregulation of this gene in the Winners prevented Loser cells elimination - blocking FWE-dependent cell competition. We also observed that PTMA subcellular localization shifts from the nucleus in $hFWE^{KO}$ to the cytoplasm in the winner cells. Moreover, in patient-derived samples, PTMA is expressed in cancer tissue and absent in normal tissue. These results suggest an FWE-PTMA interaction to promote cancer growth and progression (Chapter 3).

The significant discoveries made in this thesis prompted a comprehensive analysis and speculation that can be segmented into several distinct categories:

### 4.1 Human Flower isoforms act as Fitness Fingerprints

According to our findings, in humans, there are four isoforms of FWE: hFWE1, hFWE2, hFWE3, and hFWE4. To investigate which hFWE isoforms function as a Win or Lose during cell competition, co-culture between all possible combinations was performed using a GFP or RFP marker. We found that when human cells expressing hFWE1 or hFWE3 are in contact with cells expressing hFWE2 or hFWE4, they are always eliminated. In contrast, hFWE2 or hFWE4-expressing cells divide and grow, taking the space previously occupied by the unfit Loser cells. Therefore, cells that express hFWE1 and hFWE3 are the Lose isoforms, while cells that express hFWE2

and hFWE4 are the Win isoforms in humans. Direct contact between Winner and Loser cells is required for Loser cells elimination[1,3].

Interestingly, Fitness Fingerprints were reported to be tissue specific. While Fwe loseA or Fwe loseB expression is necessary to trigger loser cell elimination in the epithelia of the Drosophila wing disc, in neuronal cells Fwe loseA isoform does not correspond a loser marker (more)[4,6-8]. FWE is also conserved in mammals. In mice, FWE encodes four isoforms: mFwe1, mFwe2, mFwe3, and mFwe4, all transmembrane proteins. The human homologue of Flower (hFWE) has been researched and described for the first time by our group[3]. Like mFwe, hFWE encodes four distinct isoforms that are all predicted to be membrane proteins. Human orthologs of Flower (Fwe; C9ORF7; calcium channel flower domain containing 1 (CACFD1) isoform also form a “Flower code”, suggesting that hFWE is functionally conserved in humans[1,3].

Many competition mediators are conserved from *Drosophila* to humans. Winner cells feature pro-survival and pro-kill signals, including over-activation of Myc or Ras oncogenes and inactivation of P53. Loser cells, such as those with low-Myc expression, exhibit Lose markers or a reduced fitness profile. They are only eliminated when surrounded by more competent neighboring cells[9].

Studies in *Drosophila* have shown that oncogenes such as dmyc or hyperactivation of the Wnt/Wingless pathway[10–15] induce competitive growth mediated by the Drosophila Flower isoforms[4,16]. To study the impact of hFWE Win and hFWE Lose in cancer growth, the expression levels of hFWE isoforms were analyzed by qPCR in cancer tissue, benign tumors, tumor adjacent to host tissue, and normal tissue.

All hFWE isoforms were poorly expressed in normal tissue. The expression of hFWE Win isoforms in tumor tissue was higher, while hFWE Lose isoforms were significantly upregulated in stromal tissue. In the same direction, it is known that

certain mouse Fwe (mFwe) isoforms are upregulated during skin carcinogenesis, especially in areas surrounding skin papilloma[5]. Additionally, mFwe-deficient mice display normal development, phenotype, and growth but have lower susceptibility to skin papilloma, suggesting a similar role of FWE in *Drosophila*, mice, and humans[5].

Based on the observation that cancer has high Win isoform expression and tend to grow in regions where Lose isoforms is highly expressed in tissue patient sample, we hypothesized that when we have high Lose expression in the host tissue and also high levels of Win in the tumor, it might result in more aggressive tumor phenotypes. To address this, MCF-7 (breast cancer cell line) $hFWE^{(1/2/3/4)\text{-}GFP}$ cells were injected in $mFwe^{KO}$ mice for tumor formation. When mouse breast tissue was enriched with hFWE1 and cancer cells carrying hFWE2 were injected into the breast, it developed a more aggressive tumor. In contrast, hFWE1 and hFWE3 expressing cells lost their tumorigenic potential when implanted on hFWE2 or hFWE4 expressing breast. Suggesting that high hFWE Win expression in the tumor and high expression of hFWE Lose in the surrounding tissue promotes cancer growth. Furthermore, the high Win expression in tumors is insufficient to stimulate oncogenic growth because high Win in the stroma prevents the growth of high Win-expressing tumors[3].

To examine the contribution of mFWE isoforms to tumorigenesis in the host tissue, we generated ectopic tumor xenografts using $hFWE^{KO}$ HCT-116 and MCF-7 cells overexpressing hFWE2 isoform in hind leg regions of $mFWE^{WT}$ and $mFWE^{KO}$ mice. As a result, both cell lines generated larger tumors in $mFWE^{WT}$ mice compared with $mFWE^{KO}$ mice. Meaning that hFWE win expressing cells gain growth advantage in $mFWE^{WT}$ mice since the mouse can express $hFWE^{Lose}$ in stromal tissue. Recalling our previous observation from patient samples showed that the $hFWE^{Lose}$ isoform is induced in the cells surrounding the tumor tissue[3].

We decided to determine whether the upregulation of hFweLose can be induced by cells expressing hFweWin isoforms. We subsequently co-cultured

hFWE2 expressing MCF- 7 hFWEKO cells with MCF-7WT cells and found increased expression of hFweLose in MCF-7WT cells compared with a monoculture of MCF-7WT cells. In addition, we analyzed mFwe isoform expression host tissue from mFweWT mice pre- and post-xenograft with MCF-7 hFWE2 expressing cells. The mouse tissue adjacent to the tumor showed a significant increase in mFweLose isoforms post-xenograft. Additionally, the ability of tumor cells overexpressing hFWEWin isoforms to generate xenografts was reinforced by the exogenous expression of hFWELose isoforms in the host tissue mFweKO mice. All these results suggest that FWEWin expression in tumor cells induces FWELose expression in neighboring normal cells[3].

### 4.2 UNCOVER THE THERAPEUTIC POTENTIAL OF ANTIBODIES TARGETING THE HFLOWER PROTEIN.

Using nude mice, we chose cell lines with higher $hFWE^{Win}$ expression (HCT-116: colon cancer cell line; and DU-145: prostate cancer cell line) and lower $hFWE^{Win}$ expression (CCL-218: colon cancer cell line; and OVCAR-8: ovarian cancer cell line) to examine their tumorigenic potential. Additionally, combined therapy of hFWE shRNA and chemotherapy was evaluated against the tumorigenic potential of those cancer cell lines to assess the therapeutic potential of hFWE gene knockdown[3].

Compared to CCL-218 and OVCAR8, the findings revealed that DU-145 and HCT-116 had a considerably stronger tumorigenic potential and produced larger tumors[3]. Contrary to hFWE shRNA or chemotherapy (fluorouracil 5-FU for colon[17]; cisplatin and docetaxel for prostate[18] and ovarian[19]) treated xenografts, control and scrambled shRNA-treated xenografts produced much larger tumors. Chemotherapy and hFWE shRNA combination therapy further suppressed carcinogenesis. Again, treating cell lines with hFWE shRNA and combining treatment with chemotherapy reduced the presence of metastasis. Thus, we conclude that hFWE proteins can significantly affect tumorigenicity, and we suggest that drugs that target Flower and/or

Flower complex may reduce cancer progression and metastasis[3,20]. This achievement represents a conceptual advance in understanding the role of cell fitness comparison in human cancer progression.

The Flower fitness comparison approach describes a specific biological mechanism for controlling oncogenic development and metastasis. Notably, it has also been demonstrated for the first time that targeting cell competition can be combined with chemotherapy as a potential treatment to prevent colon, ovarian, and prostate cancer growth and metastasis. Consequently, it serves to uncover the therapeutic potential of antibodies directed against flower-win and/or flower-lose or complex forms and their effects on tumorigenesis. Additionally, it supports a better understanding of the mechanisms of cell competition and the exchange of relative fitness between cells.

Expression of all hFWE isoforms is very low in normal body cells, which makes it a very suitable anti-cancer therapy target[3]. Two approaches can be undertaking to study the potential of an anti-hFWE antibody against cancer: the therapeutic arm and the chemo-prevention arm.

To identify the therapeutic and clinical relevance of this finding, preclinical trial of hFlower (hFWE) monoclonal and/or polyclonal Abs against cancer can be studied in mouse (small animal) and swine (large animal) models. Aiming is to check the efficacy of the novel anti-hFWE Abs in animal models and its potential as successful examples of cancer therapy, such as trastuzumab[21] and pertuzumab[22]. Therapies aiming to stop cancer development in its early stages and preventing progression favor patient outcome. Abs targeted to Flower win and lose isoforms may block the exchange of cell fitness information between cancer and normal neighboring cells, and prevent cancer cell proliferation and growth. In addition to a stand-alone therapy, we would be able to understand the synergistic effects of Flower Abs alongside standard chemotherapy treatment options.

Another aspect is studying the role of Flower code and cell competition in regulating oncogenesis and chemo-prevention. This specific goal will explore the potential of anti-hFWE Abs as chemo-preventive agents. Regular administration of these Abs in daily life might have the potential to block oncogenesis. One of the approaches to study this, would be to label PDX-derived cancer cells with GFP using a lentiviral expression system and then inject these cells in mice undergoing anti-Flower Ab treatment. IVIS imaging[23], and (18)F- Fluorodeoxyglucose positron emission tomography imaging (FDG-PET)[24,25] can be used to observe the efficacy of various anti-Flower Abs in preventing tumor formation.

Therefore, developing effective, novel, and innovative therapeutic strategies is fundamental. Our group is one of the first to understand the translational aspect of "cell competition" in human diseases, and this process is fundamental to oncogenesis and cancer progression[3,9].

### 4.3 THE IMPORTANCE OF STUDYING HFWE BINDING PROTEINS

Proteins that interact often work together to carry out critical cellular processes such as DNA replication, protein synthesis, and signaling pathways. By studying these interactions, we gain insights into how these processes work and how they are regulated. To better understand cell competition in humans and the mechanism responsible for triggering the elimination of the Losers, we investigated hFWE binding partners.

When immunoprecipitated $hFWE^{Win}$ and $hFWE^{Lose}$ followed by Mass Spec, we identified a list of proteins interacting with both isoforms. We found that PTMA interacts with $hFWE^{Win}$ and not with $hFWE^{Lose}$ isoform.

To answer whether PTMA has a functional role in cell competition, we downregulate its expression in the Winner cells using PTMA shRNA and co-culture with Lose-expressing cells. Since many proteins' functions requires interaction with other proteins, we aimed to understand if the interaction between $hFWE^{Win}$ and PTMA is necessary for Loser's elimination. As a result, the downregulation of PTMA stopped cell competition based on the FWE code. Meaning that $hFWE^{Win}$ requires PTMA to eliminate surrounding tissue and/or promote cancer growth and invade new tissue. Moreover, when we analyzed the expression levels of PTMA in HCT-116 $hFWE^{KO\ hFWE1\text{-}GFP}$, HCT-116 $hFWE^{KO\ hFWE2\text{-}GFP}$, HCT-116 $hFWE^{KO,}$ and HCT-116 WT, we saw that PTMA it is overexpressed in hFWE2 expressing cells compared with the control HCT-116 WT. Interestingly, the expression of PTMA in the absence of hFWE protein was significantly less. The data correlate hFWE absence with PTMA low expression and increased PTMA expression in $hFWE^{Win}$-expressing cells.

PTMA is known to be involved in transcription regulation, cell cycle, apoptosis, growth, and proliferation of the cells. PTMA is a protein involved in the negative regulation of the apoptotic process[26–28], and it is located in the nucleus and/or cytoplasm of the cells. In breast cancer tissue, PTMA concentration is higher when compared with normal breast tissue. It is already a prognostic marker for hepatocarcinoma, lung, breast, prostate, bladder and stomach cancer[29–34]. Overall, high levels of PTMA in cancer may be beneficial for maintaining a high proliferation rate and protecting these cells from apoptosis. Data shows that PTMA is overexpressed in cancer tissue including gastric, colorectal and thyroid cancer[35–38]. Therefore, we analyzed the expression of PTMA in colorectal cancer and the normal tissue from 40 patient samples. Again, the IHC data show more colorectal cancer expression than normal tissue. PTMA expression was also higher in tumor invasive front. Finally, PTMA has been investigated for its potential therapeutic use in various diseases, including cancer.

Different subcellular localization of PTMA lids to different functions. For instance, in the cytoplasm, PTMA is involved in more aggressive tumors and the

probability of rescuing and promoting cell growth. Subcellular localization studies also help to improve the comprehensiveness regarding the function of a protein. Hence, we performed Immunofluorescence using an Anti-PTMA antibody to study the subcellular location in HCT-116 WT, HCT-116 *hFWE*$^{KO}$, and HCT-116 *hFWE*$^{KO+\ hFWE2\text{-}GFP}$. We saw that in the HCT-116 WT cells, PTMA localizes both in the cytoplasm and the cell's nucleus. Interestingly, PTMA localization in HCT 116 *hFWE*$^{KO}$ cells shifts to the nucleus from the cytoplasm. When we analyzed the subcellular localization of PTMA in cells overexpressing *hFWE*$^{KO+\ FWE2::GFP}$ (Win), we observed a strong cytoplasmic localization compared with the *KO* and *WT* cells.

In Chapter 2 of this thesis, we show that hFWE$^{Win}$ is overexpressed in cancer tissue and poorly expressed in the surrounding tissue. Chapter 3 also shows that PTMA it is overexpressed in hFWE$^{Win}$ cells and less in *hFWE*$^{KO}$ and hFWE$^{Lose}$ cells. PTMA localized in the cytoplasm of the hFWE$^{Win}$ cells and the nucleus of *hFWE*$^{KO}$. Moreover, IHC data show more expression of PTMA in colorectal cancer patient samples when compared with normal tissue (same expression profile as hFWE$^{Win}$ in cancer). PTMA expression is increased in proliferating cells[39–41] and in response to increased levels of c-myc[42]. A correlation between PTMA and c-myc mRNA expression has been found in human colon cancers[43,44].

Hence, we show that hFWE$^{Win}$ is sequestering PTMA, and keeping it in the cytoplasm, helping cancer grow and invade new tissue. Although we do not know which mechanism or pathway is taking place. Based on the literature, we can hypostatize how hFWE$^{Win}$ and PTMA work together to promote cancer growth. circ-0004277 is an oncogene in CRC that contribute to tumor cell proliferation and apoptosis inhibition. Studies revealed that upregulated circ0004277 was observed in CRC tissues, and a high level of circ0004277 correlated with unfavorable prognosis in CRC patients. Interestingly, this oncogene sponges miR-512-5p (kwon to change the development and progression of cancer) to upregulate the expression of PTMA in the CRC cells[45] leading to the malignant phenotype described in CRC. The same study shows that both qPCR and subcellular fractionation assays used to analyze

circ-0004277 location indicated abundant circ-0004277 in the cytoplasm of HCT-116 and Lovo colon cell lines[45].

Thus, hFWE$^{Win}$ might use this system to upregulate circ0004277 in the cytoplasm, leading to miR-512-5p sponging and finally upregulation of PTMA (Figure 1) promoting cancer growth. To test this hypothesis, we can analyze by qPCR the expression levels of the circ-0004277 in hFWE$^{Win}$-expressing cells and see whether it is upregulated or not. We can also downregulate circ-0004277 expression in hFWE$^{Win}$ and analyze PTMA expression levels, expecting it to be lower. In the same line, we can study the subcellular localization of PTMA to see if there are changes in its location in hFWE$^{Win}$ cells when circ0004277 is downregulated. To investigate whether Win expressing cells with circ0004277 downregulated will induce Lose elimination, we can co-culture both cells and analyze the apoptosis level in these two cell populations. On the other hand, hFWE$^{Win}$ can also directly overexpress PTMA in the cancer tissue using an unknown mechanism (Working Model A).

Another interesting fact is that c-myc protein activates the transcription of the PTMA gene in CRC[42,43]. Therefore, PTMA transcription may be associated or under the control of the c-myc gene in human colorectal cancer[42,43]. Taking in consideration that FWE were discovered in a myc super competition scenario, in a microarray experiment in the drosophila wing imaginal disc for genes differentially expressed early in loser cells during competition[6], another hypothesis is that c-myc increases the expression of hFWE$^{WIN}$ in the cancer cell, leading to hight levels of PTMA, and consequently the death of the Losers cells, in a non-autonomous scenario. In an autonomous scenario, c-myc might interact with PTMA leading to the survivors and/or proliferation (known to be one of the functions of PTMA in the cells) of the cancer cells. We know from the results of the competition experiment using PTMA shRNA (chapter 3) that there is no difference in the apoptosis of the hFWE$^{WIN}$ compared to hFWE$^{WIN}$ PTMA shRNA in monoculture. Meaning that, here, PTMA do not have a cell survivor role because when downregulated, cell do not die more in comparation with cells that do not have PTMA downregulated. In terms of proliferation, experiments need to be done to understand whether the c-myc activates

PTMA transcription through hFWE$^{WIN}$, leading to proliferation of the cancer cells in an autonomous scenario. To test this hypothesis, we can downregulate c-myc in the cells and analyse the expression levels of hFWE$^{WIN}$ and PTMA, and, also evaluate the proliferation of the cells. Lost and gain function experiments might help us to comprehend the cascade signalling pathway between c-myc, hFWE$^{WIN}$ and PTMA leading to loser cells elimination (Working Model B).

Another experiment that can be performed to prove that hFWE$^{Win}$ is sequestering PTMA and keep it in the cytoplasm to help cancer growth, is investigate the Win expression levels by qPCR in patient cancer samples where IHC shows a more cytoplasmic expression of PTMA. Ongoing studies are exploring a possible correlation between PTMA expression pattern and clinicopathological parameters, like tumor size, histologic subtype, tumor grade, stage, disease progression, recurrence, treatment response, and metastases.

It will also be interesting to analyse if PTMA per se is sufficient to promote Win state in the cells. In order to test if PTMA is sufficient, we can perform a competition assay with WT cells in co culture with WT cells with PTMA downregulated and see if the WT cells will behave as a winner cell, and/or overexpress PTMA in the cells and perform the competition assay.

Understanding and controlling protein-protein communication is critical for advancing our understanding of biological processes and developing new treatments for various diseases.

**Working Model:**

**A)**

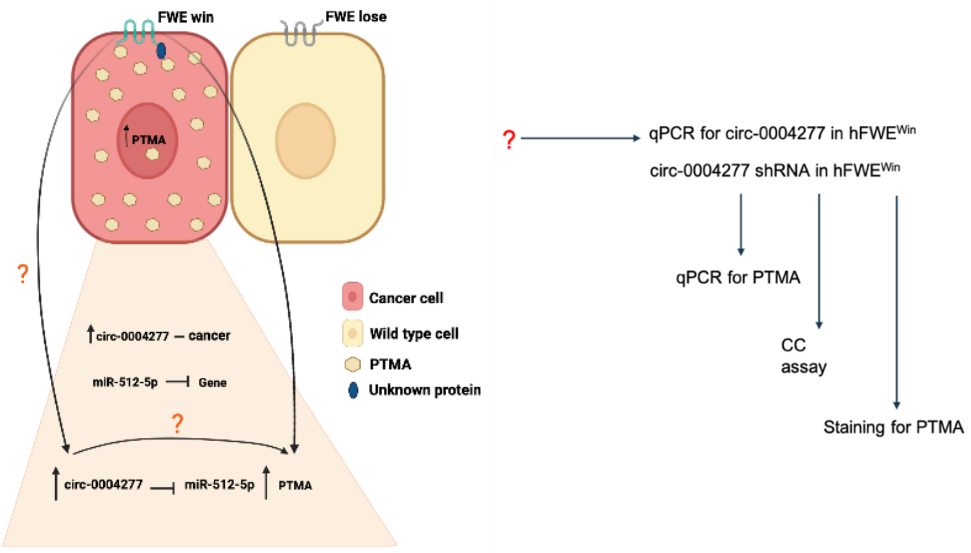


**B)**

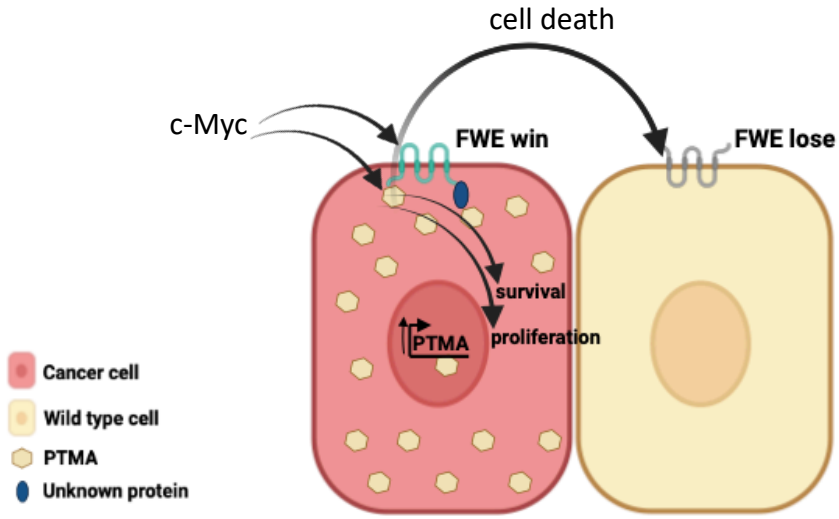

## 4.4 REFERENCES


1. Camacho, D. *et al.* SPARC-p53: The double agents of cancer. *Adv. Cancer Res.* **148**, 171–199 (2020).
2. Costa, C. M., Brás-Pereira, C. & Moreno, E. Cell Competition. in *eLS* (ed. John Wiley & Sons, Ltd) 661–671 (Wiley, 2020). doi:10.1002/9780470015902.a0028476.
3. Madan, E. *et al.* Flower isoforms promote competitive growth in cancer. *Nature* **572**, 260–264 (2019).
4. Merino, M. M. *et al.* Elimination of unfit cells maintains tissue health and prolongs lifespan. *Cell* **160**, 461–476 (2015).
5. Petrova, E., López-Gay, J. M., Rhiner, C. & Moreno, E. Flower-deficient mice have reduced susceptibility to skin papilloma formation. *Dis. Model. Mech.* dmm.008623 (2012) doi:10.1242/dmm.008623.
6. Rhiner, C. *et al.* Flower forms an extracellular code that reveals the fitness of a cell to its neighbors in Drosophila. *Dev. Cell* **18**, 985–998 (2010).
7. Merino, M. M., Rhiner, C., Portela, M. & Moreno, E. 'Fitness fingerprints' mediate physiological culling of unwanted neurons in Drosophila. *Curr. Biol. CB* **23**, 1300–1309 (2013).
8. Moreno, E., Fernandez-Marrero, Y., Meyer, P. & Rhiner, C. Brain Regeneration in Drosophila Involves Comparison of Neuronal Fitness. *Curr. Biol.* **25**, 955–963 (2015).
9. Gogna, R., Shee, K. & Moreno, E. Cell Competition During Growth and Regeneration. *Annu. Rev. Genet.* **49**, 697–718 (2015).
10. Bell, G. P. & Thompson, B. J. Colorectal cancer progression: Lessons from Drosophila? *Semin. Cell Dev. Biol.* **28**, 70–77 (2014).
11. Eichenlaub, T., Cohen, S. M. & Herranz, H. Cell Competition Drives the Formation of Metastatic Tumors in a Drosophila Model of Epithelial Tumor Formation. *Curr. Biol.* **26**, 419–427 (2016).

12. Suijkerbuijk, S. J. E., Kolahgar, G., Kucinski, I. & Piddini, E. Cell Competition Drives the Growth of Intestinal Adenomas in Drosophila. *Curr. Biol.* **26**, 428–438 (2016).

13. Vincent, J.-P., Kolahgar, G., Gagliardi, M. & Piddini, E. Steep Differences in Wingless Signaling Trigger Myc-Independent Competitive Cell Interactions. *Dev. Cell* **21**, 366–374 (2011).

14. de la Cova, C., Abril, M., Bellosta, P., Gallant, P. & Johnston, L. A. Drosophila myc regulates organ size by inducing cell competition. *Cell* **117**, 107–116 (2004).

15. Moreno, E. & Basler, K. dMyc transforms cells into super-competitors. *Cell* **117**, 117–129 (2004).

16. Levayer, R., Hauert, B. & Moreno, E. Cell mixing induced by myc is required for competitive tissue invasion and destruction. *Nature* **524**, 476–480 (2015).

17. Hadjal, Y., Hadadeh, O., Yazidi, Ce., Barruet, E. & Binétruy, B. A p38mapk-p53 cascade regulates mesodermal differentiation and neurogenesis of embryonic stem cells. *Cell Death Dis.* **4**, e737–e737 (2013).

18. Davies, A. H., Wang, Y. & Zoubeidi, A. Patient-derived xenografts: A platform for accelerating translational research in prostate cancer. *Mol. Cell. Endocrinol.* **462**, 17–24 (2018).

19. Chang, C.-E. *et al.* Novel application of pluronic lecithin organogels (PLOs) for local delivery of synergistic combination of docetaxel and cisplatin to improve therapeutic efficacy against ovarian cancer. *Drug Deliv.* **25**, 632–643 (2018).

20. Maruyama, T. & Fujita, Y. Cell competition in mammals - novel homeostatic machinery for embryonic development and cancer prevention. *Curr. Opin. Cell Biol.* **48**, 106–112 (2017).

21. Romond, E. H. *et al.* Trastuzumab plus Adjuvant Chemotherapy for Operable HER2-Positive Breast Cancer. *N. Engl. J. Med.* **353**, 1673–1684 (2005).

22. Swain, S. M. *et al.* Pertuzumab, Trastuzumab, and Docetaxel in HER2-Positive Metastatic Breast Cancer. *N. Engl. J. Med.* **372**, 724–734 (2015).

23. Kanzaki, S. *et al.* Novel In Vivo Imaging Analysis of an Inner Ear Drug Delivery System in Mice: Comparison of Inner Ear Drug Concentrations over Time after Transtympanic and Systemic Injections. *PLoS ONE* **7**, e48480 (2012).

24. Kim, J.-I. *et al.* Use of $^{18}$F-fluorodeoxyglucose positron emission tomography-computed tomography in a miniature pig (Sus scrofa domestica) with pneumonia. *Comp. Med.* **62**, 203–208 (2012).

25. Caporizzo, D. J. *et al.* Use of (18)F-fluorodeoxyglucose positron emission tomography-computed tomography to aid in diagnosing intestinal adenocarcinoma in 2 rhesus macaques (Macaca mulatta). *Comp. Med.* **64**, 211–220 (2014).

26. Chen, K. *et al.* Prothymosin-α and parathymosin expression predicts poor prognosis in squamous and adenosquamous carcinomas of the gallbladder. *Oncol. Lett.* (2018) doi:10.3892/ol.2018.7824.

27. Jiang, X. *et al.* Distinctive roles of PHAP proteins and prothymosin-alpha in a death regulatory pathway. *Science* **299**, 223–226 (2003).

28. Letsas, K. P. & Frangou-Lazaridis, M. Surfing on prothymosin alpha proliferation and anti-apoptotic properties. *Neoplasma* **53**, 92–96 (2006).

29. Magdalena, C., Dominguez, F., Loidi, L. & Puente, J. L. Tumour prothymosin alpha content, a potential prognostic marker for primary breast cancer. *Br. J. Cancer* **82**, 584–590 (2000).

30. Sasaki, H. *et al.* Expression of the prothymosin-a gene as a prognostic factor in lung cancer. *Surg. Today* **31**, 936–938 (2001).

31. Leys, C. M. *et al.* Expression and prognostic significance of prothymosin-alpha and ERp57 in human gastric cancer. *Surgery* **141**, 41–50 (2007).

32. Suzuki, S. *et al.* Expression of prothymosin alpha is correlated with development and progression in human prostate cancers. *The Prostate* **66**, 463–469 (2006).

33. Tzai, T.-S. *et al.* Urine prothymosin-alpha as novel tumor marker for detection and follow-up of bladder cancer. *Urology* **67**, 294–299 (2006).

34. Wu, C. G. *et al.* Overexpression of hepatic prothymosin alpha, a novel marker for human hepatocellular carcinoma. *Br. J. Cancer* **76**, 1199–1204 (1997).

35. Jou, Y.-C. *et al.* Prognostic relevance of prothymosin-alpha expression in human upper urinary tract transitional cell carcinoma. *Urology* **74**, 951–957 (2009).

36. Letsas, K. P., Vartholomatos, G., Tsepi, C., Tsatsoulis, A. & Frangou-Lazaridis, M. Fine-needle aspiration biopsy-RT-PCR expression analysis of prothymosin alpha and parathymosin in thyroid: novel proliferation markers? *Neoplasma* **54**, 57–62 (2007).

37. Wang, M. *et al.* Altered expression of estrogen receptor alpha and beta in advanced gastric adenocarcinoma: correlation with prothymosin alpha and clinicopathological parameters. *Eur. J. Surg. Oncol. J. Eur. Soc. Surg. Oncol. Br. Assoc. Surg. Oncol.* **33**, 195–201 (2007).

38. Zhang, M. *et al.* Increased expression of prothymosin-α, independently or combined with TP53, correlates with poor prognosis in colorectal cancer. *Int. J. Clin. Exp. Pathol.* **7**, 4867–4876 (2014).

39. Eschenfeldt, W. H. & Berger, S. L. The human prothymosin alpha gene is polymorphic and induced upon growth stimulation: evidence using a cloned cDNA. *Proc. Natl. Acad. Sci.* **83**, 9403–9407 (1986).

40. Gómez-Márquez, J. *et al.* The Expression of Prothymosin α Gene in T Lymphocytes and Leukemic Lymphoid Cells Is Tied To Lymphocyte Proliferation. *J. Biol. Chem.* **264**, 8451–8454 (1989).

41. Conteas, C. N. *et al.* Cellular levels of thymosin immunoreactive peptides are linked to proliferative events: evidence for a nuclear site of action. *Proc. Natl. Acad. Sci.* **87**, 3269–3273 (1990).

42. Eilers, M., Schirm, S. & Bishop, J. M. The MYC protein activates transcription of the alpha-prothymosin gene. *EMBO J.* **10**, 133–141 (1991).

43. Mori, M. *et al.* Prothymosin-alpha mRNA expression correlates with that of c-myc in human colon cancer. *Oncogene* **8**, 2821–2826 (1993).

44. Karetsou, Z. *et al.* Prothymosin alpha modulates the interaction of histone H1 with chromatin. *Nucleic Acids Res.* **26**, 3111–3118 (1998).

45. Yang, L. *et al.* Circular RNA hsa_circ_0004277 contributes to malignant phenotype of colorectal cancer by sponging miR-512-5p to upregulate the expression of PTMA. *J. Cell. Physiol.* jcp.29484 (2020) doi:10.1002/jcp.29484.

# Publications

Article

TRANSPARENT PROCESS OPEN ACCESS

EMBO Molecular Medicine

# Flower lose, a cell fitness marker, predicts COVID-19 prognosis

Michail Yekelchyk[1,†], Esha Madan[2,†], Jochen Wilhelm[3,4,‡], Kirsty R Short[5,‡], António M Palma[2,‡], Linbu Liao[6,‡], Denise Camacho[2], Everlyne Nkadori[7], Michael T Winters[8], Emily S Rice[8], Inês Rolim[2], Raquel Cruz-Duarte[9], Christopher J Pelham[10], Masaki Nagane[11], Kartik Gupta[12], Sahil Chaudhary[12], Thomas Braun[1,13], Raghavendra Pillappa[14], Mark S Parker[15], Thomas Menter[16], Matthias Matter[16], Jasmin Dionne Haslbauer[16], Markus Tolnay[16], Kornelia D Galior[7], Kristina A Matkwoskyj[7], Stephanie M McGregor[7], Laura K Muller[7], Emad A Rakha[17], Antonio Lopez-Beltran[2,18], Ronny Drapkin[19,20,21], Maximilian Ackermann[22,23], Paul B Fisher[24,25,26], Steven R Grossman[27,28], Andrew K Godwin[29,30], Arutha Kulasinghe[31], Ivan Martinez[8], Clay B Marsh[8], Benjamin Tang[32], Max S Wicha[33,34], Kyoung Jae Won[6,35], Alexandar Tzankov[16,*], Eduardo Moreno[2,**] & Rajan Gogna[2,6,35,***]

## Abstract

**Risk stratification of COVID-19 patients is essential for pandemic management. Changes in the cell fitness marker, *hFwe-Lose*, can precede the host immune response to infection, potentially making such a biomarker an earlier triage tool. Here, we evaluate whether *hFwe-Lose* gene expression can outperform conventional methods in predicting outcomes (e.g., death and hospitalization) in COVID-19 patients. We performed a post-mortem examination of infected lung tissue in deceased COVID-19 patients to determine *hFwe-Lose*'s biological role in acute lung injury. We then performed an observational study ($n = 283$) to evaluate whether *hFwe-Lose* expression (in nasopharyngeal samples) could accurately predict hospitalization or death in COVID-19 patients. In COVID-19 patients with acute lung injury, *hFwe-Lose* is highly expressed in the lower respiratory tract and is co-localized to areas of cell death. In patients presenting in the early phase of COVID-19 illness, *hFwe-Lose* expression accurately predicts subsequent hospitalization or death with positive predictive values of 87.8–100% and a negative predictive value of 64.1–93.2%. *hFwe-Lose* outperforms conventional inflammatory biomarkers and patient age and comorbidities, with an area under the receiver operating characteristic curve (AUROC) 0.93–0.97 in predicting hospitalization/death. Specifically, this is significantly higher than the prognostic value of combining biomarkers (serum ferritin, D-dimer, C-reactive protein, and neutrophil–lymphocyte ratio), patient age and comorbidities (AUROC of 0.67–0.92). The cell fitness marker, *hFwe-Lose*, accurately predicts outcomes in COVID-19 patients. This finding demonstrates how tissue fitness pathways dictate the response to infection and disease and their utility in managing the current COVID-19 pandemic.**

**Keywords** biomarker; cell fitness; COVID-19; flower; prognosis
**Subject Categories** Biomarkers; Microbiology, Virology & Host Pathogen Interaction
**DOI** 10.15252/emmm.202013714 | Received 10 November 2020 | Revised 14 September 2021 | Accepted 16 September 2021 | Published online 18 October 2021
**EMBO Mol Med (2021) 13: e13714**

## Introduction

To date, SARS-CoV-2 (the causative agent of COVID-19) has caused > 236 M infections and > 5 M deaths. While vaccines are now available, there are still approximately 500 K infections a day and COVID-19 will remain a public health problem for the foreseeable future. There is also a growing concern that areas with uncontrolled COVID-19 outbreaks will give rise to variants that evade vaccine-induced immunity. SARS-CoV-2 causes a broad spectrum of disease, ranging from asymptomatic to fatal infections (Flerlage *et al*, 2021). Essential in pandemic management is the development of prognostic

1–35 The list of affiliations appears at the end of this article
*Corresponding author. Tel: +41 612653229; E-mail: alexandar.tzankov@usb.ch
**Corresponding author. Tel: +351 210489380; E-mail: eduardo.moreno@research.fchampalimaud.org
***Corresponding author. Tel: +45 35331419 and +351 910225386; E-mail: rajangogna@gmail.com; rajan.gogna@bric.ku.dk
†These authors contributed equally to this work as first authors
‡These authors contributed equally to this work as second authors

biomarkers for COVID-19 patients, to help facilitate patient triage and resource prioritization. Specific patient demographics (e.g., older age) and comorbidities (e.g., diabetes, obesity, and/or cardiovascular disease) are associated with increased COVID-19 severity (Longmore *et al*, 2021). However, such clinical characteristics typically have limited prognostic value in COVID-19 patients (as demonstrated by an area under a curve [AUC] of $< 0.75$) (Yang *et al*, 2020a; Grifoni *et al*, 2021). Other prognostic biomarkers that measure the immune response to infection (e.g., C-reactive protein [CRP] and the neutrophil-lymphocyte ratio) have been proposed (Huang *et al*, 2020b). However, such biomarkers typically appear later in the infection and their utility depends on the early collection of patient blood, which may not be possible in all diagnostic settings. Rather, it would be ideal to develop a COVID-19 biomarker in nasopharyngeal samples, as this sample is almost always the first or the earliest diagnostic sample collected from patients with a suspected COVID-19 illness. Early evidence suggests nasopharyngeal samples can provide important prognostic information in the context of COVID-19 (Ziegler *et al*, 2021).

Markers of cellular fitness have yet to be investigated for their prognostic value in COVID-19. We and others have previously shown that tissues have an intrinsic surveillance mechanism by which cells continuously interact and sense the fitness status of their neighbors (Merino *et al*, 2016; Liu *et al*, 2019; Madan *et al*, 2019; Flanagan *et al*, 2021; van Neerven *et al*, 2021; Yum *et al*, 2021). Communication of cellular fitness is an essential mechanism through which relatively less fit or suboptimal cells are recognized and removed from tissues (Rhiner *et al*, 2010; Merino *et al*, 2013; Madan *et al*, 2019; Coelho & Moreno, 2020). We have identified a unique molecular mechanism of "fitness fingerprints", which executes this cell recognition and elimination system, thereby maintaining optimum tissue health over time (Rhiner *et al*, 2010; Merino *et al*, 2013). We recently found that this system functions through the human flower gene (*hFwe*) (Madan *et al*, 2019). In a number of human cancers, the noncancerous cells surrounding a tumor are forced to express a specific fitness mark, called flower lose (*hFwe-Lose*) (Madan *et al*, 2019). *hFwe-Lose*-expressing stromal cells are eliminated by competitive pressure from the aggressive, superfit, cancer cells (Moreno, 2008; Madan *et al*, 2019; Parker *et al*, 2020). This mechanism is also used by healthy tissues, where suboptimal cells, which arise due to external or internal influences (e.g., oxidative stress, inflammation, cytotoxicity, or radiation), express *hFwe-Lose* and are marked for elimination (Rhiner *et al*, 2010; Merino *et al*, 2016; Madan *et al*, 2019). Therefore, *hFwe-Lose* is a unique marker for suboptimal or unfit status of cells in many tissues or organ systems. Low division potential, genotoxic stress, cytotoxic stress, radiation, aging, and the generation of reactive oxygen species (ROS) negatively impact cellular fitness and may render a cell suboptimal (Wang *et al*, 2006; Bondar & Medzhitov, 2010; Rhiner *et al*, 2010; Merino *et al*, 2015; Akieda *et al*, 2019; Liu *et al*, 2019) (Fig 1A).

SARS-CoV-2 infection of alveolar epithelial cells can lead to cell death and tissue damage (Huang *et al*, 2020a; Xu *et al*, 2020). Specifically, the loss of epithelial cells in the lower respiratory tract disrupts the pulmonary epithelial–endothelial barrier, resulting in pulmonary edema and respiratory distress (Ackermann *et al*, 2020; Barton *et al*, 2020; Konopka *et al*, 2020; Li *et al*, 2020; Ren *et al*, 2020). SARS-CoV-2-induced cell death can also result in the release of inflammatory factors, which may further perpetuate the "cytokine storm" associated with severe disease (Li *et al*, 2020). Cells under stress, which gain suboptimal status (i.e., those that are less fit), may be at an increased risk of virus-induced cell death. This stress can be associated with the chronic inflammation characteristic of different host comorbidities such as diabetes, obesity, and COPD (Milner & Beck, 2012; Bennett *et al*, 2018; Furman *et al*, 2019; Guan *et al*, 2020; Richardson *et al*, 2020; Yang *et al*, 2020b). We therefore propose that *hFwe-Lose*, a cell fitness biomarker, may be associated with a heightened risk of SARS-CoV-2-induced cell death and therefore could be an important prognostic biomarker in COVID-19 patients.

Here, we use samples from both the lower and upper respiratory tracts of COVID-19 patients to show that *hFwe-Lose* expression has a strong prognostic value for COVID-19 patient hospitalization and death. Indeed, *hFwe-Lose* expression in the upper respiratory tract outperformed other prognostic factors such as patient age, comorbidities, and clinical markers of inflammation in predicting patient outcome.

## Results

### *hFwe-Lose* expression in lung tissue increases with age and host comorbidities

To determine whether *hFwe-Lose* expression was elevated in the lungs of older adults, *hFwe-Lose* expression was analyzed by qPCR in 86 lung tissue biopsies taken from non-COVID-19 patients aged between 20 and 82 years. Older patients showed increased *hFwe-Lose* expression ($P < 6 \times 10^{-4}$) (Fig 1B). Specifically, patients over 70, as well as those aged between 60 and 70 years old, exhibited a significant upregulation of *hFwe-Lose* expression compared with patients younger than 60 years (Appendix Fig S1A). Besides older age, comorbidities such as hypertension, obesity, COPD, diabetes mellitus, and cardiovascular disease are known risk factors for severe COVID-19 (Guan *et al*, 2020; Richardson *et al*, 2020; Williamson *et al*, 2020; Yang *et al*, 2020b; Elezkurtaj *et al*, 2021; Gao *et al*, 2021). Consistent with a link between elevated *hFwe-Lose* expression and a risk of severe COVID-19, *hFwe-Lose* expression was elevated in lung tissue biopsies from non-COVID-19 patients with comorbidities (Fig 1C). *hFwe-Lose* expression was elevated in the lungs of patients with hypertension (HT; $n = 129$), obesity ($n = 45$), COPD ($n = 51$), diabetes ($n = 48$), cardiovascular disease (CVD; $n = 63$) versus disease-free control lungs ($n = 42$). *hFwe-Lose* expression increased with the total number of patient comorbidities (Appendix Fig S1B). *hFwe-Lose* expression is associated with the presence of "less fit" cells (Madan *et al*, 2019) which may be more prevalent in the organs of older adults and those with comorbidities, both of which are known risk factors for severe COVID-19 (Longmore *et al*, 2021). If *hFwe-Lose* expression in the respiratory tract has prognostic value in the context of COVID-19, one would hypothesize that patients who died of COVID-19 would display elevated *hFwe-Lose* expression. Figure 1D illustrates an increased expression of *hFwe-Lose* in lung tissue of patients with fatal COVID-19 ($n = 11$). Although these individuals had a number of comorbidities, *hFwe-Lose* expression was significantly higher in COVID-19 patients compared to non-COVID patients with comorbidities (Fig 1 D). Moreover, among COVID-19 patients, *hFwe-Lose* expression inversely correlated with the number of days from first symptoms to

 

death ($P < 3 \times 10^{-11}$) (Appendix Fig S1C). This could suggest that *hFwe-Lose* expression may be useful in identifying, among at-risk patients (i.e., those with comorbidities), those individuals with an elevated risk of fatal COVID-19 outcome.

Collectively, the above findings suggest that *hFwe-Lose* expression may play a prognostic role in COVID-19 by identifying individuals in whom a large number of "unfit" cells are present and therefore are at increased risk of virus-induced cell death. To test this hypothesis, the lungs of 11 deceased COVID-19 patients were examined (Menter *et al*, 2020) (Appendix Table S1). Typically, the lungs of healthy patients are characterized by air-filled alveolar spaces, thin alveolar septae/gas-exchange membrane, and the absence of inflammatory cells and congestion in pulmonary capillaries (Fig 1E1). In fatal COVID-19 patients' severe congestion, exudative diffuse alveolar damage (DAD) and thromboses were observed (Fig 1E2-5). Collapsing alveoli were also observed with epithelial detachment and micro-perforations as well as several cells with karyopyknosis and karyorrhectic figures (Fig 1E2-5). This is typically indicative of apoptosis of alveolar, endothelial, and interstitial cells in infected patients and includes hyaline membrane formation, erythrocyte extravasation, prominent, enlarged, often multinucleated, and often apoptotic, type II pneumocytes, interstitial

**Figure 1. *hFwe-Lose* biomarker associated with COVID-19 mortality and host comorbidities.**

A A schematic of cell competition process. Our bodies have a natural surveillance system that optimizes tissue fitness. The process of cell competition drives healthy tissues to force suboptimal, yet viable, loser cells to undergo cell death. Various stressors and insults cause cells to alter their properties and expression of fitness biomarkers. Cellular fitness comparisons lead to the elimination of loser cells that express *hFwe-Lose*, a biomarker of reduced fitness. This mechanism is responsible for actively restoring tissue homeostasis and has important implications in response to infections and the development of malignancies. ROS: reactive oxygen species.

B *hFwe-Lose* mRNA expression is more abundant in elderly people. *hFwe-Lose* mRNA expression was analyzed by RT–qPCR in 86 lung tissue biopsies taken from non-COVID patients with age between 20 and 82 years. Older patients show a significant upregulation of *hFwe-Lose* expression. A log-linear regression model demonstrates a positive correlation between age and *hFwe-Lose* expression ($R^2 = 0.13$; slope confidence interval of 95% (CI) = [2.0–12.2]; *P*-value of the linear regression model $< 6 \times 10^{-4}$).

C *hFwe-Lose* expression is elevated in lung tissue biopsies from patients with comorbidities. Box plot illustrates an increased expression of *hFwe-Lose* in lungs of patients with hypertension (HT; $n = 129$), obesity ($n = 45$), chronic obstructive pulmonary disease (COPD; $n = 51$), diabetes ($n = 48$), cardiovascular disease (CVD; $n = 63$) versus disease-free control lungs ($n = 42$). Patient`s age is depicted in color. Two-sided Student's *t*-test was performed for each comorbidity (compared to disease-free patients), and *P*-values are presented on the plot. The central band shows the median, the box indicates the interquartile range, and the whiskers extend to the most extreme points within the 1.5-fold distance of the interquartile range above and below the box.

D *hFwe-Lose* expression is upregulated in lung tissue of COVID-19 patients. Box plot illustrates an increased expression of *hFwe-Lose* in lung tissue of patients diagnosed with COVID-19 ($n = 11$), individuals affected with host comorbidities ($n = 216$) versus disease-free control lungs ($n = 42$). Patient's age is depicted in color. Two-sided Student's *t*-test was performed (compared to disease-free patients), and *P*-values are presented on the plot. The central band shows the median, the box indicates the interquartile range, and the whiskers extend to the most extreme points within the 1.5-fold distance of the interquartile range above and below the box.

E SARS-CoV-2 infection manifests histological changes in patients' lungs as demonstrated by H&E staining. 1) For comparison, the normal lung of an elderly individual is shown, containing air-filled empty looking alveolar spaces and thin alveolar septae/gas-exchange membranes. Note that there are almost no inflammatory cells and that capillaries are only merely visible since not congested. 2) Diffuse (proliferative) alveolar damage showing evidence of cell death. An alveolar space filled with desquamated pneumocytes and macrophages, lymphocytes, and focal erythrocyte extravasation as well as one multinucleated pneumocyte type II. The still recognizable epithelial lining is detached. Cells and surfactant are lost creating perforations in the alveolar wall, allowing migration of blood cells and fluid to enter inside the alveolar space. The adjacent interstitial space is significantly widened, showing an increase in mononuclear inflammatory cells and extravasation of erythrocytes. On the top and the lower right, dilated and congested capillaries can be seen (hematoxylin and eosin (H&E) stain, 200×). a—alveolar structure destroyed by lymphocytes, desquamated epithelium, and extravasated blood; the alveoli should be empty, but here it is filled with a combination of degenerated cells and fibrin; b—next alveoli; c—expanded pulmonary interstitium. The interstitium should be as thin as 10 μm, but here it is 100 μm; d—extravasation of erythrocytes; e—lymphocytes; f—congested capillaries and arterioles; g—multinucleated alveolocyte/pneumocyte type II; h—detached epithelium; i—a histiocyte with a kidney-shaped nucleus at the bottom of the circle has ingested erythrocytes (left-handed), representing the first step of cellular elimination. Round inlet with encircled karyopyknotic, karyorrhectic, and "ghost-cell" figures indicative of apoptosis. 3) The presence of type II pneumocyte syncytial giant cells in a collapsing alveolar space with detached epithelial lining. The adjacent interstitial space shows analogous changes to the previous example. At the bottom, there is a prominently dilated and congested capillary (H&E, 200×). a—alveoli with detached epithelium; b—next alveoli; c- Extravasation of erythrocytes; d—expanded interstitium; e—lymphocytes; f—multinucleated pneumocyte type II. 4) Diffuse alveolar damage showing massive extravasation of fibrin (homogeneous eosinophilic material in the center of the alveolar space). The lining pneumocytes are almost all apoptotic/necrotic. The fibrin exudate is intermingled with mononuclear inflammatory cells and cellular debris (H&E, 200×). a—alveola; b—congested capillaries; c—fibrin; d—remnants of degenerated/dying epithelium; e—expanded interstitium; f—cellular debris consisting of macrophages, detached epithelial cells and lymphocytes; g—fully degenerated/lacking epithelial coverage within the alveoli. Round inlet with encircled karyopyknotic, karyorrhectic, and "ghost-cell" figures indicative of apoptosis. 5) Immunohistochemical stain (IHC) for fibrin showing microthrombi caused by dysfunction of endothelial cells in capillaries of the alveolar membranes/lung interstitium leading to obstruction of the microcirculation (IHC for fibrin, 200×). a—all small alveolar septal capillaries are filled out with worm-like fibrin thrombi hampering / obstructing circulation; b—normal interstitium.

F Healthy lungs show very low cleaved caspase-3-positive cells. IHC staining for cleaved caspase-3 (20×).

G Expression of cleaved (active) caspase-3 yielding apoptotic and pre-apoptotic cells: IHC for cleaved (active) caspase-3 showing a brown nuclear staining signal in respective cells. 31.5% cells were found to be caspase positive, 11.7% with high caspase-3 positivity and another 19.8% with low. These cells are mainly located in the interstitium, but also in some alveolar epithelial and endothelial compartments. In the lower right, the edge of an alveolar space containing several (pre-)apoptotic pneumocytes is seen, while in the upper left, a completely denuded/deepithelialized alveolus with two apoptotic remnants is observable (IHC for cleaved caspase-3, 20×). a—apoptotic large mononuclear cells; b—apoptotic alveolocyte / pneumocyte; i—amplification of apoptotic alveolocyte / pneumocyte. As shown in the round inlets of 1E2 and 1E4, homogeneous dark nuclear condensation up to a size of 2 μm (karyopyknosis), homogeneous pinkish-grayish nuclear condensation, large nuclear inclusion with marginalization of the condensed chromatin, coarse nuclear angulation, nose-like/polar body-like nuclear protrusions, the latter two being karyorrhectic debris, were all morphologically considered evidence of apoptosis. This has been correlated with and was reflected by the results of the cleaved caspase-3 staining on step sections. All cells were counted on the 20× fields for $n = 42$ disease-free and $n = 3$ COVID-19 autopsy patients. The expression of *hFwe-Lose* in COVID-19 patients is significantly higher than in disease-free individuals, regardless of cleaved caspase-3 staining (Cas POS: $P < 0.004$; Cas NEG: $P < 0.006$). In COVID-19 patients, we observed a significantly higher expression of *hFwe-Lose* in sections with positive cleaved caspase-3 staining ($P < 0.004$). Two-sided Student's *t*-test was performed (compared to disease-free samples and NEG samples, respectively), and *P*-values are presented on the plot. The central band shows the median, the box indicates the interquartile range, and the whiskers extend to the most extreme points within the 1.5-fold distance of the interquartile range above and below the box.

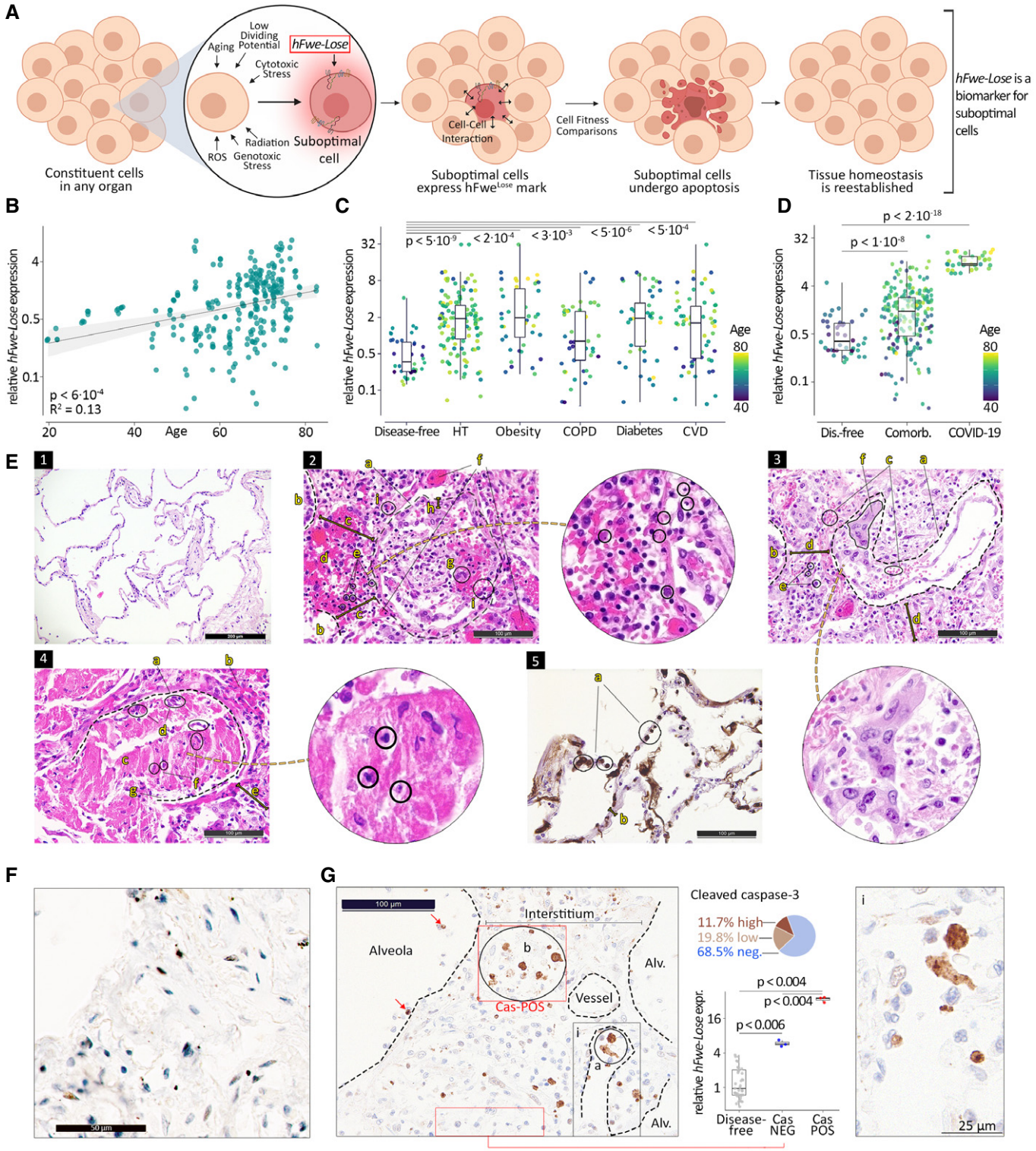


**Figure 1.**

expansion/edema with increased lymphocytes, and histiocytes (Fig 1E2-5). To further investigate cell death in these lungs, and the association with *hFwe-Lose* expression, sections from control and COVID-19 patients were stained for active/cleaved caspase-3. Limited caspase staining was observed in disease-free lungs (Fig 1 F). Interestingly, in COVID-19 patients the caspase staining was present in "patches", with the presence of both caspase-positive and caspase-negative regions (Fig 1G). This is suggestive of clonal

expansion of cells with markedly different vulnerability to apoptosis within distinct niches, as is expected in the case of flower fitness-based cellular selection and subsequent expansion. To this end, we laser-captured such regions and examined the expression of *hFwe-Lose*. We found that the caspase-positive regions had significantly higher expression, compared to disease-free lung samples (Fig 1G, right). These results indicate that high expression of the suboptimal fitness marker *hFwe-Lose* correlates with areas of increased cell death in the lung ($P < 0.004$).

### *hFwe-Lose* expression in nasopharyngeal swabs is associated with poor outcomes in COVID-19 patients

While the above data suggest that *hFwe-Lose* can be clearly detected in the lower respiratory tract in individuals at risk of severe COVID-19, as well as deceased COVID-19 patients, the lower respiratory tract is not well-suited for the detection of prognostic biomarkers, due to the difficulties associated with obtaining samples. In contrast, nasopharyngeal swabs are routinely performed in COVID-19 patients and represent a more accessible clinical sample for the discovery of prognostic biomarkers. Accordingly, nasal swabs were obtained from COVID-19 patients ($n = 283$) aged between 1 and 96 years. Swabs were taken at the very beginning of disease onset (i.e., at earliest contact with a physician, before the disease progression). The samples were taken at two independent centers from cohorts with similar baseline characteristics (Table 1). For prognostic testing purposes, we split the entire dataset into a retrospective cohort (training, $n = 203$) and a prospective cohort (validation, $n = 80$) that were used to train and validate the predictive models. Consistent with our lower respiratory tract data, *hFwe-Lose* expression in the upper respiratory tract increased with the age of COVID-19 patients (Fig 2A). The positive association of *hFwe-Lose* expression and age is also seen when analyzing patients without associated comorbidities or patients with a single comorbidity (Appendix Fig S2A). At all ages, *hFwe-Lose* expression was lower in the patients that were not hospitalized (Fig 2A). *hFwe-Lose* expression was also elevated in the nasopharyngeal swabs of patients with comorbidities associated with severe COVID-19, namely diabetes mellitus ($n = 129$), COPD ($n = 20$), obesity (BMI > 30; $n = 152$), cardiomyopathy (CM; $n = 19$), heart failure (HF; $n = 35$), hypertension (HT; $n = 121$), and chronic kidney disease (CKD; $n = 60$), compared to disease-free patients (Fig 2B). Notably, many patients had multiple comorbidities at the same time (disease-free = 96, one comorbidity = 76, two comorbidities = 55, three comorbidities = 33, four comorbidities = 18, five comorbidities = 5) (Appendix Fig S2B). Since *hFwe-Lose* expression increases with age, and older adults are more inclined to have comorbidities (Niccoli & Partridge, 2012), we created an age-adjusted statistical model to determine an unbiased correlation of comorbidity status and *hFwe-Lose* expression. The adjusted model suggests that hypertension ($P < 9 \times 10^{-9}$) and diabetes ($P < 0.04$) have the highest age-independent effect on *hFwe-Lose* expression level (Fig 2C). Importantly, among COVID-19 patients who were hospitalized within 14 days of disease progression ($n = 177$), nasopharyngeal *hFwe-Lose* expression was elevated in patients who: were admitted to ICU ($n = 34$), underwent intubation ($n = 58$), were in respiratory distress (defined as an elevated respiratory rate greater than 30) ($n = 76$), had blood oxygenation level (SpO2) less than 94% ($n = 147$), and died within 30 days of disease progression ($n = 21$) (Fig 2D). The expression of *hFwe-Lose* was also higher in patients who were hospitalized within 14 days of disease progression ($n = 177$) and who died within 30 days of disease progression ($n = 21$) versus patients who were not hospitalized (Fig 2E). We fitted a logistic model to predict the probability of hospitalization or death based on *hFwe-Lose* expression in nasal swab samples (Fig 2F). The logistic model was adjusted for age and sex. This model predicts a > 50% chance of hospitalization for (otherwise still healthy, not yet suffering from COVID-19) people who have a *hFwe-Lose* expression in their nasal swab samples that is approximately twice as large as the average *hFwe-Lose* expression in the group of non-hospitalized patients ($P < 0.001$).

### *hFwe-Lose* expression in nasopharyngeal swabs predicts outcome in COVID-19 patients

As a complementary approach to the logistic model, we used classification and regression tree (CART) analysis to find which of the variables (*hFwe-Lose* expression, age, sex, blood biomarkers, and presence of comorbidities) are valuable for the prognosis of the outcome. This method tries to find a series of partitions of the dataset that provide the most information about the outcome. This results in a tree-like structure of decisions based on the values of the variables used for prediction. The tree based on all patients ($n = 283$) is shown in Fig 3A. The partition providing the most information about the outcome is visualized as a split and is based on the *hFwe-Lose* expression. This split is done on all patients, whose outcomes are denoted underneath each split (gray: non-hospitalized, blue: hospitalized, red: dead). The subgroup of patients with *hFwe-Lose* expression < 2.45 are then split by age, and the subgroup with higher *hFwe-Lose* expression is once again split by *hFwe-Lose* expression, separating those patients with very high expression (> 4.41) from those with moderate to high expression (2.45–4.41). With each split, the coefficient of determination increases, and the relative error decreases (Barlin *et al*, 2013). The first split (*hFwe-Lose* > 2.45) increased the coefficient of determination by ~45% and reduced the relative error by ~45%. The impact of all following splits on the relative error was marginal (Fig 3B). The CART suggests the following classification of patients based on *hFwe-Lose* expression and age: (i) *hFwe-Lose* > 4.41 and age > 75 results in prediction "death". (ii) *hFwe-Lose* > 4.41 and age < 75 results in prediction "hospitalization". (iii) *hFwe-Lose* between 2.45 and 4.41 results in prediction "hospitalization". (iv) *hFwe-Lose* < 2.45 and age < 15 results in prediction "hospitalization". (v) *hFwe-Lose* between 1.1 and 2.45 and age > 44 results in prediction "hospitalization". (vi) *hFwe-Lose* between 1.1 and 2.45 and age < 44 results in prediction "non-hospitalized". (vii) *hFwe-Lose* < 1.1 results in prediction "non-hospitalized". Together, these data show that *hFwe-Lose* expression and patient age were the most useful predictors of COVID-19 outcome ($P < 0.01$). Figure 3C shows the impact of each possible predictor on the accuracy or misclassification rate that is measured as the mean decrease in the Gini coefficient obtained for the respective factor in a random forest analysis. *hFwe-Lose* expression had the highest score, followed by age and blood biomarkers. The presence of comorbidities obtained the lowest scores.

We next analyzed the impact of known COVID-19 blood biomarkers (ferritin, CRP, D-dimer, and neutrophil-lymphocyte ratio) and *hFwe-Lose* expression in nasopharyngeal swabs on the

**Table 1. Patient data: Retrospective (training) and prospective (validation) cohorts.**

| Characteristics | All ($N = 283$) | Retrospective cohort ($N = 203$) | Prospective cohort ($N = 80$) |
|---|---|---|---|
| Age, Q2 [Q1, Q3], (range), years | 55 [41,67] (1–96) | 54 [41.5,66] (1–96) | 55 [39.5,68] (5–91) |
| Male, no. (%) | 50.4 | 47.3 | 54.5 |
| Active smoker (%) | 9 (3%) | 5 (2%) | 4 (5%) |
| Former smoker (%) | 82 (29%) | 59 (29%) | 23 (29%) |
| BMI, Q2 [Q1, Q3], (range) | 28.3[24.7,34] (14.7–81.2) | 28.4 [24.8,34] (15.2–81.2) | 27.9 [24.3,34] (14.7–50.9) |
| Comorbidities, no. (%) | | | |
| Cancer | 102 (36%) | 67 (33%) | 35 (44%) |
| Chronic kidney disease | 35 (21%) | 35 (17%) | 25 (31%) |
| COPD | 20 (7%) | 12 (6%) | 8 (10%) |
| Heart failure | 35 (12%) | 15 (7%) | 20 (25%) |
| Cardiomyopathy | 19 (7%) | 10 (5%) | 9 (11%) |
| Solid organ transplant | 18 (6%) | 9 (4%) | 9 (11%) |
| Sickle cell disease | 5 (2%) | 2 (1%) | 3 (4%) |
| Type 2 diabetes mellitus | 79 (28%) | 48 (24%) | 31 (39%) |
| Hypertension | 121 (42%) | 95 (47%) | 26 (33%) |
| Medical care, no. (%) | | | |
| Physicians' evaluation as severe | 68 (24%) | 35 (17%) | 33 (41%) |
| Physicians' evaluation as moderate | 79 (28%) | 59 (29%) | 20 (25%) |
| Physicians' evaluation as mild | 136 (48%) | 109 (54%) | 27 (34%) |
| Intubation (%) | 58 (20%) | 33 (16%) | 25 (31%) |
| SpO2 < 94% | 147 (52%) | 94 (46%) | 53 (66%) |
| Respiration GT30 | 76 (27%) | 41 (20%) | 35 (44%) |
| Remdesivir treatment | 62 (22%) | 32 (16%) | 30 (38%) |
| Length of stay in hospital Q2 [Q1, Q3], (range), days | 7.1 [3.8,14.2] (1–99) | 6.9 [3.6,11.8] (1–99) | 8.3 [4,17.9] (1–40) |
| Outcome | | | |
| Hospitalized within 14 days (%) | 177 (63%) | 116 (57%) | 61 (76%) |
| Death within 30 days | 21 (7%) | 10 (5%) | 11 (14%) |
| Blood tests | | | |
| Neutrophils, per μl Q2 [Q1, Q3], (range), *(norm: 200–1000)* | 4940 [3000,8190] (100–30860) | 4675 [2990,6975] (100–19640) | 6930 [3810,10360] (1430–30860) |
| Lymphocytes (range), per μL Q2 [Q1, Q3], (range), *(norm: 100–300)* | 940 [700,1240] (50–2910) | 980 [730,1308] (220–2910) | 730 [570,1020] (50–1730) |
| Neutrophils/Lymphocytes ratio Q2 [Q1, Q3], (range), *(norm < 6.5)* | 5.1 [3.1,9.2] (0.2–98.3) | 4.8 [2.9,7.6] (0.2–45.7) | 8.4 [4.4,16.5] (1.6–98.3) |
| Ferritin Q2 [Q1, Q3], (range), ng/ml *(norm: 22–322; high: 322–900; very high: > 900)* D–dimer Q2 [Q1, Q3], (range), μg FEU/ml | 608 [222,1599] (20–7518) | 494 [197,1457] (20–7518) | 836 [319,1878] (89–3614) |
| D–dimer Q2 [Q1,Q3], (range), μg FEU/ml *(norm: < 0.5; high: 0.5–1; very high: > 1)* | 1.3 [0.8,2.7] (0.2–88.8) | 1.1 [0.7,2.4] (0.2–88.8) | 1.7 ± [1,3.6] (0.5–20.0) |
| CRP Q2 [Q1, Q3], (range), mg/dl *(norm: < 5; high: 5–50; very high: > 50)* | 5.9 [2.1,13.9] (0.1–35.8) | 5.4 [1.5,12.1] (0.1–33.6) | 6.8 [2.8,17] (0.4–35.8) |
| *hFwe-Lose* Q2 (Q1, Q3), (range), relative expression | 2.7 [1.1,3.9] (0.1–5.5) | 2.7 [1,4.0] (0.1–5.5) | 2.7 [1.7,3.6] (0.4–4.8) |

Clinical characteristics of the study patients ($n = 283$ total patients) for Figs 2–4, Appendix Figs S1 and S2. Patient Characteristics, comorbidities, clinical evaluation, hospitalization status, blood findings and *hFwe-Lose* measurements have been tabulated in the retrospective ($n = 203$) and prospective ($n = 80$) arms of the study.

age- and sex-adjusted probability of the possible outcomes (non-hospitalized, hospitalized, or dead) using mutlinominal logistic models (Appendix Fig S2C, upper row). A statistically significant association was detected between COVID-19 outcome and the concentration of all biomarkers, with an increasing probability of worse outcomes associated with increasing biomarker concentrations. However, the predictive value of these biomarkers was low, due to the large variance observed among hospitalized patients. Only *hFwe-Lose* expression was able to distinguish non-hospitalized and hospitalized outcomes. Patients with a relative *hFwe-Lose* expression of $< 1.5$ would be classified as remaining non-hospitalized, those with a larger relative expression would be classified as becoming hospitalized, whereas all other biomarkers would classify all patients as becoming hospitalized. None of the models were able to classify death as the outcome.

We additionally used binary logistic models to predict the age- and sex-adjusted probability of death from the same biomarkes (Appendix Fig S2C, lower row). All models showed a positive association of probability of death with increasing concentrations of the biomarker, but here the association between death and D-dimer concentration was not statistically significant. These models can be compared by the Akaike information criterion (AIC) that estimates the relative amount of information that the biomarker provides about the outcome classification. Lower values indicate a higher relative information content. The AIC values of all blood biomarkers are comparable, whereas the AIC for the *hFwe-Lose* expression is considerably lower, indicating that *hFwe-Lose* expression provides the most useful information to judge whether a COVID-19 patient may eventually succumb to the infection.

To further evaluate the prognostic capacity of *hFwe-Lose* expression, prognostic receiver operator characteristic value (ROC) curves were generated using the retrospective training cohort of 203 patients. Using ROC curve analysis, we identified the prognostic cut-off value of *hFwe-Lose* expression > 3.17 (for hospitalization; TPR = 0.77, FPR = 0.03) and *hFwe-Lose* expression > 4.44 (for death; TPR = 0.1, FPR = 0.08). The associated AUC values were 0.98 and

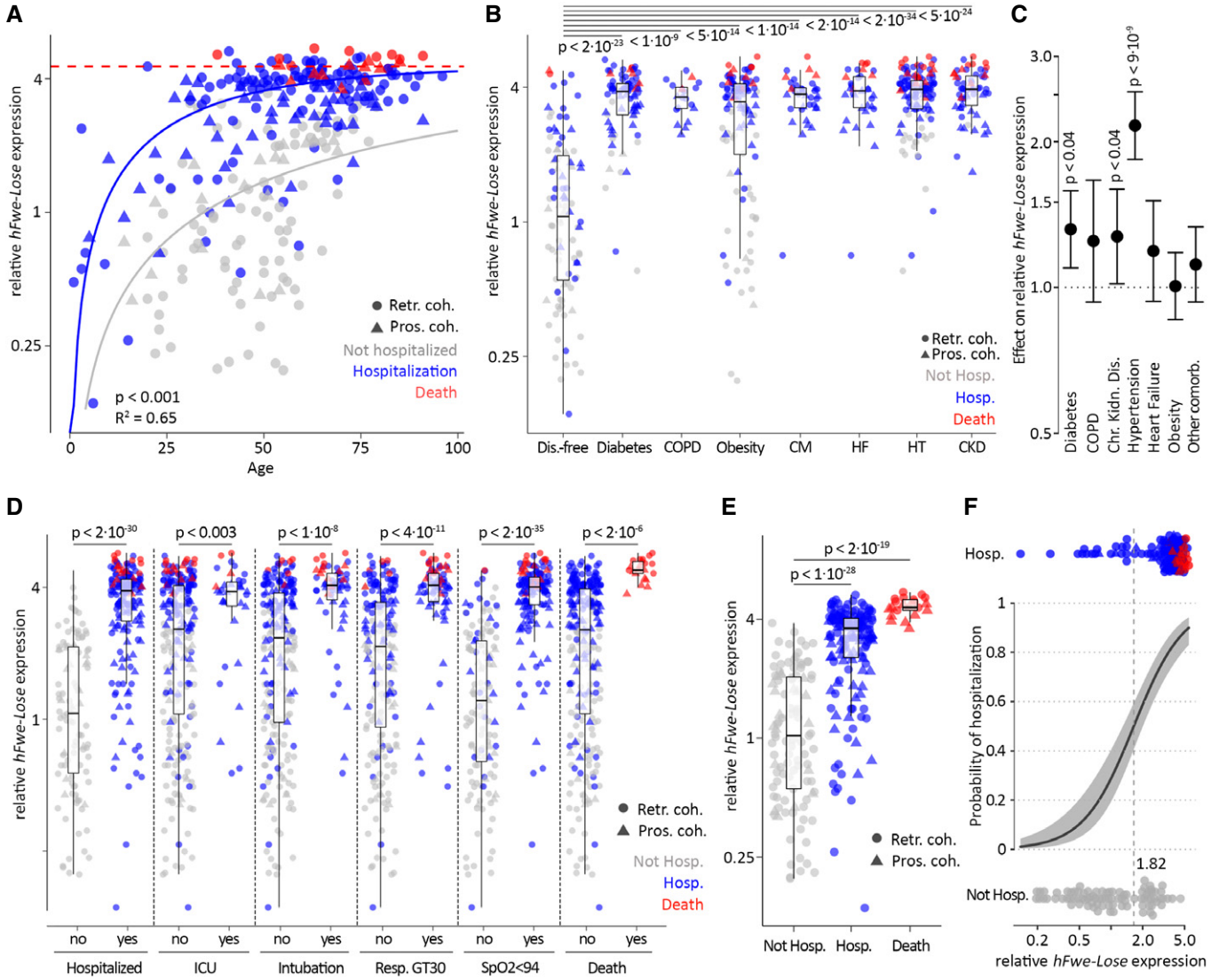


**Figure 2.**

**Figure 2. *hFwe-Lose* biomarker, measured in nasopharyngeal swab samples, associates with patients' COVID-19 disease outcome.**

A *hFwe-Lose* biomarker expression is more abundant in nasopharyngeal swab probes from older adults. *hFwe-Lose* expression was analyzed by RT–qPCR in 283 nasopharyngeal swab samples taken from patients with age between 1 and 96 years, taken at the very beginning of the disease (the earliest contact with physician, before the disease progression). The vertical axis represents relative *hFwe-Lose* expression normalized to the mean of non-hospitalized patients. Colors depict the outcome groups: non-hospitalized (gray, $n = 85$), hospitalized (blue, $n = 177$), and deceased (red, $n = 21$). The shape of data points reflects the cohorts: circles for the training cohort ($n = 203$) and triangles for the validation cohort ($n = 80$). The lines show the fitted curves of an asymptotic model with the same asymptotic value but different rate constants per group (see Materials and Methods). Due to the comparatively low number of deceased patients in the dataset ($n = 21$), the curve for this group reflects the asymptotic value. Hospitalized and deceased patients show a positive correlation of *hFwe-Lose* expression and age with a larger rate constant for the hospitalized patients ($R^2 = 0.65$). The *P*-value (< 0.001) indicates that the blue curve (for hospitalized patients) grows faster with age, compared to the gray curve (for non-hospitalized patients).

B *hFwe-Lose* expression is elevated in nasopharyngeal swab probes from patients with comorbidities. Box plots illustrate an increased relative expression of *hFwe-Lose* in nasopharyngeal swabs of patients with diabetes ($n = 129$), COPD ($n = 20$), obesity (BMI > 30; $n = 152$), cardiomyopathy (CM; $n = 19$), heart failure (HF; $n = 35$), hypertension (HT; $n = 121$), chronic kidney disease (CKD; $n = 60$) versus disease-free patients ($n = 96$). Two-sided Student's *t*-tests were performed (compared to disease-free patients), and *P*-values are presented on the plot. The vertical axis represents relative *hFwe-Lose* expression normalized to the mean of non-hospitalized patients. The color refers to the COVID-19 disease outcome: gray for not hospitalized, blue for hospitalized and red for deceased patients. The shape of data points reflects the cohorts: circles for the training cohort ($n = 203$) and triangles for the validation cohort ($n = 80$). The central band shows the median, the box indicates the interquartile range, and the whiskers extend to the most extreme points within the 1.5-fold distance of the interquartile range above and below the box.

C An age- and sex-adjusted statistical model suggests hypertension, diabetes, and chronic kidney disease to have the highest impact on *hFwe-Lose* expression. A linear regression model was created to account the patient's age upon analysis of *hFwe-Lose* expression in relation to comorbidity status. "Other comorbidity" refers to a cumulative effect of diseases or conditions, not directly associated with COVID-19 (cancer, Down syndrome, solid organ transplant, sickle cell disease, bone marrow transplant). The plot illustrates the effect of selected comorbidities (horizontal axis) on relative *hFwe-Lose* expression (vertical axis). The *P*-values of the respective linear models for all significant comorbidities are presented on the plot. The error bars represent the 95% confidence interval.

D Elevated *hFwe-Lose* expression in the nasal swab samples associates with patients' condition severity and respective medical treatment. Box plots illustrate an increased expression of *hFwe-Lose* in nasal swabs of patients, who were hospitalized within 14 days of disease progression ($n = 177$), admitted to intensive care unit (ICU) ($n = 34$), underwent intubation ($n = 58$), had respiratory rate greater than 30 (GT30; $n = 76$), had blood oxygenation level (SpO2) less than 94% ($n = 147$), and died within 30 days of disease progression ($n = 21$) versus patients without respective conditions. Pairwise two-sided Student's *t*-tests were performed (compared to patients without respective conditions), and *P*-values are presented on the plot. The vertical axis represents *hFwe-Lose* expression normalized to the mean of non-hospitalized patients. The color refers to the COVID-19 disease outcome: gray for non-hospitalized, blue for hospitalized, and red for deceased patients. The shape of data points reflects the cohorts: circles for the training cohort ($n = 203$) and triangles for the validation cohort ($n = 80$). The central band shows the median, the box indicates the interquartile range, and the whiskers extend to the most extreme points within the 1.5-fold distance of the interquartile range above and below the box.

E Elevated *hFwe-Lose* expression in nasal swab associates with patients' disease outcome. Box plot emphasizes an increased expression of *hFwe-Lose* in nasal swabs of patients, who were hospitalized within 14 days of disease progression ($n = 177$), and who died within 30 days of disease progression ($n = 21$) versus patients without respective conditions. Two-sided Student's *t*-tests were performed (compared to non-hospitalized patients), and *P*-values are presented on the plot. The vertical axis represents *hFwe-Lose* expression normalized to the mean of non-hospitalized patients. The color refers to the COVID-19 disease outcome: gray for not hospitalized, blue for hospitalized, and red for deceased patients. The shape of data points reflects the cohorts: circles for the training cohort ($n = 203$) and triangles for the validation cohort ($n = 80$). The central band shows the median, the box indicates the interquartile range, and the whiskers extend to the most extreme points within the 1.5-fold distance of the interquartile range above and below the box.

F The logistic model predicts probability of hospitalization based on *hFwe-Lose* expression in nasal swab samples. This model predicts a > 50% chance of hospitalization for people (otherwise still healthy, not yet infected with COVID-19), who have a *hFwe-Lose* expression in their nasal swab samples >1.82 than the mean of non-hospitalized patients. *P*-value of the logistic model < 0.001. The gray area shows the 95% confidence band.

0.89 for hospitalization and death, respectively (Fig 3D). Consistent with these data, there was increased expression of *hFwe-Lose* in nasal swabs of patients, who were hospitalized or died versus patients who were not hospitalized for both the retrospective (training; $n = 203$) and prospective (validation; $n = 80$) patient cohorts (Fig 3E). In the retrospective cohort, the outcome forecast was 84% correct in predicting non-hospitalization, 63% correct for hospitalization, and 100% correct for death. In the prospective cohort, the outcome prediction was 100% correct for non-hospitalization, 72% correct for hospitalization, and 55% correct for death (45% of deceased patients were predicted to be "only" hospitalized; none of deceased patients had a "not hospitalized" prediction) (Fig 3E). Confusion matrices and heatmaps were next used to visualize the sensitivity and specificity of selected cut-offs (*hFwe-Lose* expression > 3.17 for hospitalization and *hFwe-Lose* expression > 4.44 for death) (Fig 3F). In the retrospective cohort, 72 out of the total 86 not hospitalized patients were correctly predicted. Out of 107 hospitalized patients, 67 were correctly predicted while 19 were predicted to die instead and 21 were not predicted to be hospitalized. All deceased patients were correctly predicted. In the prospective cohort, all patients (19) who were not hospitalized, were correctly predicted. Out of 50 hospitalized patients, 36 were correctly predicted while 14 were predicted to be non-hospitalized. Finally, out of 10 deceased patients in the prospective cohort, 6 were correctly predicted and 5 patients were predicted to be "only" hospitalized (Fig 3F). For hospitalization prediction, positive predictive value (PPV) for the retrospective cohort was 83.7 and 87.8% for the prospective cohort. The negative predictive value (NPV) for the retrospective cohort was 67.2 and 64.1% for the prospective cohort. For death prediction, the PPV for the retrospective cohort was 34.5% while it was 100% for the prospective cohort. The NPV for the retrospective cohort was 100 and 93.2% for the prospective cohort (Fig 3F). These high negative predictive values make *hFwe-Lose* expression as a very useful biomarker for assessing mortality risk (i.e., to exclude the risk of COVID-19-related deaths), thereby confirming its potential role in triage and risk stratification of COVID-19 patients.

Finally, we evaluated the additional prognostic value of nasopharyngeal *hFwe-Lose* expression over and above conventional methods routinely used in clinical settings, such as laboratory tests alone (e.g., blood-based biomarkers) or laboratory tests together with clinical information (e.g., age and comorbidities). Specifically, the AUC

 

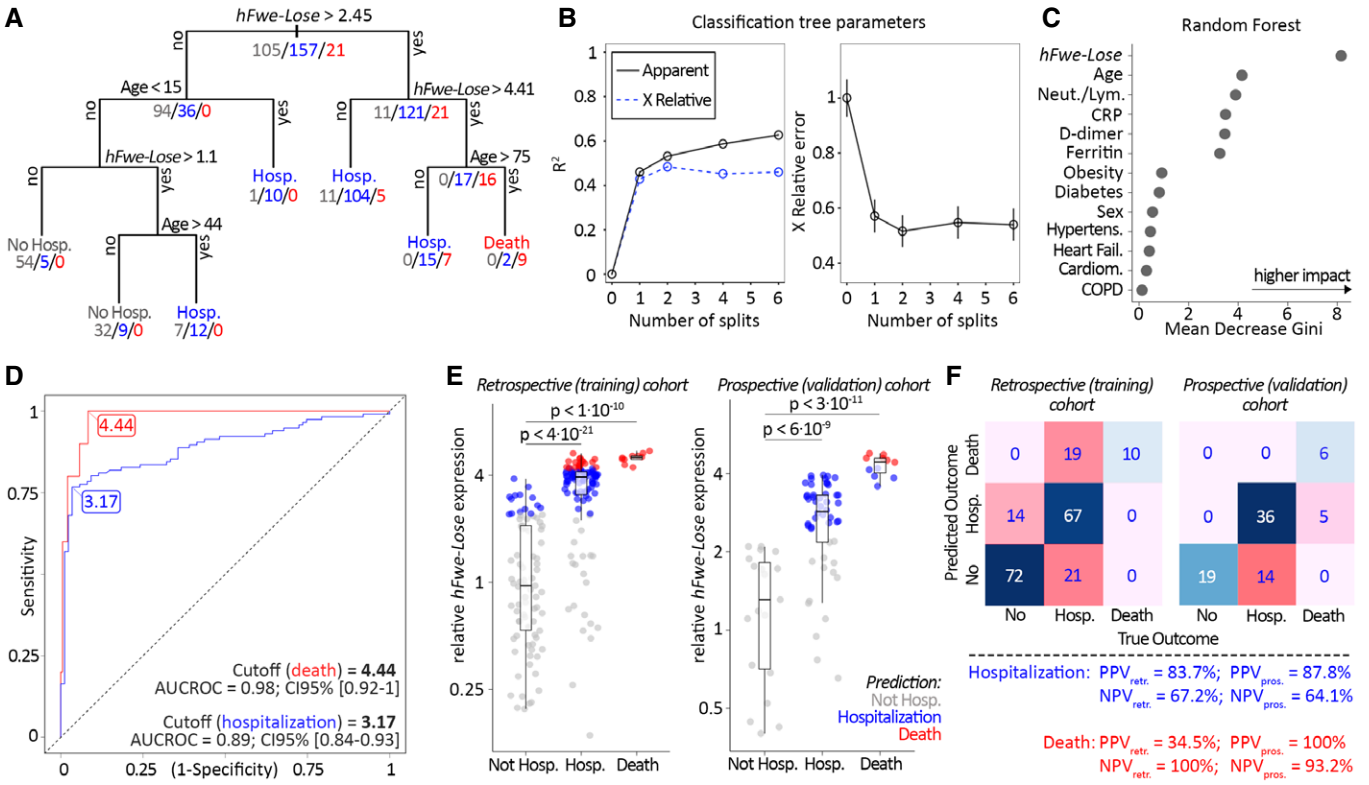


**Figure 3. *hFwe-Lose* biomarker, measured in nasal swab samples, predicts patients' COVID-19 outcome.**

A Classification and regression tree (CART) shows that *hFwe-Lose* expression in patients' nasal swab sample and patients' age is the main predictors of the outcome. The classification tree was generated using all relevant information about patients (*hFwe-Lose* expression, age, sex, presence of comorbidities (diabetes, COPD, obesity, cardiomyopathy, heart failure, hypertension)). All patients were included in the CART analysis ($n$ = 283). The CART algorithm selected *hFwe-Lose* expression and age as sole factors to determine the patients' outcome. The split cut-offs, which produce tree branches, are aimed to maximize the information gain (decrease of entropy) with each split, and in this way, the coefficient of determination increases, and the relative error decreases with each split (Barlin *et al*, 2013).

B The line plots show saturation of the coefficient of determination, as well as the plateau in X relative error. *P*-value of the classification and regression tree analysis (for all splits) < 0.01. The first split (*hFwe-Lose* > 2.45) increased the coefficient of determination by ~45% and reduced the relative error by ~45%. The impact of all following splits on the relative error was irrelevant. The error bars (plot on the right) represent ± SE.

C The *random forest* analysis shows the highest impact of the *hFwe-Lose* biomarker in the multivariate analysis of outcome prediction. The plot shows the *Mean Decrease in Gini* coefficients for the factors that were incorporated in the statistical model for the multivariate CART analysis. The Gini coefficient is a measure of the misclassification rate. The importance of a predictor is assessed by how much the predictor reduced this misclassification rate. The *hFwe-Lose* expression has the highest score, followed by age and blood biomarkers. Comorbidities show the least impact on reducing the misclassification rate.

D *hFwe-Lose* is a sensitive and specific biomarker that predicts poor COVID-19 outcome. The ROC curves illustrate the high sensitivity and (1 - specificity) of FC > 3.17 (for hospitalization; TPR = 0.77, FPR = 0.03) and FC > 4.44 (for death; TPR = 0.1, FPR = 0.08) threshold levels (AUC = 0.89 and 0.98, respectively) in prediction patients' hospitalization and death. CI 95% (hospitalization) - [0.84–0.93]; CI (death) - [0.92–1]. Only retrospective (training, $n$ = 203) patients' cohort was used for the creation of ROC curves.

E Elevated *hFwe-Lose* expression in nasal swab probes predicts patients' disease outcome. Box plots show an increased expression of *hFwe-Lose* in nasal swabs of patients, who were hospitalized or died, versus patients who were not hospitalized, for retrospective (training; $n$ = 203) and prospective (validation; $n$ = 80) patients' cohorts. Two-sided Student's *t*-test was performed, and *P*-values are presented on the plot. The vertical axis represents *hFwe-Lose* expression normalized to the mean of non-hospitalized patients. The color refers to the COVID-19 disease outcome prediction: gray for not hospitalized, blue for hospitalized, and red for deceased patients. In the retrospective cohort, the outcome prediction was 84% correct in predicting non-hospitalization, 63% correct in prediction of hospitalization, and 100% correct in death prediction. In the prospective cohort, the outcome prediction was 100% correct in predicting non-hospitalization, 72% correct in prediction of hospitalization, and 55% correct in death prediction (45% of deceased patients were predicted to be "only" hospitalized; none of deceased patients had "not hospitalized" prediction). Two-sided Student's *t*-tests were performed (compared to non-hospitalized patients), and *P*-values are presented on the plot. The central band shows the median, the box indicates the interquartile range, and the whiskers extend to the most extreme points within the 1.5-fold distance of the interquartile range above and below the box.

F The confusion matrices and heatmaps visualize the classification performance of *hFwe-Lose* expression at the selected cut-offs (FC > 3.17 for hospitalization and FC > 4.44 for death). In the retrospective (training) cohort, 72 out of the total 86 not hospitalized patients were correctly predicted; out of 107 hospitalized patients, 67 were correctly predicted, 19 were predicted to die instead, and 21 were not predicted to be hospitalized; all deceased patients were correctly predicted. In the prospective (validation) cohort, all patients (19) who were not hospitalized, were correctly predicted; out of 50 hospitalized patients, 36 were correctly predicted, 14 were predicted to be non-hospitalized; out of 10 deceased patients, 6 were correctly predicted, and 5 patients were predicted to be "only" hospitalized. For hospitalization prediction, positive predictive value (PPV) for retrospective (training) cohort is 83.7% and for prospective (validation) cohort is 87.8%. The negative predictive value (NPV) for retrospective (training) cohort is 67.2% and for prospective (validation) cohort is 64.1%. For death prediction, positive predictive value (PPV) for retrospective (training) cohort is 34.5% and for prospective (validation) cohort is 100%. The negative predictive value (NPV) for retrospective (training) cohort is 100% and for prospective (validation) cohort is 93.2%.

of nasopharyngeal *hFwe-Lose* expression was compared with blood-based biomarkers and/or patient comorbidities and age. The comorbidities used to train models included cancer, chronic kidney disease, COPD, down syndrome, heart failure, cardiomyopathy, solid organ transplant, sickle cell disease, type 2 diabetes mellitus, bone marrow transplant, and hypertension. Firstly, *hFwe-Lose* expression was compared with four known blood biomarkers (serum ferritin, CRP, D-dimer, and neutrophil-lymphocyte ratio) in predicting death of hospitalized COVID-19 patients (Fig 4A). For each biomarker, only patients who had laboratory testing performed (on admission to hospitals) were used. With AUC as the criteria, *hFwe-Lose* significantly outperformed all four biomarkers in predicting death (Fig 4A). Machine learning analysis further demonstrated that *hFwe-Lose* biomarker expression was superior to using patient age and comorbidities to predict poor COVID-19 outcomes (Fig 4B). For example, the AUC of age combined with comorbidities in predicting patient hospitalization was 0.83/0.88 (retrospective cohort/prospective cohort) while the AUC of *hFwe-Lose* expression was 0.89/0.90 (retrospective cohort/prospective cohort) (Fig 4B). Even more strikingly, the AUC of age combined with comorbidities in predicting patient death was 0.84/0.86 (retrospective cohort/prospective cohort) while the AUC of *hFwe-Lose* expression was 0.98/0.98 (retrospective cohort/prospective cohort) (Fig 4B). Finally, we assessed the predictive value of a combinatorial approach in predicting the death of COVID-19 patients. Specifically, the AUC of all blood biomarkers (serum ferritin, CRP, D-dimer, and neutrophil-lymphocyte ratio), *hFwe-Lose* expression, age + comorbidities and the combination of blood biomarkers, age, and comorbidities was assessed. In both the retrospective and prospective cohorts, *hFwe-Lose* expression had the highest AUC (0.92) compared with blood biomarkers (0.71/0.46), age and comorbidities (0.85/0.77), or the combination of both (0.92/0.67) (Fig 4B).

## Discussion

Despite the recent availability of vaccines, in 2021, SARS-CoV-2 has continued to spread and cause numerous outbreaks worldwide. Essential to the management of this pandemic is the ability to identify and, where necessary, triage COVID-19 patients at high risk of poor disease outcomes. Unfortunately, stratifying patients based on underlying comorbidities and/or advanced age has proved insufficient for this purpose as it fails to account for older individuals with mild disease or younger individuals who are admitted to ICU or succumb to the infection (Liu *et al*, 2020). Several blood-based markers of inflammation have been proposed as biomarkers for severe COVID-19. However, blood samples are typically taken later in the course of the disease and the prognostic values of these biomarkers have varied between studies (Cheng *et al*, 2020; Sahu *et al*, 2020). In contrast, biomarkers obtained from nasopharyngeal samples can be obtained early in disease course (i.e., when the patient first presents for SARS-CoV-2 testing) and can be obtained from a diverse array of diagnostic settings (including drive-through testing clinics).

Here, we provide the first evidence that nasopharyngeal expression of the cell fitness marker *hFwe-Lose* has significant prognostic value in COVID-19 patients. Indeed, AUC of the receiver operator characteristic curve for *hFwe-Lose* expression in predicting COVID-19 patient hospitalization and death was markedly greater than the AUC of blood biomarkers of inflammation, patient age plus comorbidities, or a combination of both. This represents the first evidence for cell fitness markers in predicting the prognosis of infectious disease.

At present, why *hFwe-Lose* expression in the respiratory tract is associated with severe COVID-19 remains unclear. It has been shown in the past that environmental changes within our body including nutrient state, inflammation, and notably, immune function impact relative fitness status of cells and their contribution to their tissue space. Chronic inflammation, including dietary-associated inflammation and obesity, antagonizes homeostatic fitness sensing mechanisms and results in higher retention of suboptimal cells, thereby worsening tissue fitness over time (Vermeulen *et al*, 2013; Sasaki *et al*, 2018; Bruens *et al*, 2020; Sato *et al*, 2020).

We have shown that in the absence of SARS-CoV-2, *hFwe-Lose* expression is elevated in the respiratory tract of older individuals and individuals with one or more underlying comorbidity. Importantly, *hFwe-Lose* expression was not elevated in *all* individuals in these patient groups and patient-to-patient differences in expression may reflect disease duration, patient lifestyles, disease management, and/or other factors. Nevertheless, we propose that on an individual level, elevated *hFwe-Lose* expression is indicative of a large number of unfit cells in the respiratory tract, and thereby typically associated with advanced age or underlying medical conditions. Specifically,

**Figure 4. The linear regression models show superiority of the *hFwe-Lose* biomarker to predict COVID-19 outcome, compared with conventional biomarkers.**

A *hFwe-Lose* predicts COVID-19 patients' death more accurately than other biomarkers. *hFwe-Lose* was compared with four known biomarkers (ferritin, CRP, D-dimer, and neutrophil-lymphocyte ratio, respectively) in predicting death of hospitalized patients. For each biomarker, only patients who had the information of the respective blood biomarker were used. 115 patients were used to compare ferritin and *hFwe-Lose*. 120 patients were used to compare D-dimer and *hFwe-Lose*. 127 patients were used to compare CRP and *hFwe-Lose*. 153 patients were used to compare neutrophil–lymphocyte ratio and *hFwe-Lose*. With AUC as the criteria, *hFwe-Lose* significantly outperformed all four biomarkers in predicting death in both retrospective and prospective cohorts. AUC coefficients, as well as CIs, are displayed on the plots.

B *hFwe-Lose* biomarker is superior to other markers in COVID-19 poor outcome prediction. All 283 patients were used to compare *hFwe-Lose* and age combined with comorbidities in predicting hospitalization (left) and death (middle). The AUC of age combined with comorbidities in predicting the hospitalization of the prospective cohort is 0.88 (CI - [0.81–0.96]). The AUC of *hFwe-Lose* in predicting the hospitalization of the prospective cohort is 0.90 (CI - [0.84–0.97]). *hFwe-Lose* outperformed age combined with comorbidities in predicting hospitalization. The AUC of age combined with comorbidities in predicting the death of the prospective cohort is 0.86 (CI - [0.72–1.0]). The AUC of *hFwe-Lose* in predicting the death of the prospective cohort is 0.98 (CI - [0.92–1.0]). *hFwe-Lose* significantly outperformed age combined with comorbidities in predicting death. The 105 patients who registered the information of all four known blood biomarkers (ferritin, CRP, D-dimer, and neutrophil-lymphocyte ratio) were used to compare *hFwe-Lose*, age combined with comorbidities, and the four biomarkers in predicting death (right). *hFwe-Lose* significantly outperformed age combined with comorbidities and the four biomarkers in predicting death in both retrospective and prospective cohorts derived from the 105 patients.

 

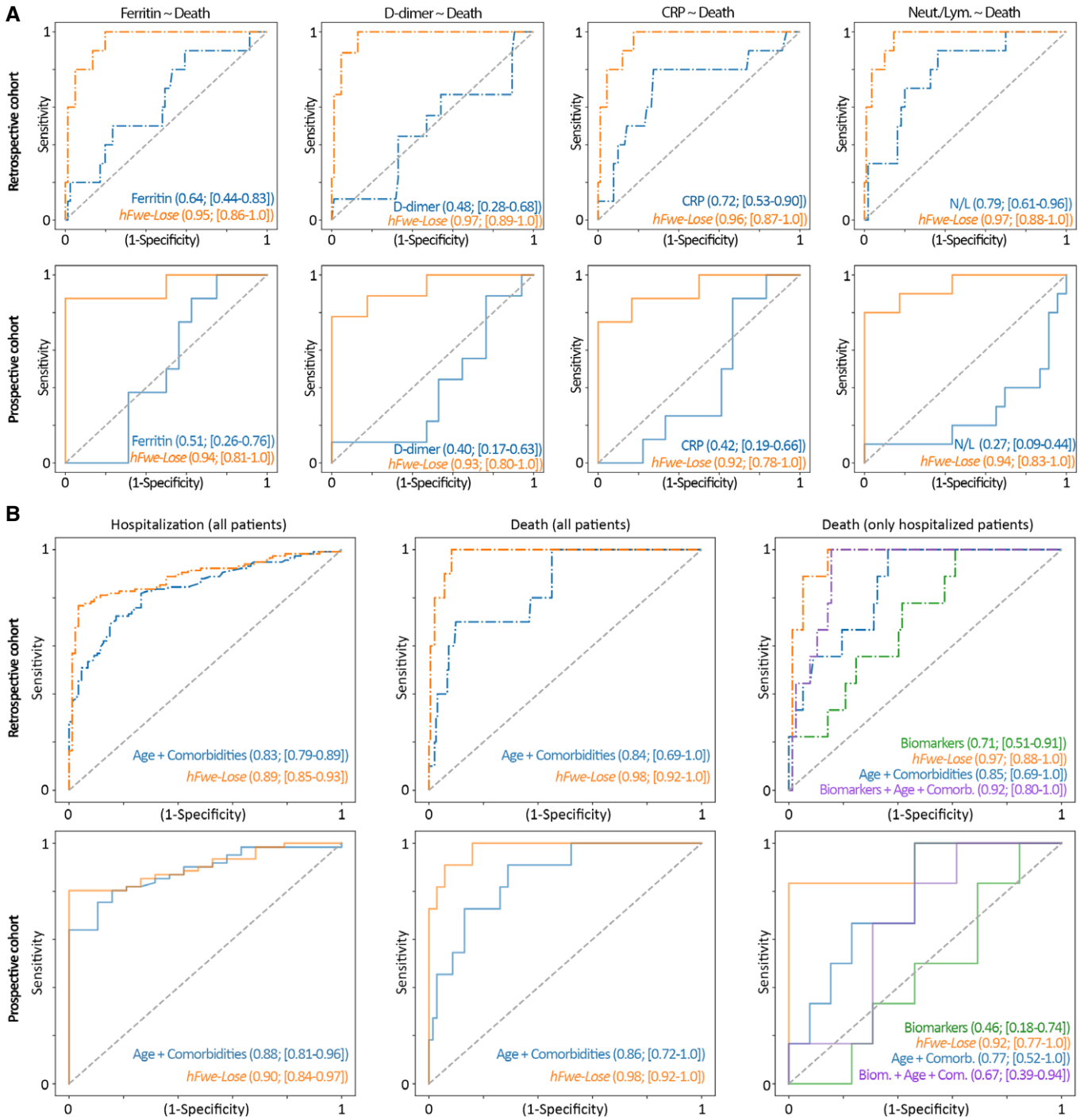


**Figure 4.**

the isoforms of the flower protein form an extracellular code that communicates fitness status between interacting cells (Rhiner *et al*, 2010; Madan *et al*, 2019). We previously found that *hFwe-Lose* is strongly induced in tumor-adjacent stromal cells that are marked for apoptotic elimination (Madan *et al*, 2019). Individuals with elevated *hFwe-Lose* expression may therefore have a larger number of cells that are susceptible to SARS-CoV-2-induced cell death. SARS-CoV-2-mediated cell death may exacerbate lung inflammation, which is a key pathological process underpinning severe respiratory failure and death in COVID-19 patients. In this regard, *hFwe-Lose* expression may act as a "susceptibility" marker for worst outcome in those with advanced age and/or multiple comorbidities or as stand-alone risk stratification marker for those who are young and without comorbidities. For example, we predict that in young, healthy adults without underlying respiratory comorbidities, the lung alveoli tissue would typically be "fit" and would consist of very few suboptimal

cells expressing *hFwe-Lose*. Upon SARS-CoV-2 infection, due to a low number of suboptimal cells, healthy and young individuals do not suffer widespread epithelial cell death. This may result in only minor to mild symptoms and enable the patient to recover without severe complications (Appendix Fig S3). In contrast, in young adults with pre-existing suboptimal cells (for whatever reason), *hFwe-Lose* expression may be an excellent prognostic biomarker to predict outcome upon COVID-19 infection, thereby allowing clinicians to identify a subgroup of young adults who may have worst clinical outcome (as opposed to young adults who have a milder, self-limiting COVID-19 illness).

The above hypothesis remains to be tested, but it raises the intriguing possibility that *hFwe-Lose* expression could be used to screen individuals for their risk of developing severe COVID-19 *prior* to SARS-CoV-2 infection. This is not currently possible with other widely used COVID-19 biomarkers (which typically detect the host response to infection) and may serve to be a powerful tool in informing individual risk–benefit analyses of receiving a COVID-19 vaccine. There is also the possibility that, as a general marker of cell fitness, *hFwe-Lose* expression has prognostic potential for other viral pathogens. Specifically, widespread cell death and pulmonary edema is a key feature of influenza virus-induced viral pneumonia (Short *et al*, 2014). As another virus of pandemic potential, the role of cell fitness markers in the prognosis of influenza remains an area of ongoing research.

Importantly, while this study clearly demonstrated a role for *hFwe-Lose* expression in COVID-19 prognostics, there are several study limitations that are important to acknowledge. Firstly, this study was performed on a US-based population. Therefore, the prognostic use of *hFwe-Lose* expression in other geographically and ethnically diverse populations needs to be established. We also did not assess the prognostic value of *hFwe-Lose* expression in combination with other predictors of COVID-19 severity. It is possible that a combinatorial approach that encompasses *hFwe-Lose* expression would further improve the associated positive and negative predictive values.

Nevertheless, the present study established a novel prognostic biomarker for COVID-19 severity and provides the first evidence for the role of cell fitness in the pathogenesis of infectious disease.

## Materials and Methods

### RNA isolation from patient FFPE samples and qPCR

Total RNA was isolated from FFPE tissue samples using the RNeasy FFPE Kit (Qiagen). Ten nanograms of total RNA was reverse transcribed to complementary DNA (cDNA) using Superscript Vilo cDNA Synthesis Kit (Thermo Fisher) per the manufacturer's instructions. Quantitative PCR (qPCR) was performed with PowerUp SYBR Green Master Mix (Thermo Fisher) using QuantStudio 5 Real-Time PCR system. The reaction conditions included an initial denaturation step at 95°C for 2 min, followed by 40 cycles of 95°C for 15 s and 60°C for 60 s. The Ct values of samples and controls were normalized to the expression level of the GAPDH housekeeping gene. The expression of *hFwe-Lose* is given as a relative change in mRNA expression to the mean of non-hospitalized samples. All qPCRs were set up in triplicate, and the experiments were performed with at least three different samples. The mRNA expression of h*Fwe*-Lose is relative to the mean of the hFwe-Lose mRNA expression in the disease-free lung samples. The following primers were used (F: forward; R: reverse): GAPDH: 5′-GGATGCAGGGATGATGTTC-3′ (F) and 5′-TGCACCACCAAC TGCTTAG-3′ (R); *hFwe-Lose*: 5′-GCGTGTGGATGATGATGG-3′ (F) and 5′-AGCAGAGAGTCCGTACA GCA-3′ (R).

### RNA isolation from patient nasal swabs and qPCR

Total RNA was isolated from clinical nasal swab samples using the RNeasy Micro Kit Protocol (Qiagen) following the protocol listed under "Isolation of total RNA from ejectable buccal swabs". Briefly, patient samples were mixed with kit-supplied Buffer RLT and vortexed for 1 min. The lysate was then transferred to a QIAshredder Mini Spin Column and centrifuged for 5 min at 12,000× *g* to filter debris and reduce viscosity from the samples. After adding one volume of 70% ethanol to the lysate, the sample was transferred to a RNeasy MiniElute Spin Column (Qiagen) and centrifuged for 15 s at 8,000× *g*. The lysate was washed with kit-supplied buffer RW1, DNase I-treated, and washed with 80% ethanol. Finally, the total RNA was eluted in 10 µl of RNase-free water.

RNA from patient nasal swabs was converted to cDNA and PCR-detected in one-step RT–qPCRs using the *Power*SYBR Green RNA-to-CT 1-*Step*Kit (Thermo Fisher) according to manufacturer instructions. One nanogram of RNA template was added per 10 µl reaction. The thermal cycling conditions included a reverse transcription step for 30 min at 48°C, DNA polymerase activation for 10 min at 95°C, followed by Denaturation for 15 s at 95°C, and Anneal/Extension for 1 min at 60°C for 40 cycles. All qPCRs were set up in technical triplicate. The mRNA expression of *hFwe-Lose* is relative to the mean of the *hFwe-Lose* mRNA expression in the nasopharyngeal samples from non-hospitalized patients. The following primers were used (F: forward; R: reverse): GAPDH: 5′-GGATGCAGGGATGATGTTC-3′ (F) and 5′-TGCACCACCAACTGCTTAG-3′ (R); *hFwe-Lose*: 5′-GCGTGTGG ATGATGATGG-3′ (F) and 5′-AGCAGAGAGTCCGTACA GCA-3′ (R).

### Immunohistochemistry and H&E staining

Conventional hematoxylin and eosin (H&E) staining was performed on deparaffinized sections of the FFPE autopsy asseverates of the lungs according to the current accredited staining protocol at the Institute of Medical Genetics and Pathology of the University Hospital Basel, Switzerland, as per May 2020. Immunohistochemistry was performed according to the current accredited staining protocols, applying the polyclonal ready-to-use antibody PP 229 AA from Biocare (Pacheco, CA, USA) against cleaved caspase-3 on an automated immunostainer Benchmark Ultra (Roche/Ventana, Tucson, AZ, USA), and the polyclonal antibody A0080 from Dako (Glostrup, Denmark) against fibrin(-ogen) at a dilution of 1:100,000 utilizing detection with a secondary anti-rabbit link antibody.

### Patient samples

FFPE tissue blocks of lung tissue were provided by Dr. Antonio Beltran at the Pathology Department, Champalimaud Foundation. All samples used in the study were de-identified, and FFPE archived samples with no attached patient information. Normal lung tissue and the lung tissue from COVID-19 patients were provided by Dr.

 

Alexandar Tzankov and were collected from deceased COVID-19 patients hospitalized at the University Hospital Basel, Switzerland, as described previously (Menter *et al*, 2020). The mean post-mortem interval from death to an autopsy was 33.3 h (11–84.5). All samples were reviewed by the institutional ethics board and determined to qualify as non-human subjects' research.

The patient samples in form of the nasopharyngeal swabs were procured from the TSB BioBank which is part of the Translational Science BioCore (TSB) affiliated with the UW Carbone Cancer Center (UWCCC), University of Wisconsin-Madison School of Medicine and Public Health, Madison, Wisconsin, USA. Informed consent was obtained from all subjects and the experiments conformed to the principles set out in the WMA Declaration of Helsinki and the Department of Health and Human Services Belmont Report. Nasopharyngeal swabs from patients positive for COVID-19 were selected based on the report from EPIC Beaker module that included results of coronavirus disease 2019 (COVID-19), PCR (UWH) test and patient demographics. Coronavirus disease 2019 (COVID-19), PCR (UWH) test was performed on nasopharyngeal swabs on Molecular Genprobe Panther Fusion platform in Molecular Diagnostics Lab. Chart review was performed on admitted patients negative for COVID-19, and patients who presented to ED with symptoms consistent with COVID-19 infection, such as fever, cough, and dyspnea, were included in the cohort. Chart review was performed on admitted patients positive for COVID-19, and patients who had only 1 positive COVID test result in their clinical history on the day of their admission were included in the cohort. The blood samples for individual patients were pulled daily for the week and then once every week for the patient duration of the hospital stay (max 1 month).

**The paper explained**

**Problem**
Assessing the degree of risk for the development of severe COVID-19 is an important consideration in the management of the current pandemic. Such a tool would be useful for the triage of patients that test positive for COVID-19, thus enabling those likely to develop severe symptoms closer monitoring and earlier access to hospitalization and intensive care.

**Results**
We performed post-mortem analysis of COVID-19-infected lung tissues and determined that the cell fitness marker, *hFwe-Lose* can precede the host immune response to infection. More importantly, the expression levels of *hFwe-Lose* outperformed conventional methods in predicting outcomes in COVID-19 patients (hospitalization or death).

**Impact**
The cell fitness marker *hFwe-Lose* accurately predicts outcomes in COVID-19 patients. This demonstrates how tissue fitness pathways dictate the response to infection and disease, and their utility in managing the current COVID-19 pandemic.

### Data analysis and biostatistics

The RT–qPCR measurements were performed in technical triplicates, while being blinded to the information about the sample. The technical triplicates (Ct values) were averaged before calculation of the dCt values. Additionally, the sample order in respective cohorts was randomized before the RT–qPCR measurements.

Data were analyzed using R 3.6.1 (R-Core-Team, 2020). *hFwe-Lose* expression, age, and outcome were analyzed using an asymptotic model of the form:

$$E(age) = A \cdot \left(1 - \exp\left(-\exp\left(r + d \cdot I_{non-hosp.}\right) \cdot age\right)\right).$$

where $E$ is the relative expression of *hFwe-Lose*, *age* is the patient's age, $A$ is the value of the asymptote, $r$ is a rate parameter, $d$ is a coefficient of the non-hospitalized group on the rate parameter, and $I_{non\text{-}hosp.}$ is an indicator variable which is 1 if the group is "non-hospitalized" and 0 otherwise. The model was fit to the retrospective data. The fit did not converge when the outcome group "death" was included, so only data from non-hospitalized and hospitalized patients were used. $R^2$ is calculated as the ratio of the residual and the total variance.

The probability of hospitalization or death and *hFwe-Lose* expression was analyzed using logistic models. Predictor variable was the logarithm of *hFwe-Lose* expression. The model included age (linear, continuous) and sex (male/female), the concentrations of blood markers (log-linear), and the presence of major known comorbidities (yes/no). The observed statistical significance of *hFwe-Lose* expression was obtained from likelihood ratio tests of the respective coefficient within the statistical model.

The classification and regression tree (CART) was created using the "rpart" R package (Therneau & Atkinson, 2019), using standard parameters. The analysis incorporated all relevant information about patients (*hFwe-Lose* expression, age, sex, presence of comorbidities (diabetes, COPD, obesity, cardiomyopathy, heart failure, hypertension)). All patients were included in the CART analysis ($n = 283$). The number of splits was automatically determined based on the saturation of the coefficient of determination, as well as on the plateauing of the relative error.

The receiver operating characteristic (ROC) curves were created using the "ROCit" R package (Khan & Brandenburger, 2020), using standard parameters. Cut-off values were determined as the threshold value with the lowest residual between true-positive rate (TPR) and false-positive rate (FPR) curve parameters (Youden index). The cut-offs from the ROC analysis were used to create confusion matrices by comparing predicted and true outcomes.

### R packages

Attached packages are as follows: randomForest_4.6-14, party_1.3-7, strucchange_1.5-2, sandwich_3.0-1, zoo_1.8-8, modeltools_0.2-23, mvtnorm_1.1-1, rpart_4.1-15, beeswarm_0.2.3, lemon_0.4.5, ROCit_2.1.1, openxlsx_4.2.3, ggrepel_0.9.1, readxl_1.3.1, tidyr_1.1.2, plyr_1.8.6, readr_1.4.0, ggplot2_3.3.3, dplyr_1.0.4, RColorBrewer_1.1-2, viridis_0.5.1, viridisLite_0.3.0, and gplots_3.1.0.

References are available at the CRAN website "packages" section (The Comprehensive R Archive Network).

### Logistic regression with scikit-learn

Logistic regression implemented in scikit-learn (Pedregosa *et al*, 2011) 23.1 in Python 3.7.4 was used as the machine learning model

to compare *hFwe-Lose* and other factors. Class weights of all models were set as "balanced" to assign proper weight to patients. All other parameters were set with default values. L2 regularization was used by default. Following loss function was used to fit our models:

$$\min_{\omega,\ c} \frac{1}{2}\omega^T\omega + C\sum_{i=1}^{n} w_i \log\left(\exp\left(-y_i\left(X_i^T\omega + c\right)\right) + 1\right)$$

$$w_i = M_{sample}/M_{class}M_{class\ i}$$

where $\omega$ is the coefficient vector, $c$ is the intercept, and $y_i$ is the label of the $i$-th sample. The value of $y_i$ can be 1 and $-1$. $X_i$ is the input vector of the $i$-th sample. $w_i$ is the weight for the $i$-th sample. Superscript $T$ refers to transposition. The default value of $w_i$ is 1. In the "balanced" model, w of the $i$-th sample is calculated by the second equation. $M_{sample}$ is the number of all samples. $M_{class}$ is the number of class. In our case, $M_{class}$ is 2. $M_{class\ i}$ is the number of the samples that are the same class of the $i$-th sample. $C$ is a constant to specify the regularization strength. $C$ is set as 1 by default.

All 283 patients were used to compare *hFwe-Lose* and age combined with comorbidities in predicting hospitalization and death. Among the 283 patients, 203 of them are retrospective and 80 of them are prospective. Among the 203 retrospective patients, 10 of them died and 116 of them were hospitalized. Among the 80 prospective patients, 11 of them died and 61 of them were hospitalized. When comparing *hFwe-Lose*, age combined with comorbidities, and four known biomarkers in predicting death, 105 patients who had information of all the four biomarkers were used. Among the 105 patients, 86 of them are retrospective and 19 of them are prospective. Among the 86 retrospective patients, 9 of them died. Among the 19 prospective patients, 6 of them died. When comparing *hFwe-Lose* and four known biomarkers separately in predicting death, patients who had information of each biomarker were used. In the comparison between *hFwe-Lose* and Ferritin, 91 retrospective records were used for training. 10 of the 91 patients died. 24 prospective records were used for validation. 8 of the 24 patients died. In the comparison between *hFwe-Lose* and D-dimer, 94 retrospective records were used for training. 9 of the 94 patients died. 26 prospective records were used for validation. 9 of the 26 patients died. In the comparison between *hFwe-Lose* and CRP, 101 retrospective records were used for training. 10 of the 101 patients died. 26 prospective records were used for validation. 8 of the 26 patients died. In the comparison between *hFwe-Lose* and neutrophil–lymphocyte ratio, 120 retrospective records were used for training. 10 of the 120 patients died. 33 prospective records were used for validation. 10 of the 33 patients died.

## Data availability

This study includes no data deposited in external repositories.

**Expanded View** for this article is available online.

### Acknowledgements

This study was supported by Swiss Cancer League, Seeds of Science, UAMS, SNSF, Fundação para a Ciência e a Tecnologia, Fundamental Mandates (Stichting tegen Kanker—Fondation contre le Cancer) to R.G.; ERC, SNSF, Josef Steiner Cancer Research Foundation, Swiss Cancer League, and Champalimaud Foundation to E. Mo.; Novo Nordisk Foundation [NNF17CC0027852] and Lundbeck Foundation [R313–2019–421] to K.J.W.; La Caixa Funding LCF/BQ/PR20/11770006 to E. Ma.; FIS (Ministry of Health), Madrid, Spain, Grant PI17/01981 to A.L-.B.;. DFG Clinical Research Unit KFO 309, and the German Center for Lung Research (DZL), DFG Collaborative Research Center SFB1021 to J.W.; Deutsche Forschungsgemeinschaft (DFG) Clinical Research Group KFO309 TP08, the DFG-funded Excellence Cluster Cardio-Pulmonary Institute (CPI), and the German Center for Lung Research (DZL) to T.B.; Botnar Research Centre for Child Health (BRCCH) (FTC-2020-10) and SNSF to A.T., T.M., M.M. & J.D.H.; Support from the Thelma Newmeyer Corman Chair in Cancer Research, the VCU Commercialization Fund and NIH/NCI R01 CA259599 to P.B.F.; Fundação para a Ciência e a Tecnologia Grant 2020.05319.BD to A.M.P.; Fundação para a Ciência e a Tecnologia Grant SFRH/BD/139138/2018 to R.C.D.; Fundação para a Ciência e a Tecnologia and PGCD—Programa de Pós-Graduação Ciência para o Desenvolvimento *Grant* SFRH / BD/135367/2017 to D.C.; Tumor Microenvironment (TME) CoBRE Grant (NIH/NIGMS P20GM121322), West Virginia IDeA-CTR (NIH/NIGMS 2U54 GM104942-03), National Science Foundation (NSF/1920920, NSF/1761792), West Virginia IDeA Network of Biomedical Research Excellence (WV-INBRE) (NIH/NIGMS P20GM103434) to I.M.; and Adelson Medical Research Foundation, NIH P50 SPORE CA228991, Honorable Tina Brozman Foundation for Ovarian Cancer Research to R.D. The author(s) thank the Translational Science Biocore (TSB) BioBank of the University of Wisconsin Carbone Cancer Center and the clinical laboratory at the University of Wisconsin Hospitals for providing specimens and associated clinical data used in this research. The Translational Science Biocore (TSB) BioBank of the University of Wisconsin Carbone Cancer Center and the clinical laboratory at the University of Wisconsin Hospitals are supported by P30 CA014520 and received dedicated support for COVID-associated work from the University of Wisconsin School of Medicine and Public Health. We thank Taylor M. Parker for thorough reading of the manuscript. We thank Dr. Timothy Eubank at WVU for his kind support with the organization and purchase of RNA extraction kits (West Virginia Clinical and Translational Science Institute (WVCTSI) Grant GM104942). We thank Aenya Gogna for supporting the entire process involving research activity and writing of the manuscript. We thank Sunita Gogna and Keshav Chandra Gogna who suffered major COVID-19 disease, and they continuously discussed their disease progression over a period of 4 months. This helped our team in deeper understanding of the subject. We sincerely thank Mr. Luís Nunes from the Ritz Carlton, Penha Longa Resort Estrada da Lagoa Azul, Linhó, Sintra, Portugal. The Penha Longa management regularly arranged for the meeting space and facilitated important discussions between collaborators during the time of total shutdown due to the declared national emergency in Portugal.

### Author contributions

MY performed all analysis, wrote the paper, and helped with study design and concept; EM performed qPCR while remaining blind to samples and clinical information and helped with study design and concept; JW performed and supervised all biostatistical analysis, supervised and contributed to data visualization, and interpretation, wrote the manuscript, and helped in data presentation; KRS performed interpretation of the clinical and bio statistical data, wrote the manuscript, and helped with study design and concept; AMP performed qPCR while remaining blind to samples and clinical information and helped with preparation of the animations; LL performed machine learning clinical analysis, wrote the manuscript, and helped in preparation of figures; DC performed qPCR while remaining blind to samples and clinical information and helped with preparation of the animations; EN helped with procurement of sample from TSB Biobank and coordinated shipment of all samples and collection of clinical data; MTW helped with RNA extraction from

 

patient nasopharyngeal swab material; ESR helped with RNA extraction from patient nasopharyngeal swab material; IR helped with procurement of lung FFPE samples and collected clinical information about comorbidity status of all samples; RC-D performed qPCR while remaining blind to samples and clinical information and helped with preparation of the animations; CJP helped with manuscript writing and biostatistical analysis; MN helped with manuscript writing and biostatistical analysis; KG helped with procurement of sample from TSB Biobank and helped with organization of the manuscript and preparation of the animations; SC helped with procurement of sample from TSB Biobank and helped with organization of the manuscript and preparation of the animations; TB provided supervision to MY; RP helped with histological reading of the COVID-19 deceased patients; MSP helped with physiological readings for the CT scans of the COVID-19 deceased patients; TM collected disease-free lung patient samples and COVID-19 autopsy samples; MM collected disease-free lung patient samples and coordinated logistics and archiving; JDH collected disease-free lung patient samples and COVID-19 autopsy samples; MT helped in study design and, provided administrative support for sample collection; KDG helped with the collection of the clinical data associated with nasopharyngeal swabs, customized reports, performed chart review, and adapted clinical workflow to retrieve appropriate specimens; KAM helped with procurement of patient samples in the form of nasopharyngeal swabs from Translational Science Biocore (TSB) BioBank of the University of Wisconsin Carbone Cancer Center, SMM- helped with procurement of patient samples in the form of nasopharyngeal swabs from Translational Science Biocore (TSB) BioBank of the University of Wisconsin Carbone Cancer Center, supervised the collection of patient information; LKM helped with procurement of patient samples in the form of nasopharyngeal swabs from Translational Science Biocore (TSB) BioBank of the University of Wisconsin Carbone Cancer Center and helped with organization of the patient data collection; EAR helped with procurement of patient samples in the form of nasopharyngeal swabs from Translational Science Biocore (TSB) BioBank of the University of Wisconsin Carbone Cancer Center and helped with histological reading of COVID-19 deceased patients; ALB helped with study design and supervised; IR helped with collection of lung patient tissue samples and helped with histological reading of COVID-19 deceased patients; RD helped in organizing the procurement of RNA Extraction kits and helped with funding the research; MA helped in organizing the procurement of COVID-19 nasopharyngeal swabs and provided input on interpretation of clinical data; PBF helped in organizing the procurement of COVID-19 nasopharyngeal swabs from Translational Science Biocore (TSB) BioBank of the University of Wisconsin Carbone Cancer Center and helped with funding the research; SRG helped in organizing the procurement of COVID-19 nasopharyngeal swabs from Translational Science Biocore (TSB) BioBank of the University of Wisconsin Carbone Cancer Center and helped with funding the research; AKG helped with manuscript writing supported study design and provided key input on interpretation of clinical data; AK helped with interpretation of clinical and bio statistical data and helped in writing the manuscript; IM helped with RNA extraction from patient nasopharyngeal swab material and supervised MTW and ESR; CBM helped with manuscript writing supported study design and provided key input on interpretation of clinical data; BT helped interpretation of clinical and biostatistical data and helped in writing the manuscript; MSW helped with manuscript writing supported study design and provided key input on interpretation of clinical data; KJW supervised LL, supervised and designed machine meaning tools to analyze clinical results, funded the research, and provided organizational support; AT helped in study design, provided administrative support for sample collection, collected disease-free lung patient samples and COVID-19 autopsy samples, performed histopathologic analysis and caspase IHC, partially wrote the manuscript, funded the research, provided organizational support, and helped with procurement of COVID-19 nasopharyngeal swabs from Translational Science Biocore (TSB) BioBank of the University of Wisconsin Carbone Cancer Center; EM provided the initial ideas for the project, helped with study design and manuscript writing, funded the research, and provided organizational support; RG designed the study, provided the initial ideas for the project, designed the study concept, funded the research, wrote the manuscript, procured patient samples, supervised the research, and established all required international collaborations.

### Conflict of interest

The authors declare that they have no conflict of interest.

## References


Ackermann M, Verleden SE, Kuehnel M, Haverich A, Welte T, Laenger F, Vanstapel A, Werlein C, Stark H, Tzankov A *et al* (2020) Pulmonary vascular endothelialitis, thrombosis, and angiogenesis in Covid-19. *N Engl J Med* 383: 120–128

Akieda Y, Ogamino S, Furuie H, Ishitani S, Akiyoshi R, Nogami J, Masuda T, Shimizu N, Ohkawa Y, Ishitani T (2019) Cell competition corrects noisy Wnt morphogen gradients to achieve robust patterning in the zebrafish embryo. *Nat Commun* 10: 4710

Barlin JN, Zhou Q, St Clair CM, Iasonos A, Soslow RA, Alektiar KM, Hensley ML, Leitao Jr MM, Barakat RR, Abu-Rustum NR (2013) Classification and regression tree (CART) analysis of endometrial carcinoma: seeing the forest for the trees. *Gynecol Oncol* 130: 452–456

Barton LM, Duval EJ, Stroberg E, Ghosh S, Mukhopadhyay S (2020) COVID-19 autopsies, Oklahoma, USA. *Am J Clin Pathol* 153: 725–733

Bennett JM, Reeves G, Billman GE, Sturmberg JP (2018) Inflammation-Nature's way to efficiently respond to all types of challenges: implications for understanding and managing "the epidemic" of chronic diseases. *Front Med* 5: 316

Bondar T, Medzhitov R (2010) p53-mediated hematopoietic stem and progenitor cell competition. *Cell Stem Cell* 6: 309–322

Bruens L, Ellenbroek SIJ, Suijkerbuijk SJE, Azkanaz M, Hale AJ, Toonen P, Flanagan DJ, Sansom OJ, Snippert HJ, van Rheenen J (2020) Calorie restriction increases the number of competing stem cells and decreases mutation retention in the intestine. *Cell Rep* 32: 107937

Cheng L, Li H, Li L, Liu C, Yan S, Chen H, Li Y (2020) Ferritin in the coronavirus disease 2019 (COVID-19): a systematic review and meta-analysis. *J Clin Lab Anal* 34: e23618

Coelho DS, Moreno E (2020) Neuronal selection based on relative fitness comparison detects and eliminates amyloid-beta-induced hyperactive neurons in *Drosophila*. *iScience* 23: 101468

Elezkurtaj S, Greuel S, Ihlow J, Michaelis EG, Bischoff P, Kunze CA, Sinn BV, Gerhold M, Hauptmann K, Ingold-Heppner B *et al* (2021) Causes of death and comorbidities in hospitalized patients with COVID-19. *Sci Rep* 11: 4263

Flanagan DJ, Pentinmikko N, Luopajärvi K, Willis NJ, Gilroy K, Raven AP, Mcgarry L, Englund JI, Webb AT, Scharaw S *et al* (2021) NOTUM from Apc-mutant cells biases clonal competition to initiate cancer. *Nature* 594: 430–435

Flerlage T, Boyd DF, Meliopoulos V, Thomas PG, Schultz-Cherry S (2021) Influenza virus and SARS-CoV-2: pathogenesis and host responses in the respiratory tract. *Nat Rev Microbiol* 19: 425–441

Furman D, Campisi J, Verdin E, Carrera-Bastos P, Targ S, Franceschi C, Ferrucci L, Gilroy DW, Fasano A, Miller GW *et al* (2019) Chronic

inflammation in the etiology of disease across the life span. *Nat Med* 25: 1822 – 1832

Gao M, Piernas C, Astbury NM, Hippisley-Cox J, O'Rahilly S, Aveyard P, Jebb SA (2021) Associations between body-mass index and COVID-19 severity in 6.9 million people in England: a prospective, community-based, cohort study. *Lancet Diabetes Endocrinol* 9: 350 – 359

Grifoni E, Valoriani A, Cei F, Vannucchi V, Moroni F, Pelagatti L, Tarquini R, Landini G, Masotti L (2021) The CALL score for predicting outcomes in patients with COVID-19. *Clin Infect Dis* 72: 182 – 183

Guan W-J, Liang W-H, Zhao YI, Liang H-R, Chen Z-S, Li Y-M, Liu X-Q, Chen R-C, Tang C-L, Wang T *et al* (2020) Comorbidity and its impact on 1590 patients with COVID-19 in China: a nationwide analysis. *Eur Respir J* 55: 2000547

Huang C, Wang Y, Li X, Ren L, Zhao J, Hu YI, Zhang LI, Fan G, Xu J, Gu X *et al* (2020a) Clinical features of patients infected with 2019 novel coronavirus in Wuhan, China. *Lancet* 395: 497 – 506

Huang I, Pranata R, Lim MA, Oehadian A, Alisjahbana B (2020b) C-reactive protein, procalcitonin, D-dimer, and ferritin in severe coronavirus disease-2019: a meta-analysis. *Ther Adv Respir Dis* 14: 1753466620937175

Khan MRA, Brandenburger T (2020) ROCit: performance assessment of binary classifier with visualization. R package version 211

Konopka KE, Wilson A, Myers JL (2020) Postmortem lung findings in a patient with asthma and coronavirus disease 2019. *Chest* 158: e99 – e101

Li S, Zhang Y, Guan Z, Li H, Ye M, Chen XI, Shen J, Zhou Y, Shi Z-L, Zhou P *et al* (2020) SARS-CoV-2 triggers inflammatory responses and cell death through caspase-8 activation. *Signal Transduct Target Ther* 5: 235

Liu K, Chen Y, Lin R, Han K (2020) Clinical features of COVID-19 in elderly patients: a comparison with young and middle-aged patients. *J Infect* 80: e14 – e18

Liu N, Matsumura H, Kato T, Ichinose S, Takada A, Namiki T, Asakawa K, Morinaga H, Mohri Y, De Arcangelis A *et al* (2019) Stem cell competition orchestrates skin homeostasis and ageing. *Nature* 568: 344 – 350

Longmore DK, Miller JE, Bekkering S, Saner C, Mifsud E, Zhu Y, Saffery R, Nichol A, Colditz G, Short KR *et al* (2021) Diabetes and overweight/obesity are independent, nonadditive risk factors for in-hospital severity of COVID-19: an international, multicenter retrospective meta-analysis. *Diabetes Care* 44: 1281 – 1290

Madan E, Pelham CJ, Nagane M, Parker TM, Canas-Marques R, Fazio K, Shaik K, Yuan Y, Henriques V, Galzerano A *et al* (2019) Flower isoforms promote competitive growth in cancer. *Nature* 572: 260 – 264

Menter T, Haslbauer JD, Nienhold R, Savic S, Hopfer H, Deigendesch N, Frank S, Turek D, Willi N, Pargger H *et al* (2020) Postmortem examination of COVID-19 patients reveals diffuse alveolar damage with severe capillary congestion and variegated findings in lungs and other organs suggesting vascular dysfunction. *Histopathology* 77: 198 – 209

Merino MM, Levayer R, Moreno E (2016) Survival of the fittest: essential roles of cell competition in development, aging, and cancer. *Trends Cell Biol* 26: 776 – 788

Merino MM, Rhiner C, Portela M, Moreno E (2013) "Fitness fingerprints" mediate physiological culling of unwanted neurons in *Drosophila*. *Curr Biol* 23: 1300 – 1309

Merino MM, Rhiner C, Lopez-Gay JM, Buechel D, Hauert B, Moreno E (2015) Elimination of unfit cells maintains tissue health and prolongs lifespan. *Cell* 160: 461 – 476

Milner JJ, Beck MA (2012) The impact of obesity on the immune response to infection. *Proc Nutr Soc* 71: 298 – 306

Moreno E (2008) Is cell competition relevant to cancer? *Nat Rev Cancer* 8: 141 – 147

Niccoli T, Partridge L (2012) Ageing as a risk factor for disease. *Curr Biol* 22: R741 – 752

Parker T, Madan E, Gupta K, Moreno E, Gogna R (2020) Cell competition spurs selection of aggressive cancer cells. *Trends Cancer* 6: 732 – 736

Pedregosa F, Varoquaux G, Gramfort A, Michel V, Thirion B, Grisel O, Blondel M, Prettenhofer P, Weiss R, Dubourg V *et al* (2011) Scikit-learn: machine learning in Python. *J Mach Learn Res* 12: 2825 – 2830

R-Core-Team (2020) *R: A language and environment for statistical computing*. Vienna, Austria: R Foundation for Statistical Computing

Ren Y, Shu T, Wu DI, Mu J, Wang C, Huang M, Han Y, Zhang X-Y, Zhou W, Qiu Y *et al* (2020) The ORF3a protein of SARS-CoV-2 induces apoptosis in cells. *Cell Mol Immunol* 17: 881 – 883

Rhiner C, Lopez-Gay JM, Soldini D, Casas-Tinto S, Martin FA, Lombardia L, Moreno E (2010) Flower forms an extracellular code that reveals the fitness of a cell to its neighbors in *Drosophila*. *Dev Cell* 18: 985 – 998

Richardson S, Hirsch JS, Narasimhan M, Crawford JM, McGinn T, Davidson KW, Barnaby DP, Becker LB, Chelico JD, Cohen SL *et al* (2020) Presenting characteristics, comorbidities, and outcomes among 5700 patients hospitalized with COVID-19 in the New York City area. *JAMA* 323: 2052 – 2059

Sahu BR, Kampa RK, Padhi A, Panda AK (2020) C-reactive protein: a promising biomarker for poor prognosis in COVID-19 infection. *Clin Chim Acta* 509: 91 – 94

Sasaki A, Nagatake T, Egami R, Gu G, Takigawa I, Ikeda W, Nakatani T, Kunisawa J, Fujita Y (2018) Obesity suppresses cell-competition-mediated apical elimination of RasV12-transformed cells from epithelial tissues. *Cell Rep* 23: 974 – 982

Sato N, Yako Y, Maruyama T, Ishikawa S, Kuromiya K, Tokuoka SM, Kita Y, Fujita Y (2020) The COX-2/PGE2 pathway suppresses apical elimination of RasV12-transformed cells from epithelia. *Commun Biol* 3: 132

Short KR, Kroeze E, Fouchier RAM, Kuiken T (2014) Pathogenesis of influenza-induced acute respiratory distress syndrome. *Lancet Infect Dis* 14: 57 – 69

Therneau T, Atkinson B (2019) rpart: recursive partitioning and regression trees. R Package Version : 41–15

van Neerven SM, de Groot NE, Nijman LE, Scicluna BP, van Driel MS, Lecca MC, Warmerdam DO, Kakkar V, Moreno LF, Vieira Braga FA *et al* (2021) Apc-mutant cells act as supercompetitors in intestinal tumour initiation. *Nature* 594: 436 – 441

Vermeulen L, Morrissey E, van der Heijden M, Nicholson AM, Sottoriva A, Buczacki S, Kemp R, Tavare S, Winton DJ (2013) Defining stem cell dynamics in models of intestinal tumor initiation. *Science* 342: 995 – 998

Wang Y, Schulte BA, LaRue AC, Ogawa M, Zhou D (2006) Total body irradiation selectively induces murine hematopoietic stem cell senescence. *Blood* 107: 358 – 366

Williamson EJ, Walker AJ, Bhaskaran K, Bacon S, Bates C, Morton CE, Curtis HJ, Mehrkar A, Evans D, Inglesby P *et al* (2020) Factors associated with COVID-19-related death using OpenSAFELY. *Nature* 584: 430 – 436

Xu Z, Shi L, Wang Y, Zhang J, Huang L, Zhang C, Liu S, Zhao P, Liu H, Zhu LI *et al* (2020) Pathological findings of COVID-19 associated with acute respiratory distress syndrome. *Lancet Respir Med* 8: 420 – 422

Yang AP, Liu JP, Tao WQ, Li HM (2020a) The diagnostic and predictive role of NLR, d-NLR and PLR in COVID-19 patients. *Int Immunopharmacol* 84: 106504

Yang J, Zheng Y, Gou X, Pu K, Chen Z, Guo Q, Ji R, Wang H, Wang Y, Zhou Y (2020b) Prevalence of comorbidities and its effects in patients infected with SARS-CoV-2: a systematic review and meta-analysis. *Int J Infect Dis* 94: 91 – 95

Yum MK, Han S, Fink J, Wu S-H, Dabrowska C, Trendafilova T, Mustata R, Chatzeli L, Azzarelli R, Pshenichnaya I *et al* (2021) Tracing oncogene-

 

driven remodelling of the intestinal stem cell niche. *Nature* 594: 442–447

Ziegler CGK, Miao VN, Owings AH, Navia AW, Tang Y, Bromley JD, Lotfy P, Sloan M, Laird H, Williams HB *et al* (2021) Impaired local intrinsic immunity to SARS-CoV-2 infection in severe COVID-19. *Cell* 184: 4713–4733.e22



**List of affiliations**

Michail Yekelchyk[1]; Esha Madan[2]; Jochen Wilhelm[3,4]; Kirsty R Short[5]; António M Palma[2]; Linbu Liao[6]; Denise Camacho[2]; Everlyne Nkadori[7]; Michael T Winters[8]; Emily S Rice[8]; Inês Rolim[2]; Raquel Cruz-Duarte[9]; Christopher J Pelham[10]; Masaki Nagane[11]; Kartik Gupta[12]; Sahil Chaudhary[12]; Thomas Braun[1,13]; Raghavendra Pillappa[14]; Mark S Parker[15]; Thomas Menter[16]; Matthias Matter[16]; Jasmin Dionne Haslbauer[16]; Markus Tolnay[16]; Kornelia D Galior[7]; Kristina A Matkowskyj[7]; Stephanie M McGregor[7]; Laura K Muller[7]; Emad A Rakha[17]; Antonio Lopez-Beltran[2,18]; Ronny Drapkin[19,20,21]; Maximilian Ackermann[22,23]; Paul B Fisher[24,25,26]; Steven R Grossman[27,28]; Andrew K Godwin[29,30]; Arutha Kulasinghe[31]; Ivan Martinez[8]; Clay B Marsh[8]; Benjamin Tang[32]; Max S Wicha[33,34]; Kyoung Jae Won[6,35]; Alexandar Tzankov[16]; Eduardo Moreno[2]; Rajan Gogna[2,6,35]

[1]Department of Cardiac Development and Remodelling, Max Planck Institute for Heart and Lung Research, Bad Nauheim, Germany. [2]Champalimaud Centre for the Unknown, Lisbon, Portugal. [3]Universities Giessen & Marburg Lung Center, German Center for Lung Research (DZL), Justus-Liebig-University, Giessen, Germany. [4]Institute for Lung Health (ILH), Universities Giessen & Marburg Lung Center, German Center for Lung Research (DZL), Justus-Liebig-University Giessen, Giessen, Germany. [5]School of Chemistry and Molecular Biosciences, The University of Queensland, Brisbane, Qld, Australia. [6]Biotech Research and Innovation Centre (BRIC), University of Copenhagen, Copenhagen N, Denmark. [7]Department of Pathology and Laboratory Medicine, University of Wisconsin Carbone Cancer Center, University of Wisconsin-Madison School of Medicine and Public Health, Madison, WI, USA. [8]Department of Microbiology, Immunology & Cell Biology and WVU Cancer Institute, West Virginia University, Morgantown, WV, USA. [9]Instituto de Medicina Molecular João Lobo Antunes, Faculdade de Medicina, Universidade de Lisboa, Lisboa, Portugal. [10]Eurofins Panlabs Inc., St. Charles, MO, USA. [11]Department of Biochemistry, School of Veterinary Medicine, Azabu University, Kanagawa, Japan. [12]Department of Surgery, School of Medicine and Public Health, University of Wisconsin, Madison, WI, USA. [13]Member of the German Center for Cardiovascular Research (DZHK), Greifswald, Germany. [14]Department of Pathology, Virginia Commonwealth University School of Medicine, Richmond, VA, USA. [15]Department of Diagnostic Radiology and Internal Medicine, Early Detection Lung Cancer Screening Program, Thoracic Imaging Division, Thoracic Imaging Fellowship Program, VCU Health Systems, Richmond, VA, USA. [16]Pathology, Institute of Medical Genetics and Pathology, University Hospital Basel and University of Basel, Basel, Switzerland. [17]Division of Cancer and Stem Cells, Department of Pathology, School of Medicine, Nottingham University Hospitals, University of Nottingham, Nottingham, UK. [18]Department of Morphological Sciences, Cordoba University, Cordoba, Spain. [19]Penn Ovarian Cancer Research Center, Department of Obstetrics and Gynecology, University of Pennsylvania Perelman School of Medicine, Philadelphia, PA, USA. [20]Graduate Program in Cell and Molecular Biology, University of Pennsylvania Perelman School of Medicine, Philadelphia, PA, USA. [21]Basser Center for BRCA, Abramson Cancer Center, University of Pennsylvania School of Medicine, Philadelphia, PA, USA. [22]Institute of Pathology and Molecular Pathology, Helios University Clinic Wuppertal, University of Witten/Herdecke, Wuppertal, Germany. [23]Institute of Functional and Clinical Anatomy, University Medical Center of the Johannes Gutenberg-University Mainz, Mainz, Germany. [24]Department of Human and Molecular Genetics, School of Medicine, Virginia Commonwealth University, Richmond, VA, USA. [25]Massey Cancer Center, Virginia Commonwealth University, Richmond, VA, USA. [26]Department of Human and Molecular Genetics, Institute of Molecular Medicine, School of Medicine, Virginia Commonwealth University, Richmond, VA, USA. [27]Department of Internal Medicine, Keck School of Medicine, Norris Comprehensive Cancer Center, Los Angeles, CA, USA. [28]University of Southern California, Los Angeles, CA, USA. [29]Department of Pathology and Laboratory Medicine, University of Kansas Medical Center, Kansas City, KS, USA. [30]University of Kansas Cancer Center, Kansas City, KS, USA. [31]The University of Queensland Diamantina Institute, The University of Queensland, Brisbane, Qld, Australia. [32]Department of Intensive Care Medicine, Nepean Hospital, Penrith, NSW, Australia. [33]Rogel Cancer Center, University of Michigan, Ann Arbor, MI, USA. [34]Department of Internal Medicine, Michigan Medicine, University of Michigan, Ann Arbor, MI, USA. [35]Faculty of Health and Medical Sciences, Novo Nordisk Foundation Center for Stem Cell Biology, DanStem, University of Copenhagen, Copenhagen N, Denmark.

CHAPTER FIVE

# SPARC-p53: The double agents of cancer

**Denise Camacho[a,†], Joana P. Jesus[a,†], António M. Palma[a,‡], Sofia A. Martins[a,‡], Alexandre Afonso[a,‡], Maria Leonor Peixoto[a], Christopher J. Pelham[b], Eduardo Moreno[a,*], Rajan Gogna[a,*]**

[a]Champalimaud Centre for the Unknown, Lisbon, Portugal
[b]Eurofins Panlabs Inc., St. Charles, MO, United States
*Corresponding authors: e-mail address: eduardo.moreno@research.fchampalimaud.org; rajan.gogna@research.fchampalimaud.org

## Contents



## Abstract

Cancer is a complex disease with high incidence and mortality rates. The important role played by the tumor microenvironment in regulating oncogenesis, tumor growth, and metastasis is by now well accepted in the scientific community. SPARC is known to participate in tumor–stromal interactions and impact cancer growth in ambiguous ways, which either enhance or suppress cancer aggressiveness, in a context-dependent manner. p53 transcription factor, a well-established tumor suppressor, has been reported to promote tumor growth in certain situations, such as hypoxia, thus

† These authors contributed equally for first author position.
‡ These authors contributed equally for second author position.

*Advances in Cancer Research*, Volume 148
ISSN 0065-230X
https://doi.org/10.1016/bs.acr.2020.05.004

displaying a duality in its action. Although both proteins are being tested in clinical trials, the synergistic relation between them is yet to be explored in clinical practice. In this review, we address the controversial roles of SPARC and p53 as double agents in cancer, briefly summarizing the interaction found between these two molecules and its importance in cancer.

## 1. Introduction

Secreted protein acidic and rich in cysteine (SPARC), also called Osteonectin or BM-40, is involved in cell–cell interactions, cell-extracellular matrix (ECM) remodeling and bone mineralization (Melouane, Yoshioka, Kanzaki, & St-Amand, 2019; Omi, Yamanouchi, Nakamura, Matsuwaki, & Nishihara, 2019; Ramu et al., 2019; Sangaletti et al., 2014). SPARC physiological functions include the maintenance of a wide range of cells and tissues, including bone, pancreatic tissue, nerve tissue and contractible cells like cardiomyocytes and vascular smooth cells (Atorrasagasti et al., 2019; Bradshaw & Sage, 2001; Deckx et al., 2019; Li et al., 2019; Melouane et al., 2019; Okura et al., 2019; Wang et al., 2019). Due to its wide range of functions, SPARC also plays a key role in tumor growth, invasion and metastasis by remodeling the extracellular matrix (ECM) and promoting epithelial-mesenchymal transition (EMT) (Bradshaw & Sage, 2001; Deckx et al., 2019; Okura et al., 2019; Podhajcer et al., 2008; Wang et al., 2019). However, SPARC expression depends on cancer type and its stages, providing different outcomes (Nagai et al., 2011; Zhu et al., 2016) since it may act as a tumor-suppressor (Sailaja et al., 2013) or a tumor-promoter (Ledda et al., 1997). The invasiveness of a tumor and its ability to form metastasis is one of the most detrimental characteristics of cancer. Numerous clinical studies have observed a connection between SPARC, metastasis and Disease-Free Survival (DFS), observations that support its future use as a biomarker (Guttlein et al., 2017; Nagai et al., 2011; Szynglarewicz et al., 2016; Witkiewicz et al., 2010; Zhu et al., 2016). Some studies identified SPARC in the serum of cancer patients, highlighting its possible application in liquid biopsies (Bloomston et al., 2007; Chung et al., 2006; Ikuta et al., 2005; Papapanagiotou et al., 2018). Due to its clinical relevance in cancer and its link to EMT and invasion, several SPARC-based clinical trials are in progress. A phase-II trial study in metastatic breast cancer patients is assessing SPARC as an exploratory biomarker in primary tumors and as a predictor

response to treatment (ClinicalTrials.gov Identifier: NCT00733408). SPARC is also being examined as a biomarker in biopsies performed before and after perioperative chemotherapy in patients with oeso-gastric adenocarcinoma (ClinicalTrials.gov Identifier: NCT02486601).

TP53 expression is normally observed in cells suffering from genotoxic stress, DNA damage or chronic inflammation. p53, via its transcriptional activity, results in cell cycle arrest, DNA repair pathways or apoptosis in damaged but viable cells (Kastenhuber & Lowe, 2017). *TP53* is one of the most frequently mutated genes in cancer and its importance as a tumor suppressor is well understood and studied. Several evidences, however, suggest this protein can act as a double agent, since some isoforms and mutations may aid oncogenesis and cancer progression (Fujita et al., 2009; Oren & Rotter, 2010). Nonetheless, this role of p53 has not yet been considered in clinical practice, where it's still mainly regarded as a tumor suppressor. Still, some p53 mutated proteins accumulate in cancer cells (Oren & Rotter, 2010; Soussi & Wiman, 2015; Terzian et al., 2008), and several clinical trials are testing vaccines against these, for example, in ovarian cancer, in combination with other drugs (ClinicalTrials.gov Identifier: NCT02275039) (ClinicalTrials.gov Identifier: NCT00844506).

Another relevant matter is their synergistic action in cancer progression. SPARC has been implicated in the regulation of p53 expression, mainly downregulating the protein and preventing apoptosis (Fenouille, Puissant, et al., 2011; Fenouille, Robert, et al., 2011). Since p53 is already a well-established agent in oncology and SPARC's influence is beginning to be understood, this review aims to further explain the functions of these proteins and their novel interaction, thus drawing attention to the importance of research on this topic and its eventual application in the clinic.

## 2. Biological functions of SPARC

Several conditions can modulate SPARC expression. It is induced during morphogenesis, during cancer progression, and also in response to tissue injury, and tissue remodeling (Bradshaw, 2012). SPARC plays pivotal roles in cell–ECM interactions, ECM remodeling and growth factor signaling. In addition, SPARC activity is reported to influence pathways associated with proliferation, migration, apoptosis, adhesion, differentiation, wound healing and epithelial-mesenchymal transition (EMT) (Bradshaw & Sage, 2001; Deckx et al., 2019; Okura et al., 2019; Podhajcer et al., 2008; Wang et al., 2019). SPARC activity is responsible for modulating ILK

activity and regulating collagen deposition and maturation during ECM remodeling (Melouane et al., 2019; Omi et al., 2019; Ramu et al., 2019; Sangaletti et al., 2014). SPARC also increases production and activity of matrix metalloproteinases (McClung et al., 2007) and regulates the activity of growth factors including NGF-β, VEGF, FGF-2 and PDGF (Brekken & Sage, 2001; McClung et al., 2007; Okura et al., 2019).

## 2.1 SPARC in EMT and metastasis

EMT is a phenotypic change that happens throughout development, during fibrosis and wound healing, and also in cancer. EMT promotes cancer cell migration and invasion. It is characterized by loss of epithelial markers such as E-cadherin and induction of mesenchymal markers such as N-cadherin and vimentin (Bierie & Moses, 2006). TGF-β has a key role in EMT promotion and is involved in an activation loop with SPARC (Bierie & Moses, 2006; Drev et al., 2019; Sun et al., 2018; Tumbarello, Andrews, & Brenton, 2016), responsible for decreasing the levels of E-cadherin, Integrin β1, Focal Adhesion Kinase (FAK) and phosphorylated FAK, and for increasing the levels of N-cadherin, vimentin and the transcriptional activity of snail (Fig. 1) (Drev et al., 2019; Fenouille, Robert, et al., 2011; Lopez-Moncada, Torres, Castellon, & Contreras, 2019; Robert et al., 2006).

## 2.2 SPARC: A double agent in cancer

In different contexts, cancer cells and their neighboring stromal cells are influenced by many cellular factors and extrinsic factors within the

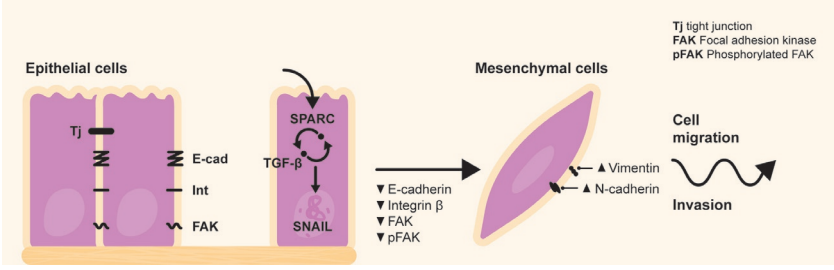


**Fig. 1** EMT promotes cancer cell migration and invasion. SPARC-TGFβ feedback loop negatively regulates the expression levels of the epithelial markers such as: E-cadherin, Integrin β1, Focal Adhesion Kinase (FAK) and phosphorylated FAK. It further increases the expression and activates transcription factor Snail, resulting in the expression of mesenchymal markers N-cadherin and vimentin, which facilitates cell migration and invasion.

microenvironment (Wang et al., 2017). Taken together, contradicting results have been reported on the role of SPARC in tumorigenesis and tumor progression (Ledda, Bravo, et al., 1997; Socha et al., 2009). Regarding cancer and adjacent tissues, SPARC is normally expressed by stromal cells (Socha et al., 2009), possessing both tumor suppressor and pro-oncogenic functions in various types of cancer (Chlenski & Cohn, 2010; Chua, Chan, & Tang, 2014; Nagaraju, Dontula, El-Rayes, & Lakka, 2014; Prada et al., 2007; Rempel et al., 1998). Its action in cancer is thought to be context-dependent and to rely on multiple aspects such as the biological activity of proteins, like matrix metalloproteinases, cathepsins and elastases, the type of tumor-initiating cell, the stage of cancer and the influence of the tumor microenvironment (Arnold & Brekken, 2009; Chua et al., 2014; Nagaraju et al., 2014). The divergent roles of SPARC in cancer are discussed below.

## 2.3 SPARC as a tumor promoter

It has been reported that SPARC displays a tumor-promoting role in cancers such as melanoma, glioblastoma, breast carcinoma, pancreatic ductal adenocarcinoma, ovarian cancer, non-small cell lung cancer and hepatocellular carcinoma (Arnold & Brekken, 2009; Briggs, Chamboredon, Castellazzi, Kerry, & Bos, 2002; Campo McKnight, Sosnoski, Koblinski, & Gay, 2006; Podhajcer et al., 2008; Socha et al., 2009). In melanoma, SPARC is highly expressed and correlates with greater proliferation and invasive phenotypic features associated with EMT (Ledda, Bravo, et al., 1997; Sosa et al., 2007). Conversely, its downregulation in melanoma cells results in decreased invasion and adhesion *in vitro*, and loss of tumorigenicity *in vivo* (Ledda et al., 1997). Of note, SPARC overexpression in neighboring fibroblasts has no effect on tumor growth, which suggests that it only affects tumor cells in melanoma (Prada et al., 2007). SPARC is also shown to be upregulated in glioblastoma cells and in invasive peripheral cells and it promotes a highly aggressive phenotype (Rempel et al., 1998; Rich et al., 2003). Mechanistically, SPARC promotes survival of glioma cells by increasing AKT activity. Activation of PI3K/AKT pro-survival pathway consequently inhibits caspase 3 activity, leading to an anti-apoptotic effect (Koukourakis et al., 2003; Shi et al., 2004). Similarly, in oral squamous cell carcinoma (OSCC), SPARC activates the PI3K/AKT/PDGFB/PDGFRβ axis, promoting cancer cell proliferation, migration and invasion (Jing et al., 2019).

The duct-lobular system of the breast is composed of luminal and myoepithelial cells (Jones et al., 2004). Most breast carcinomas arise from luminal cells, but some invasive ductal carcinomas express myoepithelial markers (Jones et al., 2004). Overexpression of SPARC in epithelial cells reportedly correlates with higher malignancy (Barth, Moll, & Ramaswamy, 2005; Jones et al., 2004). It has been reported that the administration of exogenous SPARC, as well as its endogenous upregulation, induce breast cancer cell invasion *in vitro* (Briggs et al., 2002; Campo McKnight et al., 2006). In pancreatic ductal adenocarcinoma (PDAC), SPARC is upregulated at primary and metastatic sites in comparison with normal tissue (Guweidhi et al., 2005; Ryu, Jones, Hollingsworth, Hruban, & Kern, 2001). This high expression is present in the stroma but not in cancer cells, which indicates it has a tumor promoting role in the stroma of PDAC (Infante et al., 2007). Experiments demonstrate that, in pancreatic cancer cell lines, treatment with recombinant SPARC inhibits cell growth *in vitro* (Guweidhi et al., 2005; Ryu et al., 2001). However, incubation with exogenous SPARC promotes invasiveness (Guweidhi et al., 2005; Ryu et al., 2001). SPARC expression in non-small cell lung cancer (NSCLC) shares a similar pattern to PDAC. SPARC levels are low in tumor cells due to DNA methylation and high in stromal fibroblasts, which correlates with increased growth and metastatic capacity (Andriani et al., 2018; Koukourakis et al., 2003; Suzuki et al., 2005). In hepatocellular carcinoma, the overexpression of a truncated SPARC may stimulate angiogenesis (Lau, Poon, Cheung, Yu, & Fan, 2006). In cases where truncated SPARC is overexpressed, rather than full length SPARC, a much higher density of microvessels is observed within the tumor tissue (Lau et al., 2006). A proteomics screen identified SPARC as the most highly secreted protein in non-cancer stem cells (CSCs) when compared to CSC-enriched clones of PC-3 prostate cancer cells (Mateo et al., 2014). When cell line xenografts of both clones were implanted in immunodeficient mice, treatment with SPARC-specific shRNA significantly decreased tumor volume and metastatic dissemination (Mateo et al., 2014). Results from this model indicate that paracrine signaling of SPARC has pro-tumor and pro-metastatic effects (Mateo et al., 2014). Several different studies focused on SPARC in wound healing have shown that the administration of exogenous SPARC enhances cell motility to improve wound healing (Chua et al., 2014; Nagaraju et al., 2014). These characteristics could also translate to the invasive capability of cancer cells.

## 2.4 SPARC as a tumor suppressor

SPARC expression has also been associated with tumor suppression and favorable prognosis in certain types of cancer including neuroblastoma, ovarian cancer, colorectal cancer, prostate cancer, cervical cancer and even pancreatic ductal adenocarcinoma (Arnold & Brekken, 2009; Nagaraju et al., 2014; Podhajcer et al., 2008). Neuroblastomas are composed of two different cell populations, neuroblastic cells and Schwann cells (Chlenski et al., 2002). When the tumor microenvironment is abundant in the latter, the prognosis is more favorable (Chlenski et al., 2002). SPARC expression in Schwann cells improves clinical outcome by blocking angiogenesis and impairing tumor growth (Chlenski et al., 2002). SPARC overexpression inhibits cell proliferation in neuroblastoma by increasing PTEN, with consequent suppression of AKT activity (Sailaja et al., 2013). SPARC also promotes autophagy-mediated apoptosis by inducing endoplasmic reticulum (ER) stress in neuroblastoma (Sailaja et al., 2013). A similar mechanism is observed in colorectal cancer (CRC), where SPARC binds to GRP78, promoting apoptosis by enhancing ER stress (Chern et al., 2019). In addition, SPARC inhibits cell proliferation in medulloblastoma cells by suppressing Cyclin-B and STAT3 signaling leading to G2/M cell cycle arrest (Chetty, Dontula, Ganji, Gujrati, & Lakka, 2012). Normal ovarian epithelial cells express SPARC whereas, in ovarian cancer cells, it is downregulated by epigenetic silencing (Socha et al., 2009). SPARC expression inversely correlates with tumor malignancy, and treatment with exogenous SPARC induces apoptosis in ovarian cancer cells (Yiu et al., 2001). It has also been suggested that SPARC normalizes the reactive microenvironment of ovarian cancer by interfering with the VEGF-integrin-MMP axis, thus ameliorating inflammation, decreasing proliferation and reducing vascular density in tumors (Said et al., 2007).

Epigenetic silencing of SPARC is also frequent in CRC and it correlates with cancer progression and resistance to chemotherapy (Tai, Dai, Owen, & Chen, 2005; Yang et al., 2007). Yet, treating CRC cells with demethylating agents or overexpressing SPARC can rescue its expression and enhance sensitivity to therapy (Cheetham et al., 2008; Tang & Tai, 2007). In prostate, SPARC is highly expressed in normal tissue, moderately expressed in the tumor microenvironment and downregulated in prostate cancer cells (Thomas, True, Bassuk, Lange, & Vessella, 2000). It has been shown that tumor cell proliferation and invasiveness are inversely correlated with SPARC expression levels (Said et al., 2009). Prostate cancer is known to

metastasize to the bone, and a study revealed that SPARC contributes to prostate cancer cell dormancy in the bone microenvironment (Sharma et al., 2016). SPARC is also downregulated in human cervical carcinomas through hypermethylation of its promoter (Sova et al., 2006). It is reported that the levels of methylation are directly correlated with the grade of cervical lesions, meaning that a low expression of SPARC leads to a more aggressive phenotype (Sova et al., 2006). As described earlier, SPARC expression is higher in the peritumoral stroma of PDAC than the cancer cells (Infante et al., 2007). Stromal SPARC expression correlates positively with tumorigenicity (Infante et al., 2007). However, within PDAC cancer cells, the SPARC promoter is aberrantly methylated, downregulating its expression (Brune et al., 2008; Sato et al., 2003). The depletion of this protein promotes PDAC cancer cell proliferation and results in a more aggressive phenotype (Brune et al., 2008; Sato et al., 2003). Further studies are necessary to increase our knowledge of SPARC's cell-autonomous and non-autonomous functions in cancer aiming to develop stromal therapies and benefit cancer patients.

## 2.5 SPARC as a biomarker in cancer

Due to its important roles in this field, the potential of SPARC as a biomarker has been thoroughly examined for several cancers. For these, SPARC expression and its relation to clinical outcome is promising and might eventually result in its use as a biomarker for clinical practice. Below is a compilation of some of the most prevalent cancers in which SPARC might prove worthwhile as a novel biomarker. In bladder cancer, significantly higher expression of SPARC was observed in higher grade tumors (Yamanaka et al., 2001). However, patients harboring lesions of the same grade, but with higher levels of SPARC, had a significantly worse cause-specific survival than those with low SPARC expression (Yamanaka et al., 2001). The roles of SPARC in breast cancers remain controversial. Some studies state that high levels of SPARC expression indicate greater metastatic potential, postoperative invasion and shorter time to recurrence, all linked to a poorer prognosis (Guttlein et al., 2017; Szynglarewicz et al., 2016; Witkiewicz et al., 2010). While some authors conclude that patients with higher protein levels had worse Disease Free Survival (DFS) and Overall Survival (OS), others observed these same outcomes for lower levels (Nagai et al., 2011; Zhu et al., 2016). Studies also reported that high SPARC expression has been associated with a higher chance of achieving complete

remission after treatment (Lindner et al., 2015). The same contradiction is present in cases of CRC. Increased levels of SPARC (Chew et al., 2011; Hauptman, Bostjancic, Zlajpah, Rankovic, & Zidar, 2018; Madoz-Gurpide et al., 2006) have been associated with a better response to chemotherapy (Li et al., 2019), but also linked to shorter OS and Progression Free Survival (PFS). Similarly, low expression was found to be associated with poor prognosis (Liang et al., 2010; Liu et al., 2015), with patients having a statistically significant shorter OS and PFS (Kurtul, Tasdemir, Unal, Izmirli, & Eroglu, 2017). In gastric cancer, SPARC levels have been found to be upregulated (Junnila et al., 2010; Liao et al., 2018; Sato et al., 2013; Wang et al., 2012; Wang, Lin, Chen, Chan, & Hsueh, 2004), and several studies have noted a lower OS paired with increased lymph node metastasis (Hao et al., 2019; Liao et al., 2018; Sato et al., 2013; Wang et al., 2004; Zhao, Wang, Chu, Ye, & Tao, 2010). However, the lack of correlation between SPARC and TNM staging has also been described (Junnila et al., 2010). Additionally, SPARC promoter has been found to be methylated in gastric cancers, a characteristic that correlated with poorer OS (Chen et al., 2014). The reasons for these discrepant findings in specific cancers are not clear at this time.

Regarding Lung Small Cell Carcinoma (LSCC), there are higher levels of SPARC in the tumor tissue than in corresponding non-cancerous tissues (Xu et al., 2019). The elevated expression was accompanied by poor OS in patients (Xu et al., 2019). The studies in Non-Small Cell Lung Cancer (NSCLC) mirror the results of LSCC, with SPARC's augmentation correlating with poorer OS and PFS (Koukourakis et al., 2003; Kurtul et al., 2014). In primary skin melanoma, high levels of SPARC were associated with lower OS (Pieniazek, Donizy, Halon, Leskiewicz, & Matkowski, 2016). In the serum, concentrations in early-stage melanoma patients were higher than age-matched controls (Ikuta et al., 2005). Due to the growing relevance of liquid biopsies in clinical practice, SPARC could provide an easy, non-invasive way to detect early-stage melanoma. SPARC is overexpressed in esophageal cancer, and the protein is detected in serum (Chung et al., 2006). The protein's levels are increased in Barrett's esophagus, which is considered a premalignant condition, albeit those levels were not as high as in adenocarcinoma (Botelho et al., 2010; Brabender et al., 2003). This might represent a relationship between the presence of SPARC and disease progression (Botelho et al., 2010; Brabender et al., 2003). The high SPARC levels were also related to poorer OS (Kim et al., 2010). In pancreatic cancer, SPARC levels can be diagnostic and

prognostic. Patients with pancreatic cancer tend to have high serum concentrations of SPARC, which was also found to be overexpressed in the stroma of ampulla cancers (Bloomston et al., 2007; Papapanagiotou et al., 2018). High SPARC expression in both stroma and cancer cells is associated with poorer OS (Bloomston et al., 2007; Gundewar, Sasor, Hilmersson, Andersson, & Ansari, 2015; Han et al., 2016; Infante et al., 2007; Mantoni et al., 2008; Yu et al., 2017), DFS (Yu et al., 2017), and higher likelihood of metastasis development (Bloomston et al., 2007). Pancreatic CTCs (Circulating Tumor Cells) display high SPARC expression that correlates with EMT markers (Lapin et al., 2017), reinforcing its influence in metastasis. Studies in prostate cancer show that SPARC expression correlates with poor differentiation and higher Gleason score (Derosa et al., 2012). High expression of SPARC, observed at time of prostatectomy, links with subsequent development of metastasis (Derosa et al., 2012). Another study confirmed elevated SPARC in metastatic prostate cancer tissue (Arnold & Brekken, 2009). Additionally, hypermethylation of SPARC in prostate primary tumors has been shown to associate with the presence of lymph node metastasis, higher Gleason Score and poorer OS (Liu et al., 2018). The clinical relation between SPARC expression and patient prognosis is presented in Table 1. Current results suggest cancer-specific effects of SPARC expression relative to metastasis development and patient prognosis.

## 2.6 SPARC in cell competition

During development and ageing, damaged but viable cells accumulate within tissues. Cell competition eliminates these suboptimal cells from tissues to mitigate organ dysfunction and disease (Gogna, Shee, & Moreno, 2015; Greaves & Maley, 2012; Jacobs et al., 2012; Kennedy, Loeb, & Herr, 2012; Laurie et al., 2012; Lopez-Otin, Blasco, Partridge, Serrano, & Kroemer, 2013; Neves, Demaria, Campisi, & Jasper, 2015; Vanneste et al., 2009; Vijg, 2014). In this process, directed by receptor signaling, mechanical forces, or fitness fingerprints, winner cells mark the losers to undergo caspase-dependent apoptosis (Merino, Levayer, & Moreno, 2016). Fitness fingerprints reveal optimal or suboptimal cell fitness to neighboring cells by expressing membrane proteins, such as Flower proteins (Levayer, Hauert, & Moreno, 2015; Merino et al., 2015; Moreno & Rhiner, 2014; Rhiner et al., 2010; Yao et al., 2009). Winner cells expressing Flower-Win isoforms outcompete and eliminate the cells bearing

**Table 1** SPARC expression profile in different cancers, and its relationship with clinical outcome.

| Cancer type | SPARC status | Clinical outcome |
|---|---|---|
| Bladder | Higher, in higher grade tumors | Worse cause-specific survival |
| Breast | Higher | Metastasis, postoperative invasion and shorter time to recurrence; Worse DFS and OS |
| | Higher | Better chance of complete remission after treatment |
| | Lower | Worse DFS and OS |
| Colorectal | Higher | Better response to chemotherapy |
| | Higher | Worse PFS and OS |
| | Lower | Worse PFS and OS |
| Gastric | Higher | Worse OS and more lymph node metastasis |
| | Promoter Methylated | Worse OS |
| Lung | Higher, in stroma | Worse OS and PFS |
| Esophageal | Higher, in serum and in Barret esophagus (a pre-malignant condition) | Worse OS, especially when coupled with high levels of SPP1, another secreted glycoprotein |
| Pancreatic | Higher, in stroma, in serum | Worse OS and DFS; More chance of metastasis |
| Prostate | Higher | Poor differentiation, higher Gleason score and development of metastasis |
| | Promoter methylated | Lymph Node Metastasis, Higher Gleason Score and worse OS |

Flower-Lose isoforms in a mixed population, thus translating in a "code" for comparison of relative cellular fitness (Madan et al., 2019; Merino et al., 2015; Merino, Rhiner, Portela, & Moreno, 2013; Moreno, Fernandez-Marrero, Meyer, & Rhiner, 2015; Rhiner et al., 2010). Interestingly, upregulation of SPARC on prospective loser cells initiates a compensatory mechanism that inhibits caspase activation and transiently protects the cells from death (Gogna et al., 2015; Merino et al., 2016, 2013; Portela et al., 2010). Azot is another protein expressed in loser cells

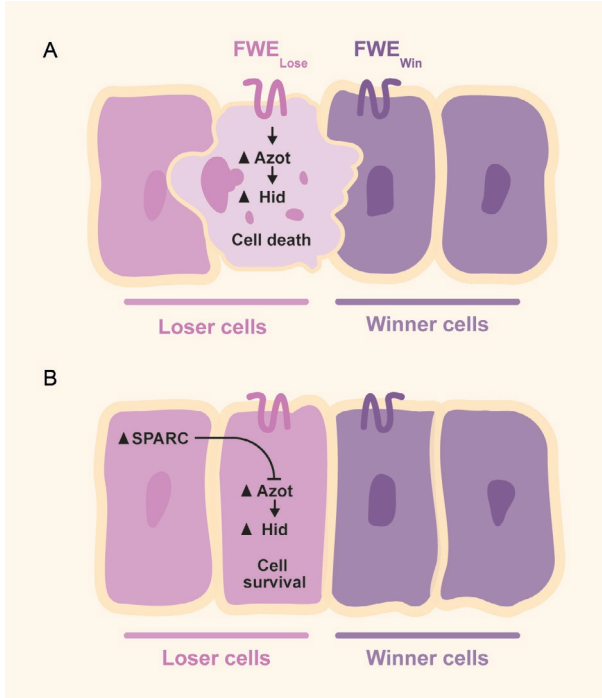


**Fig. 2** The role of SPARC in cell competition. (A) Cell competition by fitness fingerprints. Cells compare their relative expression of fitness markers, such as $Fwe^{Win}$ or $Fwe^{Lose}$, present on the cell surface. This fitness comparison leads to transcriptional activation of a novel effector protein named Azot. Increase in the Azot expression consequently increases expression of *hid* (a proapoptotic gene), inducing elimination of loser cells. (B) Overexpression of SPARC in loser cells downregulates Azot activity, protecting these cells from elimination. Thus, Loser cells in the tumor microenvironment upregulate SPARC as a defense mechanism, which functions as a natural strategy to prevent cancer growth.

that acts as a "cell fitness checkpoint" (Merino et al., 2015). This protein activates Hid pathway and consequent apoptosis of loser cells, although SPARC blocks this process by inhibiting Azot functions (Fig. 2) (de Beco, Ziosi, & Johnston, 2012; Merino et al., 2015). Cell competition gives premalignant cells a competitive advantage to grow and gain space at the cost of neighboring stromal cells (fibroblasts, immune cells, endothelial cells, epithelial cells) (Eichenlaub, Cohen, & Herranz, 2016; Levayer et al., 2015; Suijkerbuijk, Kolahgar, Kucinski, & Piddini, 2016). Near cancer tissue, these cells can upregulate SPARC as a defense mechanism to stave off elimination, which could provide a natural strategy to resist cancer initiation

and growth (Merino et al., 2015). It is also plausible that SPARC acts in an autocrine manner and activates a signaling pathway that hinders apoptosis (Portela et al., 2010).

## 3. p53: A double agent in cancer

When it was first discovered, p53 was observed to function as an oncogene (Kress, May, Cassingena, & May, 1979; Lane & Crawford, 1979; Melero, Stitt, Mangel, & Carroll, 1979). Since then, novel functions of p53 have been revealed, in which the protein regulates various cellular processes in order to maintain homeostasis, even supporting cell survival and migration, activities that can be beneficiary to oncogenesis and cancer growth and are usually controlled by oncogenes (Aylon & Oren, 2016; Vousden & Prives, 2009). These findings expand the knowledge of p53 mechanisms, sometimes revealing that they oppose to its anti-apoptotic function (Aylon & Oren, 2016; Muller, Vousden, & Norman, 2011). Furthermore, the p53-dependent cell cycle arrest is an effect widely seen in tumor suppressors but that might keep damaged cells from dying, thus promoting cancer initiation (Aylon & Oren, 2016). Although research focuses primarily on the full-length p53, some isoforms have been found to have a wide range of activities, including support toward cancer growth. These isoforms are different from the various mutations in p53 that are common in cancer, for they are found in non-transformed cells, each with their own function (Bourdon, 2007; Bourdon et al., 2005). For example, D133p53 and p53-b isoforms have contrary outcomes, where D133p53 hinders senescence, and p53-b promotes it (Fujita et al., 2009). In line with this observation, an increase of D133p53 expression, coupled with a decrease in p53-b, has been implicated in colon carcinomas (Fujita et al., 2009). As such, this difference in expressions may compose a mechanism in the transformation from adenoma to carcinoma (Fujita et al., 2009). Moreover, p53C isoform can enhance cell motility and invasion (Senturk et al., 2014), highlighting how p53 isoforms may have a role in tumor progression. Concerning *p53* mutations in cancer, most result in a stable protein, surpassing the WT p53 levels usually found in non-cancerous cells (Rotter, 1983; Soussi & Wiman, 2015). This led to the hypothesis that mutant p53 (mutp53) has active roles in cancer cells, instead of just being a product of WT p53 inactivation. These mutp53, with functions of their own, are found in many cancers, contributing to its development (Oren & Rotter, 2010). Mutp53 stability seems to rely on its inability to

activate *Mdm2* transcription, a gene transcriptionally controlled by WT p53 and implicated in its degradation by a negative feedback loop (Oren & Rotter, 2010; Terzian et al., 2008). A study in which mutp53 was encoded in a vector, described how Abelson murine leukemia-transformed cells became more tumorigenic when overexpressing said mutp53, although at the time it was thought to be the WT (Wolf, Harris, & Rotter, 1984). Furthermore, knock-in mice for numerous forms of mutant p53, developed a high number of carcinomas that were highly invasive and metastatic, when comparing to p53 knock-out mice, which in turn developed sarcomas. These results support the existence of gain of function (GOF) mutp53 isoforms, that have oncogenic properties like invasion, chemoresistance, and genomic instability (Soussi & Wiman, 2015). Adding to all these pro-tumoral processes, overexpressed mutp53 also has proliferative functions (Duan, Gao, Jin, Otterson, & Villalona-Calero, 2008; Haupt et al., 2009; Oren & Rotter, 2010; Scian et al., 2004). Tumor cells are able to control p53 transcriptional program, resulting in outcomes that may benefit the tumor, by controlling the affinity of TF toward its DNA (Aylon & Oren, 2016). This regulation is also observed for mutp53 (Aylon & Oren, 2016). For example, SWI/SNF complex can interact with mutp53 and overexpress VEGFR2, an angiogenesis regulator (Pfister et al., 2015). Mutp53 also activates MLL1/2 and MOZ, generating different chromatin states (Zhu et al., 2015). Lastly, mutp53 binds to p63 and p73, an interaction implicated in invasion and metastasis (Muller et al., 2013).

In cancer, genome instability is very frequent, especially in the advanced stages, displayed by various mutations and anomalies in chromosomes (Oren & Rotter, 2010). It has been shown that mutp53 plays a role in this process by disrupting spindle checkpoint control, which results in cells with an aberrant number of chromosomes (Oren & Rotter, 2010). This instability caused by mutp53 also translates into higher mutations rates in T-cell receptor of cells exposed to X-irradiation and augmented gene amplification (Oren & Rotter, 2010). A common characteristic of cancer cells is c-Myc overexpression, which leads to apoptosis in order to control tumorigenesis (Lotem & Sachs, 1995). However, when p53 acquires a GOF phenotype, it may create resistance to this apoptotic signal, allowing the cells to benefit from pro-proliferative signals without the threat of undergoing apoptosis (Lotem & Sachs, 1995). GOF p53 has also been implicated in the decrease of apoptosis when cells are deprived of growth factors, conferring tumor cells an advantage under factor deficient conditions (Oren & Rotter, 2010; Peled, Zipori, & Rotter, 1996). Some mutp53 overexpressed in

cancer have been described to hinder cancer cell death during chemotherapy, highlighting how the anti-apoptotic properties may have play a huge role in cancer treatment and as well as development (Oren & Rotter, 2010). Mutp53 isoforms usually appear later in oncogenesis, rather than in the beginning (Oren & Rotter, 2010). It is, therefore, possible for GOF p53 to influence metastasis potential as well (Oren & Rotter, 2010). Accordingly, gene expression profiling describes how mutp53 isoforms can act together with the *Ras* gene to express chemokines and other molecules that will contribute to the tumor's ability to invade and migrate to other tissues (Buganim et al., 2010; Oren & Rotter, 2010). More specifically, p53-R248Q, a mutp53 GOF isoform, controls the transcription of REGγ in endometrial cancer, leading to a higher proliferation, migration, invasion and EMT of cancer cells (Wang et al., 2015). This mechanism translates into a specific pathway in which mutp53 may promote cancer progression and aggressiveness (Wang et al., 2015).

Hypoxia alters the transcription regulation, as cells try to activate genes that control cell survival, angiogenesis, proliferation and apoptosis (Harris, 2002). This condition recurrently happens in tumors as they grow, so cancer cells adapted to overcome it (Harris, 2002). Until now, most oncogenic functions of p53 seem to be exclusive of mutp53. A recent study has discovered that both WT p53 and mutp53 can act as oncogenes, by cooperation with HIF-1, a transcription factor active during hypoxia (Madan et al., 2019). Although p53 is mutated in most cancers, WT p53 acquires a mutant-like conformation in the hypoxic core of tumors (Madan, Parker, et al., 2019). The study demonstrated that HIF-1 binds to the promoter of both WT and mutant p53, upregulating it (Madan, Parker, et al., 2019). This p53 is not transcriptionally functional but binds to HIF-1 through protein–protein interactions, acting as a chaperone to stabilize HIF-1's binding to its DNA response elements (Madan, Parker, et al., 2019). These HIF target genes are vital for the cell's survival and growth under hypoxia (Madan, Parker, et al., 2019). Cancers where both proteins are upregulated show a worse prognosis, which correlates with the cooperation found between HIF-1 and p53 in tumor cells in hypoxic conditions (Madan, Parker, et al., 2019).

## 3.1 p53 in cell competition

Several studies have suggested that p53 can have a major role in cell competition. It was described that hematopoietic stem cells and progenitors

(HSCPs) can sense relative levels of p53 and determine which cells are eliminated (Wagstaff et al., 2016). Essentially, cells with more DNA damage, caused by ionizing radiation (IR), present higher levels of p53 and enter a senescence-like state that stops them from proliferating and eventually leads to their replacement by neighbor cells with a lower p53 activity (Wagstaff et al., 2016). However, this process only happens when these cells are in the presence of others with lower p53 levels (Wagstaff et al., 2016). Notably, p53 mutations also give cells a winner phenotype and many target genes of p53 are upregulated in loser cells (Bierie & Moses, 2006; de la Cova et al., 2014). Thus, the inability of p53 binding to its targets, either by mutation or insufficiency, may distinguish winner and loser HSPCs (Bierie & Moses, 2006; de la Cova et al., 2014). This protein may also play a role in cell competition between winner WT and loser *Scribble*-deficient cells (de la Cova et al., 2014; Wagstaff et al., 2016). The compaction of *Scribble*-deficient cells by WT cells activates Rho-associated kinase which raises p53 levels in the loser cells, with consequent elimination by apoptosis (de la Cova et al., 2014; Wagstaff et al., 2016). p53-dependent cell competition has also been discovered in mouse embryogenesis (Zhang et al., 2017). Using haplo-insufficient mice, with Mdm2+/− Mdm4+/− double-heterozygous cells, which have a mild p53 activation that are outcompeted by WT during mouse embryogenesis (Zhang et al., 2017). When a copy of p53 is removed, this effect is no longer observed, suggesting that competition induced by mild activation of p53 contributes to the proliferation of only healthy cells during mammalian embryogenesis (Zhang et al., 2017). Another example of p53's influence is in dMyc-induced cell competition (de la Cova et al., 2014; Di Gregorio, Bowling, & Rodriguez, 2016). Cells overexpressing dMyc acquire a "supercompetitor" phenotype when WT cells are present, which ultimately leads to apoptosis of the latter cells (Di Gregorio et al., 2016). In this process, p53 is crucial to the metabolic changes inherent to the glycolytic flux needed for the proliferation of cells with high dMyc activity as they compete with WT cells. Moreover, when p53 is mutated, the winner cells cannot mark the loser for elimination, indicating that p53 might also regulate the signal for elimination and not only metabolism in winner cells (de la Cova et al., 2014; Di Gregorio et al., 2016).

## 4. SPARC-p53 network

SPARC and p53 have been shown to interact in cancer. A study focusing on melanoma demonstrated that overexpression of SPARC

promotes cell survival by stimulating MDM2 phosphorylation, with consequential activation of Akt and loss of p53 stabilization, thus hindering apoptosis (Fenouille, Puissant, et al., 2011). When SPARC is suppressed, p53 levels are regulated, activating caspase-3 and inducing cell death through the mitochondrial intrinsic pathway (Fenouille, Puissant, et al., 2011). This shows that overexpression of SPARC in the cancer acts as an oncogene pathway, capable of suppressing p53's functions. In accordance to these findings, other studies in melanoma (Fenouille, Robert, et al., 2011) and cervical cancer (Chen et al., 2012) reported how SPARC-depleted cells are forced into mitotic arrest via p21 (Cip1/Waf1/mda-6) due to p53 expression (Chen, Shi, et al., 2012; Fenouille, Robert, et al., 2011; Jiang et al., 1994, 1995), although results state that this p53-SPARC relationship and SPARC's metastatic potential are independent (Fenouille, Robert, et al., 2011). Similar studies confirm that knockdown of SPARC allows for increased p53-induced apoptosis and cell cycle arrest across cervical cancer (Chen, Shi, et al., 2012), ovarian cancer (Chen et al., 2012), glioma (Thomas et al., 2015), and pancreatic cancer (Chen, Shi, et al., 2012; Fenouille, Robert, et al., 2011). A direct SPARC-p53 interaction is a possible mechanism as both proteins were pulled down by immunoprecipitation and bound to Pax6 protein (Tripathi & Mishra, 2010). Taken together, SPARC and p53 regulate cancer cell survival by inverse effects on apoptotic pathways and related signaling mechanisms.

## 5. Conclusion and future perspectives

Despite the effort of the research community, cancer continues to affect millions of people, with a rising incidence every year (Ferlay et al., 2019). Most studies used to focus solely on the tumor, disregarding the interactions that cells establish with their neighbors and microenvironment, although this tendency has started to change. Among the proteins that partake in these interactions, SPARC is one of the most controversial, acting either as a tumor suppressor or as an oncogene, depending on cancer type (Ledda, Bravo, et al., 1997; Socha et al., 2009). This protein is responsible for modulating ECM components, facilitating EMT and influencing cancer invasion and metastasis (Bierie & Moses, 2006; Drev et al., 2019; Sun et al., 2018; Tumbarello et al., 2016). Additionally, SPARC can also have a protective function in cell competition, preventing elimination of loser cells (Portela et al., 2010). As such, it is important to further study SPARC to understand by which mechanisms it acts as a tumor-suppressor

or promoter, eventually applying them in clinical practice. Moreover, SPARC is present in the serum of some cancers (Chung et al., 2006; Ikuta et al., 2005). With the emergence of liquid biopsies, SPARC might prove to be an important target. Due to its linkage to tumor recurrence (Guttlein et al., 2017; Szynglarewicz et al., 2016; Witkiewicz et al., 2010), it could stratify patients who could benefit from a better follow-up or further treatment. All in all, when coupled with other proteins, SPARC has excellent potential as a biomarker, not only for diagnosis and staging but for prognosis and treatment.

Just like SPARC, p53 also seems to have a context-dependent behavior regarding its role in oncogenesis (Aylon & Oren, 2016; Vousden & Prives, 2009). Both WT and mutant p53 can enhance tumor growth by promoting invasion, chemoresistance, genomic instability and cell proliferation (Soussi & Wiman, 2015). In cell competition, comparing p53 relative levels of expression and activation may lead to cell death of loser cells (Bondar & Medzhitov, 2010). It is also known that, in cancer, SPARC indirectly inhibits p53 activation, inducing cell survival and cell cycle progression (Fenouille, Puissant, et al., 2011; Fenouille, Robert, et al., 2011). Yet, more studies are required to understand if SPARC and p53 can act synergistically, either to enhance tumor aggressiveness or to protect the tissue surrounding the tumor. Comprehending precisely how SPARC and p53 interact in orchestrating cancer progression, response to therapy and patient prognosis/survival represents an important endeavor with potential to uncover new and effective therapies for aggressive cancers.

## Acknowledgment

We thank Champalimaud Foundation to support this research.

## References

Andriani, F., Landoni, E., Mensah, M., Facchinetti, F., Miceli, R., Tagliabue, E., et al. (2018). Diagnostic role of circulating extracellular matrix-related proteins in non-small cell lung cancer. *BMC Cancer*, *18*, 899. https://www.ncbi.nlm.nih.gov/pubmed/30227835.

Arnold, S. A., & Brekken, R. A. (2009). SPARC: A matricellular regulator of tumorigenesis. *Journal of Cell Communication and Signaling*, *3*, 255–273. https://www.ncbi.nlm.nih.gov/pubmed/19809893.

Atorrasagasti, C., Onorato, A., Gimeno, M. L., Andreone, L., Garcia, M., Malvicini, M., et al. (2019). SPARC is required for the maintenance of glucose homeostasis and insulin secretion in mice. *Clinical Science (London, England)*, *133*, 351–365. https://www.ncbi.nlm.nih.gov/pubmed/30626728.

Aylon, Y., & Oren, M. (2016). The paradox of p53: What, how, and why? *Cold Spring Harbor Perspectives in Medicine*, *6*. https://www.ncbi.nlm.nih.gov/pubmed/27413116.

Barth, P. J., Moll, R., & Ramaswamy, A. (2005). Stromal remodeling and SPARC (secreted protein acid rich in cysteine) expression in invasive ductal carcinomas of the breast. *Virchows Archiv: An International Journal of Pathology*, *446*, 532–536. https://www.ncbi.nlm.nih.gov/pubmed/15838642.

Bierie, B., & Moses, H. L. (2006). Tumour microenvironment: TGFbeta: The molecular Jekyll and Hyde of cancer. *Nature Reviews Cancer*, *6*, 506–520. https://www.ncbi.nlm.nih.gov/pubmed/16794634.

Bloomston, M., Ellison, E. C., Muscarella, P., Al-Saif, O., Martin, E. W., Melvin, W. S., et al. (2007). Stromal osteonectin overexpression is associated with poor outcome in patients with ampullary cancer. *Annals of Surgical Oncology*, *14*, 211–217. https://www.ncbi.nlm.nih.gov/pubmed/17080236.

Bondar, T., & Medzhitov, R. (2010). p53-mediated hematopoietic stem and progenitor cell competition. *Cell Stem Cell*, *6*, 309–322. https://www.ncbi.nlm.nih.gov/pubmed/20362536.

Botelho, N. K., Schneiders, F. I., Lord, S. J., Freeman, A. K., Tyagi, S., Nancarrow, D. J., et al. (2010). Gene expression alterations in formalin-fixed, paraffin-embedded Barrett esophagus and esophageal adenocarcinoma tissues. *Cancer Biology & Therapy*, *10*, 172–179. https://www.ncbi.nlm.nih.gov/pubmed/20543560.

Bourdon, J. C. (2007). p53 and its isoforms in cancer. *British Journal of Cancer*, *97*, 277–282. https://www.ncbi.nlm.nih.gov/pubmed/17637683.

Bourdon, J. C., Fernandes, K., Murray-Zmijewski, F., Liu, G., Diot, A., Xirodimas, D. P., et al. (2005). p53 isoforms can regulate p53 transcriptional activity. *Genes & Development*, *19*, 2122–2137. https://www.ncbi.nlm.nih.gov/pubmed/16131611.

Brabender, J., Lord, R. V., Metzger, R., Park, J., Salonga, D., Danenberg, K. D., et al. (2003). Differential SPARC mRNA expression in Barrett's oesophagus. *British Journal of Cancer*, *89*, 1508–1512. https://www.ncbi.nlm.nih.gov/pubmed/14562024.

Bradshaw, A. D. (2012). Diverse biological functions of the SPARC family of proteins. *The International Journal of Biochemistry & Cell Biology*, *44*, 480–488. https://www.ncbi.nlm.nih.gov/pubmed/22249026.

Bradshaw, A. D., & Sage, E. H. (2001). SPARC, a matricellular protein that functions in cellular differentiation and tissue response to injury. *The Journal of Clinical Investigation*, *107*, 1049–1054. https://www.ncbi.nlm.nih.gov/pubmed/11342565.

Brekken, R. A., & Sage, E. H. (2001). SPARC, a matricellular protein: at the crossroads of cell-matrix communication. *Matrix Biology*, *19*, 816–827. https://www.ncbi.nlm.nih.gov/pubmed/11223341.

Briggs, J., Chamboredon, S., Castellazzi, M., Kerry, J. A., & Bos, T. J. (2002). Transcriptional upregulation of SPARC, in response to c-Jun overexpression, contributes to increased motility and invasion of MCF7 breast cancer cells. *Oncogene*, *21*, 7077–7091. https://www.ncbi.nlm.nih.gov/pubmed/12370830.

Brune, K., Hong, S. M., Li, A., Yachida, S., Abe, T., Griffith, M., et al. (2008). Genetic and epigenetic alterations of familial pancreatic cancers. *Cancer Epidemiology, Biomarkers & Prevention*, *17*, 3536–3542. https://www.ncbi.nlm.nih.gov/pubmed/19064568.

Buganim, Y., Solomon, H., Rais, Y., Kistner, D., Nachmany, I., Brait, M., et al. (2010). p53 Regulates the Ras circuit to inhibit the expression of a cancer-related gene signature by various molecular pathways. *Cancer Research*, *70*, 2274–2284. https://www.ncbi.nlm.nih.gov/pubmed/20197462.

Campo McKnight, D. A., Sosnoski, D. M., Koblinski, J. E., & Gay, C. V. (2006). Roles of osteonectin in the migration of breast cancer cells into bone. *Journal of Cellular Biochemistry*, *97*, 288–302. https://www.ncbi.nlm.nih.gov/pubmed/16173048.

Cheetham, S., Tang, M. J., Mesak, F., Kennecke, H., Owen, D., & Tai, I. T. (2008). SPARC promoter hypermethylation in colorectal cancers can be reversed by 5-Aza-2'deoxycytidine to increase SPARC expression and improve therapy response. *British Journal of Cancer*, *98*, 1810–1819. https://www.ncbi.nlm.nih.gov/pubmed/18458674.

Chen, J., Shi, D., Liu, X., Fang, S., Zhang, J., & Zhao, Y. (2012). Targeting SPARC by lentivirus-mediated RNA interference inhibits cervical cancer cell growth and metastasis. *BMC Cancer*, *12*, 464. https://www.ncbi.nlm.nih.gov/pubmed/23050783.

Chen, J., Wang, M., Xi, B., Xue, J., He, D., Zhang, J., et al. (2012). SPARC is a key regulator of proliferation, apoptosis and invasion in human ovarian cancer. *PLoS One*, *7,* e42413. https://www.ncbi.nlm.nih.gov/pubmed/22879971.

Chen, Z. Y., Zhang, J. L., Yao, H. X., Wang, P. Y., Zhu, J., Wang, W., et al. (2014). Aberrant methylation of the SPARC gene promoter and its clinical implication in gastric cancer. *Scientific Reports*, *4*, 7035. https://www.ncbi.nlm.nih.gov/pubmed/25516351.

Chern, Y. J., Wong, J. C. T., Cheng, G. S. W., Yu, A., Yin, Y., Schaeffer, D. F., et al. (2019). The interaction between SPARC and GRP78 interferes with ER stress signaling and potentiates apoptosis via PERK/eIF2alpha and IRE1alpha/XBP-1 in colorectal cancer. *Cell Death & Disease*, *10*, 504. https://www.ncbi.nlm.nih.gov/pubmed/31243264.

Chetty, C., Dontula, R., Ganji, P. N., Gujrati, M., & Lakka, S. S. (2012). SPARC expression induces cell cycle arrest via STAT3 signaling pathway in medulloblastoma cells. *Biochemical and Biophysical Research Communications*, *417*, 874–879. https://www.ncbi.nlm.nih.gov/pubmed/22206672.

Chew, A., Salama, P., Robbshaw, A., Klopcic, B., Zeps, N., Platell, C., et al. (2011). SPARC, FOXP3, CD8 and CD45 correlation with disease recurrence and long-term disease-free survival in colorectal cancer. *PLoS One*, *6,* e22047. https://www.ncbi.nlm.nih.gov/pubmed/21818290.

Chlenski, A., & Cohn, S. L. (2010). Modulation of matrix remodeling by SPARC in neoplastic progression. *Seminars in Cell & Developmental Biology*, *21*, 55–65. https://www.ncbi.nlm.nih.gov/pubmed/19958839.

Chlenski, A., Liu, S., Crawford, S. E., Volpert, O. V., DeVries, G. H., Evangelista, A., et al. (2002). SPARC is a key Schwannian-derived inhibitor controlling neuroblastoma tumor angiogenesis. *Cancer Research*, *62*, 7357–7363. https://www.ncbi.nlm.nih.gov/pubmed/12499280.

Chua, C. E., Chan, S. N., & Tang, B. L. (2014). Non-cell autonomous or secretory tumor suppression. *Journal of Cellular Physiology*, *229*, 1346–1352. https://www.ncbi.nlm.nih.gov/pubmed/24752809.

Chung, J. Y., Braunschweig, T., Hu, N., Roth, M., Traicoff, J. L., Wang, Q. H., et al. (2006). A multiplex tissue immunoblotting assay for proteomic profiling: A pilot study of the normal to tumor transition of esophageal squamous cell carcinoma. *Cancer Epidemiology, Biomarkers & Prevention*, *15*, 1403–1408. https://www.ncbi.nlm.nih.gov/pubmed/16835344.

de Beco, S., Ziosi, M., & Johnston, L. A. (2012). New frontiers in cell competition. *Developmental Dynamics*, *241*, 831–841. https://www.ncbi.nlm.nih.gov/pubmed/22438309.

de la Cova, C., Senoo-Matsuda, N., Ziosi, M., Wu, D. C., Bellosta, P., Quinzii, C. M., et al. (2014). Supercompetitor status of Drosophila Myc cells requires p53 as a fitness sensor to reprogram metabolism and promote viability. *Cell Metabolism*, *19*, 470–483. https://www.ncbi.nlm.nih.gov/pubmed/24561262.

Deckx, S., Johnson, D. M., Rienks, M., Carai, P., Van Deel, E., Van der Velden, J., et al. (2019). Extracellular SPARC increases cardiomyocyte contraction during health and disease. *PLoS One*, *14,* e0209534. https://www.ncbi.nlm.nih.gov/pubmed/30933983.

Derosa, C. A., Furusato, B., Shaheduzzaman, S., Srikantan, V., Wang, Z., Chen, Y., et al. (2012). Elevated osteonectin/SPARC expression in primary prostate cancer predicts metastatic progression. *Prostate Cancer and Prostatic Diseases*, *15*, 150–156. https://www.ncbi.nlm.nih.gov/pubmed/22343836.

Di Gregorio, A., Bowling, S., & Rodriguez, T. A. (2016). Cell competition and its role in the regulation of cell fitness from development to cancer. *Developmental Cell*, *38*, 621–634. https://www.ncbi.nlm.nih.gov/pubmed/27676435.

Drev, D., Harpain, F., Beer, A., Stift, A., Gruber, E. S., Klimpfinger, M., et al. (2019). Impact of fibroblast-derived SPARC on invasiveness of colorectal cancer cells. *Cancers (Basel)*, *11*. https://www.ncbi.nlm.nih.gov/pubmed/31554208.

Duan, W., Gao, L., Jin, D., Otterson, G. A., & Villalona-Calero, M. A. (2008). Lung specific expression of a human mutant p53 affects cell proliferation in transgenic mice. *Transgenic Research*, *17*, 355–366. https://www.ncbi.nlm.nih.gov/pubmed/17968669.

Eichenlaub, T., Cohen, S. M., & Herranz, H. (2016). Cell competition drives the formation of metastatic tumors in a drosophila model of epithelial tumor formation. *Current Biology*, *26*, 419–427. https://www.ncbi.nlm.nih.gov/pubmed/26853367.

Fenouille, N., Puissant, A., Tichet, M., Zimniak, G., Abbe, P., Mallavialle, A., et al. (2011). SPARC functions as an anti-stress factor by inactivating p53 through Akt-mediated MDM2 phosphorylation to promote melanoma cell survival. *Oncogene*, *30*, 4887–4900. https://www.ncbi.nlm.nih.gov/pubmed/21685937.

Fenouille, N., Robert, G., Tichet, M., Puissant, A., Dufies, M., Rocchi, S., et al. (2011). The p53/p21Cip1/Waf1 pathway mediates the effects of SPARC on melanoma cell cycle progression. *Pigment Cell & Melanoma Research*, *24*, 219–232. https://www.ncbi.nlm.nih.gov/pubmed/20955243.

Ferlay, J., Colombet, M., Soerjomataram, I., Mathers, C., Parkin, D. M., Pineros, M., et al. (2019). Estimating the global cancer incidence and mortality in 2018: GLOBOCAN sources and methods. *International Journal of Cancer*, *144*, 1941–1953. https://www.ncbi.nlm.nih.gov/pubmed/30350310.

Fujita, K., Mondal, A. M., Horikawa, I., Nguyen, G. H., Kumamoto, K., Sohn, J. J., et al. (2009). p53 isoforms Delta133p53 and p53beta are endogenous regulators of replicative cellular senescence. *Nature Cell Biology*, *11*, 1135–1142. https://www.ncbi.nlm.nih.gov/pubmed/19701195.

Gogna, R., Shee, K., & Moreno, E. (2015). Cell competition during growth and regeneration. *Annual Review of Genetics*, *49*, 697–718. https://www.ncbi.nlm.nih.gov/pubmed/26631518.

Greaves, M., & Maley, C. C. (2012). Clonal evolution in cancer. *Nature*, *481*, 306–313. https://www.ncbi.nlm.nih.gov/pubmed/22258609.

Gundewar, C., Sasor, A., Hilmersson, K. S., Andersson, R., & Ansari, D. (2015). The role of SPARC expression in pancreatic cancer progression and patient survival. *Scandinavian Journal of Gastroenterology*, *50*, 1170–1174. https://www.ncbi.nlm.nih.gov/pubmed/25765175.

Guttlein, L. N., Benedetti, L. G., Fresno, C., Spallanzani, R. G., Mansilla, S. F., Rotondaro, C., et al. (2017). Predictive outcomes for HER2-enriched cancer using growth and metastasis signatures driven by SPARC. *Molecular Cancer Research*, *15*, 304–316. https://www.ncbi.nlm.nih.gov/pubmed/28031408.

Guweidhi, A., Kleeff, J., Adwan, H., Giese, N. A., Wente, M. N., Giese, T., et al. (2005). Osteonectin influences growth and invasion of pancreatic cancer cells. *Annals of Surgery*, *242*, 224–234. https://www.ncbi.nlm.nih.gov/pubmed/16041213.

Han, W., Cao, F., Chen, M. B., Lu, R. Z., Wang, H. B., Yu, M., et al. (2016). Prognostic value of SPARC in patients with Pancreatic Cancer: A Systematic Review and Meta-Analysis. *PLoS One*, *11*, e0145803. https://www.ncbi.nlm.nih.gov/pubmed/26731428.

Hao, S., Lv, J., Yang, Q., Wang, A., Li, Z., Guo, Y., et al. (2019). Identification of key genes and circular RNAs in human gastric cancer. *Medical Science Monitor*, *25*, 2488–2504. https://www.ncbi.nlm.nih.gov/pubmed/30948703.

Harris, A. L. (2002). Hypoxia—A key regulatory factor in tumour growth. *Nature Reviews. Cancer*, *2*, 38–47. https://www.ncbi.nlm.nih.gov/pubmed/11902584.

Haupt, S., di Agostino, S., Mizrahi, I., Alsheich-Bartok, O., Voorhoeve, M., Damalas, A., et al. (2009). Promyelocytic leukemia protein is required for gain of function by mutant p53. *Cancer Research*, *69*, 4818–4826. https://www.ncbi.nlm.nih.gov/pubmed/19487292.

Hauptman, N., Bostjancic, E., Zlajpah, M., Rankovic, B., & Zidar, N. (2018). Bioinformatics analysis reveals most prominent gene candidates to distinguish colorectal adenoma from adenocarcinoma. *BioMed Research International*, *2018*, 9416515. https://www.ncbi.nlm.nih.gov/pubmed/30175151.

Ikuta, Y., Nakatsura, T., Kageshita, T., Fukushima, S., Ito, S., Wakamatsu, K., et al. (2005). Highly sensitive detection of melanoma at an early stage based on the increased serum secreted protein acidic and rich in cysteine and glypican-3 levels. *Clinical Cancer Research*, *11*, 8079–8088. https://www.ncbi.nlm.nih.gov/pubmed/16299239.

Infante, J. R., Matsubayashi, H., Sato, N., Tonascia, J., Klein, A. P., Riall, T. A., et al. (2007). Peritumoral fibroblast SPARC expression and patient outcome with resectable pancreatic adenocarcinoma. *Journal of Clinical Oncology*, *25*, 319–325. https://www.ncbi.nlm.nih.gov/pubmed/17235047.

Jacobs, K. B., Yeager, M., Zhou, W., Wacholder, S., Wang, Z., Rodriguez-Santiago, B., et al. (2012). Detectable clonal mosaicism and its relationship to aging and cancer. *Nature Genetics*, *44*, 651–658. https://www.ncbi.nlm.nih.gov/pubmed/22561519.

Jiang, H., Lin, J., Su, Z., Collart, F. R., Huberman, E., & Fisher, P. B. (1994). Induction of differentiation in human promyelocytic HL-60 leukemia cells activates p21, WAF1/CIP1, expression in the absence of p53. *Oncogene*, *9*, 3397–3406.

Jiang, H., Lin, J., Su, Z., Herlyn, M., Kerbel, R. S., Weissman, B. E., et al. (1995). The melanoma differentiation-associated gene mda-6, which encodes the cyclin-dependent kinase inhibitor p21, is differentially expressed during growth, differentiation and progression in human melanoma cells. *Oncogene*, *10*, 1855–1864.

Jing, Y., Jin, Y., Wang, Y., Chen, S., Zhang, X., Song, Y., et al. (2019). SPARC promotes the proliferation and metastasis of oral squamous cell carcinoma by PI3K/AKT/PDGFB/PDGFRbeta axis. *Journal of Cellular Physiology* https://www.ncbi.nlm.nih.gov/pubmed/30706473.

Jones, C., Mackay, A., Grigoriadis, A., Cossu, A., Reis-Filho, J. S., Fulford, L., et al. (2004). Expression profiling of purified normal human luminal and myoepithelial breast cells: Identification of novel prognostic markers for breast cancer. *Cancer Research*, *64*, 3037–3045. https://www.ncbi.nlm.nih.gov/pubmed/15126339.

Junnila, S., Kokkola, A., Mizuguchi, T., Hirata, K., Karjalainen-Lindsberg, M. L., Puolakkainen, P., et al. (2010). Gene expression analysis identifies over-expression of CXCL1, SPARC, SPP1, and SULF1 in gastric cancer. *Genes, Chromosomes & Cancer*, *49*, 28–39. https://www.ncbi.nlm.nih.gov/pubmed/19780053.

Kastenhuber, E. R., & Lowe, S. W. (2017). Putting p53 in context. *Cell*, *170*, 1062–1078. https://www.ncbi.nlm.nih.gov/pubmed/28886379.

Kennedy, S. R., Loeb, L. A., & Herr, A. J. (2012). Somatic mutations in aging, cancer and neurodegeneration. *Mechanisms of Ageing and Development*, *133*, 118–126. https://www.ncbi.nlm.nih.gov/pubmed/22079405.

Kim, S. M., Park, Y. Y., Park, E. S., Cho, J. Y., Izzo, J. G., Zhang, D., et al. (2010). Prognostic biomarkers for esophageal adenocarcinoma identified by analysis of tumor transcriptome. *PLoS One*, *5*, e15074. https://www.ncbi.nlm.nih.gov/pubmed/21152079.

Koukourakis, M. I., Giatromanolaki, A., Brekken, R. A., Sivridis, E., Gatter, K. C., Harris, A. L., et al. (2003). Enhanced expression of SPARC/osteonectin in the tumor-associated stroma of non-small cell lung cancer is correlated with markers of hypoxia/acidity and with poor prognosis of patients. *Cancer Research*, *63*, 5376–5380. https://www.ncbi.nlm.nih.gov/pubmed/14500371.

Kress, M., May, E., Cassingena, R., & May, P. (1979). Simian virus 40-transformed cells express new species of proteins precipitable by anti-simian virus 40 tumor serum. *Journal of Virology*, *31*, 472–483. https://www.ncbi.nlm.nih.gov/pubmed/225566.

Kurtul, N., Eroglu, C., Unal, D., Tasdemir, E. A., Orhan, O., Zararsiz, G., et al. (2014). Prognostic value of SPARC expression in unresectable NSCLC treated with concurrent chemoradiotherapy. *Asian Pacific Journal of Cancer Prevention*, *15*, 8911–8916. https://www.ncbi.nlm.nih.gov/pubmed/25374228.

Kurtul, N., Tasdemir, E. A., Unal, D., Izmirli, M., & Eroglu, C. (2017). SPARC: As a prognostic biomarker in rectal cancer patients treated with chemo-radiotherapy. *Cancer Biomarkers*, *18*, 459–466. https://www.ncbi.nlm.nih.gov/pubmed/28009327.

Lane, D. P., & Crawford, L. V. (1979). T antigen is bound to a host protein in SV40-transformed cells. *Nature*, *278*, 261–263. https://www.ncbi.nlm.nih.gov/pubmed/218111.

Lapin, M., Tjensvoll, K., Oltedal, S., Javle, M., Smaaland, R., Gilje, B., et al. (2017). Single-cell mRNA profiling reveals transcriptional heterogeneity among pancreatic circulating tumour cells. *BMC Cancer*, *17*, 390. https://www.ncbi.nlm.nih.gov/pubmed/28569190.

Lau, C. P., Poon, R. T., Cheung, S. T., Yu, W. C., & Fan, S. T. (2006). SPARC and Hevin expression correlate with tumour angiogenesis in hepatocellular carcinoma. *The Journal of Pathology*, *210*, 459–468. https://www.ncbi.nlm.nih.gov/pubmed/17029219.

Laurie, D. E., Splan, R. K., Green, K., Still, K. M., McKown, R. L., & Laurie, G. W. (2012). Detection of prosecretory mitogen lacritin in nonprimate tears primarily as a C-terminal-like fragment. *Investigative Ophthalmology & Visual Science*, *53*, 6130–6136. https://www.ncbi.nlm.nih.gov/pubmed/22871838.

Ledda, M. F., Adris, S., Bravo, A. I., Kairiyama, C., Bover, L., Chernajovsky, Y., et al. (1997). Suppression of SPARC expression by antisense RNA abrogates the tumorigenicity of human melanoma cells. *Nature Medicine*, *3*, 171–176. https://www.ncbi.nlm.nih.gov/pubmed/9018235.

Ledda, F., Bravo, A. I., Adris, S., Bover, L., Mordoh, J., & Podhajcer, O. L. (1997). The expression of the secreted protein acidic and rich in cysteine (SPARC) is associated with the neoplastic progression of human melanoma. *The Journal of Investigative Dermatology*, *108*, 210–214. https://www.ncbi.nlm.nih.gov/pubmed/9008236.

Levayer, R., Hauert, B., & Moreno, E. (2015). Cell mixing induced by myc is required for competitive tissue invasion and destruction. *Nature*, *524*, 476–480. https://www.ncbi.nlm.nih.gov/pubmed/26287461.

Li, T., Tan, X., Zhu, S., Zhong, W., Huang, B., Sun, J., et al. (2019). SPARC induces phenotypic modulation of human brain vascular smooth muscle cells via AMPK/mTOR-mediated autophagy. *Neuroscience Letters*, *712*, 134485. https://www.ncbi.nlm.nih.gov/pubmed/31499136.

Liang, J. F., Wang, H. K., Xiao, H., Li, N., Cheng, C. X., Zhao, Y. Z., et al. (2010). Relationship and prognostic significance of SPARC and VEGF protein expression in colon cancer. *Journal of Experimental & Clinical Cancer Research*, *29*, 71. https://www.ncbi.nlm.nih.gov/pubmed/20565704.

Liao, P., Li, W., Liu, R., Teer, J. K., Xu, B., Zhang, W., et al. (2018). Genome-scale analysis identifies SERPINE1 and SPARC as diagnostic and prognostic biomarkers in gastric cancer. *Oncotargets and Therapy*, *11*, 6969–6980. https://www.ncbi.nlm.nih.gov/pubmed/30410354.

Lindner, J. L., Loibl, S., Denkert, C., Ataseven, B., Fasching, P. A., Pfitzner, B. M., et al. (2015). Expression of secreted protein acidic and rich in cysteine (SPARC) in breast cancer and response to neoadjuvant chemotherapy. *Annals of Oncology*, *26*, 95–100. https://www.ncbi.nlm.nih.gov/pubmed/25355716.

Liu, Q. Z., Gao, X. H., Chang, W. J., Wang, H. T., Wang, H., Cao, G. W., et al. (2015). Secreted protein acidic and rich in cysteine expression in human colorectal cancer predicts postoperative prognosis. *European Review for Medical and Pharmacological Sciences*, *19*, 1803–1811. https://www.ncbi.nlm.nih.gov/pubmed/26044224.

Liu, T., Qiu, X., Zhao, X., Yang, R., Lian, H., Qu, F., et al. (2018). Hypermethylation of the SPARC promoter and its prognostic value for prostate cancer. *Oncology Reports*, *39*, 659–666. https://www.ncbi.nlm.nih.gov/pubmed/29207175.

Lopez-Moncada, F., Torres, M. J., Castellon, E. A., & Contreras, H. R. (2019). Secreted protein acidic and rich in cysteine (SPARC) induces epithelial-mesenchymal transition, enhancing migration and invasion, and is associated with high Gleason score in prostate cancer. *Asian Journal of Andrology*, *21*, 557–564. https://www.ncbi.nlm.nih.gov/pubmed/31031331.

Lopez-Otin, C., Blasco, M. A., Partridge, L., Serrano, M., & Kroemer, G. (2013). The hallmarks of aging. *Cell*, *153*, 1194–1217. https://www.ncbi.nlm.nih.gov/pubmed/23746838.

Lotem, J., & Sachs, L. (1995). A mutant p53 antagonizes the deregulated c-myc-mediated enhancement of apoptosis and decrease in leukemogenicity. *Proceedings of the National Academy of Sciences of the United States of America*, *92*, 9672–9676. https://www.ncbi.nlm.nih.gov/pubmed/7568195.

Madan, E., Parker, T. M., Pelham, C. J., Palma, A. M., Peixoto, M. L., Nagane, M., et al. (2019). HIF-transcribed p53 chaperones HIF-1alpha. *Nucleic Acids Research*, *47*, 10212–10234. https://www.ncbi.nlm.nih.gov/pubmed/31538203.

Madan, E., Pelham, C. J., Nagane, M., Parker, T. M., Canas-Marques, R., Fazio, K., et al. (2019). Flower isoforms promote competitive growth in cancer. *Nature*, *572*, 260–264. https://www.ncbi.nlm.nih.gov/pubmed/31341286.

Madoz-Gurpide, J., Lopez-Serra, P., Martinez-Torrecuadrada, J. L., Sanchez, L., Lombardia, L., & Casal, J. I. (2006). Proteomics-based validation of genomic data: applications in colorectal cancer diagnosis. *Molecular & Cellular Proteomics*, *5*, 1471–1483. https://www.ncbi.nlm.nih.gov/pubmed/16733264.

Mantoni, T. S., Schendel, R. R., Rodel, F., Niedobitek, G., Al-Assar, O., Masamune, A., et al. (2008). Stromal SPARC expression and patient survival after chemoradiation for non-resectable pancreatic adenocarcinoma. *Cancer Biology & Therapy*, *7*, 1806–1815. https://www.ncbi.nlm.nih.gov/pubmed/18787407.

Mateo, F., Meca-Cortes, O., Celia-Terrassa, T., Fernandez, Y., Abasolo, I., Sanchez-Cid, L., et al. (2014). SPARC mediates metastatic cooperation between CSC and non-CSC prostate cancer cell subpopulations. *Molecular Cancer*, *13*, 237. https://www.ncbi.nlm.nih.gov/pubmed/25331979.

McClung, H. M., Thomas, S. L., Osenkowski, P., Toth, M., Menon, P., Raz, A., et al. (2007). SPARC upregulates MT1-MMP expression, MMP-2 activation, and the secretion and cleavage of galectin-3 in U87MG glioma cells. *Neuroscience Letters*, *419*, 172–177. https://www.ncbi.nlm.nih.gov/pubmed/17490812.

Melero, J. A., Stitt, D. T., Mangel, W. F., & Carroll, R. B. (1979). Identification of new polypeptide species (48-55K) immunoprecipitable by antiserum to purified large T antigen and present in SV40-infected and -transformed cells. *Virology*, *93*, 466–480. https://www.ncbi.nlm.nih.gov/pubmed/222051.

Melouane, A., Yoshioka, M., Kanzaki, M., & St-Amand, J. (2019). Sparc, an EPS-induced gene, modulates the extracellular matrix and mitochondrial function via ILK/AMPK pathways in C2C12 cells. *Life Sciences*, *229*, 277–287. https://www.ncbi.nlm.nih.gov/pubmed/31150687.

Merino, M. M., Levayer, R., & Moreno, E. (2016). Survival of the fittest: Essential roles of cell competition in development, aging, and cancer. *Trends in Cell Biology*, *26*, 776–788. https://www.ncbi.nlm.nih.gov/pubmed/27319281.

Merino, M. M., Rhiner, C., Lopez-Gay, J. M., Buechel, D., Hauert, B., & Moreno, E. (2015). Elimination of unfit cells maintains tissue health and prolongs lifespan. *Cell*, *160*, 461–476. https://www.ncbi.nlm.nih.gov/pubmed/25601460.

Merino, M. M., Rhiner, C., Portela, M., & Moreno, E. (2013). "Fitness fingerprints" mediate physiological culling of unwanted neurons in Drosophila. *Current Biology*, *23*, 1300–1309. https://www.ncbi.nlm.nih.gov/pubmed/23810538.

Moreno, E., Fernandez-Marrero, Y., Meyer, P., & Rhiner, C. (2015). Brain regeneration in Drosophila involves comparison of neuronal fitness. *Current Biology*, *25*, 955–963. https://www.ncbi.nlm.nih.gov/pubmed/25754635.

Moreno, E., & Rhiner, C. (2014). Darwin's multicellularity: From neurotrophic theories and cell competition to fitness fingerprints. *Current Opinion in Cell Biology*, *31*, 16–22. https://www.ncbi.nlm.nih.gov/pubmed/25022356.

Muller, P. A., Trinidad, A. G., Timpson, P., Morton, J. P., Zanivan, S., van den Berghe, P. V., et al. (2013). Mutant p53 enhances MET trafficking and signalling to drive cell scattering and invasion. *Oncogene*, *32*, 1252–1265. https://www.ncbi.nlm.nih.gov/pubmed/22580601.

Muller, P. A., Vousden, K. H., & Norman, J. C. (2011). p53 and its mutants in tumor cell migration and invasion. *The Journal of Cell Biology*, *192*, 209–218. https://www.ncbi.nlm.nih.gov/pubmed/21263025.

Nagai, M. A., Gerhard, R., Fregnani, J. H., Nonogaki, S., Rierger, R. B., Netto, M. M., et al. (2011). Prognostic value of NDRG1 and SPARC protein expression in breast cancer patients. *Breast Cancer Research and Treatment*, *126*, 1–14. https://www.ncbi.nlm.nih.gov/pubmed/20369286.

Nagaraju, G. P., Dontula, R., El-Rayes, B. F., & Lakka, S. S. (2014). Molecular mechanisms underlying the divergent roles of SPARC in human carcinogenesis. *Carcinogenesis*, *35*, 967–973. https://www.ncbi.nlm.nih.gov/pubmed/24675529.

Neves, J., Demaria, M., Campisi, J., & Jasper, H. (2015). Of flies, mice, and men: evolutionarily conserved tissue damage responses and aging. *Developmental Cell*, *32*, 9–18. https://www.ncbi.nlm.nih.gov/pubmed/25584795.

Okura, Y., Imao, T., Murashima, S., Shibata, H., Kamikavwa, A., Okamatsu-Ogura, Y., et al. (2019). Interaction of nerve growth factor beta with adiponectin and SPARC oppositely modulates its biological activity. *International Journal of Molecular Sciences*, *20*. https://www.ncbi.nlm.nih.gov/pubmed/30934765.

Omi, S., Yamanouchi, K., Nakamura, K., Matsuwaki, T., & Nishihara, M. (2019). Reduced fibrillar collagen accumulation in skeletal muscle of secreted protein acidic and rich in cysteine (SPARC)-null mice. *The Journal of Veterinary Medical Science*, *81*, 1649–1654. https://www.ncbi.nlm.nih.gov/pubmed/31582603.

Oren, M., & Rotter, V. (2010). Mutant p53 gain-of-function in cancer. *Cold Spring Harbor Perspectives in Biology*, *2*, a001107. https://www.ncbi.nlm.nih.gov/pubmed/20182618.

Papapanagiotou, A., Sgourakis, G., Karkoulias, K., Raptis, D., Parkin, E., Brotzakis, P., et al. (2018). Osteonectin as a screening marker for pancreatic cancer: A prospective study. *The Journal of International Medical Research*, *46*, 2769–2779. https://www.ncbi.nlm.nih.gov/pubmed/29756486.

Peled, A., Zipori, D., & Rotter, V. (1996). Cooperation between p53-dependent and p53-independent apoptotic pathways in myeloid cells. *Cancer Research*, *56*, 2148–2156. https://www.ncbi.nlm.nih.gov/pubmed/8616864.

Pfister, N. T., Fomin, V., Regunath, K., Zhou, J. Y., Zhou, W., Silwal-Pandit, L., et al. (2015). Mutant p53 cooperates with the SWI/SNF chromatin remodeling complex to regulate VEGFR2 in breast cancer cells. *Genes & Development*, *29*, 1298–1315. https://www.ncbi.nlm.nih.gov/pubmed/26080815.

Pieniazek, M., Donizy, P., Halon, A., Leskiewicz, M., & Matkowski, R. (2016). Prognostic significance of immunohistochemical epithelial-mesenchymal transition markers in skin melanoma patients. *Biomarkers in Medicine*, *10*, 975–985. https://www.ncbi.nlm.nih.gov/pubmed/27586584.

Podhajcer, O. L., Benedetti, L., Girotti, M. R., Prada, F., Salvatierra, E., & Llera, A. S. (2008). The role of the matricellular protein SPARC in the dynamic interaction between the tumor and the host. *Cancer Metastasis Reviews*, *27*, 523–537. https://www.ncbi.nlm.nih.gov/pubmed/18459035.

Portela, M., Casas-Tinto, S., Rhiner, C., Lopez-Gay, J. M., Dominguez, O., Soldini, D., et al. (2010). Drosophila SPARC is a self-protective signal expressed by loser cells during cell competition. *Developmental Cell*, *19*, 562–573. https://www.ncbi.nlm.nih.gov/pubmed/20951347.

Prada, F., Benedetti, L. G., Bravo, A. I., Alvarez, M. J., Carbone, C., & Podhajcer, O. L. (2007). SPARC endogenous level, rather than fibroblast-produced SPARC or stroma reorganization induced by SPARC, is responsible for melanoma cell growth. *The Journal of Investigative Dermatology*, *127*, 2618–2628. https://www.ncbi.nlm.nih.gov/pubmed/17625595.

Ramu, I., Buchholz, S. M., Patzak, M. S., Goetze, R. G., Singh, S. K., Richards, F. M., et al. (2019). SPARC dependent collagen deposition and gemcitabine delivery in a genetically engineered mouse model of pancreas cancer. *eBioMedicine*, *48*, 161–168. https://www.ncbi.nlm.nih.gov/pubmed/31597597.

Rempel, S. A., Golembieski, W. A., Ge, S., Lemke, N., Elisevich, K., Mikkelsen, T., et al. (1998). SPARC: A signal of astrocytic neoplastic transformation and reactive response in human primary and xenograft gliomas. *Journal of Neuropathology and Experimental Neurology*, *57*, 1112–1121. https://www.ncbi.nlm.nih.gov/pubmed/9862633.

Rhiner, C., Lopez-Gay, J. M., Soldini, D., Casas-Tinto, S., Martin, F. A., Lombardia, L., et al. (2010). Flower forms an extracellular code that reveals the fitness of a cell to its neighbors in Drosophila. *Developmental Cell*, *18*, 985–998. https://www.ncbi.nlm.nih.gov/pubmed/20627080.

Rich, J. N., Shi, Q., Hjelmeland, M., Cummings, T. J., Kuan, C. T., Bigner, D. D., et al. (2003). Bone-related genes expressed in advanced malignancies induce invasion and metastasis in a genetically defined human cancer model. *The Journal of Biological Chemistry*, *278*, 15951–15957. https://www.ncbi.nlm.nih.gov/pubmed/12590137.

Robert, G., Gaggioli, C., Bailet, O., Chavey, C., Abbe, P., Aberdam, E., et al. (2006). SPARC represses E-cadherin and induces mesenchymal transition during melanoma development. *Cancer Research*, *66*, 7516–7523. https://www.ncbi.nlm.nih.gov/pubmed/16885349.

Rotter, V. (1983). p53, a transformation-related cellular-encoded protein, can be used as a biochemical marker for the detection of primary mouse tumor cells. *Proceedings of the National Academy of Sciences of the United States of America*, *80*, 2613–2617. https://www.ncbi.nlm.nih.gov/pubmed/6189126.

Ryu, B., Jones, J., Hollingsworth, M. A., Hruban, R. H., & Kern, S. E. (2001). Invasion-specific genes in malignancy: Serial analysis of gene expression comparisons of primary and passaged cancers. *Cancer Research*, *61*, 1833–1838. https://www.ncbi.nlm.nih.gov/pubmed/11280733.

Said, N., Frierson, H. F., Jr., Chernauskas, D., Conaway, M., Motamed, K., & Theodorescu, D. (2009). The role of SPARC in the TRAMP model of prostate carcinogenesis and progression. *Oncogene*, *28*, 3487–3498. https://www.ncbi.nlm.nih.gov/pubmed/19597474.

Said, N., Socha, M. J., Olearczyk, J. J., Elmarakby, A. A., Imig, J. D., & Motamed, K. (2007). Normalization of the ovarian cancer microenvironment by SPARC. *Molecular Cancer Research*, *5*, 1015–1030. https://www.ncbi.nlm.nih.gov/pubmed/17951402.

Sailaja, G. S., Bhoopathi, P., Gorantla, B., Chetty, C., Gogineni, V. R., Velpula, K. K., et al. (2013). The secreted protein acidic and rich in cysteine (SPARC) induces endoplasmic reticulum stress leading to autophagy-mediated apoptosis in neuroblastoma. *International Journal of Oncology*, *42*, 188–196. https://www.ncbi.nlm.nih.gov/pubmed/23123816.

Sangaletti, S., Tripodo, C., Vitali, C., Portararo, P., Guarnotta, C., Casalini, P., et al. (2014). Defective stromal remodeling and neutrophil extracellular traps in lymphoid tissues favor the transition from autoimmunity to lymphoma. *Cancer Discovery*, *4*, 110–129. https://www.ncbi.nlm.nih.gov/pubmed/24189145.

Sato, N., Fukushima, N., Maehara, N., Matsubayashi, H., Koopmann, J., Su, G. H., et al. (2003). SPARC/osteonectin is a frequent target for aberrant methylation in pancreatic adenocarcinoma and a mediator of tumor-stromal interactions. *Oncogene*, *22*, 5021–5030. https://www.ncbi.nlm.nih.gov/pubmed/12902985.

Sato, T., Oshima, T., Yamamoto, N., Yamada, T., Hasegawa, S., Yukawa, N., et al. (2013). Clinical significance of SPARC gene expression in patients with gastric cancer. *Journal of Surgical Oncology*, *108*, 364–368. https://www.ncbi.nlm.nih.gov/pubmed/24018911.

Scian, M. J., Stagliano, K. E., Ellis, M. A., Hassan, S., Bowman, M., Miles, M. F., et al. (2004). Modulation of gene expression by tumor-derived p53 mutants. *Cancer Research*, *64*, 7447–7454. https://www.ncbi.nlm.nih.gov/pubmed/15492269.

Senturk, S., Yao, Z., Camiolo, M., Stiles, B., Rathod, T., Walsh, A. M., et al. (2014). p53Psi is a transcriptionally inactive p53 isoform able to reprogram cells toward a metastatic-like state. *Proceedings of the National Academy of Sciences of the United States of America*, *111*, E3287–E3296. https://www.ncbi.nlm.nih.gov/pubmed/25074920.

Sharma, S., Xing, F., Liu, Y., Wu, K., Said, N., Pochampally, R., et al. (2016). Secreted Protein Acidic and Rich in Cysteine (SPARC) mediates metastatic dormancy of prostate cancer in bone. *The Journal of Biological Chemistry*, *291*, 19351–19363. https://www.ncbi.nlm.nih.gov/pubmed/27422817.

Shi, Q., Bao, S., Maxwell, J. A., Reese, E. D., Friedman, H. S., Bigner, D. D., et al. (2004). Secreted protein acidic, rich in cysteine (SPARC), mediates cellular survival of gliomas through AKT activation. *The Journal of Biological Chemistry*, *279*, 52200–52209. https://www.ncbi.nlm.nih.gov/pubmed/15469933.

Socha, M. J., Said, N., Dai, Y., Kwong, J., Ramalingam, P., Trieu, V., et al. (2009). Aberrant promoter methylation of SPARC in ovarian cancer. *Neoplasia*, *11*, 126–135. https://www.ncbi.nlm.nih.gov/pubmed/19177197.

Sosa, M. S., Girotti, M. R., Salvatierra, E., Prada, F., de Olmo, J. A., Gallango, S. J., et al. (2007). Proteomic analysis identified N-cadherin, clusterin, and HSP27 as mediators of SPARC (secreted protein, acidic and rich in cysteines) activity in melanoma cells. *Proteomics*, *7*, 4123–4134. https://www.ncbi.nlm.nih.gov/pubmed/17994631.

Soussi, T., & Wiman, K. G. (2015). TP53: An oncogene in disguise. *Cell Death and Differentiation*, *22*, 1239–1249. https://www.ncbi.nlm.nih.gov/pubmed/26024390.

Sova, P., Feng, Q., Geiss, G., Wood, T., Strauss, R., Rudolf, V., et al. (2006). Discovery of novel methylation biomarkers in cervical carcinoma by global demethylation and microarray analysis. *Cancer Epidemiology, Biomarkers & Prevention*, *15*, 114–123. https://www.ncbi.nlm.nih.gov/pubmed/16434596.

Suijkerbuijk, S. J., Kolahgar, G., Kucinski, I., & Piddini, E. (2016). Cell competition drives the growth of intestinal adenomas in drosophila. *Current Biology*, *26*, 428–438. https://www.ncbi.nlm.nih.gov/pubmed/26853366.

Sun, W., Feng, J., Yi, Q., Xu, X., Chen, Y., & Tang, L. (2018). SPARC acts as a mediator of TGF-beta1 in promoting epithelial-to-mesenchymal transition in A549 and H1299 lung cancer cells. *BioFactors*, *44*, 453–464. https://www.ncbi.nlm.nih.gov/pubmed/30346081.

Suzuki, M., Hao, C., Takahashi, T., Shigematsu, H., Shivapurkar, N., Sathyanarayana, U. G., et al. (2005). Aberrant methylation of SPARC in human lung cancers. *British Journal of Cancer*, *92*, 942–948. https://www.ncbi.nlm.nih.gov/pubmed/15756262.

Szynglarewicz, B., Kasprzak, P., Donizy, P., Biecek, P., Halon, A., & Matkowski, R. (2016). Ductal carcinoma in situ on stereotactic biopsy of suspicious breast microcalcifications: Expression of SPARC (Secreted Protein, Acidic and Rich in Cysteine) can predict postoperative invasion. *Journal of Surgical Oncology*, *114*, 548–556. https://www.ncbi.nlm.nih.gov/pubmed/27439354.

Tai, I. T., Dai, M., Owen, D. A., & Chen, L. B. (2005). Genome-wide expression analysis of therapy-resistant tumors reveals SPARC as a novel target for cancer therapy. *The Journal of Clinical Investigation*, *115*, 1492–1502. https://www.ncbi.nlm.nih.gov/pubmed/15902309.

Tang, M. J., & Tai, I. T. (2007). A novel interaction between procaspase 8 and SPARC enhances apoptosis and potentiates chemotherapy sensitivity in colorectal cancers. *The Journal of Biological Chemistry*, *282*, 34457–34467. https://www.ncbi.nlm.nih.gov/pubmed/17897953.

Terzian, T., Suh, Y. A., Iwakuma, T., Post, S. M., Neumann, M., Lang, G. A., et al. (2008). The inherent instability of mutant p53 is alleviated by Mdm2 or p16INK4a loss. *Genes & Development*, *22*, 1337–1344. https://www.ncbi.nlm.nih.gov/pubmed/18483220.

Thomas, S. L., Schultz, C. R., Mouzon, E., Golembieski, W. A., El Naili, R., Radakrishnan, A., et al. (2015). Loss of SPARC in p53-null astrocytes promotes macrophage activation and phagocytosis resulting in decreased tumor size and tumor cell survival. *Brain Pathology*, *25*, 391–400. https://www.ncbi.nlm.nih.gov/pubmed/24862407.

Thomas, R., True, L. D., Bassuk, J. A., Lange, P. H., & Vessella, R. L. (2000). Differential expression of osteonectin/SPARC during human prostate cancer progression. *Clinical Cancer Research*, *6*, 1140–1149. https://www.ncbi.nlm.nih.gov/pubmed/10741745.

Tripathi, R., & Mishra, R. (2010). Interaction of Pax6 with SPARC and p53 in brain of mice indicates Smad3 dependent auto-regulation. *Journal of Molecular Neuroscience*, *41*, 397–403. https://www.ncbi.nlm.nih.gov/pubmed/20177825.

Tumbarello, D. A., Andrews, M. R., & Brenton, J. D. (2016). SPARC regulates transforming growth factor beta induced (TGFBI) extracellular matrix deposition and paclitaxel response in ovarian cancer cells. *PLoS One*, *11*, e0162698. https://www.ncbi.nlm.nih.gov/pubmed/27622658.

Vanneste, E., Voet, T., Le Caignec, C., Ampe, M., Konings, P., Melotte, C., et al. (2009). Chromosome instability is common in human cleavage-stage embryos. *Nature Medicine*, *15*, 577–583. https://www.ncbi.nlm.nih.gov/pubmed/19396175.

Vijg, J. (2014). Somatic mutations, genome mosaicism, cancer and aging. *Current Opinion in Genetics & Development*, *26*, 141–149. https://www.ncbi.nlm.nih.gov/pubmed/25282114.

Vousden, K. H., & Prives, C. (2009). Blinded by the light: The growing complexity of p53. *Cell*, *137*, 413–431. https://www.ncbi.nlm.nih.gov/pubmed/19410540.

Wagstaff, L., Goschorska, M., Kozyrska, K., Duclos, G., Kucinski, I., Chessel, A., et al. (2016). Mechanical cell competition kills cells via induction of lethal p53 levels. *Nature Communications*, *7*, 11373. https://www.ncbi.nlm.nih.gov/pubmed/27109213.

Wang, H., Bao, W., Jiang, F., Che, Q., Chen, Z., Wang, F., et al. (2015). Mutant p53 (p53-R248Q) functions as an oncogene in promoting endometrial cancer by up-regulating REGgamma. *Cancer Letters*, *360*, 269–279. https://www.ncbi.nlm.nih.gov/pubmed/25697482.

Wang, C. S., Lin, K. H., Chen, S. L., Chan, Y. F., & Hsueh, S. (2004). Overexpression of SPARC gene in human gastric carcinoma and its clinic-pathologic significance. *British Journal of Cancer*, *91*, 1924–1930. https://www.ncbi.nlm.nih.gov/pubmed/15558074.

Wang, L., Yang, M., Shan, L., Qi, L., Chai, C., Zhou, Q., et al. (2012). The role of SPARC protein expression in the progress of gastric cancer. *Pathology Oncology Research*, *18*, 697–702. https://www.ncbi.nlm.nih.gov/pubmed/22246794.

Wang, Q., Yang, Q., Zhang, A., Kang, Z., Wang, Y., & Zhang, Z. (2019). Silencing of SPARC represses heterotopic ossification via inhibition of the MAPK signaling pathway. *Bioscience Reports*, *39*. https://www.ncbi.nlm.nih.gov/pubmed/31548362.

Wang, M., Zhao, J., Zhang, L., Wei, F., Lian, Y., Wu, Y., et al. (2017). Role of tumor microenvironment in tumorigenesis. *Journal of Cancer*, *8*, 761–773. https://www.ncbi.nlm.nih.gov/pubmed/28382138.

Witkiewicz, A. K., Freydin, B., Chervoneva, I., Potoczek, M., Rizzo, W., Rui, H., et al. (2010). Stromal CD10 and SPARC expression in ductal carcinoma in situ (DCIS) patients predicts disease recurrence. *Cancer Biology & Therapy*, *10*, 391–396. https://www.ncbi.nlm.nih.gov/pubmed/20574156.

Wolf, D., Harris, N., & Rotter, V. (1984). Reconstitution of p53 expression in a non-producer Ab-MuLV-transformed cell line by transfection of a functional p53 gene. *Cell*, *38*, 119–126. https://www.ncbi.nlm.nih.gov/pubmed/6088057.

Xu, J., Yang, S., Gu, X., Shen, H., Wang, L., Xu, W., et al. (2019). SPARC correlates with unfavorable outcome and promotes tumor growth in lung squamous cell carcinoma. *Experimental and Molecular Pathology*, *110*, 104276. https://www.ncbi.nlm.nih.gov/pubmed/31233732.

Yamanaka, M., Kanda, K., Li, N. C., Fukumori, T., Oka, N., Kanayama, H. O., et al. (2001). Analysis of the gene expression of SPARC and its prognostic value for bladder cancer. *The Journal of Urology*, *166*, 2495–2499. https://www.ncbi.nlm.nih.gov/pubmed/11696817.

Yang, E., Kang, H. J., Koh, K. H., Rhee, H., Kim, N. K., & Kim, H. (2007). Frequent inactivation of SPARC by promoter hypermethylation in colon cancers. *International Journal of Cancer*, *121*, 567–575. https://www.ncbi.nlm.nih.gov/pubmed/17397030.

Yao, C. K., Lin, Y. Q., Ly, C. V., Ohyama, T., Haueter, C. M., Moiseenkova-Bell, V. Y., et al. (2009). A synaptic vesicle-associated Ca2 + channel promotes endocytosis and couples exocytosis to endocytosis. *Cell*, *138*, 947–960. https://www.ncbi.nlm.nih.gov/pubmed/19737521.

Yiu, G. K., Chan, W. Y., Ng, S. W., Chan, P. S., Cheung, K. K., Berkowitz, R. S., et al. (2001). SPARC (Secreted Protein Acidic and Rich in Cysteine) induces apoptosis in ovarian cancer cells. *The American Journal of Pathology*, *159*, 609–622. https://www.ncbi.nlm.nih.gov/pubmed/11485919.

Yu, X. Z., Guo, Z. Y., Di, Y., Yang, F., Ouyang, Q., Fu, D. L., et al. (2017). The relationship between SPARC expression in primary tumor and metastatic lymph node of resected pancreatic cancer patients and patients' survival. *Hepatobiliary & Pancreatic Diseases International*, *16*, 104–109. https://www.ncbi.nlm.nih.gov/pubmed/28119265.

Zhang, G., Xie, Y., Zhou, Y., Xiang, C., Chen, L., Zhang, C., et al. (2017). p53 pathway is involved in cell competition during mouse embryogenesis. *Proceedings of the National Academy of Sciences of the United States of America*, *114*, 498–503. https://www.ncbi.nlm.nih.gov/pubmed/28049824.

Zhao, Z. S., Wang, Y. Y., Chu, Y. Q., Ye, Z. Y., & Tao, H. Q. (2010). SPARC is associated with gastric cancer progression and poor survival of patients. *Clinical Cancer Research*, *16*, 260–268. https://www.ncbi.nlm.nih.gov/pubmed/20028745.

Zhu, J., Sammons, M. A., Donahue, G., Dou, Z., Vedadi, M., Getlik, M., et al. (2015). Gain-of-function p53 mutants co-opt chromatin pathways to drive cancer growth. *Nature*, *525*, 206–211. https://www.ncbi.nlm.nih.gov/pubmed/26331536.

Zhu, A., Yuan, P., Du, F., Hong, R., Ding, X., Shi, X., et al. (2016). SPARC overexpression in primary tumors correlates with disease recurrence and overall survival in patients with triple negative breast cancer. *Oncotarget*, 7, 76628–76634. https://www.ncbi.nlm.nih.gov/pubmed/27421134.

LETTER

https://doi.org/10.1038/s41586-019-1429-3

# Flower isoforms promote competitive growth in cancer

Esha Madan[1,2], Christopher J. Pelham[2,3,10], Masaki Nagane[4,10], Taylor M. Parker[2,5,10], Rita Canas-Marques[1], Kimberly Fazio[6], Kranti Shaik[6], Youzhong Yuan[2], Vanessa Henriques[1], Antonio Galzerano[1], Tadashi Yamashita[4], Miguel Alexandre Ferreira Pinto[1], Antonio M. Palma[1], Denise Camacho[1], Ana Vieira[1], David Soldini[7], Harikrishna Nakshatri[5], Steven R. Post[2], Christa Rhiner[1], Hiroko Yamashita[8], Davide Accardi[1], Laura A. Hansen[6], Carlos Carvalho[1], Antonio L. Beltran[1], Periannan Kuppusamy[9], Rajan Gogna[1,2]* & Eduardo Moreno[1]*

**In humans, the adaptive immune system uses the exchange of information between cells to detect and eliminate foreign or damaged cells; however, the removal of unwanted cells does not always require an adaptive immune system[1,2]. For example, cell selection in *Drosophila* uses a cell selection mechanism based on 'fitness fingerprints', which allow it to delay ageing[3], prevent developmental malformations[3,4] and replace old tissues during regeneration[5]. At the molecular level, these fitness fingerprints consist of combinations of Flower membrane proteins[3,4,6]. Proteins that indicate reduced fitness are called Flower-Lose, because they are expressed in cells marked to be eliminated[6]. However, the presence of Flower-Lose isoforms at a cell's membrane does not always lead to elimination, because if neighbouring cells have similar levels of Lose proteins, the cell will not be killed[4,6,7]. Humans could benefit from the capability to recognize unfit cells, because accumulation of damaged but viable cells during development and ageing causes organ dysfunction and disease[8–17]. However, in *Drosophila* this mechanism is hijacked by premalignant cells to gain a competitive growth advantage[18]. This would be undesirable for humans because it might make tumours more aggressive[19–21]. It is unknown whether a similar mechanism of cell-fitness comparison is present in humans. Here we show that two human Flower isoforms (hFWE1 and hFWE3) behave as Flower-Lose proteins, whereas the other two isoforms (hFWE2 and hFWE4) behave as Flower-Win proteins. The latter give cells a competitive advantage over cells expressing Lose isoforms, but Lose-expressing cells are not eliminated if their neighbours express similar levels of Lose isoforms; these proteins therefore act as fitness fingerprints. Moreover, human cancer cells show increased Win isoform expression and proliferate in the presence of Lose-expressing stroma, which confers a competitive growth advantage on the cancer cells. Inhibition of the expression of Flower proteins reduces tumour growth and metastasis, and induces sensitivity to chemotherapy. Our results show that ancient mechanisms of cell recognition and selection are active in humans and affect oncogenic growth.**

*C9ORF7* (also known as *CACFD1*; referred to here as *hFWE*) encodes human Flower (hFWE) and generates four protein-coding splice variants (*hFWE1–hFWE4*) (Fig. 1a). Mining of the Encode database[22] showed high levels of acetylation at the 27th lysine residue of the histone H3 protein (H3K27Ac) and hypersensitivity to DNAase-I around the +1 open reading frame (ORF) (Extended Data Fig. 1a, b), suggesting that the *hFWE* locus is transcriptionally active[23]. The *hFWE* exons are conserved (Extended Data Fig. 1c), and alternative splicing produces four hFWE isoforms of transmembrane proteins, with membrane-spanning domains as predicted (Fig. 1b). To identify potential hFWE$^{Win}$ or hFWE$^{Lose}$ isoforms (as observed in *Drosophila*[6]), we generated CRISPR-assisted MCF-7 *hFWE$^{KO}$* cells that expressed individual hFWE isoforms and used them for a co-culture protocol (Extended Data Fig. 1d). MCF-7 *hFWE$^{KO}$* cells lacked expression of *hFWE* mRNA (Extended Data Fig. 1e), but did not differ from wild-type cells in terms of proliferation (BrdU and MTT assays), cell-cycle, reactive oxygen species (ROS), annexin-V, and clonogenic assays (Extended Data Fig. 1f–k). Lentivirus-assisted overexpression of the four hFWE isoforms had no effect on cell proliferation, cell death, cell volume, cellular sphericity, or annexin-V staining when compared to MCF-7 *hFWE$^{KO}$* cells (Extended Data Figs. 1l, m, 2a–f, Supplementary Video 1). From these data, we conclude that, as in *Drosophila*[3,6,18,24], human cells homogenously expressing single hFWE isoforms do not undergo apoptosis.

To identify potential hFWE$^{Win}$ and hFWE$^{Lose}$ isoforms, we performed live-cell imaging (Extended Data Fig. 1d), which showed that cells expressing hFWE1 or hFWE3 undergo cell death only when co-cultured with cells expressing either hFWE2 or hFWE4; cell death was accompanied by increased proliferation of cells expressing hFWE2 or hFWE4 (Fig. 1c, Extended Data Figs. 3a, b, 4a, Supplementary Videos 2–5). These findings suggest that hFWE2 and hFWE4 function as hFWE$^{Win}$ isoforms whereas hFWE1 and hFWE3 function as hFWE$^{Lose}$ isoforms. Furthermore, elimination of hFWE$^{Lose}$-expressing cells occurred through caspase-dependent apoptosis, because the addition of the caspase inhibitor Z-VAD-FMK inhibited this process and annexin-V staining (Extended Data Figs. 4b, 5a, b, 6a, Supplementary Videos 6, 7). Cells expressing individual isoforms (hFWE1–hFWE4) did not induce loss of co-cultured *hFWE$^{KO}$* cells, indicating that hFWE-mediated cell elimination requires cells that express both hFWE$^{Win}$ and hFWE$^{Lose}$ (Extended Data Fig. 6b, Supplementary Video 8). Elimination of hFWE$^{Lose}$ cells was dependent on contact with hFWE$^{Win}$ cells, because no apoptosis was observed during imaging of low-density-plated hFWE1–GFP$^{+}$ and hFWE2–RFP$^{+}$ cells (Extended Data Fig. 6c, Supplementary Video 9). We tested whether factors secreted by hFWE$^{Win}$-expressing cells were involved in cell elimination by transferring conditioned medium from hFWE2-expressing cells onto hFWE1-expressing cells and found that it had no significant effect on cell death (Extended Data Fig. 6d). Live-cell calcium imaging using Fluo-4AM dye showed that expression of individual hFWE isoforms in MCF-7 *hFWE$^{KO}$* cells had no effect on cellular calcium levels (Extended Data Fig. 7a, b), and the calcium chelator BAPTA-AM did not interfere with the elimination of hFWE$^{Lose}$-expressing cells (Extended Data Fig. 7c), suggesting that hFWE

[1]Champalimaud Centre for the Unknown, Lisbon, Portugal. [2]Department of Pathology, University of Arkansas for Medical Sciences, Little Rock, AR, USA. [3]Center for Clinical Pharmacology, Washington University School of Medicine and St. Louis College of Pharmacy, St. Louis, MO, USA. [4]Department of Biochemistry, School of Veterinary Medicine, Azabu University, Kanagawa, Japan. [5]Department of Biochemistry and Molecular Biology, IU Simon Cancer Center, Indiana University School of Medicine, Indianapolis, IN, USA. [6]Department of Biomedical Sciences, Creighton University, Omaha, NE, USA. [7]Institute for Surgical Pathology, University Hospital and University of Zurich, Zurich, Switzerland. [8]Department of Breast Surgery, Hokkaido University Hospital, Sapporo, Japan. [9]Department of Radiology and Medicine, Norris Cotton Cancer Center, Geisel School of Medicine, Dartmouth College, Lebanon, NH, USA. [10]These authors contributed equally: Christopher J. Pelham, Masaki Nagane, Taylor M. Parker. *e-mail: rajan.gogna@research.fchampalimaud.org; eduardo.moreno@research.fchampalimaud.org

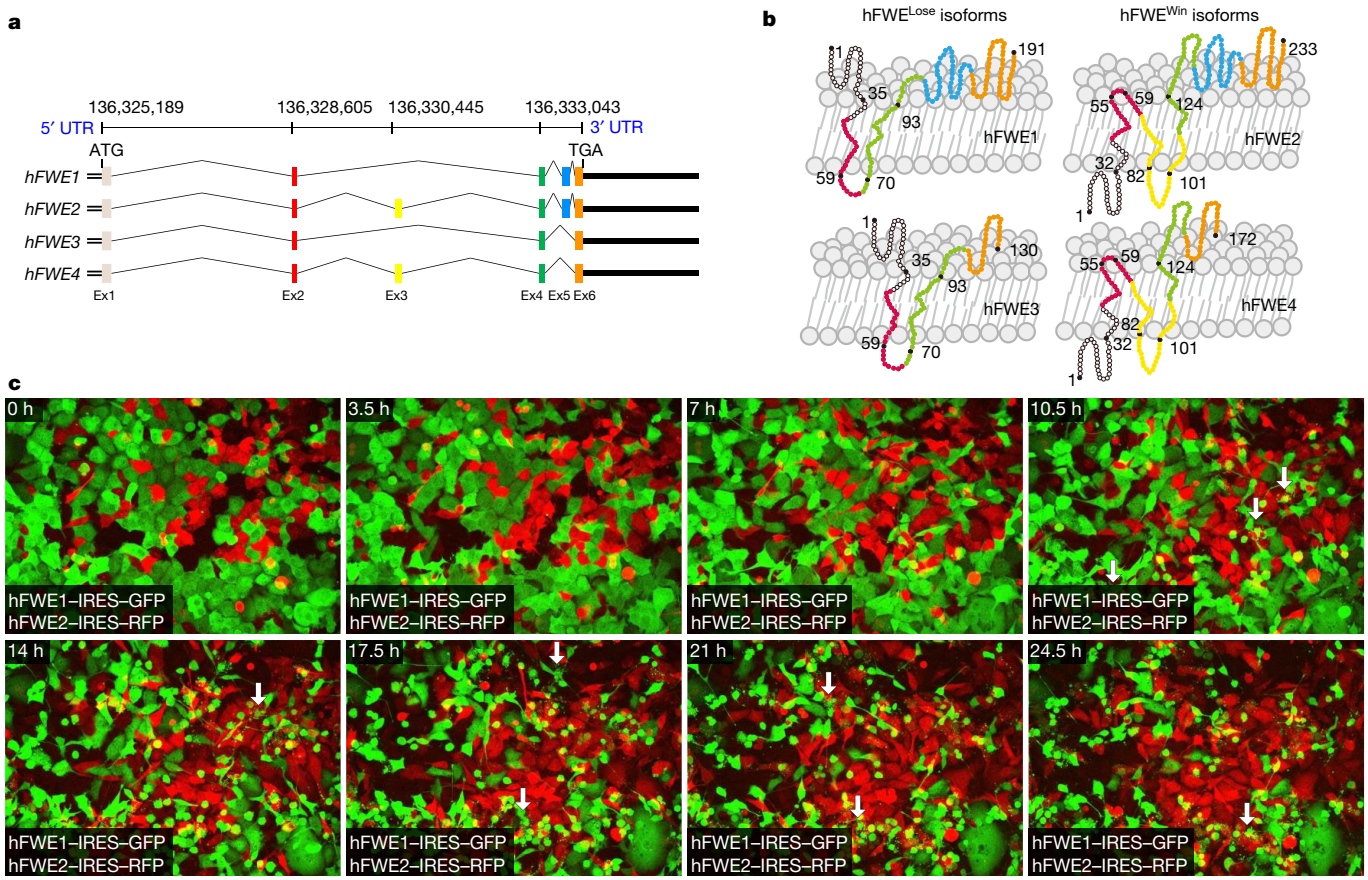


**Fig. 1 | Characterization of human Flower isoforms and competition between Winner and Loser cells. a**, A schematic representing the *hFWE* gene locus and its six exons, which alternatively splice to generate four hFWE isoforms (hFWE1–hFWE4). **b**, Model depicting the transmembrane structures of the four hFWE proteins. The colour coding of amino acid chains is complementary to the colour coding of *hFWE* exons and shows the contributions and locations of the amino acid sequences coded by each exon. **c**, Live-cell imaging shows competition between $hFWE^{KO}$ MCF-7 cells expressing hFWE1–IRES–GFP (green) and hFWE2–IRES–RFP (red) isoforms; cells carrying the hFWE1 isoform are eliminated. $n = 3$ biologically independent experiments with similar results.

isoforms do not function as calcium transporters[25–27] and their function is calcium-independent. We conclude that human Flower proteins work as canonical fitness fingerprints.

To study the role of Flower proteins in human cancer, we used quantitative PCR (qPCR) to measure the expression of hFWE isoforms in laser-captured formalin-fixed paraffin-embedded (FFPE) samples of cancerous and adjacent stromal tissue from individuals with malignant tumours (25 breast, 21 colon), benign tumours (10 breast, 10 colon), and normal tissue (10 breast, 10 colon, from matched patients; Fig. 2a). All hFWE isoforms showed poor expression in normal tissue. The tumour tissue showed increased expression of $hFWE^{Win}$ isoforms, and stromal tissue showed significant upregulation of $hFWE^{lose}$ isoforms (more in malignant tumours than in benign tumours and their stroma; Fig. 2a). Sequential laser capture of breast and colon stromal tissue showed a significant increase in expression of $hFWE^{Lose}$ isoforms in the first 400 μm from the edge of the tumour tissue (Extended Data Fig. 7d), where genes involved in the regulation of apoptosis were concurrently upregulated (Extended Data Fig. 7e). Fluorescence in situ hybridization (FISH) showed increased expression of $hFWE^{Win}$ isoforms exclusively in breast cancer cells (Extended Data Fig. 7f); further qPCR showed that, unlike tumour epithelial cells, normal epithelial cells do not exhibit high $hFWE^{Win}$ expression (Extended Data Fig. 7g). MCF-7 $hFWE^{KO}$ cells expressing hFWE2 induced apoptosis of co-cultured primary epithelial cells or fibroblasts (isolated from normal breast tissue; Extended Data Fig. 8a).

We generated two anti-hFWE antibodies (one against the N terminus that is common to all four isoforms, and the other specific to the $hFWE^{Win}$ isoforms (encoded by exon 3)). We used immunohistochemistry to validate the antibody specificity in sections of $hFWE^{KO}$ cells overexpressing hFWE1, hFWE2, hFWE3 or hFWE4 (Extended Data Figs. 8b, 9a). Immunostaining with anti-$hFWE^{Win}$ and anti-hFWE-N-term antibodies produced positive membrane staining in breast cancer cells (Extended Data Fig. 9b). Immunohistochemistry with the anti-$hFWE^{Win}$ antibody showed that $hFWE^{Win}$ was expressed exclusively in breast, colon, and squamous cell carcinoma (SCC) cancers (Fig. 2b, Extended Data Figs. 7h, 9c). Immunohistochemistry of the same breast, colon, and SCC cancers with anti-hFWE-N-term antibodies—which recognize both $hFWE^{Win}$ and $hFWE^{Lose}$ isoforms—showed staining of both cancer and stromal cells (Fig. 2b, Extended Data Figs. 7h, 9c). Both antibodies showed poor staining in normal tissue (Extended Data Fig. 9c). Our main observations from this analysis were that both types of hFWE isoform tend to be low in healthy tissue, $hFWE^{Win}$ isoforms are upregulated in cancer tissue (more in malignant than in benign cancers), and levels of $hFWE^{Lose}$ isoforms are unusually high in the cancer-adjacent stroma.

These results suggested that tumour cells exhibit high $hFWE^{Win}$ expression and tend to grow in areas of stroma with high $hFWE^{Lose}$ expression. To investigate whether overexpression of $hFWE^{Lose}$ in host tissue and $hFWE^{Win}$ in the tumour might result in aggressive tumour growth, we generated $Fwe^{KO}$ mice[26] bearing orthotopic breast tumours derived from MCF-7 cells. Individual hFWE isoforms were overexpressed in the mammary tissue of $Fwe^{KO}$ mice to study the effects of host cells, and $hFWE^{KO}$ MCF-7 cells overexpressing GFP-tagged individual hFWE isoforms were used to generate the tumours (Fig. 3a). When we analysed all possible combinations, we found that MCF-7 $hFWE^{KO}$ cells expressing hFWE2–GFP or hFWE4–GFP generated

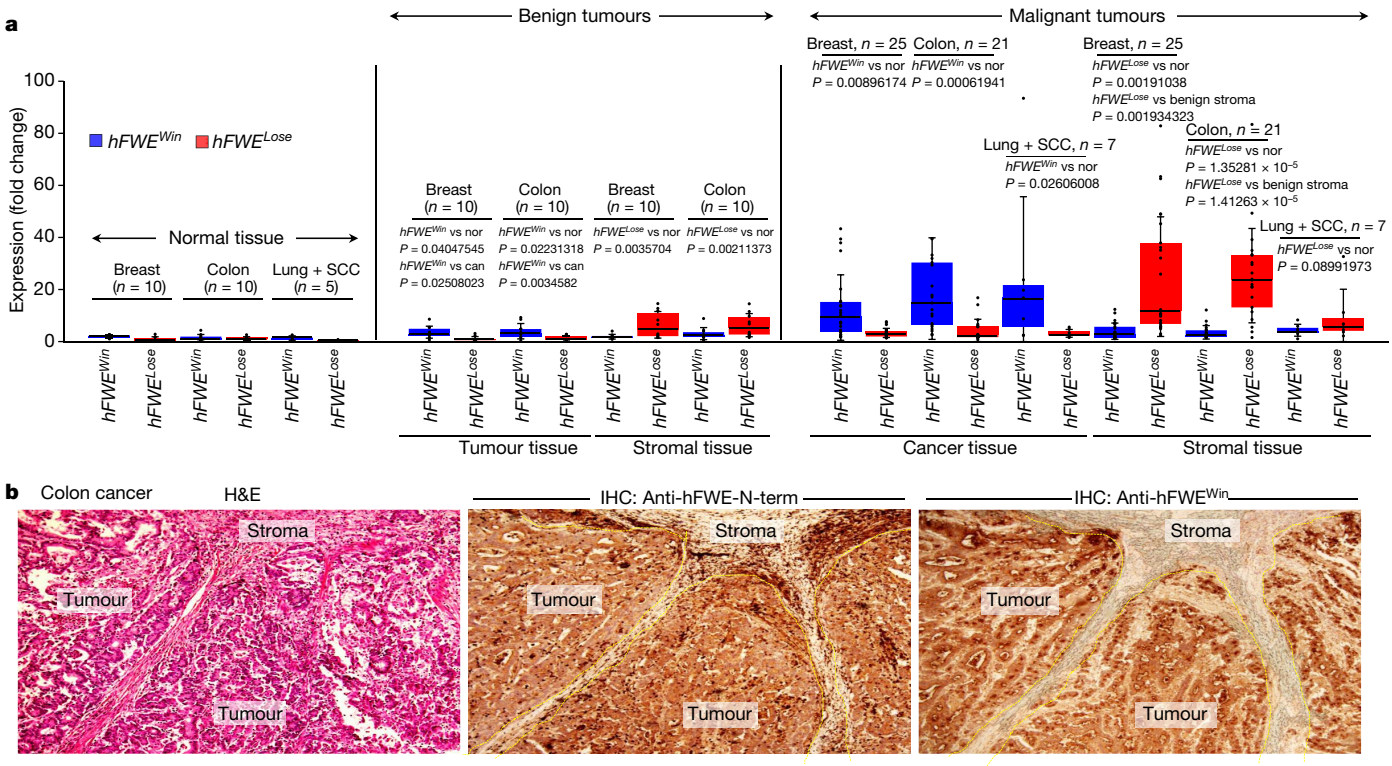


**Fig. 2 | Flower isoforms and human cancer. a**, Expression of hFWE$^{Win}$ and hFWE$^{Lose}$ mRNA is observed in benign and malignant tumours, their respective stroma (from same samples) and healthy tissue (laser microdissected, FFPE samples). Poor expression was observed in healthy tissue; hFWE$^{Win}$ isoforms were upregulated in benign tumour tissue; and hFWE$^{Lose}$ isoforms were upregulated in stromal tissue. In malignant tumours, hFWE$^{Win}$ isoforms were significantly upregulated in cancer tissue and hFWE$^{Lose}$ isoforms were significantly upregulated in stromal tissue. hFWE$^{Win}$ expression ratio for normal:benign tumour:malignant tumour, 1:2.328:11.369. hFWE$^{Lose}$ expression ratio for normal:benign stroma:malignant stroma, 1:6.513:24.694. By binary logistic regression analysis, hFWE$^{Win}$ in cancer (with $P = 0.006$) and hFWE$^{Lose}$ in stroma (with $P = 0.015$) together have predictive capacity for malignant tumours of 86.3%. *n* represents the number of biologically independent experiments and fold change is calculated against the expression of hFWE$^{Win}$ isoforms in normal breast tissue. Box plots show median, first and third quartiles, positive and negative error values (s.d.). All statistically significant *P* values are shown (two-tailed *t*-test). Nor, normal tissue; can, cancer tissue. **b**, Left, haematoxylin and eosin (H&E) stained colon cancer and stromal samples. Right, immunostaining of colon cancer samples shows the abundance of hFWE$^{Win}$ isoforms. Middle, staining with anti-hFWE-N-term antibody shows staining in both tumour and stroma. This experiment was repeated independently three times with similar results.

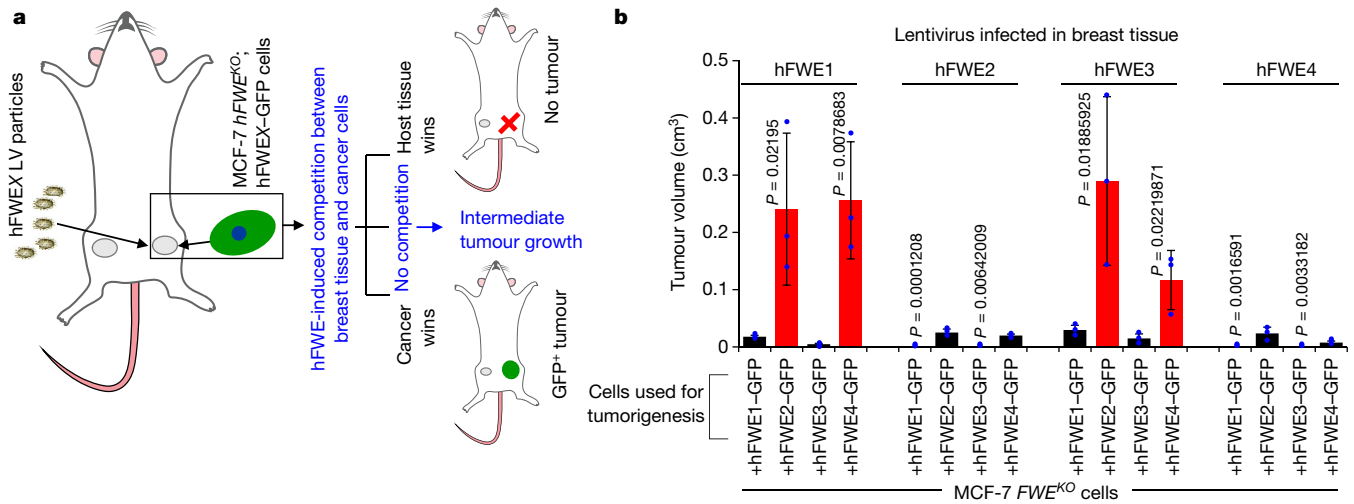


**Fig. 3 | Lose isoform in stroma and Win isoform in tumour cooperate to induce aggressive cancer growth. a**, Schematic of mouse model used to study competition between injected hFWE$^{Win}$- or hFWE$^{Lose}$-expressing cancer cells and hFWE$^{Win}$- or hFWE$^{Lose}$-expressing host tissue. hFWE*X* represents any one of hFWE1–hFWE4. LV, lentivirus. **b**, Tumour volumes were measured and analysed for each of the 16 combinations of hFWE*X*–IRES–GFP expression in MCF-7 *hFWE$^{KO}$* xenografted cells and hFWE isoform expression within *Fwe$^{KO}$* mouse mammary tissue (28-day study). Reduced tumour growth was observed when mammary tissue expressed hFWE$^{Win}$ isoforms and cancer cells expressed hFWE$^{Lose}$ isoforms. Increased tumour growth was observed when mammary tissue expressed hFWE$^{Lose}$ isoforms and cancer cells expressed hFWE$^{Win}$ isoforms. $n = 3$, all statistically significant *P* values shown, two-tailed *t*-test, mean ± s.d.

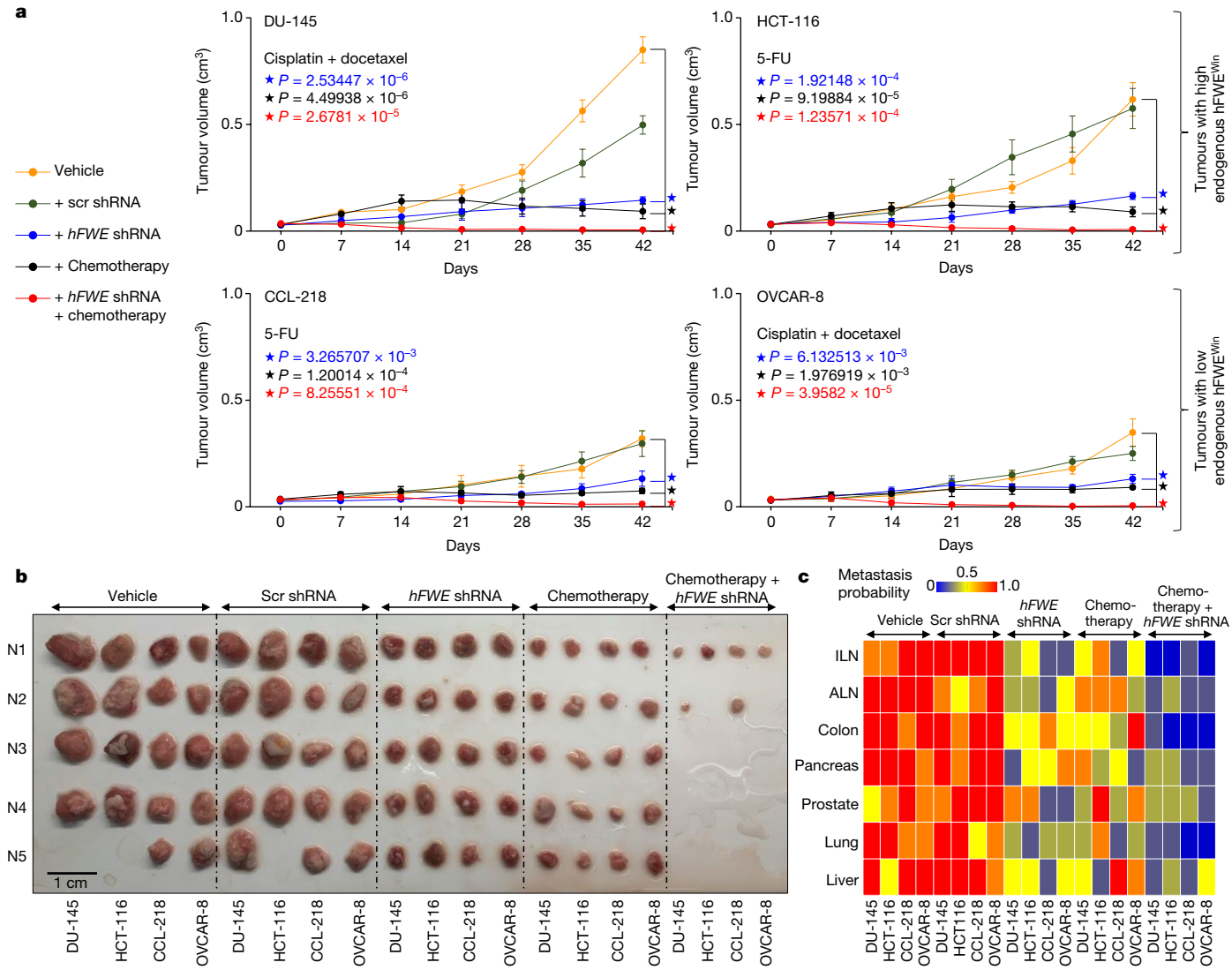


**Fig. 4 | *hFWE* knockdown inhibits tumorigenicity and improves chemotherapy efficiency. a**, **b**, The effect of shRNA-mediated *hFWE* knockdown on the tumour growth potential of DU-145 (prostate), HCT-116 (colon), CCL-218 (colon) and OVCAR-8 (ovarian) cell lines was tested. Orange, control vehicle-treated tumours; green, negative control non-specific scrambled (Scr) shRNA-treated tumours; blue, tumours treated with a cocktail of anti-*hFWE* shRNA, resulting in a significant reduction in tumour volume; black, cisplatin + docetaxel for prostate (DU-145) and ovarian (OVCAR-8) lines and 5-FU for colon cancer lines (HCT-116 and CCL-218); red, a combination of *hFWE* knockdown with chemotherapy abolishes tumour burden in several cases and overall significantly reduces tumour growth. $n = 5$ biologically independent experiments, *P* values shown, mean ± s.d., one-tailed *t*-test. **c**, The effect of treatment with vehicle, scrambled shRNA, *hFWE* shRNA, chemotherapy, and a combination of *hFWE* shRNA and chemotherapy on metastasis. Heat map scale indicates the probability of metastasis, which is significantly reduced by treatment with *hFWE* shRNA or a combination of *hFWE* shRNA and chemotherapy (compare groups 1 and 2 with groups 3, 4 and 5; $n = 5$ each group).

aggressive tumours when implanted into mammary tissue expressing hFWE1 or hFWE3 (Fig. 3b, Extended Data Fig. 9d). The results suggest that interactions between expression of $hFWE^{Win}$ isoforms in tumours and $hFWE^{Lose}$ isoforms in the stroma are important for tumour growth.

We investigated the role of host tissue hFWE isoforms by using hFWE2-overexpressing $hFWE^{KO}$ HCT-116 and MCF-7 cells to generate tumours in $Fwe^{WT}$ and $Fwe^{KO}$ mice. Both HCT-116 $hFWE2^{+}$ and MCF-7 $hFWE2^{+}$ tumours were larger with higher incidences of metastasis in $Fwe^{WT}$ mice than in $Fwe^{KO}$ mice (Extended Data Fig. 9e–g). The expression of $hFWE^{Lose}$ isoforms was upregulated in wild-type MCF-7 cells when they were co-cultured with hFWE2-expressing $hFWE^{KO}$ MCF-7 cells (Extended Data Fig. 10a, b). Similarly, expression of $hFWE^{Lose}$ isoforms was increased in tumour-adjacent tissue from $Fwe^{WT}$ mice after implantation of hFWE2-expressing MCF-7 tumours when compared with before (Extended Data Fig. 10c). From these experiments, we conclude that the expression of Win isoforms in the tumour is sufficient to induce increased expression of Lose isoforms non-autonomously in the surrounding cells. These data show that stromal Lose and tumoral Win isoforms cooperate to promote aggressive cancer growth.

Next, we tested whether inhibition of Flower could provide anti-cancer benefits. Amongst ectopic tumours derived from $hFWE^{WT}$ and $hFWE^{KO}$ HCT-116 cells, those derived from $hFWE^{WT}$ cells were larger (Extended Data Fig. 10d, e). Knockdown of *hFWE* expression by short hairpin RNA (shRNA) in $hFWE^{WT}$ HCT-116 cells before xenografting (Extended Data Fig. 10g, h) reduced both tumour volume and probability of metastasis (Extended Data Fig. 10d–f). The growth (Extended Data Fig. 10d, e) and metastatic potential (Extended Data Fig. 10f) of HCT-116 tumours treated with shRNA targeting *hFWE* was rescued by ectopic expression of codon-optimized *hFWE2* cDNA (which is unaffected by anti-*hFWE* shRNA) (Extended Data Fig. 10h). In a gain-of-function experiment, we overexpressed hFWE2 in CCL-218 (colon cancer) cells, which express low levels of $hFWE^{Win}$ isoforms; this resulted in a nearly threefold increase in their tumour growth potential (Extended Data Fig. 10i, j).

We screened a panel of 18 metastatic cell lines of multiple origins (breast, colon, prostate, pancreatic, and ovarian) for hFWE$^{Win}$ expression (Extended Data Fig. 10j). Cells with higher (HCT-116 colon and DU-145 prostate) or lower (CCL-218 colon and OVCAR-8 ovarian) expression of hFWE$^{Win}$ were selected, and their tumorigenic potential was observed. We tested the therapeutic potential of *hFWE* gene knockdown (Extended Data Fig. 10g) in combination with standard-of-care chemotherapy against the tumorigenic potential of these cancer cell lines. DU-145 and HCT-116 cells had significantly higher tumorigenic potential and generated larger tumours than CCL-218 and OVCAR-8 cells (Fig. 4a, b). *hFWE* knockdown significantly reduced tumour volumes (Fig. 4a, b). Control xenografts and those treated with scrambled shRNA generated much larger tumours than xenografts treated with anti-*hFWE* shRNA or chemotherapy (fluorouracil (5-FU) for colon cancer[28], or cisplatin and docetaxel for prostate[29] and ovarian[30] cancer). Treatment with a combination of anti-*hFWE* shRNA and chemotherapy further reduced, and in some cases completely eliminated, tumorigenesis (Fig. 4a, b). Control experiments demonstrated the efficiency of *hFWE* shRNA in all tumours (Extended Data Fig. 10k). Metastatic probability was reduced markedly upon *hFWE* knockdown and even further by combined treatment with chemotherapy (Fig. 4c). Thus, we conclude that human hFWE proteins can have a powerful effect on tumorigenicity and propose that therapies targeting these proteins have the potential to impair cancer growth and metastasis.

We have shown that the human Flower protein code mediates competitive interactions that depend on cell contact and caspase-dependent apoptosis but not on calcium transport. Homogeneous expression of any of the four Flower proteins does not trigger cell elimination or affect cell fitness in terms of proliferation, survival, or clonogenicity. Cell elimination requires different levels of Win and Lose isoforms in neighbouring cells, demonstrating that relative levels of these proteins are more important than absolute levels for cell selection. In addition, we find that human tumours use cell fitness markers to gain a competitive advantage over neighbouring cells. This work represents a conceptual advance in understanding the role of cell fitness comparisons in the progression of human cancer. It describes a concrete molecular mechanism that regulates oncogenic growth and metastasis via the Flower fitness comparison system. This appears to be a striking general feature of solid tumours and an unrecognized prerequisite for tumour growth. Notably, we also show that inhibition of cell competition can be combined with standard-of-care chemotherapy to further prevent tumour growth and metastasis of colon, ovarian and prostate cancers.

## Online content

Any methods, additional references, Nature Research reporting summaries, source data, extended data, supplementary information, acknowledgements, peer review information; details of author contributions and competing interests; and statements of data and code availability are available at https://doi.org/10.1038/s41586-019-1429-3.

Received: 4 May 2016; Accepted: 26 June 2019;
Published online 24 July 2019.

1. Medzhitov, R. & Janeway, C. A. Jr Decoding the patterns of self and nonself by the innate immune system. *Science* **296**, 298–300 (2002).
2. Vivier, E. et al. Innate or adaptive immunity? The example of natural killer cells. *Science* **331**, 44–49 (2011).
3. Merino, M. M. et al. Elimination of unfit cells maintains tissue health and prolongs lifespan. *Cell* **160**, 461–476 (2015).
4. Merino, M. M., Rhiner, C., Portela, M. & Moreno, E. "Fitness fingerprints" mediate physiological culling of unwanted neurons in *Drosophila*. *Curr. Biol.* **23**, 1300–1309 (2013).
5. Moreno, E., Fernandez-Marrero, Y., Meyer, P. & Rhiner, C. Brain regeneration in *Drosophila* involves comparison of neuronal fitness. *Curr. Biol.* **25**, 955–963 (2015).
6. Rhiner, C. et al. Flower forms an extracellular code that reveals the fitness of a cell to its neighbors in *Drosophila*. *Dev. Cell* **18**, 985–998 (2010).
7. Merino, M. M., Levayer, R. & Moreno, E. Survival of the fittest: essential roles of cell competition in development, aging, and cancer. *Trends Cell Biol.* **26**, 776–788 (2016).
8. Gogna, R., Shee, K. & Moreno, E. Cell competition during growth and regeneration. *Annu. Rev. Genet.* **49**, 697–718 (2015).
9. Di Gregorio, A., Bowling, S. & Rodriguez, T. A. Cell competition and its role in the regulation of cell fitness from development to cancer. *Dev. Cell* **38**, 621–634 (2016).
10. Greaves, M. & Maley, C. C. Clonal evolution in cancer. *Nature* **481**, 306–313 (2012).
11. Jacobs, K. B. et al. Detectable clonal mosaicism and its relationship to aging and cancer. *Nat. Genet.* **44**, 651–658 (2012).
12. Kennedy, S. R., Loeb, L. A. & Herr, A. J. Somatic mutations in aging, cancer and neurodegeneration. *Mech. Ageing Dev.* **133**, 118–126 (2012).
13. Laurie, C. C. et al. Detectable clonal mosaicism from birth to old age and its relationship to cancer. *Nat. Genet.* **44**, 642–650 (2012).
14. López-Otín, C., Blasco, M. A., Partridge, L., Serrano, M. & Kroemer, G. The hallmarks of aging. *Cell* **153**, 1194–1217 (2013).
15. Vanneste, E. et al. Chromosome instability is common in human cleavage-stage embryos. *Nat. Med.* **15**, 577–583 (2009).
16. Vijg, J. Somatic mutations, genome mosaicism, cancer and aging. *Curr. Opin. Genet. Dev.* **26**, 141–149 (2014).
17. Neves, J., Demaria, M., Campisi, J. & Jasper, H. Of flies, mice, and men: evolutionarily conserved tissue damage responses and aging. *Dev. Cell* **32**, 9–18 (2015).
18. Levayer, R., Hauert, B. & Moreno, E. Cell mixing induced by myc is required for competitive tissue invasion and destruction. *Nature* **524**, 476–480 (2015).
19. Klein, C. A. Selection and adaptation during metastatic cancer progression. *Nature* **501**, 365–372 (2013).
20. Maruyama, T. & Fujita, Y. Cell competition in mammals—novel homeostatic machinery for embryonic development and cancer prevention. *Curr. Opin. Cell Biol.* **48**, 106–112 (2017).
21. Moreno, E. Is cell competition relevant to cancer? *Nat. Rev. Cancer* **8**, 141–147 (2008).
22. ENCODE Project Consortium. An integrated encyclopedia of DNA elements in the human genome. *Nature* **489**, 57–74 (2012).
23. Ji, X. et al. Chromatin proteomic profiling reveals novel proteins associated with histone-marked genomic regions. *Proc. Natl Acad. Sci. USA* **112**, 3841–3846 (2015).
24. Moreno, E. & Rhiner, C. Darwin's multicellularity: from neurotrophic theories and cell competition to fitness fingerprints. *Curr. Opin. Cell Biol.* **31**, 16–22 (2014).
25. Chang, H. F. et al. Cytotoxic granule endocytosis depends on the Flower protein. *J. Cell Biol.* **217**, 667–683 (2018).
26. Petrova, E., López-Gay, J. M., Rhiner, C. & Moreno, E. Flower-deficient mice have reduced susceptibility to skin papilloma formation. *Dis. Model. Mech.* **5**, 553–561 (2012).
27. Xue, L. et al. Voltage-dependent calcium channels at the plasma membrane, but not vesicular channels, couple exocytosis to endocytosis. *Cell Rep.* **1**, 632–638 (2012).
28. Zhang, P. et al. Curcumin synergizes with 5-fluorouracil by impairing AMPK/ULK1-dependent autophagy, AKT activity and enhancing apoptosis in colon cancer cells with tumor growth inhibition in xenograft mice. *J. Exp. Clin. Cancer Res.* **36**, 190 (2017).
29. Davies, A. H., Wang, Y. & Zoubeidi, A. Patient-derived xenografts: A platform for accelerating translational research in prostate cancer. *Mol. Cell. Endocrinol.* **462**, 17–24 (2018).
30. Chang, C. E. et al. Novel application of pluronic lecithin organogels (PLOs) for local delivery of synergistic combination of docetaxel and cisplatin to improve therapeutic efficacy against ovarian cancer. *Drug Deliv.* **25**, 632–643 (2018).

## METHODS

**Bio-informatics analysis.** Encode data for the *CACFD1* (*hFWE*) gene were collected systematically from the UCSC Genome Browser. The trans-membrane structures for human hFWE isoforms were predicted using Predictprotein 2013 software from the Technical University of Munich.

**Established cell lines and culture conditions.** A2780-CR, A2780-CS, CCL-218, DU-145, HCC-1954, HCT-116, MCF-7, MCF 10A, MD-4, MD-7, MDA-MB-231, MDA-MB-468, PC-3, SK-BR-3, TR-127, TR-182 and ZR-75 cells were procured with certificates of authentication from the American Type Culture Collection (ATCC). HEK293 cells were procured from Cell Biolabs. OVCAR-4 and OVCAR-8 cells were kindly provided by S. Karuppaiyah (Ohio State University). In brief, all cell lines were cultured as suggested by the ATCC in Dulbecco's modified Eagle's medium (DMEM) or RPMI 1640 (Corning) supplemented with 10% (v/v) heat-inactivated fetal bovine serum (FBS) (Gibco) and 1% (v/v) penicillin/streptomycin (Thermo Fisher Scientific) and incubated at 37 °C in a humidified atmosphere of 95% air and 5% $CO_2$. Cell lines were tested for mycoplasma contamination.

**Transfections and preparation of lentiviral particles.** All transfections were performed using Lipofectamine 3000 (Thermo Fisher Scientific). Lentiviral particles encoding Cas9 + *hFWE* single guide RNA (sgRNA), *hFWE* shRNA, and cDNA for hFWE1–hFWE4 were generated using HEK293T cells and their respective packaging. The viral particles were concentrated by centrifuging the supernatant at 22,000 r.p.m. for 2 h at 20 °C. The pellet was re-suspended in 200 μl 1× HBSS, purified by layering the 200 μl of viral preparation on 1.5 ml of 20% sucrose (in HBSS) and centrifugation at 22,000 r.p.m. for 2 h at 20 °C, and then the pellet was re-suspended in 100 μl 1× HBSS. The titre of lentiviral particles was determined using a p24 ELISA kit (Cell Biolabs); $10^9$ TU $ml^{-1}$ was used for cell culture experiments, and $10^{11}$ TU $ml^{-1}$ was used for in vivo infections. For infection of target cells, lentiviral particles were diluted in culture medium containing 5 μg $ml^{-1}$ polybrene (Thermo Fisher Scientific).

**Generation of MCF-7 and HCT-116 *hFWE$^{KO}$* cells.** Stable knockout of *hFWE* was performed using lentiCRISPR V2 vector (Addgene) expressing both Cas9 and sgRNA targeting the *hFWE* gene loci. Cloning of sgRNA targeting *hFWE* gene loci was performed as described previously[31,32]. Lentiviral particles were generated by transfection of HEK293T cells with lentiCRISPRs, psPAX2, and pMD2.G plasmids (Addgene) and the virus was collected 48 h later[31,32]. MCF-7 and HCT-116 cells were infected with lentiviral particles, and 48 h later the medium was replaced with culture medium containing 2 μg $ml^{-1}$ puromycin (Thermo Fisher Scientific). After 2 weeks of puromycin selection, single-cell colonies were isolated via ring cloning. DNA from each colony was extracted using QuickExtract (Epicentre). To confirm that an indel was present at both alleles, the region, including the target site, was amplified using PCR. The PCR products were ligated into pBlueScript (Addgene) for cloning and sequencing. Oligos for creating CRISPRs: CACFD1-csp1a: CACCGCATGACGTGGTGGTACCGC, CACFD1-csp1b: AAACGCGGTACCACCACGTCATGC, CACFD1-csp2a: caccTTTCAAGCTTGCGCGATCTC, CACFD1-csp2b: aaacGAG ATC GCG CAA GCT TGA AA, CACFD1-csp3a: CACCGGGCTGTGAGCTGCGCCTGA, CACFD1-csp3b: AAACTCAGGCGCAGCTCACAGCCC. Primers used for PCR to check deletion: CACFD1-PCR-csp1F: aagcttTAT GCT CCC TCT CCC ACA AGG C, CACFD1-PCR-csp1R: ctcgagGAC TGG ATA CTC ACA GAC TGC CC, CACFD1-PCR-csp2F: aagcttCTT CTG GGT GCT GTG AGA ACT GTG, CACFD1-csp2R: ctcgagGGA CGG CCA TGC ATT ACT CAC.

**shRNAs.** Stable knockdown of *hFWE* was performed using lentiviral constructs (Genscript) containing shRNA targeting *hFWE*. The shRNA sequences were: 5′-TCTGGCCTCTTCAACTGCATCACCATCCA-3′; 5′-TGAATGCC TTCATCTTGTTGCTGTGTGAG-3′; 5′-CGCTCCTGGCAGAAGGCT GTCTTCTACTG-3′; and 5′-GGCAGCAGGCGGATGAGGAGAAGCTCGCG-3′. The lentiviral packaging was performed in 293FT cells using ViraSafe Lentivirus Packaging System (Pantropic Cell Biolabs), as per the manufacturer's instructions and previously stated. Forty-eight hours after transduction, cells were selected with 2 μg $ml^{-1}$ puromycin in growth medium for 10 days and single colonies were selected and propagated. Gene knockdown efficiency was assessed by qPCR.

***hFWE* cDNA overexpression.** The pCDH-CMV-MCS-EF1α-copGFP and pCDH-CMV-MCS-EF1α-RFP vectors expressing individual hFWE isoforms 1–4 were obtained from System BioSciences. GFP-IRES-Isoform-1-4_OptHs vectors were obtained from ATUM. The lentiviral packaging was performed in 293FT cells using ViraSafe Lentivirus Packaging System (Pantropic Cell Biolabs) per the manufacturer's instructions.

**MTT assay.** We seeded $1 \times 10^4$ MCF-7 wild-type of *hFWE$^{KO}$* cells into 96-well plates overnight. Next, the culture medium was removed and cells were washed with PBS, and then incubated with 0.5 mg/ml 4,5-dimethylthiazol-2-yl-2,5-diphenyltetrazolium bromide (MTT; Sigma-Aldrich) in fresh culture medium for 3 h at 37 °C. The culture medium was carefully aspirated, and the formazan product was dissolved in 180 μl DMSO. Cell viability was measured as the difference between the absorptions at wavelengths of 570 and 650 nm. All experiments were performed in triplicate and repeated three times.

**Colony formation assay.** MCF-7 wild-type and MCF-7 *hFWE$^{KO}$* cells were seeded into 6-well culture plates ($1 \times 10^3$ cells per well) and then cultured under standard conditions over 21 days. The medium was replaced every third day. Finally, the cells were fixed with methanol and then stained with crystal violet (Sigma Aldrich). All experiments were performed in triplicate and replicated three times.

**BrdU assay.** Cellular proliferation was measured using the Cell Proliferation ELISA BrdU Colorimetric Assay Kit (Roche Applied Science). We plated $1 \times 10^3$ MCF-7 wild-type or *hFWE$^{KO}$* cells per well in 96-well plates. Twenty-four hours after plating, cells were labelled with BrdU in fresh culture medium overnight at 37 °C. Cells were then fixed and denatured for 30 min, followed by incubation with peroxidase substrate solution at 25 °C and the reaction was stopped using 1 M $H_2SO_4$. An absorbance wavelength of 450 nm and reference wavelength of 690 nm were used. All experiments were performed in triplicate and replicated three times.

**ROS measurement.** ROS levels were determined by incubating MCF-7 wild-type and *hFWE$^{KO}$* cells in serum-free DMEM containing 10 μM 2′,7′-dichlorodihydrofluorescein diacetate (H-DCFDA; Thermo Fisher Scientific) for 30 min at 37 °C. Cells were trypsinized and were washed twice in PBS, and the final cell pellet was re-suspended in PBS. DCF intensity was measured by flow cytometry using the BD-LSRII H274 per manufacturer's instructions. All experiments were performed in triplicate and replicated three times.

**Apoptosis and cell cycle analysis.** At the endpoint of monoculture or co-culture experiments, cells were stained with annexin-V (Thermo Fisher Scientific) per the manufacturer's instructions. Flow cytometry was performed to detect apoptotic cells by observing FITC-conjugated and pacific blue-conjugated annexin-V staining. For cell cycle analysis, MCF-7 wild-type and MCF-7 *hFWE$^{KO}$* cells were fixed in 70% ethanol. Fixed cells were washed with cold PBS and stained with 50 μg $ml^{-1}$ propidium iodide (Thermo Fisher Scientific). Flow cytometry for apoptosis detection and cell cycle distribution profiles was performed using MACSQuant Analyzer (Miltenyi Biotec) and analysed using FlowJo software (Treestar).

**Live-cell imaging of cell competition assay.** MCF-7 *hFWE$^{KO}$* cells were infected with lentiviral particles expressing GFP- or RFP-tagged hFWE1–hFWE4 isoforms and cultured for 24 h. $RFP^+$ and $GFP^+$ cells were sorted by flow cytometry using the BD FACS ARIA III (BD Biosciences). Overexpression of *hFWE* in sorted cell populations was measured by qPCR and only sorted batches with high expression of hFWE1–hFWE4 (characterized by *hFWE* Ct value of ~14, with *GAPDH* Ct value of ~21) were used. Equal numbers of MCF-7 cells expressing GFP- or RFP-tagged hFWE1–hFWE4 were co-plated in a glass-bottom dish (Matek) in the specified combinations and co-cultured under normal conditions for 24 h. Cells were then subjected to live-cell imaging for the indicated times and processed for apoptosis detection by annexin-V staining. To study caspase-dependency for cell death, MCF-7 *hFWE$^{KO}$* cells expressing $hFWE^{Win}$ were co-cultured with MCF-7 *hFWE$^{KO}$* cells expressing $hFWE^{Lose}$ in the presence of the caspase inhibitor Z-VAD-FMK (20 μM, Sigma-Aldrich) for 24 h. We next performed live-cell imaging at the indicated times, and, at the study endpoint, cells were processed for apoptosis detection by annexin-V staining when indicated. To observe the contact-dependency of cell competition, an equal number of MCF-7 *hFWE$^{KO}$* cells expressing hFWE1–GFP and MCF-7 *hFWE$^{KO}$* cells expressing hFWE2–RFP were co-plated at low density, followed by live-cell imaging. For conditioned medium experiments, medium was collected from MCF-7 *hFWE$^{KO}$* cells expressing hFWE2 cDNA, centrifuged at 1,000 r.p.m. for 5 min, and then added to target MCF-7 *hFWE$^{KO}$* cells expressing hFWE1–GFP. Cells were subsequently cultured for 24 h, then we performed live-cell imaging at the indicated times. Live-cell imaging was performed using Leica TCS SP8 confocal laser microscopy (Leica Microsystems), a Nikon A1 HD25 confocal microscope (Nikon), and a Zeiss LSM-800 with Airy Scan Confocal Microscope (Zeiss). Analysis of cell motility, cell count and cell death was performed manually using Fiji software (http://fiji.sc/) and the analysis of average cell volume and average cell sphericity were performed using Imaris7.6.5 software (Bitplane).

**Cell competition assay with normal breast cells.** MCF-7 *hFWE$^{KO}$* cells were infected with lentiviral particles expressing hFWE2–GFP and cultured for 24 h. MCF-7 *hFWE$^{KO}$* cells expressing hFWE2–GFP were subsequently cultured on their own or co-cultured with an equal number of normal breast primary epithelial cells or fibroblasts. Cells from each combination were collected at the indicated times for annexin-V staining and the percent of apoptotic cells was measured in the GFP-positive and GFP-negative populations using flow cytometry. Human epithelial cells and fibroblasts were isolated from normal breast tissue from fresh or cryopreserved, de-identified tissues; samples were obtained from the Komen Tissue Bank (KTB) at IU School of Medicine, Indianapolis, after informed consent from the donors. All experiments were carried out in accordance with the approved guidelines of the Indiana University Institutional Review Board, which determined the study to be non-human subjects research. International Ethical Guidelines for Biomedical Research Involving Human Subjects were followed. Proceedures for isolation of primary cells from biopsies and propagation have been described[33].

**Determination of cellular calcium levels.** MCF-7 *hFWE$^{KO}$* cells and MCF-7 *hFWE$^{KO}$* cells infected with lentiviral particles expressing hFWE1–4 isoforms

individually were plated in glass-bottom dishes (Matek). After 24 h, cells were incubated with the fluorescent dye Fluo-4AM (Thermo Fisher Scientific) as per the manufacturer's protocol for 40 min, washed with PBS, and then incubated for an additional 15 min to complete the de-esterification of the dye. Live-cell imaging was immediately performed at the indicated times to determine cellular $Ca^{2+}$ levels using TCS SP8 (Leica) confocal imaging. An excitation wavelength of 494 nm and an emission wavelength of 506 nm were used. Results were quantified by measuring the $Ca^{2+}$ indicator mean fluorescence intensity (MFI) in all cell combinations using Fiji. All experiments were performed in triplicate and repeated three times.

**BAPTA-AM.** MCF-7 *hFWE*$^{KO}$ cells were infected with lentiviral particles expressing hFWE1–RFP or hFWE2–GFP and cultured for 24 h. Then, MCF-7 *hFWE*$^{KO}$ cells expressing hFWE1–RFP and MCF-7 *hFWE*$^{KO}$ cells expressing hFWE2–GFP were co-plated in equal numbers and co-cultured for 24 h in the presence or absence of BAPTA-AM (10 μM, Thermo Fisher Scientific). Cells were collected for annexin-V staining and flow cytometry analysis.

**Laser-capture microdissection.** FFPE tissue sections (5-μm thick) were subjected to laser capture microdissection using the Leica Microsystems at UNMC; Zeiss Palm MicroBeam IV Laser Capture Microdissection system at Thornwood facility and Michigan University. Matched H&E-stained sections were used to demarcate cancer versus stroma. Adjacent normal tissues were microdissected in precise increments of 200 μm in distance perpendicular from the boundary of tumour mass. Captured tissue was collected into the adhesive cap (Zeiss).

**Immunohistochemistry.** Matched normal and tumour patient samples of breast and colon origin were formalin-fixed and paraffin-embedded. FFPE tissues were cut into sections of 5 μm and were stained with H&E or hFWE antibodies. Samples were deparaffinized in xylene and rehydrated in a graded series of ethanol. Antigen retrieval was performed in 10 mM EDTA buffer pH 9 for 20 min at 96–98 °C. Samples were allowed to cool at room temperature for 20 min, and blocked in 1% peroxide solution for 10 min, followed by washing with TBS + 0.5% Triton X-100. Slides were blocked in 3% bovine serum albumin (BSA, Sigma-Aldrich), then incubated with anti-hFWE-N-term (Ab1; 1:500) and anti-hFWE$^{Win}$ (Ab4; 1:500) primary antibodies (Genscript) in blocking solution overnight at 4 °C. The sections were incubated in goat anti-mouse IgG HRP-conjugated secondary antibody (1:2,000, Thermo Fisher Scientific) for 1 h at 25 °C and then developed with 3,3′-diaminobenzidine (DAB, Vector Labs) for 10 min to visualize the colour of the reaction.

**Immunofluorescence.** For immunofluorescent and immunocytological staining for hFWE in human tissue and cells, anti-hFWE-N-term (Ab1) and anti-hFWE$^{Win}$ (Ab4) antibodies were used at 1:500 final dilution, and goat anti-mouse IgG AlexaFluor 488 (1:1,000, Thermo Fisher Scientific) was used as the secondary antibody. SCC, colon, and normal skin FFPE samples were cut into 5-μm sections and stained with H&E or hFWE antibodies. Immunofluorescence experiments were performed as described previously[34] and refined for the hFWE antibodies. Serial sections were incubated with anti-hFWE-N-term and anti-hFWE$^{Win}$ antibodies overnight at 4 °C. Sections were incubated with secondary antibody for 2 h and nuclei were counterstained with 4′,6-diamidino-2-phenylindole (DAPI, Sigma-Aldrich, 1 μg ml$^{-1}$).

**Immunocytochemistry.** MCF-7 *hFWE*$^{KO}$ cells and MCF-7 *hFWE*$^{KO}$ cells expressing one of hFWE1–hFWE4 were collected by trypsinization and the cell pellet was resuspended in pre-heated 1.5% agarose + 2% sucrose solution, homogenized, and allowed to solidify. The agarose block was placed in 30% sucrose overnight. Eight-micrometre-thick sections were prepared using a Cryostat 3050S (Leica) and slides were stained using the Bond Polymer Refine Detection Kit (Leica) per the manufacturer's instructions. Slides were then incubated with anti-hFWE-N-term and anti-hFWE$^{Win}$ antibodies for 15 min and subsequently processed using Leica Detection Polymer and developed with DAB according to the kit instructions.

To analyse the membrane topology of hFWE isoforms, MCF-7 *hFWE*$^{KO}$ cells were plated in Nunc LabTek-II 4-chambered coverglass (Thermo Fisher Scientific) overnight and then transfected with cDNA for hFWE1–hFWE4 using Lipofectamine 3000. After 24 h, the cells were fixed with 3.7% paraformaldehyde in PBS for 15 min, and then permeabilized with 0.1% Triton X-100 in TBS for 7 min or non-permeabilized. Subsequently, the cells were blocked with 3% BSA and incubated with anti-hFWE-N-term or anti-hFWE$^{Win}$ primary antibody in 3% BSA for 4 h, washed three times with 1× PBS and stained with secondary antibody for 2 h. Nuclei were counterstained with Hoechst 33258 (Thermo Fisher Scientific). Images were acquired with a Zeiss LSM880 inverted by using a Plan-ApoChromat 20×/0.8 dry lens. An argon laser with 25 mW of head power and a 405 Diode laser with 30 mW head power were used to excite AlexaFluor488 and Hoechst, respectively. The signal detected was limited to the portions of the visible spectrum between 495 and 545nm and 420 and 480nm by using BP filters in front of a ZEISS Airy Scan detector. The images were acquired in super-resolution mode with an XY sampling factor (pixel size) of 55 nm. A volume of approximately 12 μm was acquired around the central plane of each cell with a *z*-step of 342 nm. After the acquisition, the images were processed in order to reassign the information collected by the 32 Airy detectors to their source point and obtain a theoretical resolution of 233 nm for the A488 channel and 204 nm for the Hoechst channel.

**Fluorescent in situ hybridization.** FFPE breast cancer sections (5-μm thick) were stained with H&E to verify that the slides included both cancer and normal tissue. Next, 5-μm-thick serial sections were prepared for processing with the in situ + ISH Tissue Assay kit (Affymetrix) according to the manufacturer's instructions. Probe sets were designed by Affymetrix to detect exon 3 and exon 4 of *CACFD1* mRNA. After deparaffinization, slides were subjected to heat pretreatment (90 °C, 30 min) and protease digestion, (40 °C, 20 min). Then sections were hybridized with probe following the signal-amplification step. Sections were developed using kit-supplied Fast Red substrate and counterstained with DAPI. All sections were mounted with DAKO UltraMount Permanent Mounting Medium (Agilent). Fluorescent images were acquired using a BZ-X700 microscope (Keyence).

**RNA isolation and quantitative RT–PCR analysis.** Total RNA was isolated from cancer cell lines, patient tumour samples, and mouse tumour xenografts using the PureLink RNA Mini kit (Qiagen). Total RNA was isolated from laser-captured FFPE tissue samples using the RNeasy FFPE kit (Qiagen). Ten nanograms of total RNA was reverse-transcribed to complementary DNA using Superscript Vilo cDNA synthesis kit (Thermo Fisher) per the manufacturer's instructions. Quantitative PCR (qPCR) was performed with PowerUp SYBR Green master mix (Thermo Fisher) using the Rotor Gene Q (Qiagen), BioRad CFX96, QuantStudio 6 (ABI) or Light cycler 96 instrument (Roche). The reaction conditions included an initial denaturation step at 95 °C for 2 min, followed by 40 cycles of 95 °C for 15 s and 60 °C for 60 s. Data were analysed using the comparative $C_t$ method[35]. The $C_t$ values of samples and controls were normalized to the expression level of the *GAPDH* housekeeping gene. All qPCR reactions were set up in triplicate and the experiments were performed with at least three different samples. The following primers were used (F: forward; R: reverse): *GAPDH*: 5′-GGATGCAGGGAT GATGTTC-3′ (F) and 5′-TGCACCACCAACTGCTTAG-3′ (R); *hFWE1*: Ex2–4 5′-GCGTGTGGATGATGATGG′ (F) and Ex5 5′-CCTGTCTTGTCCCCTC TGA-3′ (R); *hFWE2*: Ex3 5′-CTGCCAGTTCATCGAGTTTG-3′ (F) and Ex5 5′-CCTGTCTTGTCCCCTCT GA-3′ (R); *hFWE3*: Ex2–4 5′-GCGTGTGG ATGATGATGG-3′ (F) and Ex4–6 5′-AGATCGCATCGCCCTTT-3′ (R); *hFWE4*: Ex3 5′-CTGCCAGTTCATCGAGTTTG-3′ (F) and Ex4–6 5′-GATCGCATCGCCCTTTT-3′ (R); *hFWE$^{Win}$*: 5′-GCCTTCATCTTGT TGCTGTG-3′ (F) and 5′-CATCCCGCAGTAGAAGACAG-3′ (R); *hFWE$^{Lose}$*: 5′-GCGTGTGGATGATGATGG-3′ (F) and 5′-AGCAGAGAGTCCGTACA GCA-3′ (R); mouse *Fwe1* 5′-TCCACACTTCTCTGGTTCTG-3′ (F) and 5′-GTGAGTA CTGC TGTC TAGCC-3′ (R); mouse *Fwe2* 5′-CGATGCCATTTCTTATGCTC-3′ (F) and 5′-TGACACTCAGTCTTCTCCAG-3′ (R); mouse *Fwe3* 5′-CAAA CACAGTAGCTGAGAAGG-3′ (F) and 5′- TAGAGGGAAATGGTGTTT CT G-3′ (R); mouse *Fwe4* 5′- GTTTGCTAAATCCTGGGTGTC-3′ (F) and 5′-GCGTTCAT GATCATCCACAC-3′ (R); mouse *Gapdh* 5′-GTATGT CGTGGAGTCTACTG-3′ (F) and 5′-TCATCATACTTGGCAGGTTT-3′ (R) as described previously[26].

**The human apoptosis PCR array.** The Human Apoptosis RT2 Profiler PCR array kit (PAHS-3012; SA-Bio Sciences) was used to profile the expression of 354 genes involved in apoptosis and qPCR was performed per the manufacturer's instructions.

**Epithelial cell isolation.** hFWE$^{Win}$ expression was observed in the total normal tissue and the epithelial fraction isolated from breast, colon, and lung tissue samples. All samples were purchased from Tissue For Research, UK (https://biobankonline.com/) and all tissue samples were procured with donor consent. For extraction of the epithelial cells, approximately 120–150 g of the normal tissue samples were used as starting material for tissue digestion. Samples were handled in sterile conditions. Fatty tissue was manually separated, using sterile scalpels and forceps. Subsequently, the epithelial-enriched tissue was manually minced into small pieces. The tissue was sequentially digested using a slow digestion process (overnight at low enzymatic concentration) followed by sequential filtering to support the growth of the epithelial cell fractions as described previously[36].

**Patient samples.** For FISH, breast tumour specimens were provided by the Department of Breast Surgery, Hokkaido University Hospital. For qPCR experiments, samples of benign (10 breast and 10 colon) and malignant tumour (25 breast and 21 colon) were provided by the Department of Pathology, UAMS, USA; samples of malignant lung (4) and normal tissue (2 lung and 1 skin) were procured from the Department of Pathology, Locarno Hospital, Switzerland; and samples of SCC (3) and normal skin (2) were obtained from the Department of Pathology, Creighton University School of Medicine, USA. The same set of normal and malignant SCC samples were also used for immunofluorescent staining. FFPE breast and colon cancer samples used for immunohistochemistry (IHC) and fresh normal breast samples were provided by the Pathology Department, Champalimaud Foundation.

All samples used in the study were de-identified, FFPE archived samples with no attached patient information, and were collected with informed consent from donors. All samples were reviewed by the IRB boards at UAMS, Hokkaido

University Hospital, Locarno Hospital, Creighton University School of Medicine, Champalimaud Foundation and determined to qualify as non-human subjects research.

**Cancer xenografts.** C57BL/6 mice were obtained from the Geisel School of Medicine, Dartmouth College. Male and female Swiss nude mice were purchased from Charles River. All animal protocols were approved by the Institutional Animal Care and Use Committee of Dartmouth, and the Institutional Animal Ethics Committee at Champalimaud Foundation. All mice were housed in laminar flow cabinets under specific pathogen-free conditions. Food and water were available ad libitum for the duration of the studies. *Fwe*$^{KO}$ mice were generated using female C57BL/6 mice as described earlier[1]. For the generation of tumours in C57BL/6 mice, cyclosporin A (30 mg kg$^{-1}$; Sigma-Aldrich) was injected intraperitoneally as described[37]. Cell line xenografts were established as described previously[38–40]. In brief, MCF-7, HCT-116, DU-145, CCL-218, and OVCAR-8 cells at 70–90% confluency were trypsinized and cell viability, required to be at least >95%, was determined by Trypan blue exclusion assay. Cells were re-suspended in 80 μl serum-free medium with 1:1 Matrigel at a final concentration of $1 \times 10^6$ cells ml$^{-1}$ and stored on ice. For all tumour cell injections, animals were first anaesthetized with 1.5–3% isoflurane with 30% oxygen.

For overexpression of individual hFWE isoforms in mouse mammary tissue, 50 μl lentiviral particles ($10^{11}$ TU ml$^{-1}$) expressing individual GFP-tagged hFWE1–hFWE4 isoforms were injected into the mammary tissue of immunosuppressed C57BL/6 *Fwe*$^{KO}$ mice as described[41]. For injection of MCF-7 *hFWE*$^{KO}$ cells expressing GFP-tagged hFWE1–hFWE4, a pellet of 17-β-oestradiol (0.18 mg per pellet, 60-day release; Innovative Research of America) was subcutaneously implanted into *Fwe*$^{KO}$ mice 3 days before cell injection. One week after lentiviral treatment, MCF-7 *hFWE*$^{KO}$ cells expressing GFP-tagged hFWE1–hFWE4 were injected into the mammary tissue. After 4 weeks, mice were monitored for bioluminescent signal using an IVIS 200 system (Xenogen).

For cell line xenograft tumour studies established in male and female Swiss athymic nude mice (age 4–6 weeks), an 80-μl cell suspension containing $1 \times 10^6$ cells was subcutaneously injected into the hind legs of athymic mice. The vehicle control used for these studies was DMSO. To rescue hFWE2 expression in HCT-116 *hFWE*$^{WT}$ tumours, 14 days after cell line injection, tumour-bearing mice were randomly selected and lentiviral particles expressing hFWE2 were injected directly into the established tumour as described previously[42,43]. Chemotherapy treatments were initiated when tumours reached an approximate size of 0.03 cm$^3$; tumour-bearing mice were randomized to receive 30 mg kg$^{-1}$ 5-FU as described[28] or 4 mg kg$^{-1}$ cisplatin + docetaxel as described[30]. Tumour volumes were carefully monitored after treatment using Vernier caliper measurements of length, width, and height, and volumes were calculated using the formula for a semi-ellipsoid ($4/3\pi r^3/2$), as described previously[38,44]. Tumour size did not exceed the maximum size of 1.28 cm$^3$ as specified by institutional policies. The investigators were blinded during experiments or outcome assessment. No statistical methods were used to predetermine sample size.

**Statistical analysis.** All values are expressed as means ± s.d. of independent experiments. Differences between groups were evaluated by Student's *t*-test (two-sided) or Tukey–Kramer test, and considered to be significant at $P < 0.05$.

**Reporting summary.** Further information on research design is available in the Nature Research Reporting Summary linked to this paper.

## Data availability

All data generated or analysed during this study are included in the paper, its Extended Data and its Supplementary Information. The source data for Figs. 2–4 and Extended Data Figs. 1–10 are available online.


31. Sanjana, N. E., Shalem, O. & Zhang, F. Improved vectors and genome-wide libraries for CRISPR screening. *Nat. Methods* **11**, 783–784 (2014).
32. Shalem, O. et al. Genome-scale CRISPR-Cas9 knockout screening in human cells. *Science* **343**, 84–87 (2014).
33. Prasad, M. et al. Dual TGFβ/BMP pathway inhibition enables expansion and characterization of multiple epithelial cell types of the normal and cancerous breast. *Mol. Cancer Res.* **17**,1556–1570 (2019).
34. Yanagida, J. et al. Accelerated elimination of ultraviolet-induced DNA damage through apoptosis in CDC25A-deficient skin. *Carcinogenesis* **33**, 1754–1761 (2012).
35. Schmittgen, T. D. & Livak, K. J. Analyzing real-time PCR data by the comparative C(T) method. *Nat. Protoc.* **3**, 1101–1108 (2008).
36. Zubeldia-Plazaola, A. et al. Comparison of methods for the isolation of human breast epithelial and myoepithelial cells. *Front. Cell Dev. Biol*. **3**, 32 (2015).
37. Jivrajani, M., Shaikh, M. V., Shrivastava, N. & Nivsarkar, M. An improved and versatile immunosuppression protocol for the development of tumor xenograft in mice. *Anticancer Res.* **34**, 7177–7183 (2014).
38. Gogna, R., Madan, E., Kuppusamy, P. & Pati, U. Chaperoning of mutant p53 protein by wild-type p53 protein causes hypoxic tumor regression. *J. Biol. Chem*. **287**, 2907–2914 (2012).
39. Hadjal, Y., Hadadeh, O., Yazidi, C. E., Barruet, E. & Binétruy, B. A p38MAPK-p53 cascade regulates mesodermal differentiation and neurogenesis of embryonic stem cells. *Cell Death Dis*. **4**, e737 (2013).
40. Madan, E. et al. SCO2 induces p53-mediated apoptosis by Thr845 phosphorylation of ASK-1 and dissociation of the ASK-1-Trx complex. *Mol. Cell. Biol*. **33**, 1285–1302 (2013).
41. Annunziato, S. et al. Modeling invasive lobular breast carcinoma by CRISPR/Cas9-mediated somatic genome editing of the mammary gland. *Genes Dev*. **30**, 1470–1480 (2016).
42. Akhtar, J., Wang, Z., Yu, C. & Zhang, Z. P. Effectiveness of local injection of lentivirus-delivered stathmin1 and stathmin1 shRNA in human gastric cancer xenograft mouse. *J. Gastroenterol. Hepatol*. **29**, 1685–1691 (2014).
43. Zheng, J. Y. et al. Regression of prostate cancer xenografts by a lentiviral vector specifically expressing diphtheria toxin A. *Cancer Gene Ther*. **10**, 764–770 (2003).
44. Madan, E. et al. TIGAR induces p53-mediated cell-cycle arrest by regulation of RB-E2F1 complex. *Br. J. Cancer* **107**, 516–526 (2012).



**Acknowledgements** This study was supported by ERC, SNSF, Josef Steiner Cancer Research Foundation, Swiss Cancer League and Champalimaud Foundation to E.M.; and Swiss Cancer League, LB692, LB506, Seeds of Science, Winthrop P Rockefeller Cancer Institute and Creighton University startup funds to R.G. We thank K. Polyak for experimental suggestions; J. Billheimer and A. Dhiman for help with analysis; A. Gogna for support; and the MTT platform (R. Tomás), the Histopathology Platform (I. Terras Marques, M. I. Romano, S. Casimiro and S. Dias) and the Rodent platform at the Champalimaud Centre for the Unknown.


**Author contributions** R.G. and E. Moreno conceptualized the idea, initiated the project, provided research support, designed, analysed, and interpreted the experiments and wrote the manuscript. E. Madan analysed the experiments, wrote the manuscript, and performed imaging, qPCR, flow-cytometry and mouse studies. R.G. designed and analysed the experiments, wrote the manuscript, created molecular biology design, and performed imaging analysis, clonogenicity assay, FISH-molecular design, IHC, mouse studies, and chemotherapy designs. C.J.P. analysed the experiments, helped in the preparation of figures, formatted and wrote the manuscript and performed statistical analysis, cell culture experiments, calcium imaging, low-density plating and conditioned medium experiments, and knockout and wild-type cell interactions. M.N. analysed the experiments, helped in the preparation of figures, and performed statistical analysis, flow-cytometry experiments and analysis, and FISH. T.M.P. analysed the experiments, helped in preparation of figures, formatted and wrote the manuscript, performed statistical analysis and cell culture experiments, extracted and cultured normal and epithelial cells from breast tissue, and performed laser-capture microdissection, qPCR, flow-cytometry and virus production. R.C.-M., A.G., V.H., Y.Y., T.Y., D.S., S.R.P. and H.Y. assisted in procuring tissue samples and IHC. K.F. performed IHC. K.S., A.M.P. and D.C. assisted with experiments and analysis. C.R. assisted with manuscript writing. M.A.F.P. and A.V. assisted with flow-cytometry experiments. D.A. assisted with confocal microscopy. H.N. provided normal breast cells. L.A.H. provided SCC samples, supervised K.F. for IHC in SCC and edited the manuscript. P.K. provided research support, and helped with data analysis, organization, and editing of the manuscript. C.C. and A.L.B. provided a clinical perspective, and helped with the procurement of tissue samples, design of IHC experiments, and design of clinical experiments such as the inclusion of chemotherapy.

**Competing interests** : The authors declare no competing interests.

**Additional information**


**Supplementary information** is available for this paper at https://doi.org/10.1038/s41586-019-1429-3.



**Correspondence and requests for materials** should be addressed to R.G. or E. Moreno

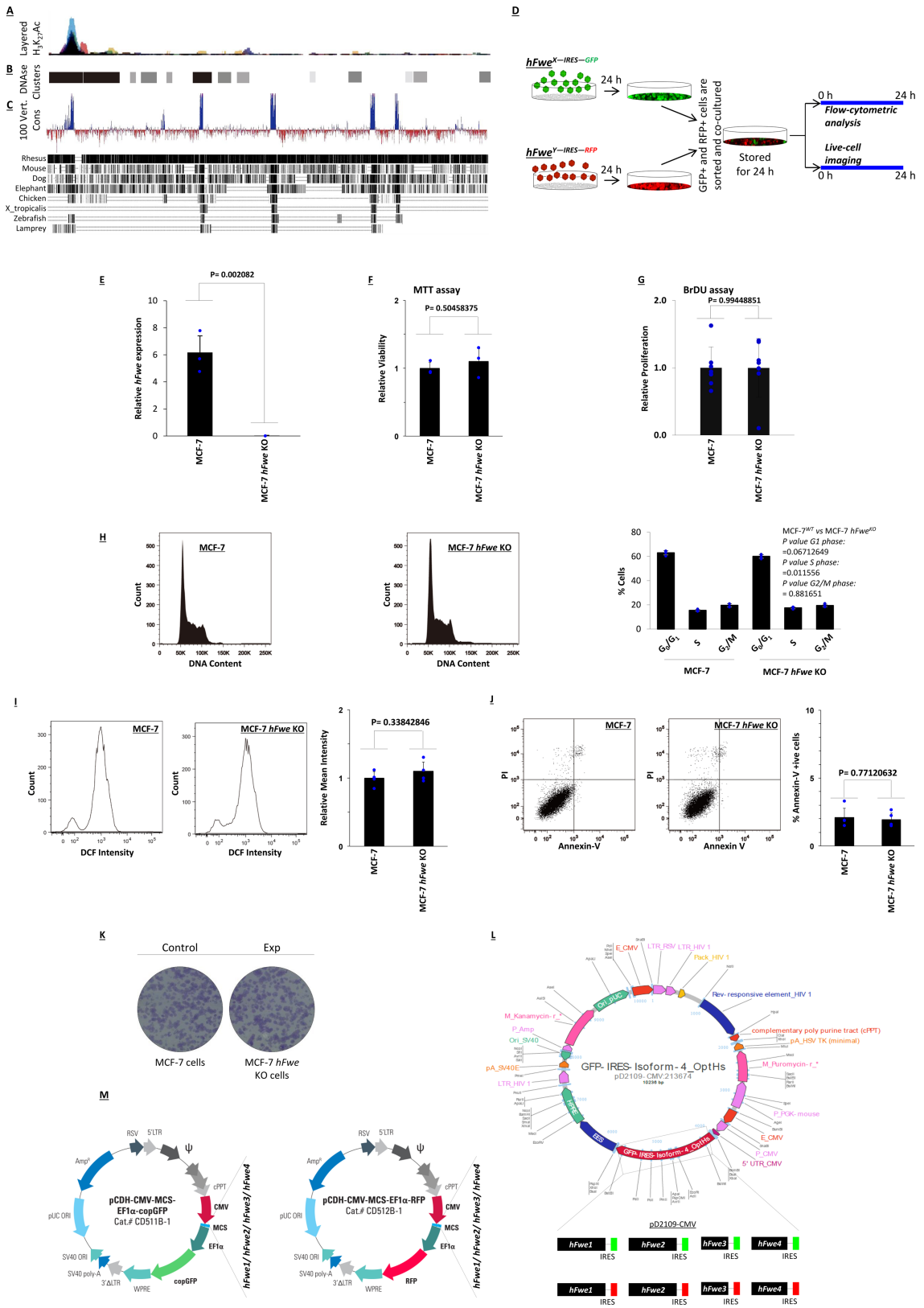


**Extended Data Fig. 1** | See next page for caption.

**Extended Data Fig. 1 | Knockout of the *hFWE* gene in MCF-7 cells does not affect their cellular functions. a**, ENCODE data mining for chromatin immunoprecipitation (ChIP) with $H_3K_2Ac$ antibody shows active euchromatin status of the *hFWE* promoter. **b**, ENCODE data mining for DNAase-I hypersensitivity analysis shows footprints of DNA unwinding at the locations of *hFWE* exons. **c**, Phylogenetic analysis. Exon sequences are highly conserved amongst vertebrates except exon 5, which is more specific to mammals. **d**, Pictorial representation of the protocol for the functional analysis of hFWE isoforms in cell culture. MCF-7 $hFWE^{KO}$ cells were infected with lentiviruses encoding each hFWE isoform alongside an independent GFP or RFP tag. Transduced cells were sorted for $RFP^+$ and $GFP^+$ populations, plated together and co-cultured for 24 h. Co-cultured cells were then studied for a further 24 h using live-cell imaging and flow cytometry. **e**, To obtain human cells expressing single hFWE isoforms, MCF-7 cells (breast cancer origin) were selected and MCF-7 $hFWE^{KO}$ cells were generated. qPCR analysis of relative transcript synthesis of *hFWE* exon 1 from MCF-7 $hFWE^{WT}$ and MCF-7 $hFWE^{KO}$ cells shows lack of gene product in the knockout cells ($n = 3$ biologically independent experiments). **f**, MTT assay shows that knockout of the *hFWE* gene does not affect cell viability and mitochondrial activity in MCF-7 cells ($n = 3$ biologically independent experiments). **g**, BrdU assay shows that knockout of the *hFWE* gene does not affect cellular proliferation rates of MCF-7 cells ($n = 7$ biologically independent experiments). **h**, Cell-cycle distribution was examined by analysing DNA content. Propidium iodide staining and subsequent flow cytometric analysis show that knockout of the *hFWE* gene does not affect the cell-cycle progression of the MCF-7 cells ($n = 3$ biologically independent experiments). **i**, Flow cytometric analysis of ROS via measurement of DCF fluorescence shows that knockout of the *hFWE* gene does not alter cellular ROS in MCF-7 cells ($n = 4$ biologically independent experiments). **j**, Annexin-V staining shows that knockout of the *hFWE* gene does not affect cellular apoptosis in MCF-7 cells ($n = 4$ biologically independent experiments). **k**, The clonogenic assay shows that knockout of the *hFWE* gene does not affect the ability of MCF-7 cells to form colonies ($n = 3$). **l**, Diagrammatic representation of the hFWEX–IRES–GFP/RFP lentiviral constructs. Eight lentiviral constructs were prepared by cloning *hFWE1/2/3/4–IRES–GFP/RFP* into pD2109-CMV lentiviral vectors. **m**, Eight additional constructs were prepared by cloning *hFWE1/2/3/4* into dual promoter pCDH-CMV-MCS-EF1α-copGFP and pCDH-CMV-MCS-EF1α-copRFP (System Biosciences), respectively. **e**–**j**, *P* values shown, two-tailed *t*-test, mean ± s.d.

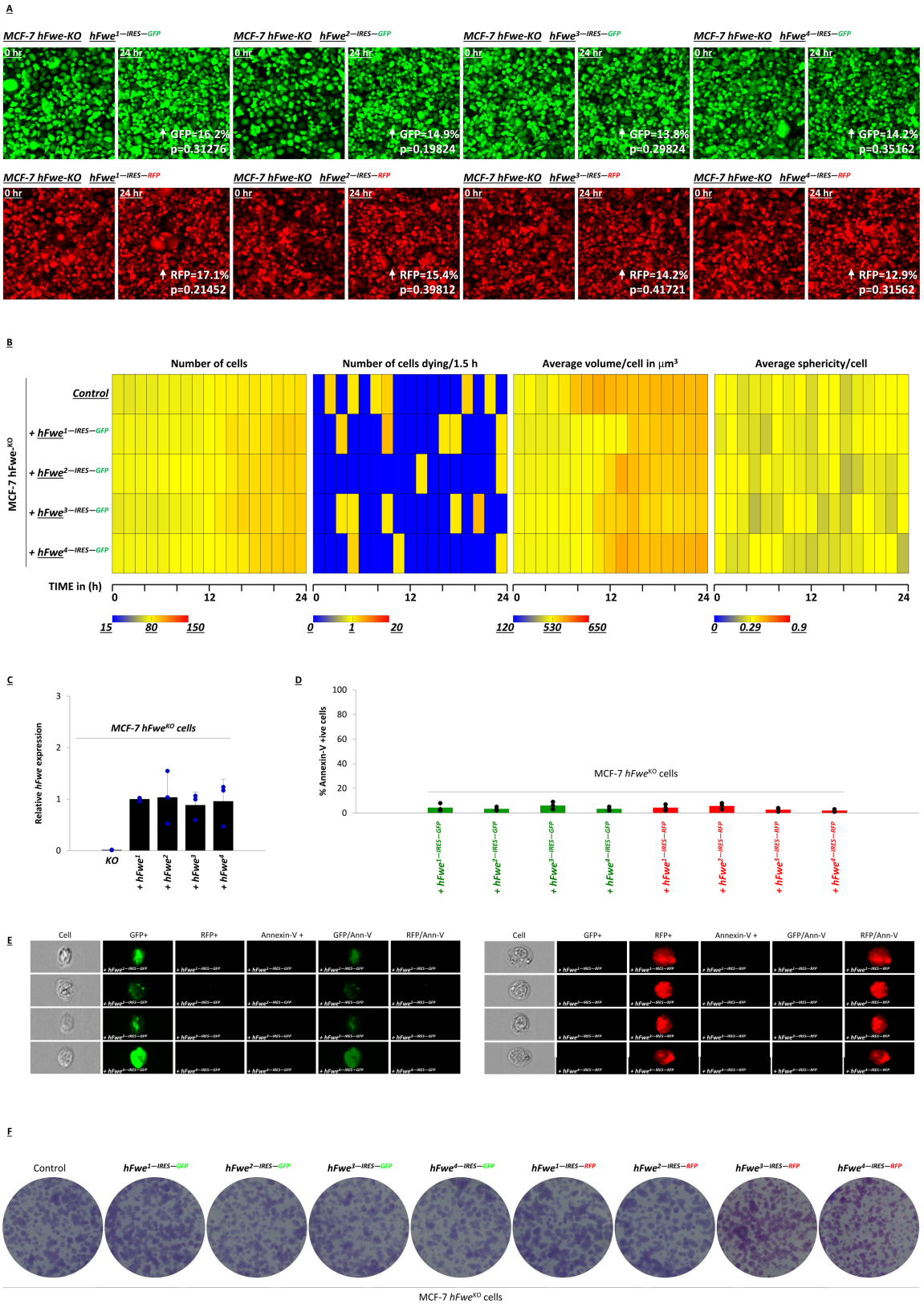


**Extended Data Fig. 2** | See next page for caption.

**Extended Data Fig. 2 | Overexpression of single hFWE isoforms in MCF-7 *hFWE$^{KO}$* cells does not alter viability. a**, MCF-7 *hFWE$^{KO}$* cells were infected with each *hFWE1/2/3/4–GFP/RFP* construct independently and the cells were monitored via live-cell imaging. Images at 24 h show that MCF-7 *hFWE$^{KO}$* cells homogenously expressing single hFWE isoforms do not undergo cell death ($n = 3$ biologically independent experiments, *P* values shown, two-tailed *t*-test). **b**, Analysis of live-cell imaging is shown as heat maps to represent the total number of cells, number of cells dying every 1.5 h, average cellular volume and average cellular sphericity; each block represents a gradient scale of low (blue), medium (yellow) and high (red) number or shape or size of the cells ($n = 3$, analysis performed using manual tool from Fiji and automated tools from Imaris, Genie tool used for representing data as heat maps). **c**, qPCR analysis of MCF-7 *hFWE$^{KO}$* cells expressing each of four hFWE isoforms showed comparable lentiviral-mediated expression of hFWE1, hFWE2, hFWE3 or hFWE4 ($n = 3$ biologically independent experiments, mean ± s.d., ANOVA showed no significant differences). **d**, Flow cytometry-based annexin-V staining shows that overexpression of individual hFWE1/2/3/4–GFP/RFP isoforms does not induce apoptosis in MCF-7 *hFWE$^{KO}$* cells ($n = 3$ biologically independent experiments, mean ± s.d., ANOVA showed no significant differences). **e**, Annexin-V staining and flow cytometry-based cell imaging (image stream) also show that overexpression of individual hFWE isoforms does not induce apoptosis ($n = 3$). **f**, Long-term effect of overexpression of single hFWE isoforms with GFP or RFP reporters over 21 days using clonogenic assay. The overexpression of hFWE isoforms does not affect the colony formation ability of MCF-7 *hFWE$^{KO}$* cells ($n = 3$).

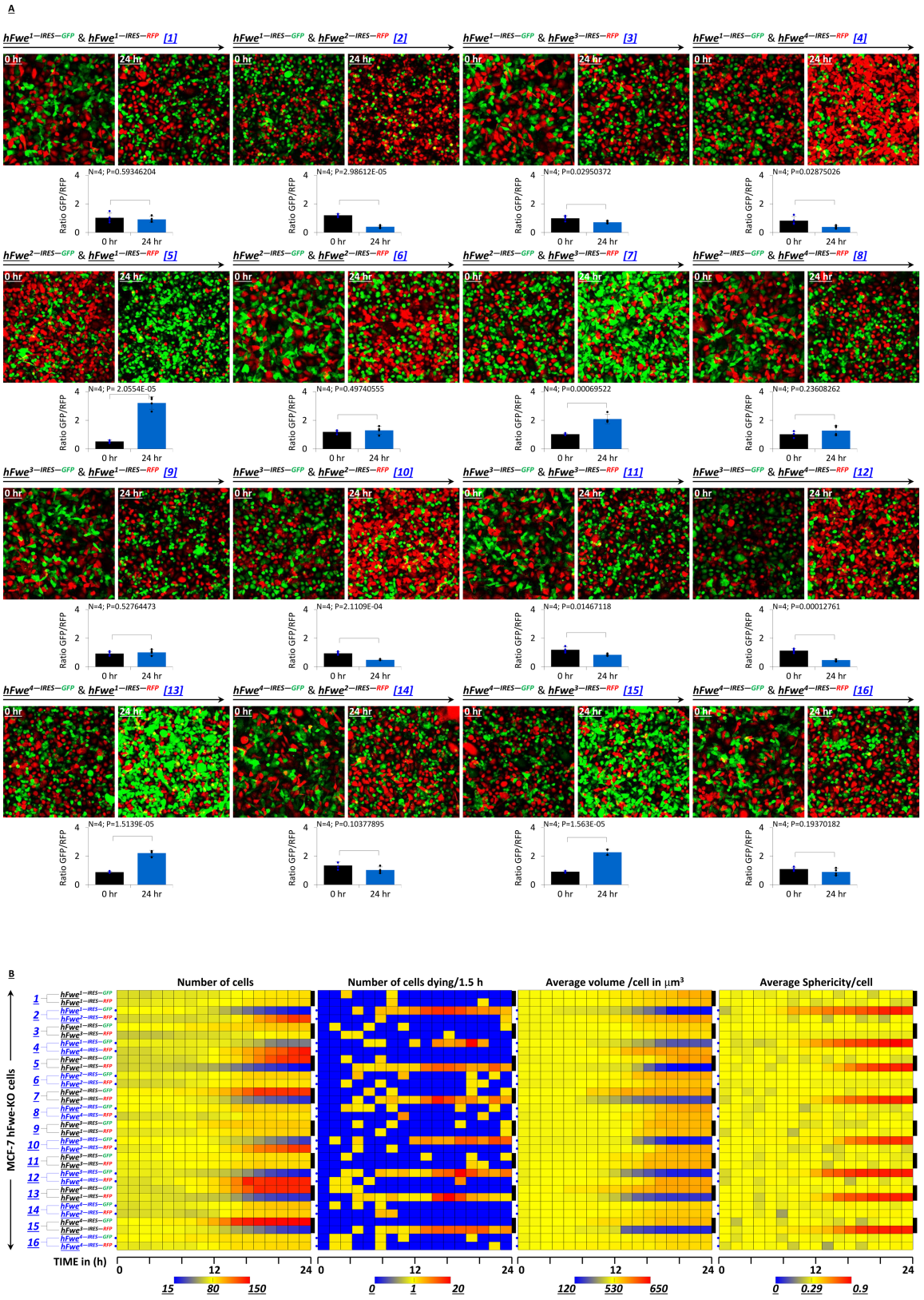


**Extended Data Fig. 3** | See next page for caption.

**Extended Data Fig. 3 | Live-cell imaging of co-culture assay using MCF-7 *hFWE*$^{KO}$ cells transduced with hFWE isoforms. a**, Results from 24-h live-cell imaging experiments of co-cultures of MCF-7 *hFWE*$^{KO}$ cells expressing the four hFWE isoforms. In [1], MCF-7 *hFWE*$^{KO}$ cells expressing hFWE1–IRES–GFP were co-cultured with cells expressing hFWE1–IRES–RFP. GFP$^{+}$ and RFP$^{+}$ cells were monitored at 0 and 24 h to follow the effects of hFWE isoforms on cell proliferation. The ratio of GFP$^{+}$ to RFP$^{+}$ cells did not vary significantly between 0 and 24 h. In co-culture experiments [2], MCF-7 *hFWE*$^{KO}$ cells expressing hFWE1–IRES–GFP were co-cultured with cells expressing hFWE2–IRES–RFP. The population of RFP$^{+}$ cells was significantly higher at 24 h than at 0 h, indicating competition between hFWE1–IRES–GFP and hFWE2–IRES–RFP cells. Each co-culture combination is presented amongst the four hFWE isoforms along with IRES–GFP or IRES–RFP co-expression. Cells expressing hFWE2 or hFWE4 emerged as winners when co-cultured with cells expressing hFWE1 or hFWE3 regardless of GFP or RFP reporter. The ratio of GFP$^{+}$ to RFP$^{+}$ cells at 0 and 24 h for each co-culture experiment is presented quantitatively below. The ratios at 0 and 24 h for each combination were compared statistically using a two-tailed *t*-test assuming unequal variances; $n = 4$ biologically independent experiments, *P* values shown, mean ± s.d. **b**, Analysis of live-cell imaging is shown as heat maps to represent the total number of cells, the number of cells that died every 1.5 h, average cellular volume, and average cellular sphericity. The co-culture combinations are indicated on the left. For example, the co-culture combination of cells expressing hFWE1–IRES–GFP with cells expressing hFWE2–IRES–RFP results in the death of hFWE1–IRES–GFP cells at the expense of an increase in the number of hFWE2–IRES–RFP cells. Analysis of all co-culture combinations is presented. The data support the idea that cells expressing hFWE1 or hFWE3, when co-cultured with cells expressing hFWE2 or hFWE4, undergo cell death accompanied by loss of differentiated cellular architecture, indicated by decreased cellular volume (blue) and increased cellular sphericity (red). Each block represents a gradient scale of low (blue), medium (yellow) and high (red) for the number, size or shape of the cells ($n = 4$, analysis performed using the manual tool from Fiji and automated tools from Imaris, Genie tool used for representing data as heat maps).

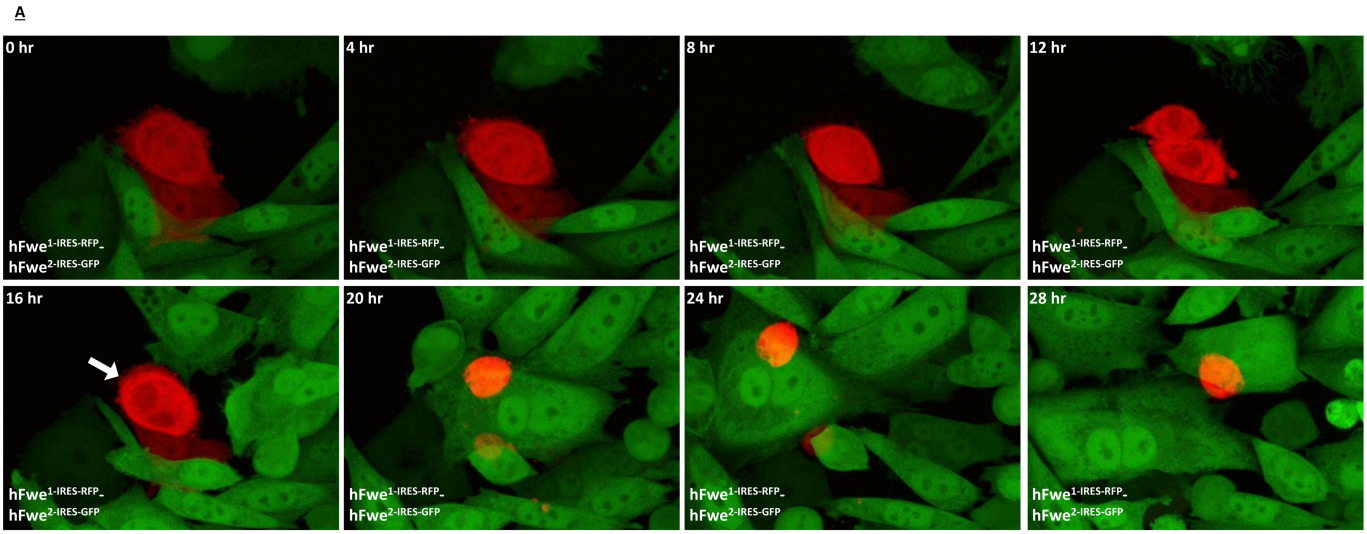


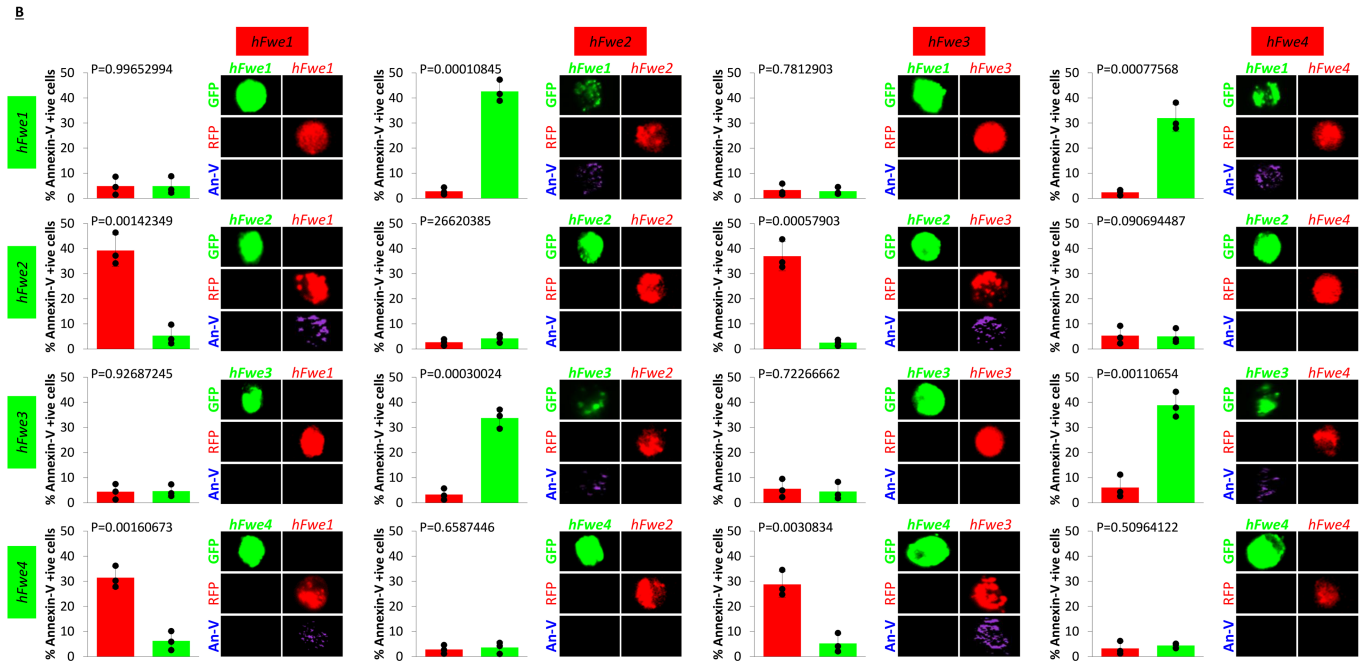


**Extended Data Fig. 4 | High-resolution imaging of competition-induced Loser cell death. a**, High-resolution live-cell imaging experiment (28 h) showing cell competition in MCF-7 *hFWE*$^{KO}$ cells expressing hFWE1–IRES–RFP and hFWE2–IRES–GFP isoforms. The co-culture results show elimination of cells carrying the Lose isoform (hFWE1–IRES–GFP); $n = 3$ biologically independent experiments with similar results. **b**, The results of live-cell imaging were confirmed using annexin-V staining and flow-cytometry-based imaging of GFP$^+$ and RFP$^+$ cells for each co-culture combination. Cells were sorted following 24 h of co-culture, and the percentage of apoptotic cells is displayed. The flow-based imaging of these cells is also presented and shows no GFP$^+$ signal in RFP-sorted cells or RFP$^+$ signal in GFP-sorted cells. The annexin-V$^+$ signal is shown in purple. For example, co-culture of cells expressing hFWE1–IRES–GFP with cells expressing hFWE2–IRES–RFP results in apoptosis of hFWE1–IRES–GFP cells, as indicated by the annexin-V$^+$ signal. Together, results from live-cell imaging and flow cytometry demonstrate that cells expressing hFWE$^{Lose}$ isoforms (hFWE1 or hFWE3) undergo apoptosis when in competition with cells expressing hFWE$^{Win}$ isoforms (hFWE2 or hFWE4) ($n = 3$ biologically independent experiments, *P* values shown, two-tailed *t*-test, was performed for *P*-value calculations, mean ± s.d.).

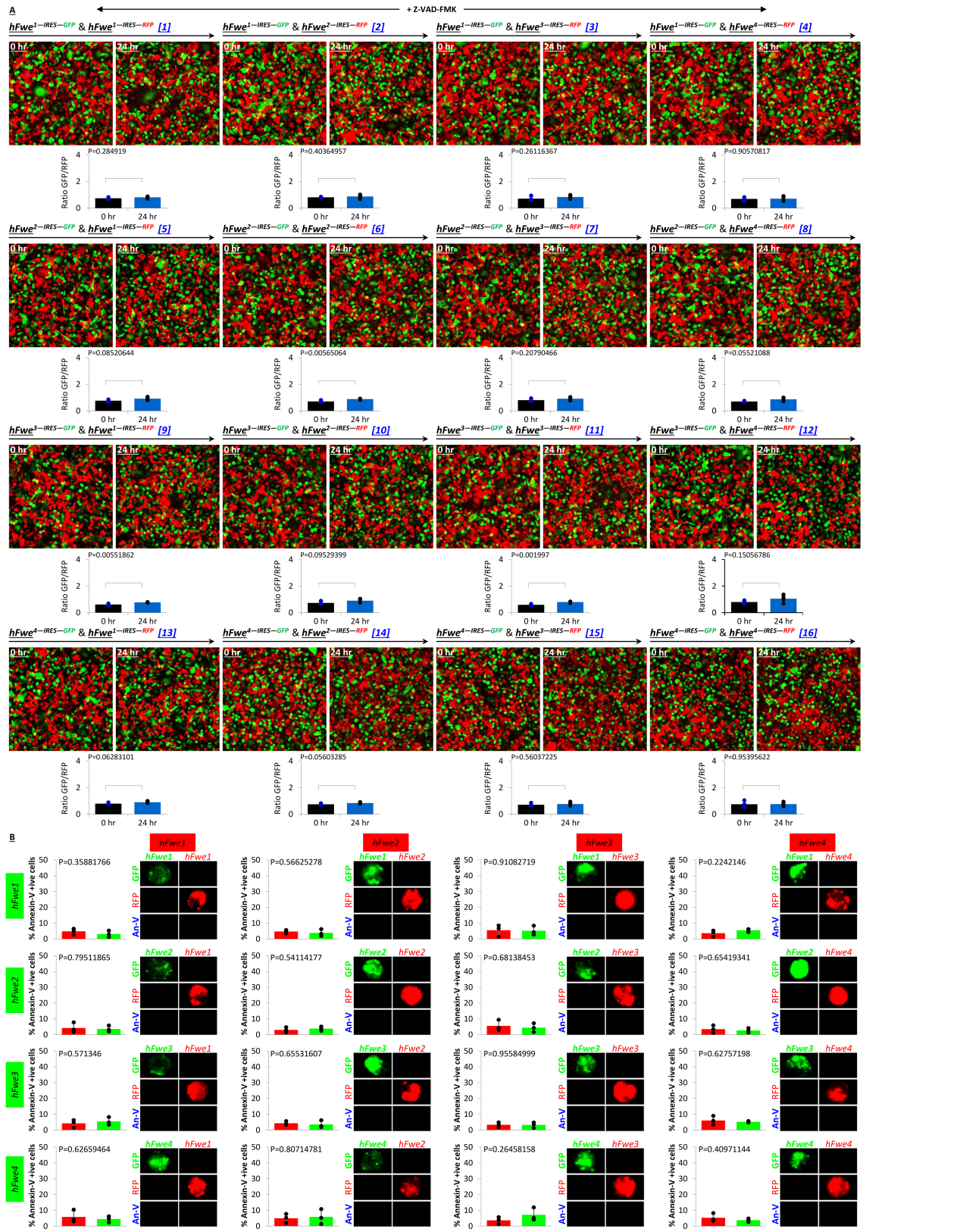


**Extended Data Fig. 5 | Cells expressing hFWE$^{Lose}$ isoforms undergo caspase-dependent apoptosis during co-culture with cells expressing hFWE$^{Win}$ isoforms. a**, The effect of incubation with the pan-caspase inhibitor Z-VAD-FMK (20 μM) on co-culture of cells expressing hFWE$^{Win}$ or hFWE$^{Lose}$ isoforms. Caspase inhibition by Z-VAD-FMK rescued hFWE$^{Lose}$ cells expressing hFWE1 or hFWE3 from undergoing cell death induced by co-culture with hFWE$^{Win}$ cells expressing hFWE2 or hFWE4. The ratio of GFP$^+$ to RFP$^+$ cells at 0 and 24 h for each co-culture experiment is presented quantitatively below. The ratios at 0 and 24 h for each combination were compared statistically using a two-tailed *t*-test assuming unequal variances ($n = 4$ biologically independent experiments, *P* values shown, mean ± s.d.). **b**, Annexin-V staining and flow cytometry-based imaging of GFP$^+$ and RFP$^+$ cells for each co-culture combination confirms that incubation with Z-VAD-FMK prevents apoptosis in co-culture of cells expressing hFWE$^{Win}$ or hFWE$^{Lose}$ isoforms ($n = 3$ biologically independent experiments, *P* values shown, two-tailed *t*-test, mean ± s.d.).

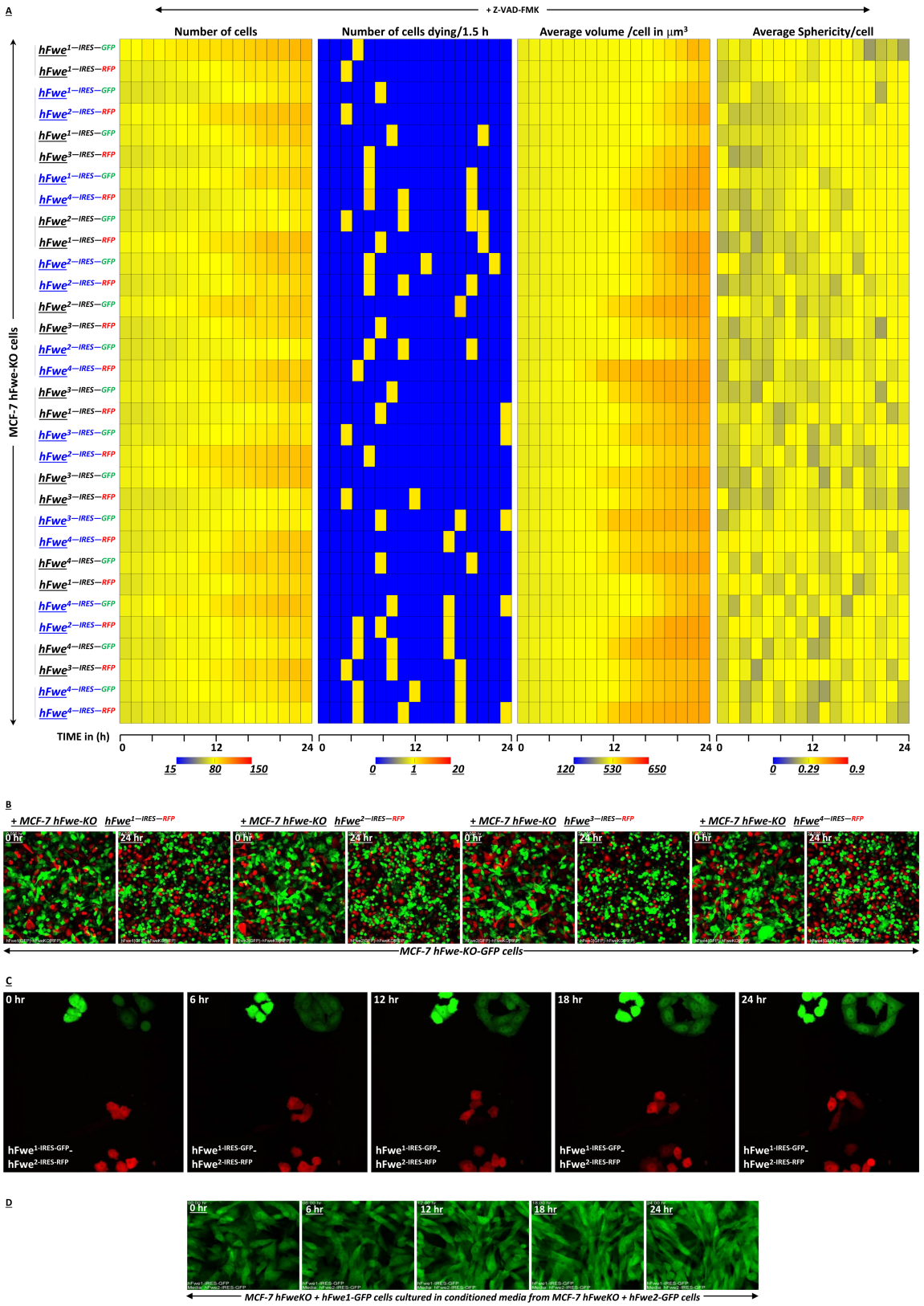


**Extended Data Fig. 6** | See next page for caption.

**Extended Data Fig. 6 | Characterization of competition in co-culture assay of cells expressing hFWE$^{Win}$ or hFWE$^{Lose}$ isoforms. a**, Analysis of live-cell imaging is shown as heat maps to represent the total number of cells, number of cells that died every 1.5 h, average cellular volume, and average cellular sphericity. Each block represents a gradient scale of low (blue), medium (yellow) and high (red) number, shape or size of cells. Treatment with Z-VAD-FMK blocked hFWE$^{Win}$ cell-induced death of co-cultured hFWE$^{Lose}$ cells, resulting in equal ratios of GFP$^{+}$ and RFP$^{+}$ populations ($n = 4$, analysis performed using the manual tool from Fiji and automated tools from Imaris, Genie tool used for representing data as heat maps). **b**, Imaging results show that MCF-7 *hFWE*$^{KO}$ cells expressing each hFWE isoform independently do not outcompete co-cultured *hFWE*$^{KO}$ cells, consistent with a mechanism of *hFWE*-mediated cell death supported by the presence of both hFWE$^{Win}$ and hFWE$^{Lose}$ isoforms ($n = 3$). **c**, Culling of cells expressing hFWE$^{Lose}$ isoforms appeared to be contact dependent. Live-cell imaging was performed on low-density-plated MCF-7 *hFWE*$^{KO}$ cells expressing hFWE1–IRES–GFP and hFWE2–IRES–RFP. Results show cell proliferation and absence of cell death in either cell population under conditions of low-density plating ($n = 3$ biologically independent experiments). **d**, The potential effect of secreted factors from cells expressing hFWE$^{Win}$ isoforms was investigated. Conditioned medium from MCF-7 *hFWE*$^{KO}$ cells expressing hFWE2–IRES–GFP did not affect viability when transferred to a culture of MCF-7 *hFWE*$^{KO}$ cells expressing hFWE2–IRES–GFP and imaged over 24 h ($n = 3$).

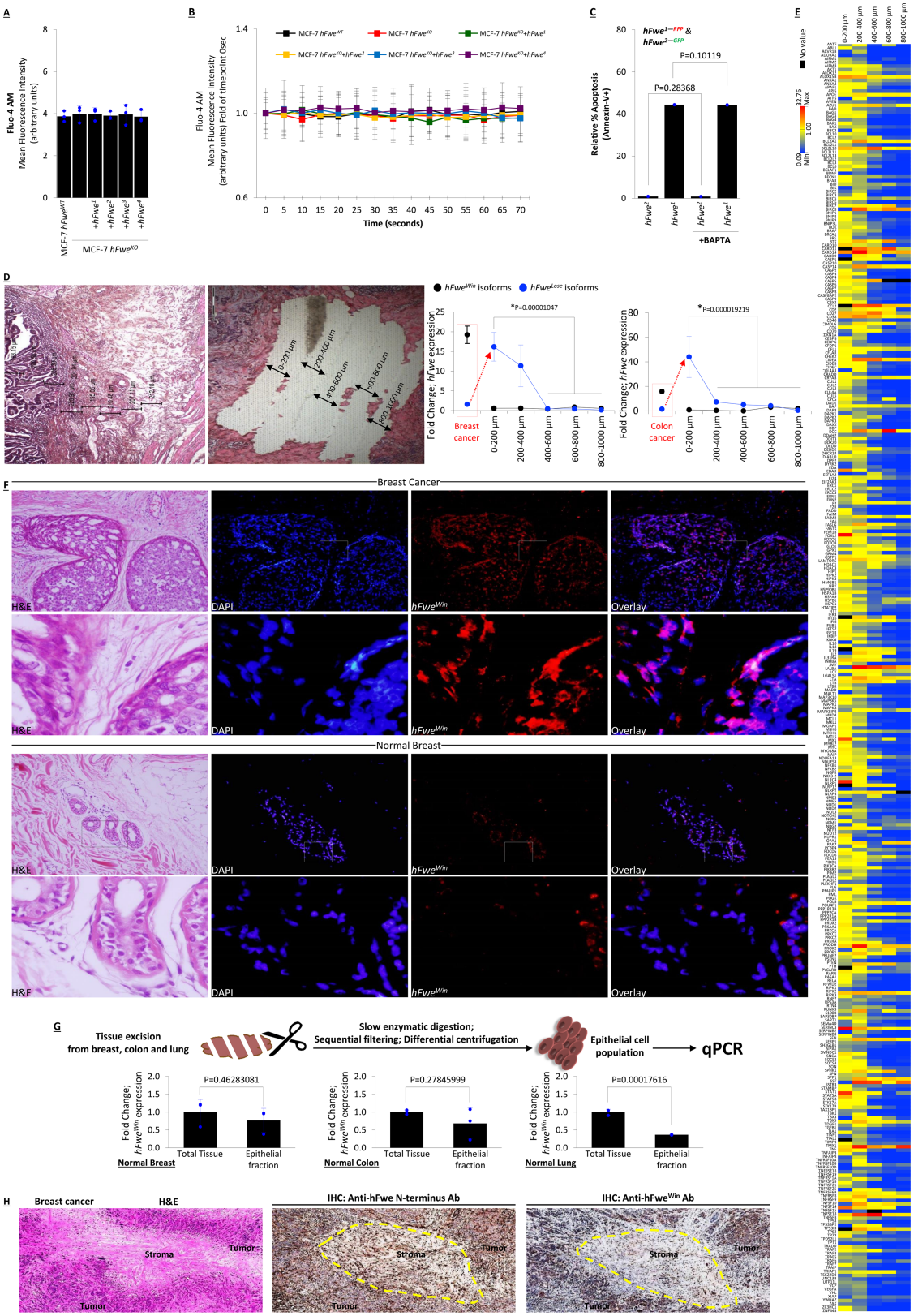


**Extended Data Fig. 7** | See next page for caption.

**Extended Data Fig. 7 | Calcium-independent mechanism of hFWE-mediated cell competition. a**, The potential effect of individual hFWE isoforms on intracellular calcium levels was investigated. Live-cell imaging was performed to detect levels of Fluo-4AM in MCF-7 *hFWE*$^{KO}$ cells and MCF-7 *hFWE*$^{KO}$ cells overexpressing single hFWE isoforms ($n = 3$ biologically independent experiments, ANOVA showed no significant differences, mean ± s.d.). **b**, Live-cell imaging at 5-s intervals over 1 min showed constant levels of Fluo-4AM in MCF-7 *hFWE*$^{KO}$ cells and MCF-7 *hFWE*$^{KO}$ cells overexpressing single hFWE isoforms ($n = 3$ biologically independent experiments, ANOVA showed no significant differences, mean ± s.d.). **c**, hFWE-mediated cell competition assay carried out in the presence or absence of the calcium chelator BAPTA-AM. Treatment with BAPTA-AM did not affect the ability of MCF-7 *hFWE*$^{KO}$ cells expressing hFWE2 to kill co-cultured MCF-7 *hFWE*$^{KO}$ cells expressing hFWE1 ($n = 3$ biologically independent experiments, *P* values shown, two-tailed *t*-test found no significant differences, mean ± s.d.). **d**, Laser-capture microdissection was performed in increments of 200 μm in distance perpendicular to the defined boundary of breast tissue tumour mass. Representative images are shown for breast cancer tissue section before and after laser capture. hFWE$^{Lose}$ isoforms were upregulated in tumour-adjacent host tissue nearest to breast cancer (0–400 μm) or colon cancer (0–200 μm). hFWE$^{Win}$ isoforms were highly enriched within breast or colon tumour tissue but not adjacent tissue ($n = 3$ biologically independent experiments, mean ± s.d., fold change calculated relative to the external reference of the expression of hFWE$^{Win}$ isoforms in normal breast tissue, *P* values shown, two-tailed *t*-test). **e**, qPCR array was used to examine the expression of 354 genes involved in apoptotic pathways in samples of laser-captured tumour-adjacent host tissue. Gene expression heat map shows that host tissue in the immediate vicinity of cancer (0–400 μm) displayed upregulation of genes involved in apoptotic pathways. Host tissue farther away (400–1,000 μm) from the tumour edge displayed basal levels of apoptosis-related genes. The heat map shows apoptotic genes that were induced (red), suppressed (blue) or unchanged (yellow) in expression. Black represents unsuccessful runs ($n = 3$). **f**, FISH shows the expression of hFWE$^{Win}$ isoforms in FFPE samples of breast cancer tissue (top) and normal breast tissue (bottom). First column, H&E staining; second column, control DAPI staining; third column, expression of hFWE$^{Win}$ isoforms within tumour tissue; fourth column, overlay of DAPI and hFWE$^{Win}$ isoforms. Magnified images below each panel show expression of hFWE$^{Win}$ isoforms specifically in tumour tissue, as these isoforms are poorly expressed in the stromal tissue surrounding the tumour and normal breast tissue ($n = 3$ for all staining). **g**, Schematic depicting the process of epithelial cell isolation from normal breast, colon, and lung tissue. Expression of the four hFWE isoforms was compared in epithelia versus total tissue by qPCR analysis ($n = 3$ biologically independent experiments, all statistically significant *P* values shown, two-tailed *t*-test, mean ± s.d.). **h**, IHC staining of FFPE samples of breast cancer with newly developed antibodies against hFWE. Breast cancer and stromal regions are shown in the H&E images (left). The anti-hFWE$^{Win}$ antibody is specific to Win isoforms hFWE2 and hFWE4 whereas the anti-hFWE-N-term antibody targets the common N terminus and recognizes all four isoforms. Immunohistochemistry staining shows the abundance of hFWE$^{Win}$ isoforms within the breast cancer samples in human tumours. From this, we conclude that hFWE$^{Win}$ proteins are expressed in the tumour but not in the stroma. To demonstrate the expression of Lose isoforms in the stroma, we compared the staining of all hFWE isoforms using our N-terminal-specific antibody with the poor expression of hFWE$^{Win}$ in the stroma. The anti-hFWE-N-term antibody shows strong immunoreactivity and equal distribution of staining in the tumour and stromal tissue. We find no positive signal for hFWE$^{Win}$ isoforms in the stroma, but we find strong expression of total hFWE (hFWE$^{Win}$ and hFWE$^{Lose}$ combined) in the stroma near the tumour. From this, we can conclude that Lose isoforms are expressed in the stroma. This experiment was repeated independently three times with similar results.

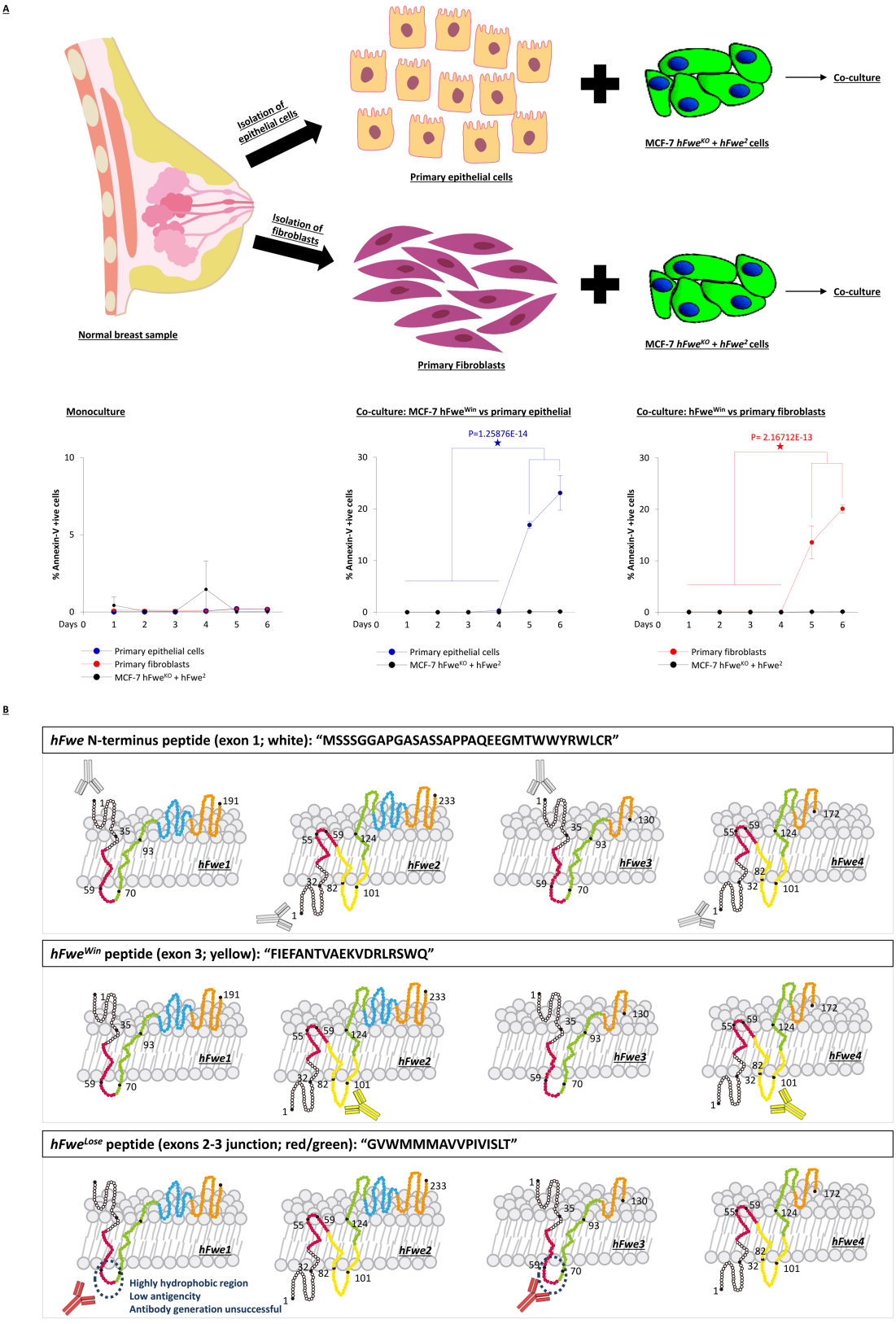


**Extended Data Fig. 8 | Dynamics of hFWE-mediated cell competition between cancer and normal cells. a**, Protocol for observing hFWE-mediated cell competition between hFWE$^{Win}$-expressing cancer cells and primary cultures of human epithelial cells and fibroblasts. MCF-7 *hFWE$^{KO}$* cells overexpressing hFWE$^{Win}$ isoforms outcompeted and induced apoptosis of co-cultured primary breast normal epithelial cells or fibroblasts over 6 days ($n = 3$ biologically independent experiments, all statistically significant $P$ values are shown, ANOVA, mean ± s.d.). **b**, hFWE$^{Win}$ isoforms (hFWE2 and hFWE4) and hFWE$^{Lose}$ isoforms (hFWE1 and hFWE3) are characterized by intra-exonic inclusions. The in silico model shows predicted transmembrane structures of the four hFWE proteins. An antibody was raised against the common N terminus (exon 1), which is included in all four isoforms. Another antibody was raised to specifically recognize the hFWE$^{Win}$ isoforms (which share exon 3). Owing to the similarity in sequences to hFWE$^{Win}$ isoforms and low antigenicity of the peptide sequence at the junction of exons 2 and 4, generation of an antibody specific to hFWE$^{Lose}$ isoforms was not possible.

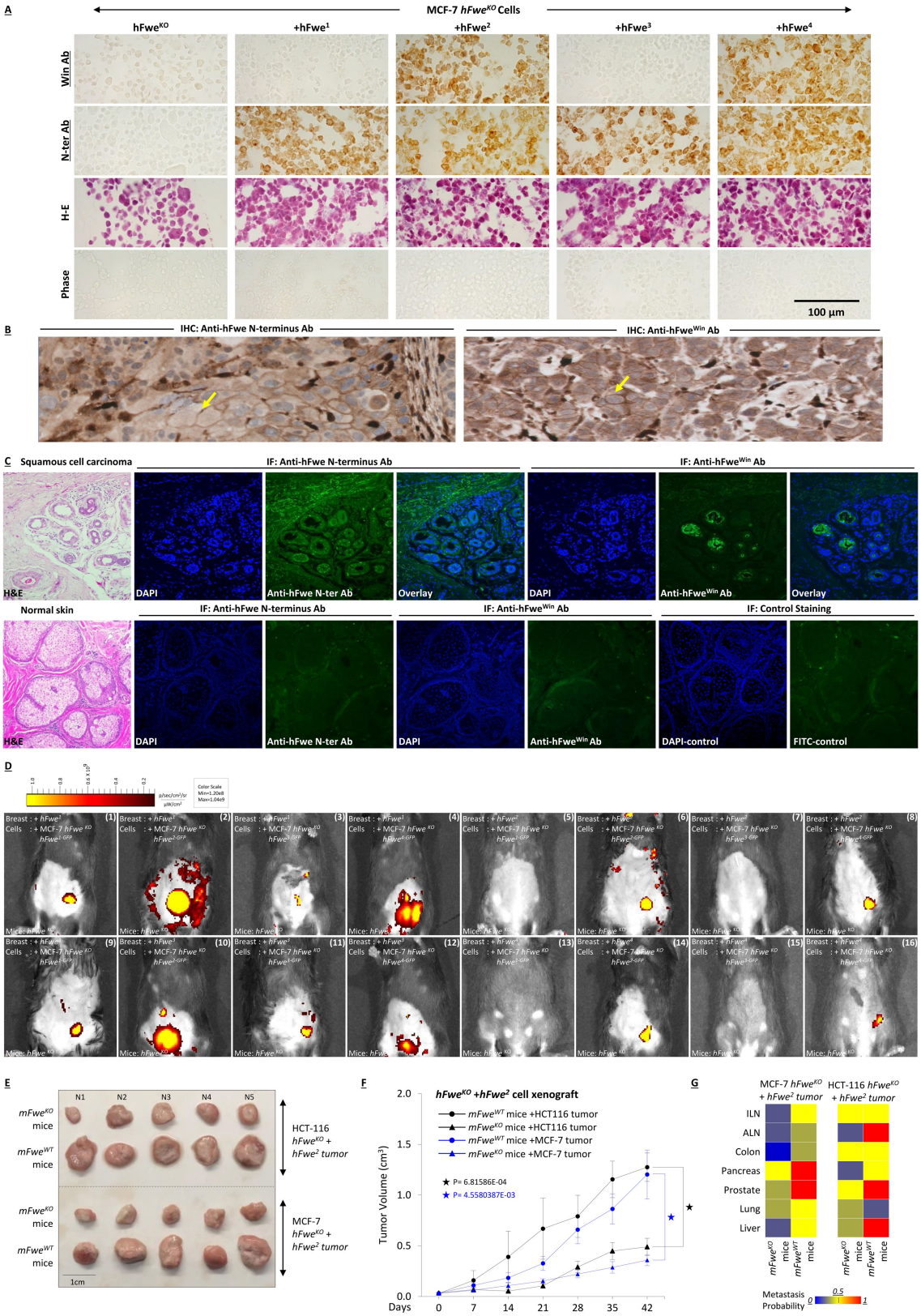


**Extended Data Fig. 9** | See next page for caption.

**Extended Data Fig. 9 | Generation of antibodies against hFWE$^{Win}$ isoforms (hFWE2 and hFWE4) or the common hFWE N terminus and expression in human cancers. a**, Immunocytochemistry of hFWE isoforms in paraffin-embedded and sectioned human MCF-7 cells using novel anti-hFWE antibodies. The specificity was validated by immunocytochemistry of MCF-7 *hFWE$^{KO}$* cells with or without overexpression of individual hFWE isoforms. Cells were stained with anti-hFWE-N-term antibody or anti-hFWE$^{Win}$ antibody. Immunocytochemistry results confirm antibody specificity in paraffin sections with MCF-7 *hFWE$^{KO}$* cells with or without overexpression of individual hFWE isoforms. The anti-hFWE$^{Win}$ antibody does not stain sections with *hFWE$^{KO}$* cells, and recognizes specifically hFWE2 and hFWE4, but not the hFWE$^{Lose}$ isoforms hFWE1 and hFWE3 (row 1). The anti-hFWE-N-term antibody is also negative for staining in control *hFWE$^{KO}$* cells but detected positive membrane staining for each of the four hFWE isoforms (row 2; $n = 3$). **b**, Immunohistochemistry of hFWE proteins in sections from clinical breast cancer samples ($n = 3$). Arrows indicate membrane staining. **c**, Immunofluorescence staining of hFWE proteins in human SCC tissue shows an abundance of hFWE$^{Win}$ isoforms within defined cancer lesions, whereas the anti-hFWE-N-term antibody stained both stroma and cancer tissue (top; $n = 3$) when compared with normal skin (bottom; $n = 3$). **d**, Tumour volumes were measured and analysed for each of the 16 combinations of hFWE*X*–IRES–GFP expression in MCF-7 *hFWE$^{KO}$* xenografted cells and hFWE isoform expression within *Fwe$^{KO}$* mouse mammary tissue ($n = 3$). In vivo bioluminescence imaging (using the IVIS system) was used to detect and measure the fluorescence of GFP$^{+}$ cancer cells in tumours resulting from all genetic combinations at 28 days post-implantation. Substantially reduced tumour growth was observed when mammary tissue expressed hFWE$^{Win}$ isoforms and cancer cells expressed hFWE$^{Lose}$ isoforms. By contrast, tumour growth is strongly promoted when mammary tissue expresses hFWE$^{Lose}$ isoforms and cancer cells express hFWE$^{Win}$ isoforms ($n = 3$). **e**, Tumorigenic potential of HCT-116 (colon origin) or MCF-7 (breast origin) *hFWE$^{KO}$* cells overexpressing hFWE2 in recipient *Fwe$^{WT}$* and *Fwe$^{KO}$* mice. Tumour growth of both *Fwe$^{KO}$* breast and colon cancer cell lines overexpressing the Win isoform hFWE2 was greater in *Fwe$^{WT}$* mice than in *Fwe$^{KO}$* mice. Photos of resected tumours are shown. **f**, Tumour volumes were measured every week over 42 days for groups shown in **a**. *hFWE$^{KO}$* colon- or breast-derived tumours overexpressing hFWE2 showed significantly higher growth in *Fwe$^{WT}$* mice than in *Fwe$^{KO}$* mice ($n = 5$, *P* values shown, one-tailed *t*-test, mean ± s.d.). **g**, At the conclusion of tumour growth experiments, mice were examined for the presence or absence of metastases in inguinal lymph nodes (ILN), axillary lymph nodes (ALN), colon, pancreas, prostate, lung, and liver. Heat map scale indicates the probability of metastasis. Results show a marked reduction in the metastatic potential of both breast and colon cancer *hFWE$^{KO}$* cells overexpressing hFWE2 when xenografted into *Fwe$^{KO}$* mice as compared to *Fwe$^{WT}$* mice ($n = 5$ each group).

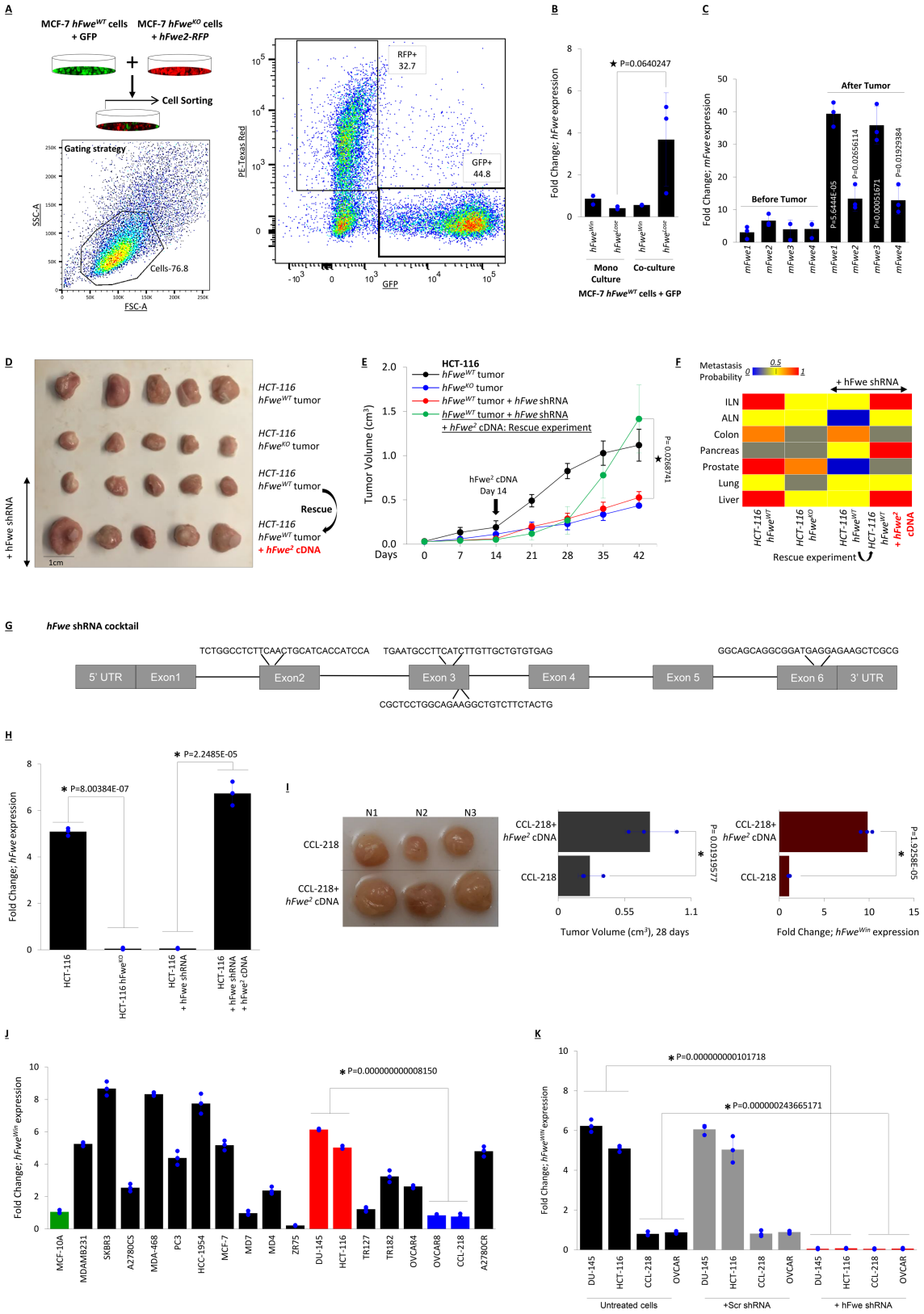


**Extended Data Fig. 10** | See next page for caption.

**Extended Data Fig. 10 | Endogenous hFWE in human cancer cell lines and tumorigenic potential. a**, Culture experiments were conducted to examine the dynamics of $hFWE^{Win}$ and $hFWE^{Lose}$ isoform expression. MCF-7 $hFWE^{KO}$ cells expressing hFWE2–RFP were co-cultured with wild-type MCF-7 cells expressing GFP for 24 h and sorted for analysis of hFWE isoform expression. $n = 3$ biologically independent experiments with similar results. **b**, Co-culture of MCF-7 $hFWE^{KO}$ cells expressing hFWE2–RFP with wild-type MCF-7 cells expressing GFP caused upregulation of $hFWE^{Lose}$ isoforms in wild-type MCF-7 cells. qPCR analysis of the expression of $hFWE^{Win}$ and $hFWE^{Lose}$ isoforms in $GFP^+$ wild-type MCF-7 cells sorted from co-culture shows a significant increase in $hFWE^{Lose}$ isoforms (bar 4) when compared with monocultured wild-type MCF-7 cells (bar 2). $n = 3$ biologically independent experiments with similar results; fold change calculated relative to the expression of $hFWE^{Win}$ isoforms in monocultured $GFP^+$ wild-type MCF-7 cells, all statistically significant $P$ values shown, two-tailed $t$-test, mean ± s.d. **c**, MCF-7 cells expressing hFWE2 were xenografted into $Fwe^{WT}$ mice to assess their tumorigenic potential and the host expression of endogenous hFWE isoforms compared to control. The mouse tissue adjacent to the tumour showed a significant increase in expression of $hFWE^{Lose}$ isoforms at 21 days post-xenograft. $n = 3$ biologically independent experiments with similar results; all statistically significant $P$ values shown, one-tailed $t$-test, mean ± s.d. **d**, The effect of anti-*hFWE* shRNA cocktail on the tumorigenic potential of HCT-116 cells. Row 1, growth potential of HCT-116 $hFWE^{WT}$ cells. Row 2, knockout of *hFWE* in these cells significantly reduced tumour growth. Row 3, treatment of HCT-116 $hFWE^{WT}$ cells with anti-*hFWE* shRNA reduced tumour volume. Row 4, Rescue experiment in which similar *hFWE* shRNA-treated tumours to row 3 were infected with lentivirus overexpressing hFWE2 14 days after implantation. These tumours are significantly larger than those in row 3. **e**, Tumour volumes for experiments shown in Fig. 4a were measured weekly, and growth patterns were analysed over 42 days for groups shown in **a**. Growth curves show the reduced growth of tumours from HCT-116 $hFWE^{KO}$ cells (blue) and *hFWE* shRNA-treated HCT-116 $hFWE^{WT}$ cells (red). Green line shows rescue experiment and growth pattern changes in *hFWE* shRNA-treated HCT-116 $hFWE^{WT}$ tumours expressing with hFWE2 ($n = 5$, $P$ values shown, one-tailed $t$-test, mean ± s.d.). **f**, All mice used in the study were examined for the presence or absence of metastases in ILN, ALN, colon, pancreas, prostate, lung and liver. Heat map scale indicates the probability of metastasis. Metastatic potential was reduced by knockout or knockdown of *hFWE* in HCT-116 cells (compare column 1 with columns 2 and 3). The rescue of tumour growth by re-introduction of *hFWE2* cDNA was accompanied by an increase in metastasis of these cells (compare column 3 with column 4; $n = 5$ each group). **g**, A cocktail of shRNAs were designed to knock down all four isoforms of hFWE. All shRNAs were checked for off-target effects. **h**, Gene expression analysis confirmed deletion of total *hFWE* in HCT-116 $hFWE^{KO}$ cells. Exogenous expression of *hFWE2* cDNA was detectable as the total *hFWE* expression in wild-type HCT-116 cells co-treated with anti-*hFWE* shRNA (observed in resected tumours). $n = 3$ biologically independent experiments, fold change calculated relative to expression of $hFWE^{Win}$ isoforms in MCF-10A cells, $P$ values shown, two-tailed $t$-test, mean ± s.d. **i**, Tumorigenic potential of wild-type CCL-218 cells and CCL-218 cells overexpressing hFWE2. Xenografts overexpressing *hFWE2* cDNA showed increased tumour volume at 28 days. Photos of resected tumours are shown. $n = 3$ biologically independent experiments with similar results, all statistically significant $P$ values shown, ANOVA, mean ± s.d. Control qPCR experiment demonstrates the overexpression of *hFWE2* in CCL-218 tumours at day 28. $n = 3$ biologically independent experiments, fold change calculated relative to expression of $hFWE^{Win}$ isoforms in MCF-10A cells, $P$ values shown, two-tailed $t$-test, mean ± s.d. **j**, Endogenous expression of the four hFWE isoforms in 19 cancer cell lines of multiple origins ($n = 3$ biologically independent experiments, fold change is calculated relative to expression of $hFWE^{Win}$ isoforms in MCF-10A cells, $P$ values shown, ANOVA, mean ± s.d.). **k**, Gene expression analysis shows efficient shRNA-mediated knockdown of total *hFWE* in HCT-116, DU-145, CCL-218 and OVCAR-8 tumours (observed in resected tumours). $n = 3$ biologically independent experiments, fold change calculated relative to expression of $hFWE^{Win}$ isoforms in MCF-10A cells, $P$ values shown, ANOVA, mean ± s.d.

nature research

Corresponding author(s): Dr. Eduardo Moreno
Dr. Rajan Gogna

Last updated by author(s): Apr 26, 2019

# Reporting Summary

Nature Research wishes to improve the reproducibility of the work that we publish. This form provides structure for consistency and transparency in reporting. For further information on Nature Research policies, see Authors & Referees and the Editorial Policy Checklist.

## Statistics

For all statistical analyses, confirm that the following items are present in the figure legend, table legend, main text, or Methods section.

| n/a | Confirmed |
|---|---|
| ☐ | ☒ The exact sample size (*n*) for each experimental group/condition, given as a discrete number and unit of measurement |
| ☐ | ☒ A statement on whether measurements were taken from distinct samples or whether the same sample was measured repeatedly |
| ☐ | ☒ The statistical test(s) used AND whether they are one- or two-sided<br>*Only common tests should be described solely by name; describe more complex techniques in the Methods section.* |
| ☐ | ☒ A description of all covariates tested |
| ☐ | ☒ A description of any assumptions or corrections, such as tests of normality and adjustment for multiple comparisons |
| ☐ | ☒ A full description of the statistical parameters including central tendency (e.g. means) or other basic estimates (e.g. regression coefficient) AND variation (e.g. standard deviation) or associated estimates of uncertainty (e.g. confidence intervals) |
| ☐ | ☒ For null hypothesis testing, the test statistic (e.g. *F*, *t*, *r*) with confidence intervals, effect sizes, degrees of freedom and *P* value noted<br>*Give P values as exact values whenever suitable.* |
| ☒ | ☐ For Bayesian analysis, information on the choice of priors and Markov chain Monte Carlo settings |
| ☒ | ☐ For hierarchical and complex designs, identification of the appropriate level for tests and full reporting of outcomes |
| ☒ | ☐ Estimates of effect sizes (e.g. Cohen's *d*, Pearson's *r*), indicating how they were calculated |

*Our web collection on statistics for biologists contains articles on many of the points above.*

## Software and code

Policy information about availability of computer code

| | |
|---|---|
| Data collection | Zen2.3 SP1, CFX manager, Step1 softwarev2.3, Amnis ImageStream MK II Imaging, Becton Dickinson FACS ARIA Fusion, Becton Dickinson FACS ARIA IIIu, Becton Dickinson-LSRII H274, MACSQuant Analyzer, Palm Robo Software, IVIS 200 Vivo Vision System (Xenogen), Philip Ultra Fast Scanner 1.6, Leica TCS SP8 confocal laser microscope, Nikon A1 HD25 confocal microscope, Zeiss LSM-800 with Airy Scan Confocal Microscope, BZ-X700 microscope, Leica Cryostat 3050S, Leica Microsystems, Zeiss Palm MicroBeam IV Laser Capture Microdissection system, PredictProtein 2013. |
| Data analysis | Flow-Jo.V9, Flow-Jo.V10, BD FACS DIVA, Inspire Imaris, Fiji, IVIS 200 Vivo Vision System (Xenogen), CFX manager, Step1 softwarev2.3.Microsoft excel was used to calculate mean, standard deviation, and p value. |

For manuscripts utilizing custom algorithms or software that are central to the research but not yet described in published literature, software must be made available to editors/reviewers. We strongly encourage code deposition in a community repository (e.g. GitHub). See the Nature Research guidelines for submitting code & software for further information.

## Data

Policy information about availability of data

All manuscripts must include a data availability statement. This statement should provide the following information, where applicable:

- Accession codes, unique identifiers, or web links for publicly available datasets
- A list of figures that have associated raw data
- A description of any restrictions on data availability

Source data for Figures 2-4 and Extended Data Figures 1-8, 10 are provided with the paper.

# Field-specific reporting

Please select the one below that is the best fit for your research. If you are not sure, read the appropriate sections before making your selection.

☒ Life sciences ☐ Behavioural & social sciences ☐ Ecological, evolutionary & environmental sciences

For a reference copy of the document with all sections, see nature.com/documents/nr-reporting-summary-flat.pdf

# Life sciences study design

All studies must disclose on these points even when the disclosure is negative.

| | |
|---|---|
| Sample size | Power analysis (what method of power analysis) was used as method to determine sample size where ever was appropriate. |
| Data exclusions | No data was excluded from analysis. |
| Replication | All experiments were repeated minimum with 3 replicates with reproducible results. No replicates were excluded. |
| Randomization | All mice were randomly allocated to the experimental groups |
| Blinding | Investigators were blinded during data collection and analysis for the following experiments:<br>1. Gene expression analysis of Fwe using RNA collected from laser-capture microdissected FFPE human cancer samples, and qPCR apoptosis gene microarray (Fig 2 A-C). |

# Reporting for specific materials, systems and methods

We require information from authors about some types of materials, experimental systems and methods used in many studies. Here, indicate whether each material, system or method listed is relevant to your study. If you are not sure if a list item applies to your research, read the appropriate section before selecting a response.

## Materials & experimental systems

| n/a | Involved in the study |
|---|---|
| ☐ | ☒ Antibodies |
| ☐ | ☒ Eukaryotic cell lines |
| ☒ | ☐ Palaeontology |
| ☐ | ☒ Animals and other organisms |
| ☒ | ☐ Human research participants |
| ☒ | ☐ Clinical data |

## Methods

| n/a | Involved in the study |
|---|---|
| ☒ | ☐ ChIP-seq |
| ☐ | ☒ Flow cytometry |
| ☒ | ☐ MRI-based neuroimaging |

## Antibodies

| | |
|---|---|
| Antibodies used | 2 Anti-Flower Primary Antibodies; a) Anti-Win Ab; Dilution: 1:500 and b) Anti-N-ter Ab; Dilution: 1:500<br>Secondary Ab used for tissue immunohistochemistry: Goat Anti-Mouse IgG HRP-conjugated (Thermo Fisher Sci); Dilution: 1:2000<br>Secondary Ab used for tissue immunofluorescence and immunocytochemistry: Goat Anti-Mouse IgG Alexa Fluor 488 (Thermo Fisher Sci); Dilution: 1:1000 |
| Validation | The antibodies were custom synthesized in partnership with Genscript, USA. All the antibodies were authenticated and validated as part of custom order by Genscript. We have also validated the specificity of our antibodies and presented data in manuscript in the following immunocytochemistry experiments:<br>1. Anti-Fwe-Win Antibody: Positive signal observed in MCF-7 hFwe KO cells+hFwe-Win isoforms and negative signal in MCF-7 hFwe KO cells and MCF-7 hFwe KO cells+hFwe-Lose isoforms.<br>2. Anti-N-ter Antibody: Positive signal observed in MCF-7 hFwe KO cells+hFwe-Win/Lose isoforms and no signal detected in MCF-7 hFwe KO cells. |

## Eukaryotic cell lines

Policy information about cell lines

| | |
|---|---|
| Cell line source(s) | The following cell lines included in this study were obtained from ATCC: A2780-CR, A2780-CS, CCL-218, DU-145, HCC-1954, HCT-116, MCF-7, MCF 10A, MD-4, MD-7, MDA-MB-231, MDA-MB-468, PC-3, SK-BR-3, TR-127, TR-182, ZR-75. HEK293 were obtained from Cell Biolabs, Inc. OVCAR-4, OVCAR-8 were kindly provided by Selvendiran Karuppaiyah, Ohio State University. Normal epithelial cells and fibroblasts isolated from normal breast tissue were kindly provided by Harikrishna Nakshatri, |

| | |
|---|---|
| | Komen Tissue Bank, Indiana University Purdue University Indianapolis. |
| Authentication | All cell lines were authenticated or received with certificates for authentication. |
| Mycoplasma contamination | All cells were tested and were certified as negative for mycoplasma contamination. |
| Commonly misidentified lines (See ICLAC register) | No commonly misidentified cell lines as per ICLAC were included in this study. |

## Animals and other organisms

Policy information about studies involving animals; ARRIVE guidelines recommended for reporting animal research

| | |
|---|---|
| Laboratory animals | Female and male Swiss nude mice age 4-6 weeks; female Fwe-Knockout and Fwe-Wildtype C57BL/6 mice age 4-6 weeks were used in this study. |
| Wild animals | No wild animals were included in this study. |
| Field-collected samples | No field-collected samples were included in this study. |
| Ethics oversight | All animal work was approved by Institutional Animal Care and Use Committee (IACUC) affiliated with Dartmouth College and Institutional Animal Ethics Committee at Champalimaud Foundation. |

Note that full information on the approval of the study protocol must also be provided in the manuscript.

## Flow Cytometry

### Plots

Confirm that:

☒ The axis labels state the marker and fluorochrome used (e.g. CD4-FITC).

☒ The axis scales are clearly visible. Include numbers along axes only for bottom left plot of group (a 'group' is an analysis of identical markers).

☒ All plots are contour plots with outliers or pseudocolor plots.

☒ A numerical value for number of cells or percentage (with statistics) is provided.

### Methodology

| | |
|---|---|
| Sample preparation | All samples were prepared as described in the Methods section. |
| Instrument | Amnis ImageStream MK II Imaging, Becton Dickinson FACS ARIA Fusion, Becton Dickinson FACS ARIA IIIu, Becton Dickinson-LSRII H274, MACSQuant Analyzer, LSR Fortessa X20, BD FACS Aria Fusion, BD FACS ARIA III |
| Software | FlowJo.V9, FlowJo.V10 |
| Cell population abundance | High purity sorted samples were used in the study. |
| Gating strategy | All preliminary FSC/SCC gates to remove debris and other events of the starting cell population and boundaries between positive and negative staining cell populations are defined. Gating strategies are explained in in detail in the legends and methods sections. Fig ED10D presents a figure exemplifying the gating strategy. |

☒ Tick this box to confirm that a figure exemplifying the gating strategy is provided in the Supplementary Information.



**ITQB NOVA, Avenida da República, 2780-157 Oeiras, Portugal** | Tel +351 214 469 100 | itqb.unl.pt